Lattices of Shiba states in supramolecular architectures

Yingzheng Gao

PSL UNIVERSITÉ PARIS

THÈSE DE DOCTORAT
DE L'UNIVERSITÉ PSL

Préparée à ESPCI
Laboratoire de Physique et d'Étude des Matériaux
Quantum Specs Group

Lattices of Shiba states in supramolecular architectures (Réseau d'impuretés Shiba dans des réseaux supramoléculaires)

Soutenue par
Yingzheng GAO
Le 01 Feb 2023

École doctorale n°564
École Doctorale Physique en Île-de-France

Spécialité
Quantum physics of condensed matter

Composition du jury :

Lucas De' Medici Prof., LPEM-ESPCI	Président
Laurence Masson Prof., CINaM Marseille	Rapportrice
Fabien Silly Chercheur HDR, CEA Saclay	Rapporteur
Claude Chapelier Chercheur HDR, CEA Grenoble	Examinateur
Stéphane Pons Chercheur, LPEM-ESPCI	Co-directeur de thèse
Dimitri Roditchev Prof., LPEM-ESPCI	Directeur de thèse

ESPCI PARIS | PSL

Introduction

Interaction between local moments and itinerant electrons may give rise to the magnetic polarization of the Fermi sea and/or to more exotic phenomena near Fermi level such as a mass renormalisation of the conduction electrons and a non magnetic ground state due to the Kondo effect. Once superconductivity is introduced into the system, the magnetic moment of the impurity, if rigid enough, can induce Yu-Shiba-Rusinov states which may form new topological states when coupled to each others. These phenomena have been widely studied in recent years, as they are central to design emerging spintronics devices and quantum-based technology. In this context, magnetic molecules forming hybrids with superconductors are promising building blocks of these kinds of devices. However the fundamental properties of supramolecular assemblies of magnetic molecules on normal or superconducting metal surfaces are still to be studied. In this thesis we have used scanning tunneling microscopy/spectroscopy (STM/STS) techniques to study organization, electronic, magnetic and superconducting properties of magnetic self-assembled supramolecular systems on normal and superconducting metal surfaces.

In the first two chapters, we introduce the knowledge on the interactions of magnetic impurities deposited on normal and superconducting metal surfaces. Then we present the experimental and numerical techniques that were used to prepare the samples, acquire the data and analyze them. The experimental setup is also briefly described.

In the following chapters, we detail the results obtained during the study of the structural and electronic properties of:

1. $\mathrm{Fe-DPyDBrPP}$ molecules on Au(111) surface
2. $\mathrm{Fe-DBrDPP}$ molecules on superconducting Pb(110) surface

In the first case, the magnetic $\mathrm{Fe-DPyDBrPP}$ molecules are deposited on Au(111) surface. We reported the reversible transition from S = 1 spin state to mixed-valence state. We have shown that the spin state transition is controlled by the adsorption site which can induce charge fluctuations. By manipulating the molecules with the microscope tip, we also succeeded in controlling the induced charge fluctuations, fabricating intermediate states with mixed-valence properties.

In the second case, we studied the magnetic $\mathrm{Fe-DBrDPP}$ molecule, whose spin state is S = 1, on the surface of superconducting Pb. We found several self-assembled supramolecular systems (orders "4mer", "0B" and "1B"). The "4mer" molecules have the weakest coupling to

the substrate due to the formation of a compact lattice. They show only inelastic spin excitation signature (SF) in the low energy spectra, indicating that magnetic anisotropy dominates the coupling with the substrate. Both "0B", "1B" molecules are strongly coupled to the substrate, resulting in two Shiba states in the gap. From our analysis, the two Shiba states originate from different molecular orbitals with different orbital characteristics. In addition, we also found that the local environment of the molecule also plays an important role in the electronic properties of the molecule. For the "0B" molecule, the inter-molecular interaction can make the "0B" molecule extremely sensitive to external perturbations and in particular to the presence of the microscope tip. We have been able to observe the evolution of the excitation characteristic of SF towards Shiba physics under the effect of the interaction with the tip. During the evolution, we observed an intermediate regime where the SF signature outside the gap and the Shiba state coexist.

The results we have presented in this thesis should help us to better understand the relationship between the structure of porphyrin-based magnetic supramolecular systems deposited on metals and superconductors on their electronic properties. The emerging charge effect induced by the structural conformation and the interaction with the substrate observed in both systems could eventually be used for spin state control, which is essential for the development of molecular spintronic devices.

List of Abbreviations

$\mathrm{Fe-DBrDPP}$	Fe 5,15-dibromo-10,20-diphenyl porphyrin
$\mathrm{Fe-DPyDBrPP}$	Fr 5,15-dipyridyl-10,20-dibromophenyl porphyrin
2D/3D	Two dimensional/Three dimensional
BCS	Bardin-Cooper-Schrieffer
CS1/CS2	Channel 1/2 Shiba states
DOS	Density of States
FM/AFM	Ferromagnetic/Antiferromagnetic
FOA/FOB	molecular Frontier orbital A/B
OMBE/MBE	(Organic)Molecular-Beam-Epitaxy
IR1/IR2	Intermediate-Regime 1/2
MIM	Metal-Insulator-Metal
NRG	Numerical renormalization group
RKKY	Ruderman-Kittel-Kasuya-Yosida
SC	Superconductor
SF	Spin-Flip
SIS	Superconductor-Insulator-Superconductor
SO/SOI/SOC	Spin-Orbit/Spin-Orbit Interaction/Coupling
STM/STS	Scanning tunneling microscopy/spectroscopy
UHV	Ultra High Vacuum
YSR	Yu-Shiba-Rusinov

List of Symbols

D	Uniaxial magnetic anisotropy
E	Transverse magnetic anisotropy
k_B	Boltzmann Constant
T	Temperature
T_c	Critical temperature
e	Electron charge
m	Free electron mass
I	Current
V	Voltage
dI/dV	Conductance
Δ	Superconducting gap width
E_F	Fermi energy
E_b	Bound state energy
ϕ	Electrical potential
ψ	Wave function

Contents

Chapter 1

Magnetic impurities on metal surface

1.1 Introduction

Interaction between local moments and itinerant electrons may give rise to the magnetic polarization of the Fermi sea [1–3] and/or to more exotic phenomena near Fermi level such as a mass renormalization of the conduction electrons and a non magnetic ground state due to the Kondo effect. Once superconductivity is introduced into the system, the magnetic moment of the impurity, if rigid enough, can induce Yu-Shiba-Rusinov states (latter called Shiba states) which may form new topological states when coupled to each others. These phenomena are widely studied in recent years, as they are central to design emerging spintronics devices and quantum-based technology.

In this chapter we will introduce the basic theoretical aspects of the interaction between magnetic moment and conduction electrons in normal metals and superconductors.

At the first stage shown in section (1.2), we consider the case of conduction electrons in a normal metal which can be considered as quasi-free electron gas. We will start with the introduction of impurity problem where Kondo effect is raised (section (1.2.1)) and then the Anderson impurity model used to describe Kondo effect (sections (1.2.2) and (1.2.3)). After that we will study the interaction between a spin-1/2 impurity with conduction electrons and understand the formation of Kondo ground state in section (1.2.4), then in section (1.2.5) we will extend the study to a spin-1 impurity and examine the effect of magnetic anisotropy, hybridization and charge fluctuations on spin state of impurity by looking at simulated excitation spectrum. In the end of first stage we will discuss about multiple impurities problem in section (1.2.6) and acquire the basic understanding of impurity lattice.

At the second stage shown in section (1.3), we adopt the same structure as first stage but we consider the conduction electrons in a superconductor which can no more be considered as quasi-free electron gas. We will start with the introduction of superconductivity phenomena (section (1.3.1)) and the BCS theory that explains superconductivity in a microscopic view (section (1.3.2)). After that we will introduce Yu-Shiba-Rusinov magnetic bound state which is a result of interaction between spin-1/2 impurity with superconductor in section (1.3.3), then in section (1.3.4) we will extend the study to a spin-1 impurity interacting with superconductor in

which we study the simulated excitation spectrum and corresponding ground state and excited states. In the end of second stage, we will also discuss about the impurity lattice problem for a superconductor in section (1.3.5).

At final stage shown in section (1.4), we will introduce the concept of self-assembled magnetic molecule system that we propose to study throughout this thesis.

1.2 Magnetic impurity in interaction with a normal metal

Strongly correlated systems have drawn great attention in condensed matter physics in cases when many-body interaction dominates the kinetic energies, giving rise to exotic material behavior such as Mott insulator, heavy fermion electronic systems, fractional quantum Hall systems... One important class of the many-body interactions is the interaction between local magnetic moments and conduction electrons. This usually refers to impurity problem where magnetic impurities are present in the normal (non superconducting) metal.

The problem of impurities dates back to the early 1930s. In 1934 de Haas et. al. [4] had discovered that the electrical resistivity of gold wires does not decrease monotonically as temperature decreases but rather increase below a characteristic temperature. This strange upturn of resistivity is in contrast with understanding that resistivity is caused by scattering of conduction electrons by nuclei that vibrates around their equilibrium lattice positions, as temperature decreases, the lattice vibration is suppressed and resistivity should decrease monotonically to a constant value. In 1964, Jun Kondo successfully explained the abnormal resistivity behavior at low temperature by considering interaction between magnetic impurities inside the metals with conduction electrons. Kondo had adopted a perturbation approach by using the so-called Kondo model [5] and found a logarithmic divergence of resistivity below a characteristic temperature T_K (now called Kondo temperature) as magnetic impurities open a new scattering channel.

1.2.1 Kondo effect

The general condition for developing the Kondo effect is that the internal degree of freedom of an impurity state is degenerate and allows spin reversal ($\Delta_s = \pm 1$). For example, in Fig. 1.1), the spin degree of freedom is involved when a 3d state at $E_F - \epsilon_d$ of a magnetic atom is singly occupied (S = 1/2) and interacts with the conduction electrons of the metal sample. In this case, the hybridization causes broadening of the 3d level spanning over an energy Δ and the on-site Coulomb repulsion U prevents double occupation of the 3d level.

The scattering process of the Kondo effect is illustrated in Fig. 1.1 (b) where the unpaired electron in the 3d state and a conduction electron flip their spin via virtual intermediate states. As a result of this scattering process, a resonance emerges at the Fermi level in the density of states. This resonance is called Abrikosov-Suhl resonance [7–9] or Kondo resonance. It is localized at the Fermi energy, indicating a zero energy cost for the elastic spin reversal of the impurity. The width and shape of the resonance determine the Kondo temperature (T_K) of the system. This is

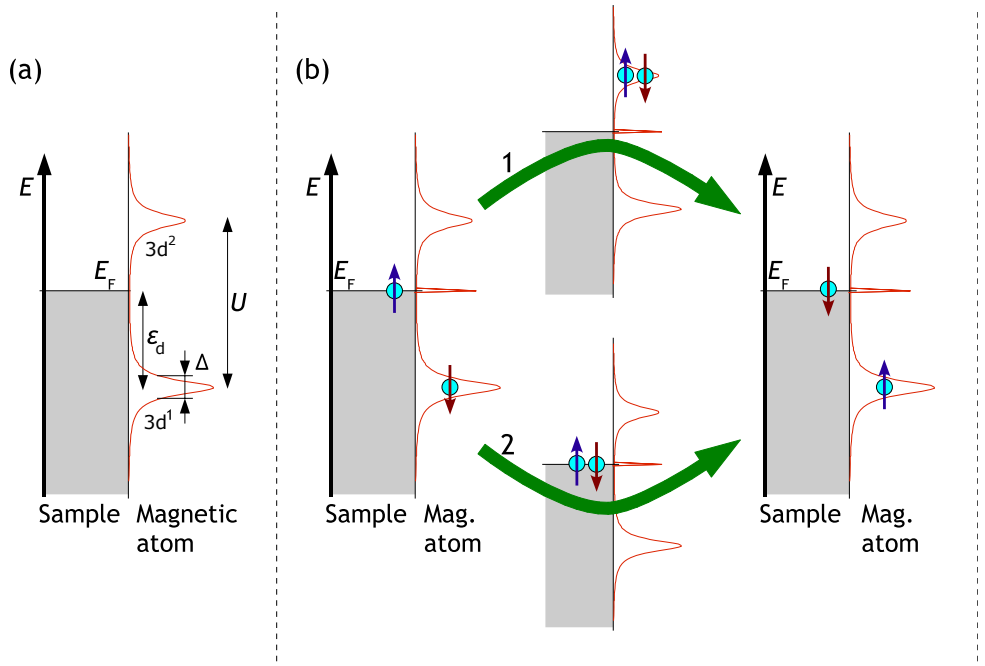

Figure 1.1: Microscopic view of Kondo effect. (a) Energy-dependent LDOS of a magnetic atom embed in normal metal. (b) The spin of the singly occupied 3d state can be flipped by a conduction electron with opposite spin near Fermi level through two intermediate states 1 or 2 where 3d state is fully occupied or empty. Image adapted from [6].

the most common Kondo effect, where only the spin degree of freedom is involved and it is also called the spin-Kondo effect. The spin-Kondo effect has been extensively studied theoretically and experimentally over the past decades.

Other degrees of freedom like orbital quantum number can also give rise to so-called orbital Kondo effect ([10]) where degenerate orbitals response for elastic spin flip process. The SU(4) (Spin-1/2 $\bigotimes$ Orbital = SU(4)) Kondo effect has been discovered in metal surface [11], quantum dots [12, 13], carbon nanotubes [14] and possibly molecular systems [15].

1.2.2 Anderson impurity model

In order to describe the Kondo effects we adopt the Anderson impurity model proposed by Anderson in 1961 [16] for which a single two-level impurity interacting with conduction electrons can be written as:

$$H = \sum_{k,\sigma} \epsilon_k c^\dagger_{k\sigma} c_{k\sigma} + \epsilon_d \sum_\sigma d^\dagger_\sigma d_\sigma + U d^\dagger_\uparrow d_\uparrow d^\dagger_\downarrow d_\downarrow + \sum_{k,\sigma} V_k (c^\dagger_{k\sigma} d_\sigma + h.c) \tag{1.1}$$

where the first term is the Hamiltonian that describes the kinetic energy of the conduction electrons in a normal metal, the next two terms describe the impurity energy levels with on-site Coulomb repulsion, the last term is called hybridization term and describes the hybridization between impurity level with conduction electrons.

Other terms can also be introduced depending on the specific systems. For instance, Hund's coupling and inter-orbital Coulomb repulsion need to be considered for a high spin impurity

showing degenerate levels. Also, an impurity adsorbed on a metal surface usually exhibits a non-null magnetic anisotropy which lifts the degeneracy of the impurity levels because of the crystal field splitting induced by the breaking of crystal inversion symmetry at the surface. Another example is the case of a system composed of multiple impurities where the spin-spin interaction between impurities should be included in the Hamiltonian.

1.2.3 Impurity deposited on a metal surface

In our work, we used a scanning tunneling microscope (STM) to study magnetic molecules adsorbed on metal surfaces, hence we will focus our discussion on the systems consisting of magnetic impurities adsorbed on metal surfaces (Fig. 1.2 (a)). Top figure of Fig. 1.2 (b) shows a typical schematic energy level of spin-1 nanomagnet with non zero uniaxial anisotropy D and transverse anisotropy E, the bottom figure of (b) illustrate the conductance behavior of such magnet as a function of bias voltage obtained in tunneling experiments.

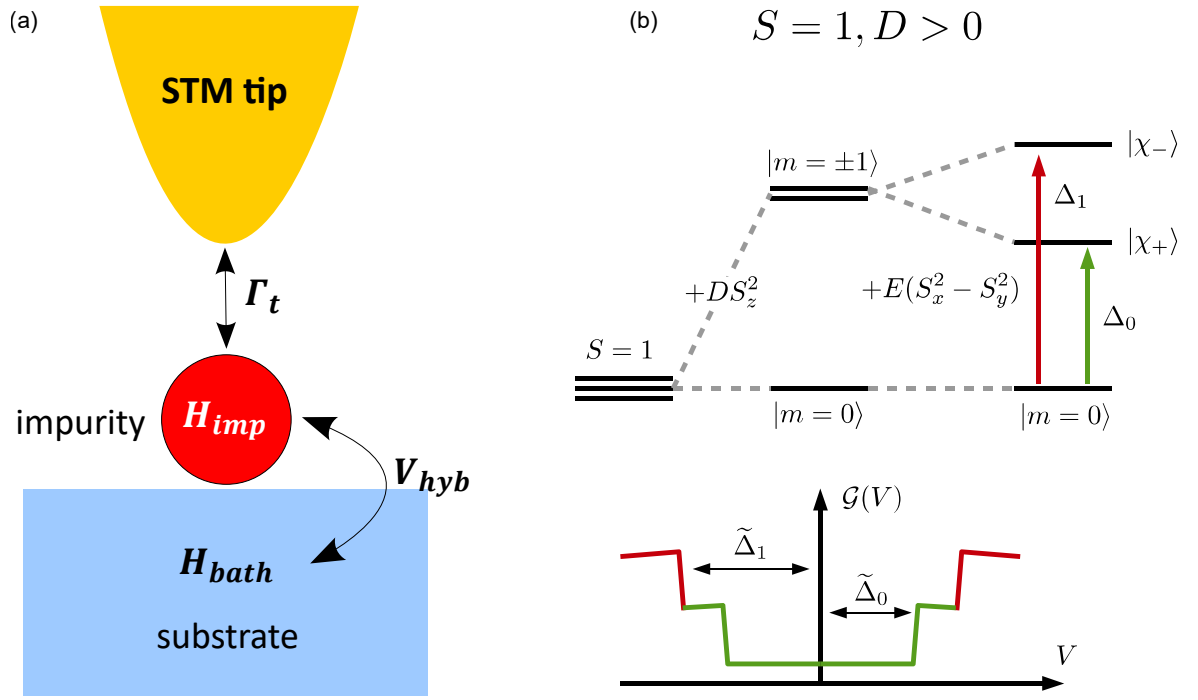

Figure 1.2: Scanning tunneling spectroscopy experiment of a magnetic impurity adsorbed on metal surface. (a) Schematic model of STM experiment. Γ_t is the tunneling rate of electrons between the STM tip and impurity levels described by H_{imp}, Γ_t is weak with respect to the hybridization V_{hyb} between impurity and conduction electrons in metal substrate described by H_{bath}. (b) Top: Illustration of splitting of spin-1 impurity state in presence of non-zero magnetic anisotropy with D the uniaxial anisotropy and E the transverse anisotropy. Bottom: schematic tunneling conductance spectrum showing two symmetric conductance steps with respect to the Fermi level corresponding to the two spin excitations illustrated in upper figure. Image adapted from [17].

Here, we adopt the multi-orbital Anderson model used in David Jacob's work [17, 18] because it is trustfully reproducing our observed results.

$$H = H_{imp} + H_{bath} + V_{hyb} \tag{1.2}$$

The full Hamiltonian is divided into four parts: H_{imp} represents the Hamiltonian describing the spin impurity possessing multiple unpaired electrons in d orbitals, H_{bath} the Hamiltonian describing the conducting electrons in the reservoir and V_{hyb} the hybridization term describing the coupling between spin impurity with conduction electrons. The impurity Hamiltonian is thus:

$$H_{imp} = \epsilon_d \hat{N}_d + U \sum_{\alpha} \hat{n}_{\alpha\uparrow}\hat{n}_{\alpha\downarrow} + U^{'} \sum_{\alpha\neq\alpha^{'}} \hat{n}_{\alpha}\hat{n}_{\alpha^{'}} - J_H \sum_{\alpha\neq\alpha^{'}} \vec{S}_{\alpha} \cdot \vec{S}_{\alpha^{'}} + D\hat{S}_z^2 + E(\hat{S}_x^2 - \hat{S}_y^2) \quad (1.3)$$

where ϵ_d are the single particle energies of d orbitals, $\hat{N}_d = \sum_{\alpha,\sigma} \hat{n}_{\alpha\sigma}$ the number operator for all d orbitals, $\hat{n}_{\alpha\sigma} = d^{\dagger}_{\alpha\sigma} d_{\alpha\sigma}$ the number operator of single d orbital α with spin σ and $d^{\dagger}_{\alpha\sigma}(d_{\alpha\sigma})$ is the fermionic creation (annihilation) operator, U and $U^{'}$ the intra- and inter-orbital Coulomb repulsion, J_H the Hund's coupling, $\vec{S}_{\alpha} = \sum_{\sigma\sigma^{'}} d^{\dagger}_{\alpha\sigma} \vec{\tau}_{\sigma\sigma^{'}} d_{\alpha\sigma^{'}}$ the total spin of d orbital α, D and E the uniaxial anisotropy and in-plane (transverse) anisotropy. The second term in equation (1.2) describes the conduction electrons in a normal metal:

$$H_{bath} = \sum_{k,\alpha,\sigma} \epsilon_{k\alpha} c^{\dagger}_{k\alpha\sigma} c_{k\alpha\sigma} \quad (1.4)$$

where $\epsilon_{k\alpha}$ is the energy of conduction electrons with momentum k and spin σ that couple to d orbital α. And the third term in equation (1.2) denotes hybridization term between impurity with conduction electrons:

$$V_{hyb} = \sum_{k,\alpha,\sigma} V_{k\alpha}(c^{\dagger}_{k\alpha\sigma} d_{\alpha\sigma} + h.c) \quad (1.5)$$

The hybridization function is then written as:

$$\Delta^{hyb}_{\alpha}(\omega) = \sum_{k} \frac{\mid V_{k\alpha} \mid^2}{\omega + \mu - \epsilon_{k\alpha} + i\eta} \quad (1.6)$$

The imaginary part of the hybridization function $\Gamma_{\alpha} = -\mathrm{Im}\Delta_{\alpha}$ is used to describe the exchange coupling strength between orbital α and the conduction electrons. Strictly speaking the hybridization Γ differs from the exchange coupling J_K adopted in Kondo model, but Kondo model and Anderson model [16] are in fact equivalent through Schrieffer-Wolff transformation [19] and J_K is directly proportional to Γ, thus in this work the physical meaning of these two physical quantities can be substituted.

1.2.4 spin-1/2 impurity

Now we can estimate the evolution of the ground state of a magnetic impurity on a surface due to the hybridization with the surface conduction electrons by considering a simple model solved by Fulde [20]. In this model, a singly occupied orbital (S = 1/2) couples to a singly occupied orbital of a metal. The energies of two orbitals are ϵ_d and ϵ_{metal} with $\Delta\epsilon = \epsilon_{metal} - \epsilon_d > 0$. It is reasonable to make some assumptions where: 1). The impurity has a rigid spin S = 1/2 by setting

$U \to \infty$. 2). The inter-orbital Coulomb interaction $U^{'}$ is neglected. 3). the hybridization V between the two orbitals is weak ($V << \Delta\epsilon$). 4). the out of plane and in-plane magnetic anisotropy energies D and E are neglected as a spin-1/2 system is not influenced by them. Then the Hamiltonian describing the two-level system is:

$$H = \epsilon_d \sum_\sigma d^\dagger_\sigma d_\sigma + U\hat{n}^d_\uparrow \hat{n}^d_\downarrow + \epsilon_{metal} \sum_\sigma c^\dagger_\sigma c_\sigma + V \sum_\sigma (c^\dagger_\sigma d_\sigma + h.c) \tag{1.7}$$

In order to advance in the understanding, we first turn off the hybridization ($V = 0$) and look for the eigenstates of the spin. The ground state has energy $\epsilon_d + \epsilon_{metal}$ and consists of a singlet (S = 0) and three fold degenerate triplet (S = 1) (Fig. 1.3 (a)). The system has one excited state of energy $2\epsilon_{metal}$.

Once the hybridization V is turned on, the singlet state and the excited state are coupled, giving rise to a new ground state of energy $\epsilon_d + \epsilon_{metal} - \frac{2V^2}{\Delta\epsilon}$ and a new excited state of energy $2\epsilon_{metal} + \frac{2V^2}{\Delta\epsilon}$ (Fig. 1.3 (b)).

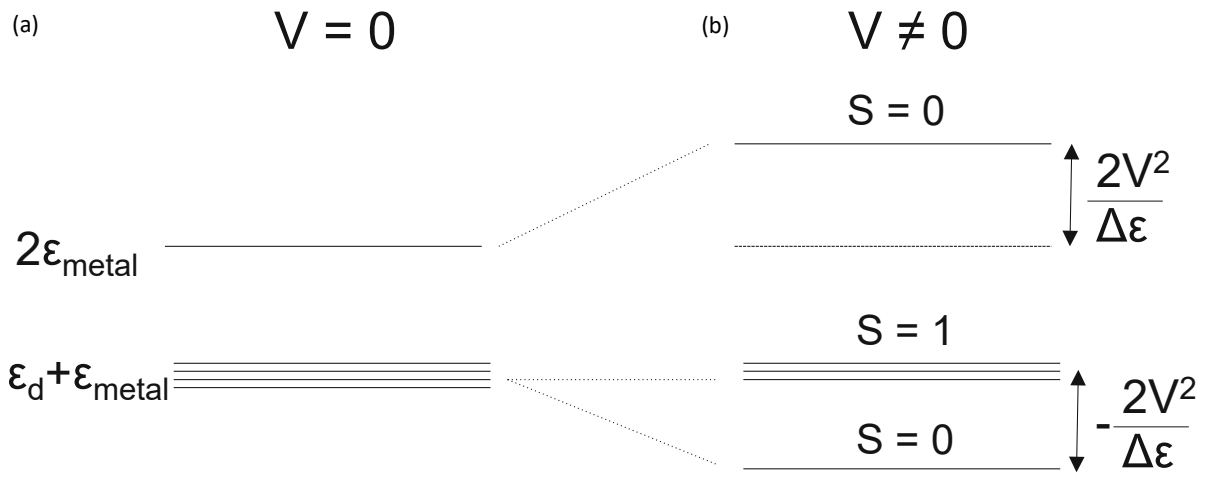

Figure 1.3: Simple model illustrating the evolution of the ground state due to hybridization. Two unpaired electrons localized in a d orbital of the impurity and metal orbital with energies ϵ_d and ϵ_{metal} respectively. The on-site Coulomb interaction on the d state is infinity so that the double occupancy is forbidden. Coulomb interaction in the metal is neglected. Inter-orbital Coulomb interaction is also neglected. (a) When the hybridization is off, $V = 0$, the ground state has four fold degeneracy with energy $\epsilon_d + \epsilon_{metal}$, indicating four configurations with two electrons in two different orbitals. The singlet excited state has energy $2\epsilon_{metal}$, indicating double occupancy of metal orbital. (b) When hybridization is non-null $V \neq 0$, S = 0 singlet state becomes the new ground state, indicating the hybridization favors a non-magnetic ground state for spin-1/2 impurity. Image adapted from [21].

1.2.5 spin-1 impurity

So far we have considered the spin-1/2 impurity problem where the resonance at the Fermi level is the result of a single electron coupled with conduction electrons. In the following we present the case of a spin-1 impurity with two unpaired electrons coupled with the conduction electrons. To do so, we will evaluate the ground state and simulate the tunneling conductance spectra of

an impurity of S = 1 in a metal following the approach adopted by David Jacob [18] using the equation (1.2) [1]

It should be noted that in the following discussion two channels (d orbitals) are considered to be identical, i.e. same energy ϵ_d and same hybridization with conduction electrons Γ_α. [2]

Effect of magnetic anisotropy

We first evaluate the effect of the magnetic anisotropy on the ground state of a spin-1 impurity. Unlike the spin-1/2 case which always exhibits double degenerate states [26], spin-1 impurity has a triplet ground state characterized by $m_z = 0, \pm 1$. With non-null out of plane and in-plane magnetic energy anisotropy ($D \neq 0$ and $E \neq 0$, respectively), the degeneracy of the triplet state is lifted. The uniaxial anisotropy D lifts the degeneracy between $|m_z = 0\rangle$ and $|m_z = \pm 1\rangle$ states, depending on the sign of D the ground state can be a singlet ($|m_z = 0\rangle$ for $D > 0$) or a doublet ($|m_z = \pm 1\rangle$ for $D < 0$).

The transverse anisotropy E will further lift the degeneracy of $|m_z = \pm 1\rangle$ doublet resulting a complete split configuration. The splitting of the ground state in presence of positive values of D and E is presented in Fig. 1.2 (b) upper figure. In this precise case, the only possible spin excitation can only occur between $|m_z = 0\rangle$ ground state and the split doublet states $|\chi_-\rangle$, $|\chi_+\rangle$ with excitation energy $\Delta_0 = D+E$ and $\Delta_1 = D-E$ respectively. These spin excitation energy is called inelastic spin excitation (see section 2.2.4) and can be measured by tunneling conductance spectra, giving rise to steps of conductance symmetric with respect to Fermi level [27, 28], as shown in Fig. 1.2 (b) lower figure. The two spin excitations indicated in the upper figure are resolved by two symmetric steps at voltage $\tilde{\Delta}_0/e$ and $\tilde{\Delta}_1/e$ in conductance spectra where $\tilde{\Delta}_0$, $\tilde{\Delta}_1$ are renormalized (effective) spin excitation energy which depend on bare excitation energy Δ_0, Δ_1 (anisotropy parameters D, E), hybridization Γ_α for each orbital and charge fluctuations.

The effect of anisotropy on the dI/dV spectra of spin-1 impurity is presented in Fig. 1.4. The impurity parameters used for simulation are: $U = 3.5$ eV, $U' = 2.5$ eV and $J_H = 0.5$ eV so that the spin-1 ($N_d = 2$) impurity is at particle-hole symmetry point (half-filling condition) where $\epsilon_d^* = -\frac{U}{2} - (U' - \frac{J_H}{2})(N_d - 1) = -4$ eV, the hybridization $\Gamma/\pi = 50$ meV for both orbitals and temperature $k_B T = 0.1$ meV, i.e. $T \approx 1$ K.

In Fig. 1.4 (a) the transverse anisotropy E is set to zero and several positive uniaxial anisotropy $D > 0$ are tested. When D is small, the splitting of triplet ground state is not obvious and we can still observe the Kondo peak (purple line) signature due to the elastic spin flip process occurred in degenerate triplet states. When D becomes larger, the Kondo peak splits and gradually evolves to steps signature shown in Fig. 1.4 (a). This means Kondo effect and inelastic spin excitation have the same magnetic origin and they can not coexist in presence of positive uniaxial

[1] The tunneling conductance spectra obtained in a microscopy experiment reveal the local density of states of the impurity on which spin-flip effects are superimposed (see section (2.2.4)).

[2] In the real case, the Kondo effect of a spin-1 impurity is more complicated as two channels can couple differently with the conduction electrons depending on the orbital geometry. This may result in the so-called underscreened Kondo effect, where only one channel develops a fully screened Kondo effect while the other orbital has a residual spin [22–25] at a given temperature. In the following the underscreened Kondo effect will not be considered.

anisotropy D. This evolution between Kondo peaks and steps signature for spin-1 system has been observed in cobalt complexes in which D is precisely controlled without modifying other parameters [29]. In Fig. 1.4 (b) the effect of transverse anisotropy E is estimated. As E increase the step signature at each side splits to double steps signature, indicating the splitting of excited states $|m_z = \pm 1\rangle$ that leads to different excitation energies $\tilde{\Delta}_0$ and $\tilde{\Delta}_1$. These double steps signature have been observed in several spin-1 impurity [30–33].

For negative uniaxial anisotropy $D < 0$ and zero transverse anisotropy $E = 0$ (not shown here) the ground state is a doublet $|m_z = \pm 1\rangle$. The spin flip can not directly occur between them as $\Delta m_z = 2$, nevertheless spin flip can occur via the excited state $|m_z = 0\rangle$, in this case Kondo effect will coexist with inelastic spin excitation ($|m_z = \pm 1\rangle \rightarrow |m_z = 0\rangle$) and a Kondo peak with two side steps will be observed in conductance spectra [18].

Roughly speaking, the presence of a magnetic anisotropy tends to lift the degeneracy of spin states and suppress the Kondo effect, as a result, the impurity becomes "decoupled" from the metal, this case refers to so-called atomic limit where the system has a well-defined valency and quantized spin (Fig. 1.2 (b)).

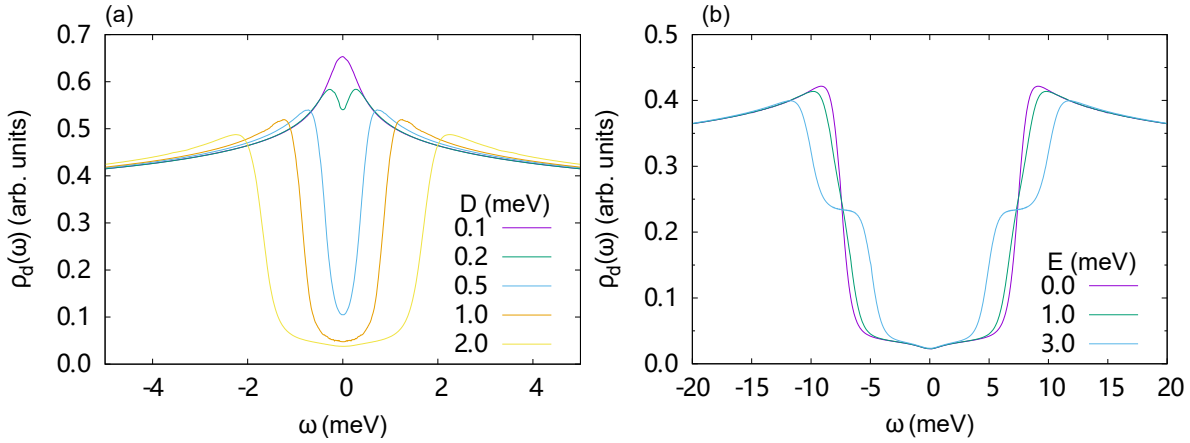

Figure 1.4: Effect of magnetic anisotropy on ground state and calculated spectral intensity for a spin-1 impurity. (a) calculated spectral intensity for several values of uniaxial anisotropy D for interaction parameters: hybridization $\Gamma/\pi = 50$ meV for both orbitals and at temperature $k_B T = 0.1$ meV, i.e. $T \approx 1$ K. (b) calculated spectral intensity for several values of transverse anisotropy E, $D = 8.7$ meV for interaction parameters: hybridization $\Gamma/\pi = 50$ meV for both orbitals and at temperature $k_B T = 0.4$ meV, i.e. $T \approx 4$ K. Image adapted from [18].

Effect of hybridization

For magnetic anisotropy, it tends to lift degeneracy and to "decouple" impurity from the metal, while the coupling strength Γ tends to renormalize magnetic anisotropy and recover the degeneracy [34]. We can estimate the effect of the hybridization Γ on the conductance spectra and on renormalized (effective) spin excitation energies $\tilde{\Delta}_0$, $\tilde{\Delta}_1$ shown in Fig. 1.5 where impurity parameters are the same as that in Fig. 1.2 ($U = 3.5$ eV, $U' = 2.5$ eV, $J_H = 0.5$ eV, $\epsilon_d^* = -4$ eV; with anisotropy parameters: $D = 8.7$ meV, $E = 3$ meV at temperature $k_B T = 0.4$ meV, i.e. $T \approx 4$ K). The choice of anisotropy parameters $D, E = 8.7, 3$ meV corresponds to the typical

values of porphyrin/phthalocyanine based magnetic molecule adsorbed on metal surface [30–33] which are also similar to what we have observed in our work.

From Fig. 1.5 we can find two important points: as the hybridization Γ increases 1). the conductance steps become broader. 2). the conductance steps move toward Fermi level (to lower effective energy). The first point is the direct result of the hybridization to the conduction states, this indicates that we can extract coupling strength Γ by introducing a characteristic parameter that describes the broadening of step function in a fitting procedure. The second point correspond to the reduction of the effective spin excitation energies $\tilde{\Delta}_0$, $\tilde{\Delta}_1$ due to hybridization Γ [35]. It should be noted that even for a quite large value of Γ the stepped structure is completely washed out but Kondo peak feature still not emerges, instead a dip at Fermi level subsists. This is an indication that the uniaxial anisotropy D is hardly overcome by Γ-hybridization, and this was explained by NRG calculations demonstrating that the anisotropy term $D\hat{S}_z^2$ is always enhanced at the lowest energy scales [23, 36].

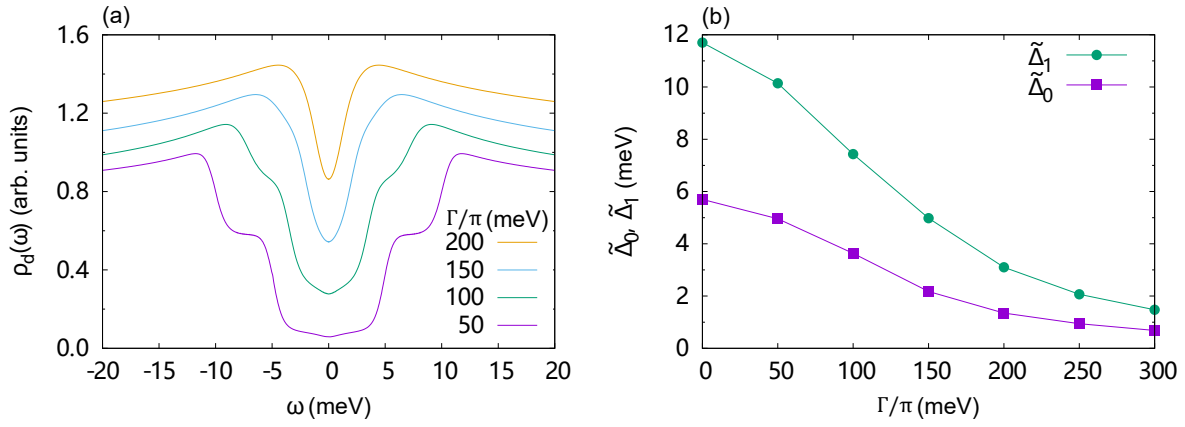

Figure 1.5: Effect of hybridization on the spectral intensity and effective inelastic spin excitation energies of spin-1 impurity. (a) Calculated spectral intensity for several values of hybridization Γ (same for both orbitals). (b) Renormalized inelastic spin excitation energies $\tilde{\Delta}_0$, $\tilde{\Delta}_1$ as function of the hybridization Γ. (a) and (b) anisotropy parameters: $D = 8.7$ meV, $E = 3$ meV, temperature $k_BT = 0.4$ meV, i.e. $T \approx 4$ K. Image adapted from [18].

The simulation results presented above show the competition between magnetic anisotropy and hybridization. The former one tends to lift degeneracy, resulting a SF gap in conductance spectra. The latter one tends to recover degeneracy by renormalising magnetic anisotropy, resulting reduced SF gap size. This competition has been already studied in several systems such as $S = 3/2$ cobalt atom deposited on Cu_2N [34, 37] where cobalt atom shows degenerate quadruplet ground state that is split into a degenerate doublet ground state and a degenerate doublet excited state in presence of magnetic anisotropy (Fig. 1.6 (c)). Depending on the adsorption sites the coupling Γ between impurity with substrate renormalizes anisotropy differently, resulting various values of inelastic spin excitation energy and influences the Kondo signature (Fig. 1.6 (b)).

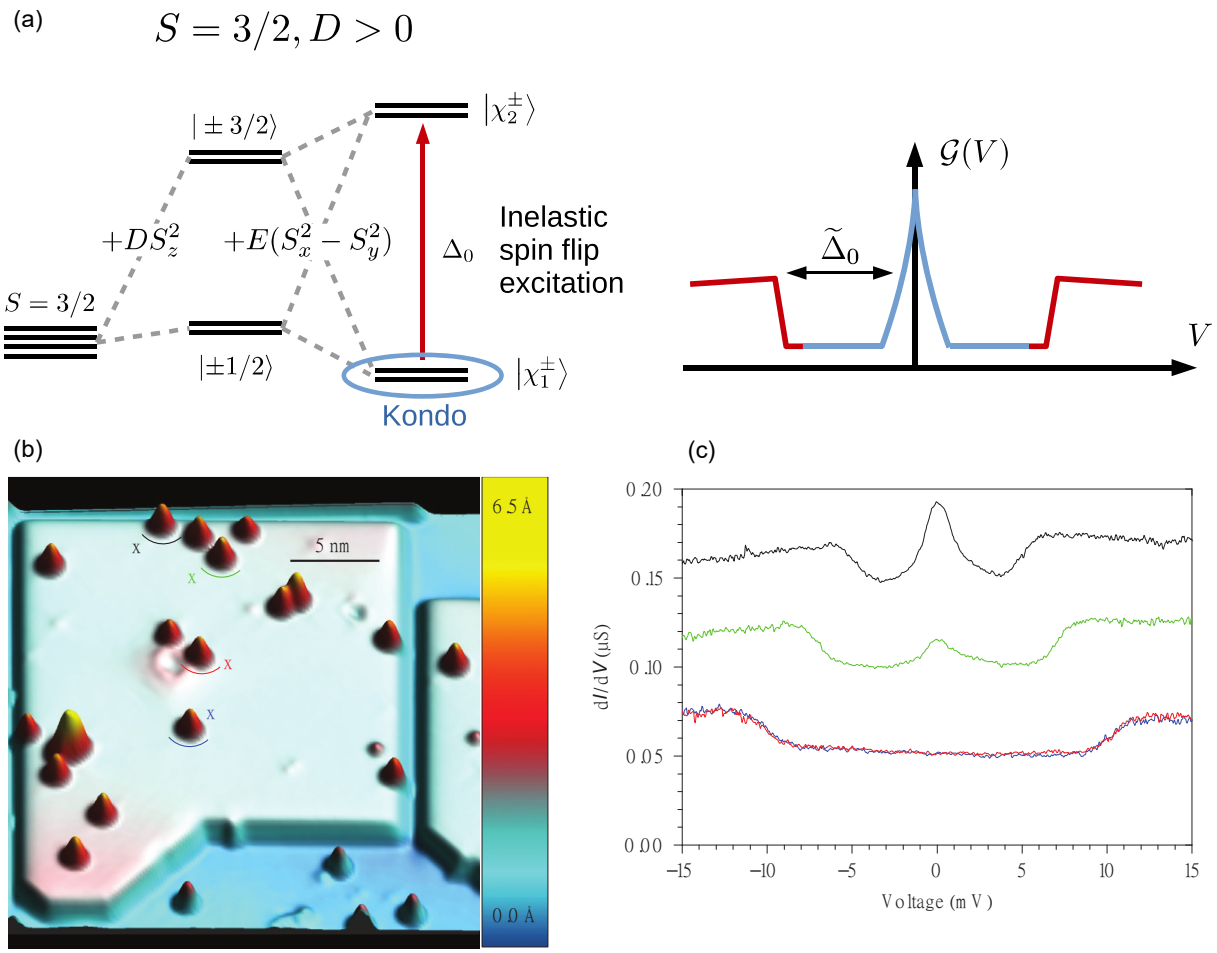

Figure 1.6: Study of Co adatoms on Cu_2N island. (a) Illustration of the evolution of the S = 3/2 quadruplet ground state in presence of non-zero magnetic anisotropy. (b) Topography image of Co adatoms adsorbed on different sites of Cu_2N island (setpoint: 100mV, 100pA). Colored arcs label different Co atoms. (c) dI/dV spectra (setpoint: 15 mV, 1 nA) taken on four Co atoms of corresponding colors in (b), spectra shifted for clarity. The Co atoms near the island edge (black and green) have a higher coupling strength than those at center (red and blue), resulting lower magnetic anisotropy (steps closer to Fermi level) and stronger Kondo peak. Experimental results taken from [34].

Effect of charge fluctuations

So far we have considered only the half-filling (particle-hole symmetry) condition for a spin-1 impurity [3]. In reality the hybridization can also shift the impurity level away from the Fermi level due to charge fluctuation of an energy $\delta\epsilon_d$. The example taken here correspond to a negative charge fluctuation from the metallic reservoir, $\delta\epsilon < 0$, so that the d level moves deeper with respect to the Fermi energy. The resulting total charge on the impurity is then larger than 2, $N_d = 2 + \delta N$. As we consider the perturbation of a spin-1 impurity with two half-filled d orbitals contacting with metallic reservoir, receiving a charge δN will reduce the total momentum supported by impurity:

$$\langle S^2 \rangle_{N_d} = (1 - \delta N)\langle S^2 \rangle_{N=2} + \delta N \langle S^2 \rangle_{N=3} \tag{1.8}$$

[3] where impurity parameters are $U = 3.5$ eV, $U' = 2.5$ eV, $J_H = 0.5$ eV and $N_d = 2$ so that $\epsilon_d^* = -\frac{U}{2} - (U' - \frac{J_H}{2})(N_d - 1) = -4$ eV

The reduction of total momentum will also reduce magnetic anisotropy D, E because $N = 3$ corresponds to the spin = 1/2 case which is immune to magnetic anisotropy. Hence the inelastic spin excitation energies will be renormalized by the momentum reduction:

$$\tilde{\Delta}_n(\Gamma, \mathrm{N_d}) = (1 - \delta \mathrm{N})\tilde{\Delta}_\mathrm{n}(\Gamma, \mathrm{N} = 2) \qquad \text{with} \quad \mathrm{n} = 0, 1 \tag{1.9}$$

Fig. 1.7 (a) shows the simulated spectra of a spin-1 impurity for several values of detuning energy $\delta\epsilon$ by using same parameters as in Fig. 1.5. The effect of increasing the detuning energy $\mid \delta\epsilon \mid$ is first similar to that of hybridization (Fig. 1.5 (a)) where the step features move closer to Fermi energy, indicating a renormalization of the inelastic spin excitation energies $\tilde{\Delta}_0$, $\tilde{\Delta}_1$ due to charge fluctuation. Secondly the spectra become more and more asymmetric as $\mid \delta\epsilon \mid$ increases due to the breaking of particle-hole symmetry by charge fluctuation. Increasing the asymmetry yields a spectral lineshape similar to Fano lineshapes commonly attributed to the emergence of Kondo effect in tunneling conductance spectroscopy experiments (see Fig. 2.12). However here, the Fano-like lineshape (orange curve in Fig. 1.7 (a)) is simply explained by inelastic spin excitations in presence of charge fluctuation.

Fig. 1.7 (b) displays the effective inelastic spin excitation energies $\tilde{\Delta}_0$, $\tilde{\Delta}_1$ and the impurity charge $\langle N_d \rangle$ as function of the detuning energy $\delta\epsilon$. The dash lines indicate the reduction of the inelastic spin excitation energies according to equation (1.9) where only the effect of the reduction of the momentum is considered. For small detuning energy (charge fluctuation) the dash line fits well with solid line, indicating that the renormalization of the inelastic spin excitation energies is mainly the effect of spin reduction. For large detuning energy, the deviation between solid and dash lines becomes significant, indicating that in addition to the momentum reduction, the charge fluctuation directly contributes to the renormalization of the inelastic spin excitation energies.

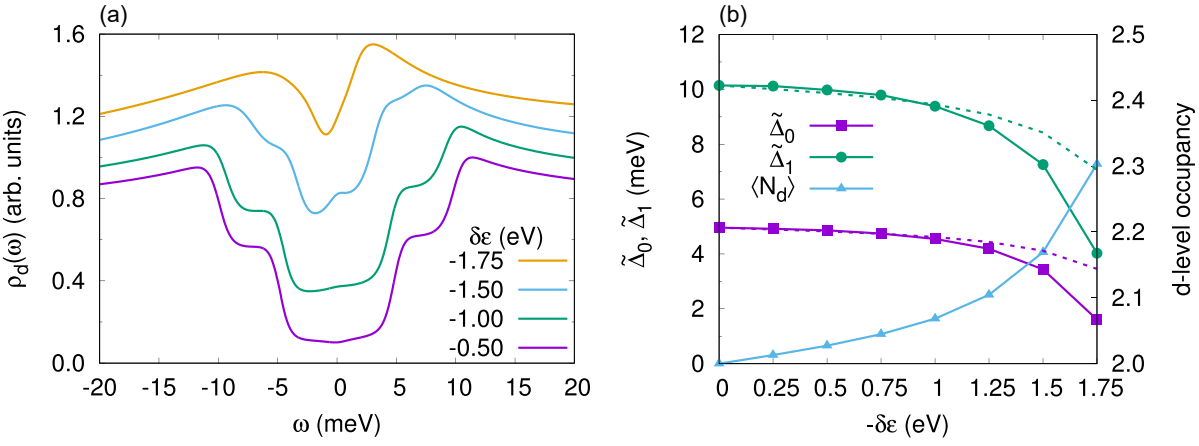

Figure 1.7: Effect of the charge fluctuations on the calculated spectral intensity and effective elastic spin excitation energies of a spin-1 impurity. (a) calculated spectral intensity for several values of detuning energy $\delta\epsilon$. Anisotropy parameters are $D = 8.7$ meV, $E = 3$ meV with hybridization $\Gamma/\pi = 50$ meV and at temperature $k_B T = 0.4$ meV, i.e. $T \approx 4$ K. spectra have been normalized and shifted for clarity. (b) Renormalized inelastic spin excitation energies $\tilde{\Delta}_0$, $\tilde{\Delta}_1$ and impurity charge $\langle N_d \rangle$ as function of detuning energy $\delta\epsilon$. Dashed lines correspond to the renormalization only due to the reduction of the spin according to (1.9). Image adapted from [17].

Thus the charge fluctuations due to particle-hole symmetry breaking plays a similar role to hybridization that can renormalize magnetic anisotropy. Furthermore, charge fluctuation can asymmetrize the spectra, resulting a Fano-like spectral shape in a inelastic spin excitation, this should be carefully handled because Kondo and inelastic spin flip represent two different phenomena.

To end the discussion about spin-1 impurity, here we make some brief additions: 1.) Detuning of impurity level and charge fluctuation effect is universal in impurity problem where impurity can denote/acquire charge to/from the substrate, sometime the charge fluctuation is so strong that impurity's magnetism is quenched [38, 39] or a non-magnetic impurity becomes magnetic [40, 41]. The calculation here considers only relatively weak charge fluctuation. In our experiment we have tuned the charge fluctuation from weak to large amplitude that reduces total spin from S = 1 to S = 1/2. What we have seen in this section can explain just a part of our experimental results. 2). For a multiple orbital spin impurity, Hund's coupling that aligns spins of different orbitals also plays an important role suppressing Kondo singlet formation [42, 43]. In presence of strong charge fluctuation the impurity can enter the so-called Hund's impurity regime [44, 45] where charge fluctuation coexists with sizeable magnetic moment. This regime should correspond to what we call intermediate regimes in our results (see section (3.7)). 3). The asymmetric spectra caused by impurity level detuning in Anderson model (1.2) can also be derived from Kondo model in which the asymmetry is characterized by the ratio between exchange coupling and potential scattering [32, 46, 47]. Their physical meaning is the same, because Anderson impurity model and Kondo model are equivalent to each other under Schrieffer-Wolff transformation [19].

1.2.6 Multiple impurities problem

So far we have addressed the single impurity Kondo problem. We will now have a brief overview of the collective behavior of magnetic impurities, from two-impurity problem to the impurity lattice. We limit the discussion to the systems consisting of impurities deposited on surfaces which are accessible by STM. Although the interaction between impurities in bulk system leads to many fascinating phenomena such as heavy-fermion compound, unconventional superconductivity [48], they will not be introduced in this manuscript.

Kondo impurities

We start with the interaction between two Kondo impurities. The interactions between two magnetic impurities can be of several origins: magnetic dipolar coupling, direct exchange coupling or Ruderman-Kittel-Kasuya-Yosida (RKKY) interaction [1–3]. The dipolar coupling decreases as $1/r^3$ with r the distance between impurities and the direct exchange coupling demands the overlap of orbitals. Thus these two coupling are expected to occur in extreme short range ($r \sim$few$\mathring{\text{A}}$ for d orbital impurities on surface). RKKY interaction is an indirect spin-spin interaction mediated by the conduction electrons of the metal substrate. In the present case, it is expected

to persist to longer range than direct exchange coupling [49]. It is considered as the main contributor to spin-spin interaction in impurities problem [50] and can be ferromagnetic (FM) or antiferromagnetic (AFM) depending on r [51] (Fig. 1.9 (a)). In 2007 Wahl et al. [52] had examined the interactions between two Co atoms at different distance r on Cu(100) surface. By looking at conductance spectra, they found that at small distance $r < 4\text{Å}$ the coupling between Co atoms are FM and at $r = 5\text{Å}$ the coupling is AFM where Kondo peak in conductance spectra is suppressed for FM coupling and splits for AFM coupling. For $r > 6\text{Å}$ no obvious change on Kondo feature was detected. Latter works had shown that both FM and AFM couplings tend to suppress the Kondo effect [53–55], driving the two-impurity system to coupled triplet or singlet ground state (Fig. 1.8 (a)).

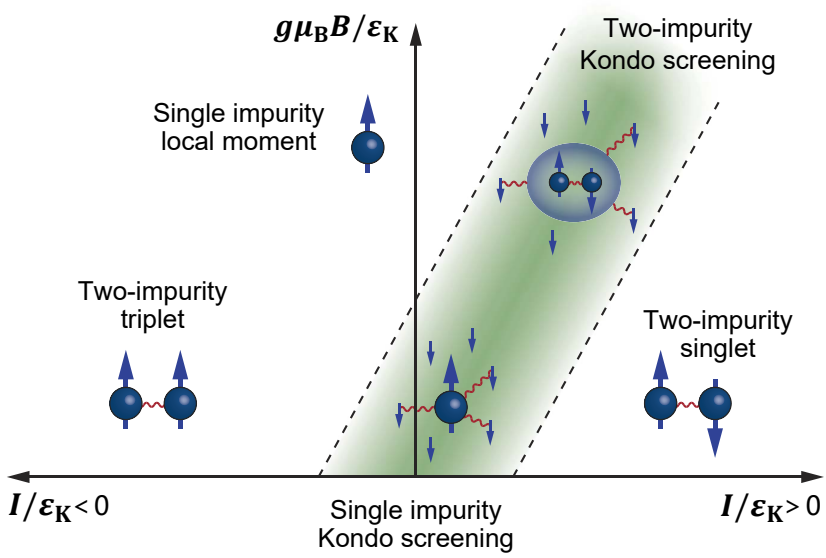

Figure 1.8: Phase diagram of two-impurity Kondo problem. Schematic phase diagram of two Kondo impurities coupled with interaction strength I and under external magnetic field B transverse to the main anisotropy axis. Kondo screening occurs in the green shaded region. At $B = 0$, when $\mid I \mid$ is small with respect to characteristic Kondo energy $\epsilon_K = k_B T_K$, two spins are independently screened by the substrate electrons, while $\mid I \mid >> \epsilon_K$ a non-magnetic singlet (AFM) or high-spin triplet (FM) state forms, suppressing Kondo effect to occur. At large B, for AFM coupling $I > 0$ a new correlated state in which both spins are screened could form. Image adapted from [55].

Kondo lattice usually refers to long range magnetic order. However Mermin–Wagner theorem [56] states that long range magnetic order cannot persists in 2D systems. Thus realising long range magnetic order in quasi-2D system consisting of Kondo impurities on metal surface is one of the intriguing challenges. To form Kondo lattice on metal surface, it requires that the magnetic impurities form 2D periodic lattice on the surface in which both Kondo effect and inter-impurity interaction are present. Hence self-assembled magnetic molecules is one of the ideal candidate to realise Kondo lattice on metal surface. Tsukahara et al. [57] formed 2D Kondo lattice in self-assembled Fe phthalocyanine (FePc) molecules superlattices on Au(111) surface, and found that Kondo state of single molecule splits when number of neighboring molecules increases (distance between neighboring molecules was $r = 1.47$ nm), indicating RKKY mediated AFM coupling between neighboring molecules. When Kondo lattice is formed, a small gap at the Fermi level

emerges, the gap probably signifies two dispersless states that characterize heavy-fermion behavior [58] (Fig. 1.9 (b)). Other kinds of self-assembled magnetic molecules on different surfaces have been reported in which RKKY or direct exchange serve as inter-impurity coupling [59–62].

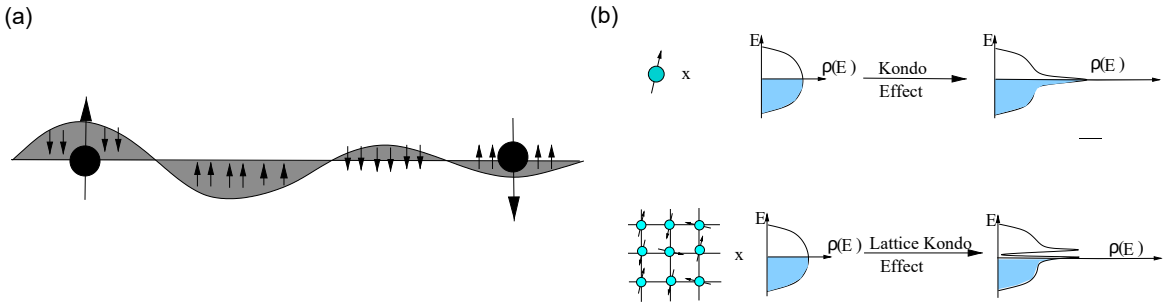

Figure 1.9: Illustration of RKKY interaction and Kondo lattice effect. (a) RKKY interaction: Spin impurity showing Kondo screening cloud (left) generates spin polarized oscillation in conduction electrons and couples with other spin impurity (right) indirectly. (b) Inter-impurity coupling in Kondo lattice creates a new resonance peak in conduction sea in each unit cell, which is a signature of heavy electron behavior. Image adapted from [48].

It worth pay attention to the following facts: 1). A magnetic impurity that couples to non-magnetic ligands (e.g. non-magnetic atom, organic ligand) might also vary Kondo feature through different mechanisms such as changing anisotropy [63] and modifying spin polarized orbital. These effects are especially important concerning non-point like magnetic molecules that consists of transition metal (TM) atom coupled to organic ligands [64]. 2). Change of Kondo feature when Kondo lattice builds up does not necessary indicate the presence of spin-spin interactions because Kondo temperature T_K is related to ρJ_K where ρ is the DOS at Fermi level and J_K the coupling strength between spin and conduction electrons. Iancu et al. [65] had found that Kondo feature of a magnetic molecule narrows (T_K decreases) when the number of neighboring molecules increases, while the decrease of T_K is due to the reduction of surface electron density ρ by electron scattering from neighboring molecules rather than the inter-impurity spin-spin interactions. Also Mugarza et al. [40] had found similar effect where J_K of magnetic molecule decreases as neighboring molecule number increases. When neighbors are more than 3, Kondo feature is completely lifted. This is due to the presence of neighboring molecules that decouples it from the substrate i.e. decrease of J_K.

Other kinds of self-assembled method to realise inter-impurity interaction are also developed such as self-assembled chemically bonded molecular chain [66, 67] or lattice. In this case, the inter-impurity interaction should occur through their chemical bond rather than via substrate electrons so that this method should ensure a large inter-impurity interaction.

non-Kondo impurities

Depending on the nature of impurities and substrates (e.g. the inter-impurity interaction, substrate commensurability) the impurity lattice does not always form Kondo lattice. Other types of lattice can also be obtained: For example if the impurity is in atomic limit (i.e. negligible

hybridization) the long range indirect inter-impurity RKKY interaction is impossible to occur, only short range direct exchange interaction is likely to occur. In this case, the self-assembled magnetic molecular lattice on metal surface is unlikely to develop long range spin-spin interactions, and each unit cell tends be an isolated magnetic moment [68]. Besides Kondo lattice other long range orders may be developed such as antiferroelastic spin-crossover magnetic molecule chain [67] where magnetic Ni atoms in the chain show alternately low-spin (S = 0) and high-spin (S = 1) state along the chain.

1.3 Magnetic impurity interacting with a superconducting metal

In this section we will consider the interaction between magnetic impurity with superconducting substrate. We first introduce the notion of superconductivity and then the Bardeen-Cooper-Schrieffer (BCS) theory that first describes superconductivity in microscopic view. BCS theory had introduced a pairing mechanism to describe s-wave superconductor where superconductivity is described by means of Cooper pairs formed by electrons with opposite spins and momentum. After that we will adopt the same manner as in normal metal case to study the effect of magnetic impurity interacting with s-wave superconductor and understand how it suppresses superconductivity by forming Yu-Shiba-Rusinov (YSR) state.

1.3.1 Superconductivity

Superconductivity refers to the phenomena where the electrical resistivity of a material vanishes upon cooling below its critical temperature (also called transition temperature). It was first discovered in 1911 by Onnes [69] who had found that the resistivity of Hg sudden drops to zero at liquid helium temperature. The same experiments had been implemented in subsequent years and superconductivity was discovered in several materials with different structures and critical temperature.

Besides the zero resistivity property of a superconductor, there were another two important experimental discoveries that played a crucial role in understanding the inner mechanism of superconductivity phenomena. The first is Meissner effect. In 1933 Meissner and Ochsenfeld [70] discovered that the superconductor is a perfect diamagnet, which means it expels any external magnetic field. The second is the isotope effect. It was first predicted by Fröhlich [71] and observed by Maxwell and Reynolds et al. [72, 73] in 1950. They found different superconducting critical temperatures for different isotope of Hg which have the same electronic properties but different ionic masses. The first effect implies that the electron spin must have played a import role in forming superconducting state. The second effect implies that the electron-phonon interaction, which is related to ionic mass, should also be one of the ingredient in forming superconducting state. It is thanks to the discoveries of these two effects that the superconductivity phenomena could finally be understood in microscopic view afterwards.

1.3.2 BCS Theory

In 1957 Bardeen, Cooper and Schrieffer published the first microscopic theory describing superconductivity [74]. They proposed that in a superconductor, there exists a phonon mediated electron-electron interaction (Fig. 1.10 (a)). An electron with initial state $\mid k_1\rangle$ (momentum $\vec{k_1}$) is scattered by the lattice, changing its momentum to $\vec{k_1} - \vec{q}$ and emitting a phonon with momentum $\vec{q}$, later another electron with initial state $\mid k_2\rangle$ is scattered to final state $\mid k_2 + q\rangle$ by adsorbing this phonon before it decays.

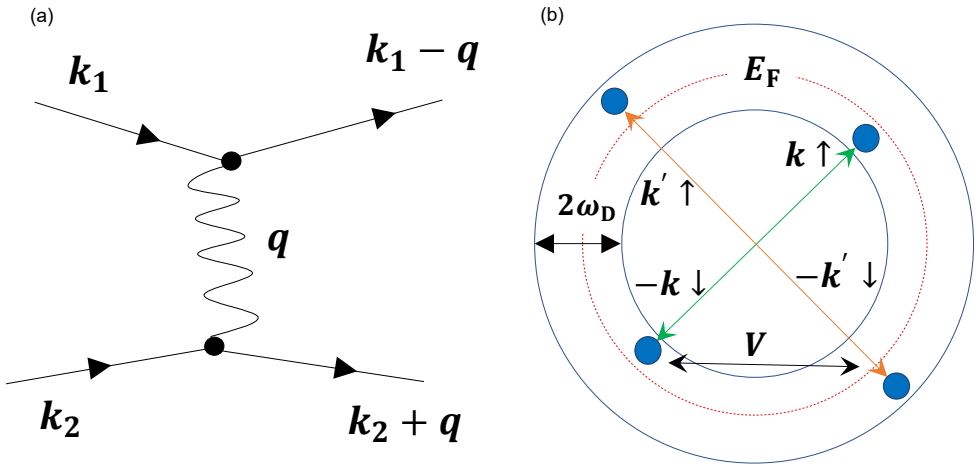

Figure 1.10: Illustration of BCS interaction. (a) Phonon mediated electron-electron interaction. (b) In BCS model, the effective attractive interaction V acts on electron pairs that have zero momentum, zero spin and within energy window of ω_D around Fermi level.

There are few important remarks about this interaction: 1). Two electrons interacts with each other via emitting and absorbing phonon, resulting zero energy dissipation in this process which is consistent with superconductivity phenomena that electrons can move in the lattice without being scattered. 2). Unlike Coulomb interaction which is a photon mediated instantaneous process, the phonon mediated interaction is "retarded" as it involves the motion of heavy ion core, this indicates that before the phonon is adsorbed by the second electron the first electron has travelled a long distance since it emits the phonon. This leads to an effective attractive interaction over a distance ξ. 3). As a result of this attractive interaction, two electrons are coupled together, forming the so-called Cooper pair with characteristic size ξ. Cooper pair notion is one of the essential ingredients in BCS theory as we will discuss in the following section. 4). For a conventional s-wave superconductor ξ is related to the coherence length of a superconductor [75] which is deduced from Ginzburg–Landau theory [76] and defines a length scale over which superconductor order parameter Δ can vary.

The general form of an electron-electron interaction Hamiltonian can be written as:

$$H = \sum_{k,\sigma} \epsilon_k c^\dagger_{k\sigma} c_{k\sigma} + \sum_{k_1,k_2,k_3,k_4,\sigma_1,\sigma_2} U_{k_1,k_2,k_3,k_4} c^\dagger_{k_1\sigma_1} c^\dagger_{k_2\sigma_2} c_{k_3\sigma_2} c_{k_4\sigma_1} \tag{1.10}$$

where $c^\dagger_{k\sigma}$ ($c_{k\sigma}$) is the fermionic creation (annihilation) operator of particle with momentum k

and spin σ. U denotes effective electron-electron interaction.

This is a general expression that contains an arbitrary electron-electron interaction term U where the interacting mechanism is not specified. In order to deduce BCS Hamiltonian from equation (1.10) we consider the interaction shown in Fig. 1.10 (a). First of all, the electron-electron interaction is a phonon mediated attractive local one, U can be replaced by a constant value $-V$ ($V > 0$) which is only non zero only for electrons with energy inferior to Debye energy (e.g. $\mid \epsilon_k - E_F \mid < \omega_D$). This explains the isotope effect where the mass of ion M affects Debye energy ω_d, which affects pairing electrons that responsible for superconducting transition temperature. Secondly the momentum conservation should be taken into account where $\vec{k_1} + \vec{k_2} = \vec{k_3} + \vec{k_4} = \vec{K}$. It can be derived from the centre of mass framework that the pairing mainly occurs for the electrons with opposite momentum (e.g. $\vec{K} = \vec{0}$). Finally the spin conservation, though the spin degree of freedom does not appear explicitly in Fig. 1.10 (a), the Cooper pair wavefunction must be antisymmetric according to Pauli exclusion principle, this involves the both spin (S) and orbital (L) degrees of freedom and requires them to satisfy antisymmetry condition $(-1)^L(-1)^{S+1} = -1$ (if spin and orbital are not coupled). As V is considered as purely local interaction so that only electrons with angular momentum $L = 0$ are allowed to interact, thus in order to satisfy antisymmetry condition, only spin singlet pairing is allowed ($S = 0$), implying that Cooper pairs are formed by electrons with opposite spins (Fig. 1.10 (b)). $(L = 0, S = 0)$ correspond to so-called s-wave superconductor, which also known as conventional superconductor.

Now we can write the BCS Hamiltonian describing s-wave superconductors:

$$H = \sum_{k,\sigma} \epsilon_k c^\dagger_{k\sigma} c_{k\sigma} - V \sum_{k,k'} c^\dagger_{k'\uparrow} c^\dagger_{-k'\downarrow} c_{-k\downarrow} c_{k\uparrow} \tag{1.11}$$

And the BCS ground state:

$$\mid \psi_{BCS} \rangle = \prod_k (u_k + v_k P^\dagger_k) \mid 0 \rangle \tag{1.12}$$

with

$$P^{(\dagger)}_k = c^{(\dagger)}_{k\uparrow} c^{(\dagger)}_{-k\downarrow} \tag{1.13}$$

where $P^{(\dagger)}_k$ is the Cooper pair creation (annihilation) operator which creates a Cooper pair formed by a pair of electrons of state $\mid k \uparrow \rangle$ and $\mid -k \downarrow \rangle$ respectively. u_k and v_k are for now the amplitudes that follow the normalization condition $\mid u_k \mid^2 + \mid v_k \mid^2 = 1$, their physical meaning will be discussed later.

The physical meaning of BCS ground state (1.12) is obvious: The superconducting ground state is a coherent state of the Cooper pair operator which creates pair of electrons states with zero total momentum and zero total spin.

We are interested in quasiparticle DOS given by BCS Hamiltonian, hence we want it to be diagonalizable in the proper basis. To do so, we first adopt mean field approach of superconduc-

tivity proposed in Bogoliubov-de Gennes (BdG) approach [77] to dissolve quartic interacting term to quadratic terms by Wick's theorem:

$$c^{\dagger}_{k'\uparrow}c^{\dagger}_{-k'\downarrow}c_{-k\downarrow}c_{k\uparrow} \quad \approx \quad < c^{\dagger}_{k'\uparrow}c^{\dagger}_{-k'\downarrow} > c_{-k\downarrow}c_{k\uparrow} + c^{\dagger}_{k'\uparrow}c^{\dagger}_{-k'\downarrow} < c_{-k\downarrow}c_{k\uparrow} > \tag{1.14}$$

Then we introduce the gap-operator Δ defined as:

$$\Delta^{(\dagger)} = V\sum_{k}^{\omega_d} < c^{(\dagger)}_{k\uparrow}c^{(\dagger)}_{-k\downarrow} > \tag{1.15}$$

which is determined by the expectation value of a occupied or unoccupied pair. In this way the original BCS Hamiltonian can be simplified via mean field approach:

$$H = \sum_{k,\sigma}\epsilon_k c^{\dagger}_{k\sigma}c_{k\sigma} - \sum_{k}(\Delta c^{\dagger}_{k\uparrow}c^{\dagger}_{-k\downarrow} + \Delta^{*}c_{-k\downarrow}c_{k\uparrow}) + Constant \tag{1.16}$$

This is mean-field Hamiltonian for BCS theory which is widely adopted for describing conventional superconductor. Though the mean field approach does not provide the exact solution, here for the BCS interaction considering only zero momentum pairs e.g. infinite range interaction between pairs in real space, the mean field approach provides nearly exact solution. This mean-field Hamiltonian can be written in Nambu basis [78] with Nambu spinors $\Psi_k = (c^{\dagger}_{k\uparrow}, c_{-k\downarrow})$.

$$H = \sum_{k}\Psi^{\dagger}_{k}H_{BdG}\Psi_k \tag{1.17}$$

with H_{BdG} the BdG Hamiltonian:

$$H_{BdG} = \begin{bmatrix} \epsilon_k & \Delta \\ \Delta^{*} & -\epsilon_k \end{bmatrix} \tag{1.18}$$

Now we have a diagonalizable Hamiltonian describing superconductor, it is easy to calculate the eigenenergies:

$$\pm E_k = \pm\sqrt{\epsilon_k^2 + \Delta^2} \tag{1.19}$$

And the corresponding eigenvectors are:

$$(u_k, v_k), \quad -(-v_k^{*}, u_k^{*}) \tag{1.20}$$

The physical meaning of E_k is excitation energy to inject an electron or hole to BCS ground state. It has a minimum value $\mid \Delta \mid$, this means there exists a gap of energy $\mid \Delta \mid$ that forbids the excitation (Fig. 1.11 (a)) occurring inside it. u_k and v_k are the amplitudes that we have seen in equation (1.12), they are also the components of eigenvector of BdG Hamiltonian (1.20) and related to creator (annihilator) of so-called Bogoliubov quasiparticles ($a_k^{\dagger}$ (a_k)) in Nambu

representation which are the elementary excitations of superconducting ground state:

$$a_k^\dagger = (a_{k\uparrow}^\dagger, a_{-k\downarrow}) = \Psi_k^\dagger \begin{pmatrix} u_k & -v_k^* \\ v_k & u_k^* \end{pmatrix} = (c_{k\uparrow}^\dagger, c_{-k\downarrow}) \begin{pmatrix} u_k & -v_k^* \\ v_k & u_k^* \end{pmatrix} \tag{1.21}$$

$$H = \sum_k \Psi_k^\dagger H_{BdG} \Psi_k = \sum_k a_k^\dagger E_k \tau_3 a_k \tag{1.22}$$

where τ is the Pauli matrix with $\tau_3 = \begin{bmatrix} 1 & 0 \\ 0 & -1 \end{bmatrix}$. The derived quasiparticle DOS ρ_{BCS} of a s-wave superconductor is written as:

$$\rho(E) = \rho_0 \frac{E}{\sqrt{E^2 - \Delta^2}} \tag{1.23}$$

with ρ_0 the quasiparticle density of states in the normal state at Fermi energy. This is a remarkable result from the BCS theory, it predicts the existence of a superconducting gap of size $2 \mid \Delta \mid$ at the Fermi energy and two singularities at the edges of gap $\pm \mid \Delta \mid$ which lead to a divergence in the spectrum. The predicted shape can be verified in a direct tunneling experiment, and the divergence are characterized as so-called coherence peaks (Fig. 1.11 (b)) or BCS peaks.

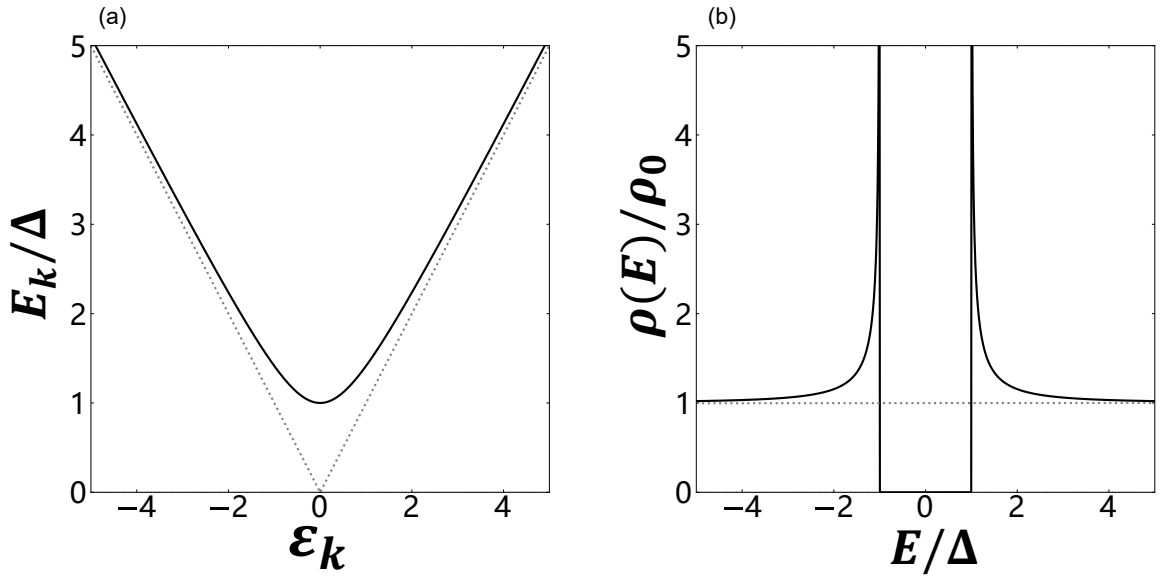

Figure 1.11: BCS density of states. (a) Excitation spectrum of a BCS superconductor. Only positive part is shown. (b) BCS quasiparticle DOS as function of energy. Dash lines for both figures correspond to the spectrum/DOS in absence of BCS interaction (normal metal).

1.3.3 YSR state - spin-1/2 impurity

Now we can finally estimate the effect of magnetic impurities presence in superconductors. We will still limit our discussion in adsorbed impurities on metal surfaces and in conventional s-wave superconductor where superconductivity is described by means of Cooper pairs formed by

electrons with opposite spins and momentum. The effect of impurity has already been introduced in Kondo section where the impurity couples antiferromagneticly with conduction electrons. This will compete with pairing effect and as a result impurity inside superconductor plays the role of a local pair breaking potential that suppresses the superconductivity. The consequence of a local depairing potential is the emergence of excited state that spatially localized around impurity site and energetically situated inside superconducting gap. This state is called Yu-Shiba-Rusinov (YSR) state or Shiba state which was first deduced by Luh Yu, Hiroyuki Shiba, and A. I. Rusinov [79–81].

Electronic properties of Shiba states

To understand the electronic properties of Shiba state, we start with the simplest case where a spin-1/2 impurity interacts with a superconductor, the single channel Anderson impurity model is written as:

$$H = H_{SC} + H_{imp} + V_{hyb} \tag{1.24}$$

$$H_{SC} = \sum_{k,\sigma} \epsilon_k c^\dagger_{k\sigma} c_{k\sigma} - \sum_k (\Delta c^\dagger_{k\uparrow} c^\dagger_{-k\downarrow} + \Delta^* c_{-k\downarrow} c_{k\uparrow}) \tag{1.25}$$

$$H_{imp} = \epsilon_d \sum_\sigma d^\dagger_\sigma d_\sigma + U \hat{n}^d_\uparrow \hat{n}^d_\downarrow \tag{1.26}$$

$$V_{hyb} = V \sum_{k,\sigma} (c^\dagger_{k\sigma} d_\sigma + h.c) \tag{1.27}$$

where H_{SC} represents the mean-field Hamiltonian for BCS superconductor, H_{imp} describing the spin impurity possessing single unpaired electrons in d orbital and V_{hyb} the hybridization term describing the coupling between spin impurity with conduction electrons.

One can calculate the energy of Shiba state in strong coupling where $\Gamma \sim \mid V \mid^2 >> \Delta$ by adopting mean field approach [82] or in general case through quantum spin treatment [83–85]. Here we adopt the results obtained by Huang et. al. [82] in which energy of Shiba state is written:

$$\pm E_b = \pm\Delta \frac{(E_J^2 - \Gamma^2 + E_U^2)}{\sqrt{(\Gamma^2 + (E_J - E_U)^2)(\Gamma^2 + (E_J + E_U)^2)}} \tag{1.28}$$

where $-E_J + E_U$ ($E_J + E_U$) are the energies of occupied (empty) d level beneath (above) Fermi level of impurity. E_b is the energy of Shiba state, "b" stands bound state energy in YSR problem. The $\pm$ values correspond to the electron-like and hole-like components of a Shiba state (Fig. 1.12).

By means of facilitating the description, both components can also be regarded as "states" (though this description is not exact) and they are fully spin polarized with opposite spins [86]. The expression (1.28) can be re-written with following form:

$$\pm E_b = \pm\Delta \frac{(1 - \alpha^2 + \beta^2)}{\sqrt{(\alpha^2 + (1 - \beta)^2)(\alpha + (1 + \beta)^2)}} \tag{1.29}$$

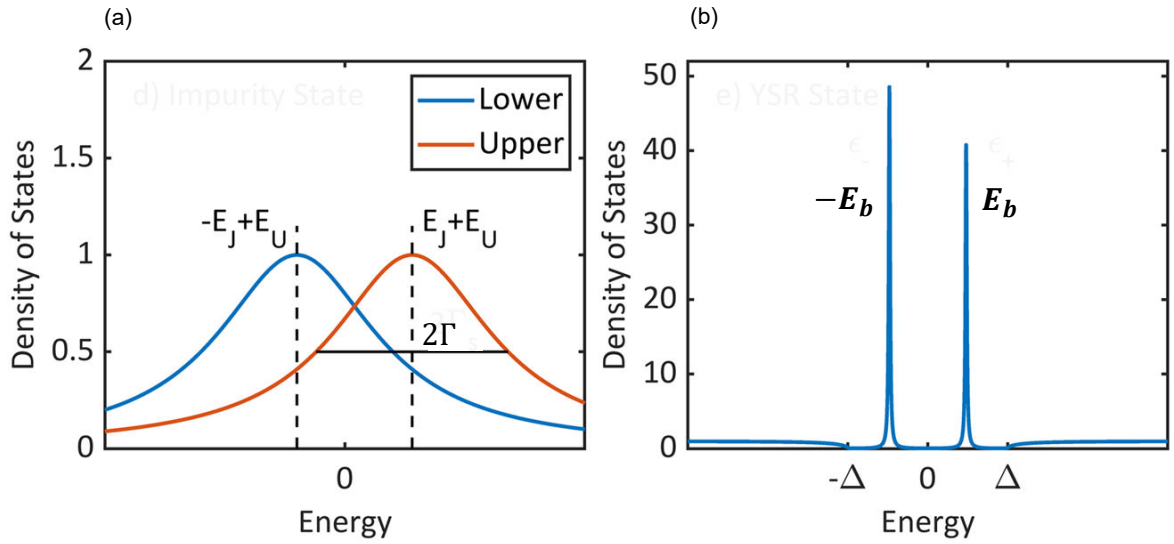

Figure 1.12: Schematic illustration of a single channel Anderson impurity states. (a) Spectral functions of occupied and empty states at energies of $-E_J + E_U$ and $E_J + E_U$ respectively. (b) The resulting YSR states at energies of $\pm E_b$ in the superconducting regime. Image adapted from [82].

where α and β are parameters related magnetic and potential scattering respectively in Kondo model and $\alpha = \Gamma/E_J$ and $\beta = E_U/E_J$ through Schrieffer–Wolff transformation [19]. In classical limit $\alpha = \pi\rho_0 JS/2$ and $\beta = \pi\rho_0 K$ where J denotes the magnetic coupling, S the spin of impurity, K the potential scattering and ρ_0 the DOS at Fermi level in normal metal with the relation $J \to 0$, $S \to \infty$ and $JS \to constant$, this indicates the magnetic impurity plays a role of a local magnetic field and has no internal dynamics [87]. By introducing scattering phase $\delta^{\pm}$ defined as $\tan(\delta^{\pm}) = \beta \pm \alpha$ we will have [88]:

$$\pm E_b = \pm\Delta\cos(\delta^+ - \delta^-) \tag{1.30}$$

To study the dependence of Shiba energies on magnetic coupling, we can assume the particle-hole symmetry condition where $\beta = 0$, and the expression (1.29) becomes the famous form:

$$\pm E_b = \pm\Delta\frac{1-\alpha^2}{1+\alpha^2} \tag{1.31}$$

The energy of Shiba states E_b as function of α is shown in Fig. 1.13 (b) and the DOS of Shiba states is shown in lower figure of Fig. 1.13 (a). We observe that Shiba states are characterized as a pair of in-gap resonances symmetric in energy with respect to Fermi level. These resonances represent the quasiparticle excitation from the ground to the first excited state of system described by Hamiltonian (1.24). When coupling strength J is small and the Shiba states lie close to the gap edge, by increasing J the energies of states move closer to the Fermi level. At a specific point $\alpha = 1$ the energies of Shiba state equal exactly to zero, this correspond to a level crossing point where a quantum phase transition occurs. This transition results a change of ground state as a result of competition between J and pairing interaction Δ.

To understand the ground state and excited state properties, it is easier to consider a quantum spin-1/2 impurity where Kondo temperature T_K is used to characterize coupling strength. By assuming T_{cri} the critical value of T_K that the quantum phase transition happens ($T_{cri} \sim 0.3\Delta/k_B$ [83, 84]), we can draw the evolution of ground state and excited state in upper figure of Fig. 1.13 (a). When T_K is comparable with Δ, i.e. T_K is neither too small or too larger with respect to Δ, there are three regimes: 1) For weak coupling $T_K < T_{cri}$, the opening of superconducting gap (forming Cooper pairs) occurs first and depletes the DOS around Fermi level, this results an incomplete screening which corresponds to a many-body ground state consisting of BCS ground state with a S = 1/2 impurity state, thus a doublet free-spin ground state (blue curve in upper figure of Fig. 1.13 (a)). 2) For strong coupling $T_K > T_{cri}$, the Kondo resonance (HWFM of the order of $k_B T_K$) will coexist with in-gap states [89–91], in this case the ground state will be a Kondo-screened singlet (red curve in upper figure of Fig. 1.13 (a)). 3) For $T_K \sim T_{cri}$, free-spin state (red) and Kondo-screened state (blue) can cross each other, indicating the quantum phase transition.

The excitation changes the total spin of $\Delta S = \pm 1/2$ by exciting the system from free-spin doublet ground state to Kondo-screened singlet excited state or from Kondo-screened singlet ground state to free-spin double state excited state [92].

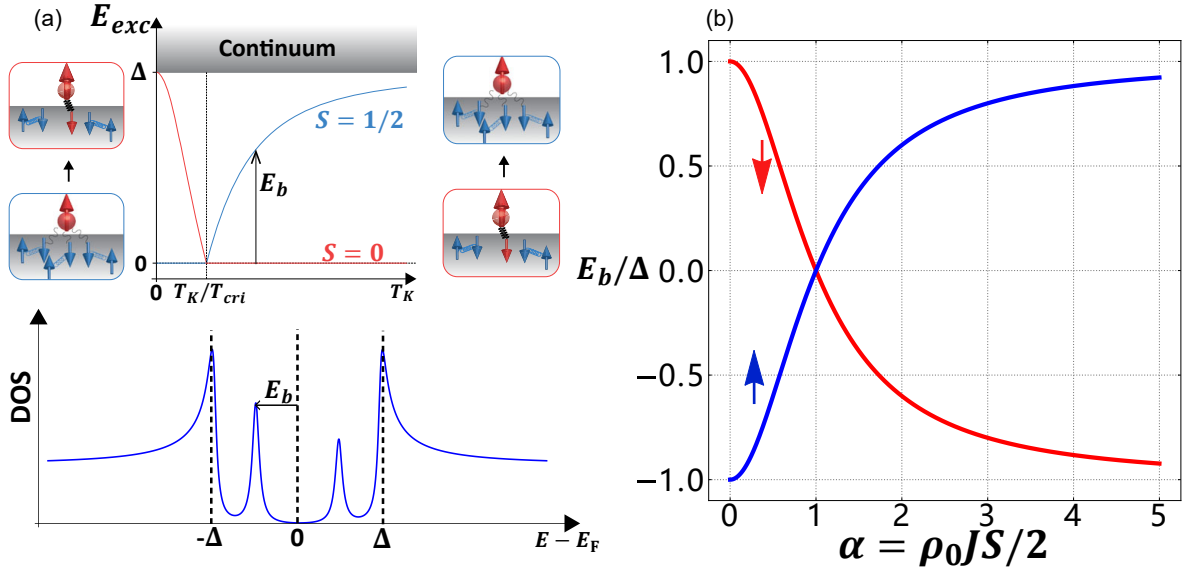

Figure 1.13: Schematic illustration of quasiparticle excitation corresponding Shiba energy. (a) Top: Schematic dependence of ground and excited states of a spin-1/2 impurity adsorbed on a superconducting substrate on Kondo temperature T_K. At weak coupling ($T_K < T_{cri} \sim 0.3\Delta$) the ground state is free-spin doublet state (blue curve) and excited state is Kondo-screened singlet state (red curve). Across critical coupling T_{cri} the roles of ground state and excited state revers. Image adapted from [93]. Bottom: The excitation between ground state and excited state with energy E_b gives rise to a pair of in-gap resonances at energy $\pm E_b$ with respect to Fermi level. Here we have plotted the general case of Shiba states where the electron-like ($+E_b$) and hole-like ($-E_b$) peaks have asymmetric spectral weigh due to the potential scattering that breaks particle-hole symmetry ($E_U \neq 0$). (b) Energy of the electron (red) and hole (blue) component of Shiba state as a function of α at particle-hole symmetry point.

When T_K is not comparable with Δ there are two limits: 1) $T_K << \Delta$, this corresponds the case where no screening can occur as opening of superconducting gap depletes the states

available on Kondo energy scale T_K. The Shiba states will lie close to the gap edge [94, 95]. 2) $T_K >> \Delta$, this corresponds to the case that Kondo effect dominants the pairing and the classic limit starts to fall apart. The energy of Shiba states still follow the expression (1.31) but with $\alpha = \frac{\pi\Delta}{4k_B T_K}\ln(\frac{4\mathrm{k_B T_K}}{\pi\Delta}\mathrm{e})$ with e the natural exponent [96].

Another important aspect related to Shiba states is the relative spectral weight between electron-like and hole-like peaks. As shown in the lower figure of Fig. 1.13 (a) where the asymmetry spectral weight of two peaks $I = \frac{I_+ - I_-}{I_+ + I_-}$ is not zero due to the potential scattering that breaks particle-hole symmetry [88] where $I_{+/-}$ stands for the spectral weight of electron-like (hole-like) peak. Upon phase transition the asymmetry I will change its sign as a result of level crossing of two peaks, thus sign change of asymmetry is recognized as change of ground state [85, 93]. Nevertheless it should be noted that this method may not be always valid because the asymmetry also depends on orbital properties of magnetic impurity [97] and tunneling condition during experiments [98].

Wavefunction of Shiba state

For the wavefunction of Shiba states, we start with considering the wavefunction of Shiba state generated by a point-like impurity adsorbed on a s-wave bulk (3D) superconductor surface that posses an isotropic Fermi surface. The results were found by Rusinov [81] that for $r >> \lambda_F = 2\pi/k_F$ the wave function of hole-like $(-)$ and electron like $(+)$ states can be written as:

$$\psi_\pm(r) \propto \frac{\sin(k_F r + \delta^\pm)}{k_F r} e^{-|\sin(\delta^+ - \delta^-)|r/\xi} \tag{1.32}$$

where k_F denotes the Fermi wave vector, ξ the coherence length of superconductor.

We notice that both electron-like and hole-like components of Shiba states extend away from the impurity site with oscillation $k_F r$, but there exists a spatial phase shift between them $(\delta^+ - \delta^-)$. The spatial dephasing results a dephase of spectral weight (related to LDOS $\propto \mid \psi_\pm(r) \mid^2$) that can be directly probed in STM experiments [99, 100]. Another important dependence of wavefunction of Shiba state is the envelope term $e^{-r/\xi}/r$, indicating that in 3D LDOS of Shiba state decay as $1/r^2$ in short range and as $e^{-r/\xi}$ in long range.

However in a 2D or quasi-2D superconductors the interaction between layers is weak, the Shiba state LDOS decays as $1/r$, resulting a longer range extension of Shiba states [101, 102] which can be used to study the interaction between Shiba states [103].

At range of the order of atomic orbital (< 1 nm), the point-like assumption is not valid and the wavefunction of Shiba states is intimately related to the geometry of orbital that generates them [100, 104–107]. For instance, Shiba states originated from d_{z^2} orbital or $d_{x^2-y^2}$ orbital have different shapes because the two orbitals have different spatial extension and symmetry (Fig. 1.15 (a)). The spatial dephasing behavior also happens in short range, for a single d orbital that gives rise to Shiba states with wavefunction $\psi_\pm$, the shape of ψ_+ and ψ_- can be very different. As illustration in Fig. 1.15 (e) the shape of electron component $\mid \psi_+ \mid^2$ resembles the original d orbital while the hole component $\mid \psi_- \mid^2$ deviates a lot.

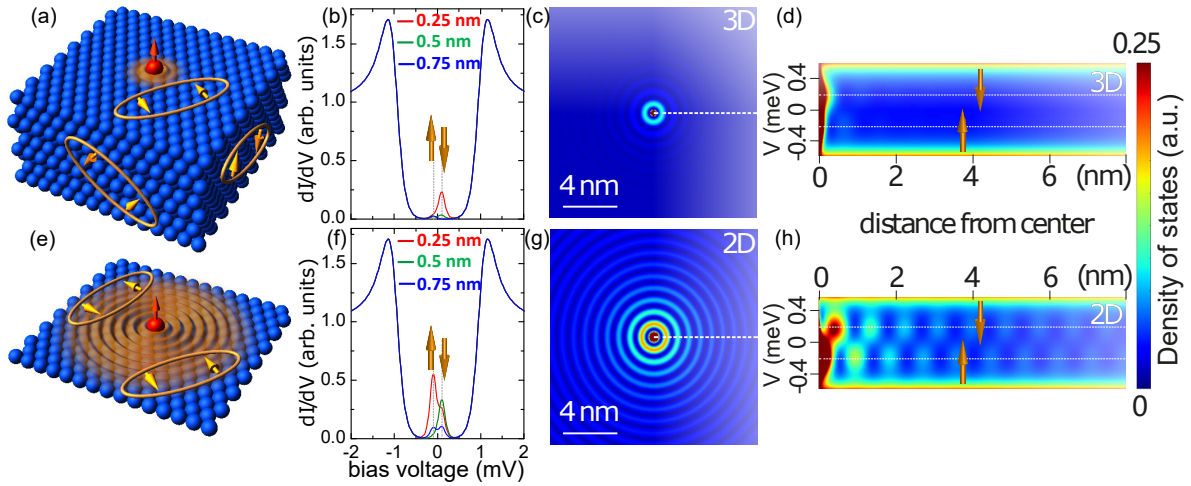

Figure 1.14: Spatial extension of Shiba states in 2D and 3D case. (a)-(d) Calculated behavior of Shiba state in isotropic s-wave superconductor substrate with 3D electronic band structure. (a) Schematic illustration of interaction between a point-like classical magnetic impurity with Cooper pairs. (b) Calculated dI/dV spectra at different distances marked with different colors from the impurity site. In-gap spin polarized states are marked by up or down arrow. (c) Simulated dI/dV map around the impurity, showing the spatial extension of Shiba states. (d) Calculated dI/dV spectra taken along the dash white line in (c). (e)-(h) play the same role as (a)-(d) but for a 2D substrate. Image adapted from [101].

1.3.4 spin-1 impurity

In this section we will consider the case of spin-1 impurity that possesses two unpaired electrons in orbitals coupled to superconductors. We still adapt the same idea of Kondo paragraph (1.2.5) where we evaluate the ground state and simulated excitation spectral in tunneling experiments as function of different parameters. The results present here are mainly taken from a recent review of von Oppen et.al. [108] where they have studied in-gap tunneling excitations of single spin impurity of S = 1, 3/2, 2 and 5/2 adsorbed on superconductor surface in STM experiments. The model used in their work is Kondo model, yet we can still adopt Anderson model used in Kondo paragraph (1.2) without losing generality:

$$H = H_{SC} + H_{imp} + V_{hyb} \tag{1.33}$$

$$H_{SC} = \sum_{k,\alpha,\sigma} \epsilon_{k\alpha} c^{\dagger}_{k\alpha\sigma} c_{k\alpha\sigma} - \sum_{k,\alpha} (\Delta c^{\dagger}_{k\alpha\uparrow} c^{\dagger}_{-k\alpha\downarrow} + \Delta^{*} c_{-k\alpha\downarrow} c_{k\alpha\uparrow}) \tag{1.34}$$

$$H_{imp} = \epsilon_d \hat{N}_d + U \sum_{\alpha} \hat{n}_{\alpha\uparrow} \hat{n}_{\alpha\downarrow} + U' \sum_{\alpha \neq \alpha'} \hat{n}_{\alpha} \hat{n}_{\alpha'} - J_H \sum_{\alpha \neq \alpha'} \vec{S}_{\alpha} \cdot \vec{S}_{\alpha'} + D\hat{S}_z^2 + E(\hat{S}_x^2 - \hat{S}_y^2) \tag{1.35}$$

$$V_{hyb} = \sum_{k,\alpha,\sigma} V_{k\alpha} (c^{\dagger}_{k\alpha\sigma} d_{\alpha\sigma} + h.c) \tag{1.36}$$

where ϵ_d are the single particle energies of d orbitals, $\hat{N}_d = \sum_{\alpha,\sigma} \hat{n}_{\alpha\sigma}$ the number operator for all d orbitals, $\hat{n}_{\alpha\sigma} = d^{\dagger}_{\alpha\sigma} d_{\alpha\sigma}$ the number operator of single d orbital α with spin σ and $d^{\dagger}_{\alpha\sigma}(d_{\alpha\sigma})$ is the fermionic creation (annihilation) operator, U and U' the intra- and inter-orbital Coulomb

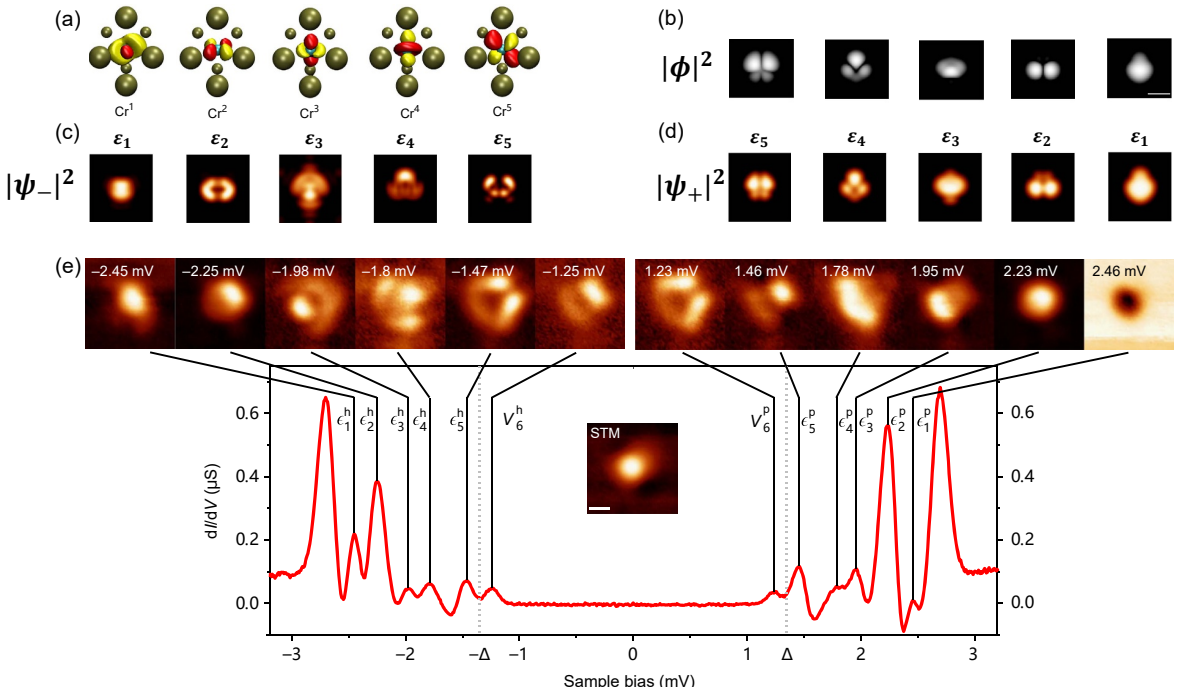

Figure 1.15: STM experiments of Shiba states created by Cr atom on Pb(111) surface. (a) Top view of wavefunction amplitude isosurfaces of five spin polarized orbitals of Cr atom embedded in Pb(111) surface. Cr atom is presented by center blue sphere with seven nearest Pb atoms presented by yellow sphere. These five states (Cr^1 to Cr^5) are only ones with relevant weight from the original d manifold of the Cr atom. (b) Top view of squared amplitude modulus $|\ \phi\ |^2$ of five states shown in (a), scale bar 0.5 nm. (c)(d) Simulation results of top view of $|\ \psi_+\ |^2$ and $|\ \psi_-\ |^2$ for orbitals of energy ϵ_1 to ϵ_5 that correspond to Cr^1 to Cr^5 in (a). (e) dI/dV maps over the Cr atom at the different energies of the in-gap states. Peaks labeled by $\epsilon_n^{p(h)}$ correspond to the electron or hole excitation of Shiba state at energy ϵ_n with $n = 1, 2, 3, 4, 5$. $V_6^{p(h)}$ is the thermal replica of $\epsilon_5^{h(p)}$ due to the use of superconducting tip. Image adapted from [104].

repulsion, J_H the Hund's coupling, $\vec{S}_\alpha = \sum_{\sigma\sigma'} d^\dagger_{\alpha\sigma}\vec{\tau}_{\sigma\sigma'}d_{\alpha\sigma'}$ the total spin of d orbital α, D and E the uniaxial anisotropy and in-plane (transverse) anisotropy.

The exchange coupling J_α in Kondo model is directly proportional to the imaginary part of hybridization function $\Gamma_\alpha = -\mathrm{Im}\Delta_\alpha$, and it will be used to characterize the coupling strength between impurity with superconductor in the following writing. In order to explain our experiment results, we focus on spin-1 impurity with $\alpha = 1, 2$ where J_1 does not necessary equal to J_2.

Single channel case

We starts with single channel case where J_1 varies and $J_2 = 0$, this indicates one channel (orbital) is decoupled from the substrate and there will be at most one pair of Shiba states. This consideration is reasonable for some systems, e.g. a spin-1 impurity with two unpaired electrons located respectively in d_{z^2} and $d_{x^2-y^2}$ orbitals, when it is absorbed on metal surface d_{z^2} orbital will couple better with substrate while $d_{x^2-y^2}$ can be decoupled from substrate, leading to a nearly zero $J_{d_{x^2-y^2}}$ thus only one Shiba state in spectrum [40].

As we have learnt from the previous paragraph that for a spin-1/2 impurity the exchange

coupling J competes with pairing strength Δ where the former one prefers Kondo-screened singlet state by binding with a quasiparticle. Here we use letter Q to represent the number of quasiparticles that bind to impurity (e.g. $Q = 1$ signifies that impurity spin is reduced by 1/2, $Q = 2$ then reduced by 1. Hence the ground state can be characterized by the notion (Q, S_z) where S_z refers to the spin state quantum number.

The phase diagram of single channel spin-1 impurity as function of uniaxial anisotropy D and pairing strength Δ is shown in Fig. 1.16 (a) where transverse anisotropy E is set to zero and $J_1 = 1$. In (a) we have three different states in different colors of blue, orange, green and labelled by $(0, \pm 1)$, $(0, 0)$, $(1, \pm 1/2)$ respectively. The orange one $(0, 0)$ and blue one $(0, \pm 1)$ lie in large pairing strength $\Delta > J_1$ region, these correspond to the case where Kondo screening is absent ($Q = 0$) and the ground state is determined by the sign of anisotropy D that lifts S = 1 triplet states degeneracy. We notice that the presence of anisotropy $\mid D \mid$ tends to suppress Kondo screening as $Q = 0$ holds even for $J_1 > \Delta$, this is consistent with what we observe in Kondo case where magnetic anisotropy favors atomic limit (section 1.2.5). But unlike Kondo paragraph here anisotropy renormalization is not taken into account which means that J and D are considered independent on each other.

Fig. 1.16 (b-c) show the sub-gap excitation energies as function of D under the condition of (a) at $\Delta = 1.2 > J_1 = 1$ and $\Delta = 0.8 < J_1 = 1$ respectively. The excitation considers only the transition between ground state and excited state shown in (a) with selection rule ($\Delta Q = 1$, $\Delta S_z = \pm 1/2$). Background color and line color represent the ground state and excited state respectively with the same notion as in (a). In (b) where $\Delta = 1.2$ the ground state can be either $(0, \pm 1)$ (blue background on the left) or $(0, 0)$ (orange background on the right) depending on the sign of D, the excited state can only be $(1, \pm 1/2)$ (green line). The minimum energy lies at interface between blue and orange background corresponding to a phase transition between $(0, \pm 1)$ and $(0, 0)$ ground state. As the phase transition does not satisfy the fermionic parity change condition ($\Delta Q = 1$, $\Delta S_z = \pm 1/2$) the excitation between them can not induce in-gap states.

In Fig. 1.16 (c) where $\Delta = 0.8$ the ground state can be $(0, \pm 1)$, $(0, 0)$ or $(1, \pm 1/2)$, when ground state is $(1, \pm 1/2)$ (green background) two pairs of Shiba states corresponding transition to different excited states (blue and orange lines) can be observed. The interface between blue and green background corresponds to a quantum phase transition between $(0, \pm 1)$ and $(1, \pm 1/2)$ states while the interface between green and orange background refers to a transition between $(1, \pm 1/2)$ and $(0, 0)$, these two quantum phase transitions involve fermionic parity change thus the excitation energies equal exactly to zero.

A few additional points to be noted here: 1). For a non-zero transverse anisotropy E, it will lifts the degeneracy of $(0, \pm 1)$ (blue) state, this will result a splitting of Shiba peaks in the spectra [87, 90]. 2). In Fig. 1.16 (c) we see that the presence of D splits $(0, 0)$ and $(0, \pm 1)$ states by "pushing" one of them towards bottom (low energy) which finally becomes ground state and the other towards the gap (high energy) which can possible move to the continuum states outside the gap. This case will not be included in this model where only comparable J, D and Δ are

discussed and in-gap Shiba states always exist. 3). Referring to above-gap excitation the most common one is the inelastic spin excitation with the selection rule ($\Delta Q = 0$, $\Delta S_z = \pm 1$). In excitation spectrum its character is a symmetric steps feature with respect to Fermi level (see section 2.2.4). This feature is usually observed in atomic limit impurity where J is small compared to magnetic anisotropy [109, 110]. In a superconductor, the steps always locate outside the superconducting gap as pairing potential forbids inelastic excitation to occur inside the gap. 4). The coexistence of Shiba states and inelastic spin excitation has been reported in some papers with high spin impurity ($S \geq 1$) [103, 111] where both in-gap and out-gap feature are observed. These two phenomena have different excitation mechanism (Shiba: $(\Delta Q = 1, \Delta S_z = \pm 1/2)$, Inelastic: $(\Delta Q = 0, \Delta S_z = \pm 1)$), the gap-crossing phenomena where out-gap inelastic feature transfers to in-gap states have been reported in magnetic molecular system [103], including this thesis (see section (4.6.3)).

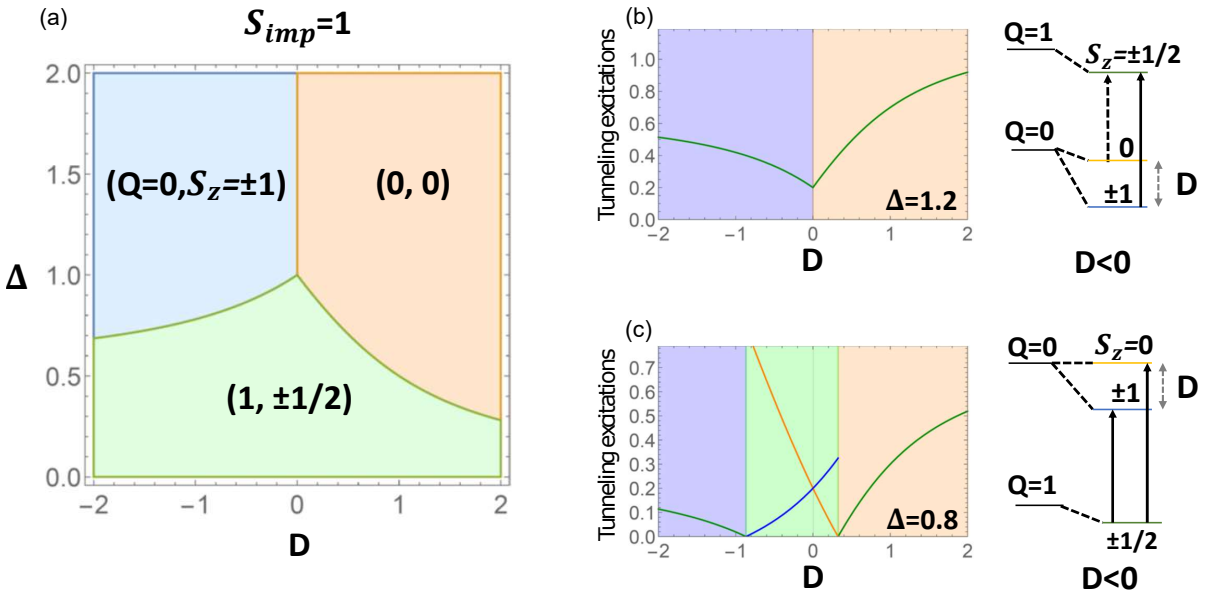

Figure 1.16: Phase diagram and corresponding sub-gap tunneling excitation energy for single channel spin-1 impurity. (a) Phase diagram illustrating ground state of single channel spin-1 impurity as function of uniaxial anisotropy D and pairing strength Δ. Transverse anisotropy E is set to 0, exchange coupling $J_1 = 1$ and $J_2 = 0$. Ground states are labeled by (Q, S_z) where Q denotes the number of bound quasiparticles to the impurity and S_z the projection of the total spin. Different ground states are presented in different colors, they are also illustrated in the right figures of (b). (b) Sub-gap tunneling excitation energies of single channel spin-1 impurity as function of uniaxial anisotropy D. Background color and line color refer to ground state and excited state respectively (same color coding as in the corresponding phase diagram in (a)). Transverse anisotropy E is set to 0, exchange coupling $J_1 = 1$ and $J_2 = 0$. Pairing strength $\Delta = 1.2$. The maximal excitation energy is the corresponding Δ. Right diagram illustrates the energy levels of different states at small negative value of D. (c) Same as (b) but with a different pairing strength $\Delta = 0.8$. Image adapted from [108].

Two-channel case

Now we consider the general case of two-channel spin-1 impurity where J_2 is not longer zero. The phase diagram of ground state is presented in Fig. 1.17 (a-d) in which transverse anisotropy E is still set to zero. We found a new ground state $(Q = 2, S_z = 0)$ compared to the single

channel case. This new ground state $(2, 0)$ corresponds to the case where J_1 and J_2 are both large enough that two channels enters Kondo-screened regime, resulting two quasiparticles bonded to the impurity site and total spin is reduced to zero. Intermediate singly-screened state $(1, \pm 1/2)$ can occur when $J_1 \neq J_2$.

Fig. 1.17 (e-h) show the sub-gap excitation energies as function of D with different values of J_1, J_2 and Δ indicated in the corresponding figure.

For unequal exchange couplings of the two channels ($J_1 \neq J_2$) there are two tunneling excitations out of the ground state and three different scenarios: 1). At small coupling strength $\Delta > J_1 > J_2$ (Fig. 1.17 (e)), the ground state will be unscreened states $(0, \pm 1)$ or $(0, 0)$ depending on the sign of D and the excited state will be $(1, \pm 1/2)$, this case resembles the single channel case with $\Delta > J$ in Fig. 1.16 (b). 2). At intermediate coupling strength $J_1 > \Delta > J_2$ (Fig. 1.17 (f)), the unscreened ground state regions (blue and orange background for large $\mid D \mid$) the excitation diagram is similar to single channel case with $\Delta < J$ in Fig. 1.16 (c), but for a singly-screened ground state $(1, \pm 1/2)$ (green background for small $\mid D \mid$) the excited states can be unscreened states (blue and orange lines) or the doubly screened state (red lines). 3). At strong coupling strength $J_1 > J_2 > \Delta$ (Fig. 1.17 (g)), the ground state is $(2, 0)$ or $(0, 0)$ depending on J_1, J_2, D and Δ, the excited state is $(1, \pm 1/2)$.

For equal exchange couplings $J_1 = J_2$, two excitations lines overlap with each other resulting one line in the diagram. When $\Delta > J_1 = J_2$ the ground state is unscreened states $(1, \pm 1)$ or $(1, 0)$ depending on the sign of D and the excited state will be $(1, \pm 1/2)$, the excitation diagram will be the same as single channel case with $\Delta > J$ in Fig. 1.16 (b). When $\Delta < J_1 = J_2$, the excitation diagram is presented in Fig. 1.17 (h).

In this section the sub-gap excitation energies and the corresponding ground states and excited states have been studied in detail which will greatly benefit the understanding of our experiment results. Nevertheless Shiba physics involves additional characterization such as peak spectral weight and orbitals pattern of Shiba states, these features are especially important when studying non-point-like impurity such as magnetic molecule that posses extended (or collective) spin polarized orbitals that are different from atomic orbitals. To accurately explain various kinds of behaviors in our systems, we are still facing many difficulties which are beyond our current knowledge.

1.3.5 Multiple impurities problem

Just like the inter-impurity interaction can lead to Kondo lattice in normal metal where heavy electron band exists. In superconductors the inter-impurity can lead to so-called Shiba lattice where in-gap Shiba states of each impurity interact with others, giving rise to the formation of in-gap Shiba band (also called impurity band) [80, 112]. Realisation of Shiba band has drawn great attention because it could enter topological phase (when topological order is introduced) hosting Majorana bound states that can be used as topological qubits for decoherence-resistant quantum computation [113–116].

Shiba band is the same as electronic band structure described in solid-state physics, the only

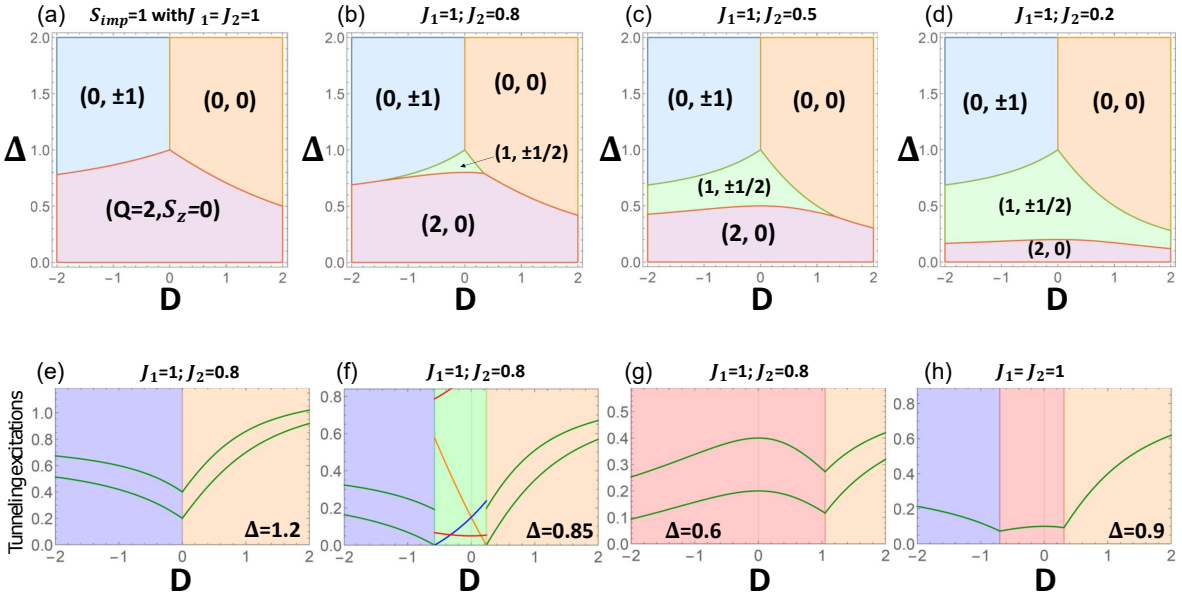

Figure 1.17: Phase diagram and corresponding sub-gap tunneling excitation energy for two-channel spin-1 impurity. (a)-(d) Phase diagram illustrating ground state of two-channel spin-1 impurity as function of uniaxial anisotropy D and pairing strength Δ. Transverse anisotropy E is set to 0, exchange coupling J_11 and J_2 are indicated. Ground states are labeled by (Q, S_z) where Q denotes the number of bound quasiparticles to the impurity and S_z the projection of the total spin. Different ground states are presented in different colors. (e)-(h) Sub-gap tunneling excitation energies of two-channel spin-1 impurity as function of uniaxial anisotropy D. Background color and line color refer to ground state and excited state respectively (same color coding as in the corresponding top phase diagram). Transverse anisotropy E is set to 0, exchange coupling J_1,J_2 and pairing strength Δ are indicated. The maximal excitation energies shown are the corresponding Δ. Image adapted from [108].

difference is that the interacting levels are in-gap Shiba states rather than atomic orbitals. The first step towards Shiba band is the formation of Shiba dimer where a spin-spin interaction couples two Shiba impurities. Same as what we have introduced in interaction between Kondo impurities paragraph (1.2.6), the coupling between impurities occur through various mechanisms. Depending on inter-impurity distance r there are two major ways: 1). At small distance where r is of the order of coherence length of Shiba states, the Shiba states of different impurities are expected to overlap. 2). At large distance where overlapping is not strong, the coupling will be mainly substrate mediated RKKY interaction. The studies of interacting Shiba states have been carried out experimentally [91, 106, 117–120] and theoretically [121, 122].

The phase diagram illustrating the ground state of interacting spin-1/2 Shiba dimer is shown in Fig. 1.18 which is obtained by Numerical renormalization group (NRG) calculation performed by Yao et.al. [122]. The concerned variables are RKKY coupling strength I ($I < 0$ for FM coupling, $I > 0$ for AFM coupling), pairing strength Δ, exchange coupling between impurity dimer and substrate T_K and overlap parameter $\mathcal{S} = \frac{\sin(k_F r)}{k_F r}$ responsible for the hybridization of the Shiba states. As a results of competition between these variables, there are five competing subgap Shiba dimer states (T_0,S_0,$D_\pm$,S_2) shown in Fig. 1.18 (a-b). These states are labelled by (S, Q, P) where S denotes the total spin, Q the number of quasiparticles bound to dimer and P the parity.

1). For large values of $\Delta/T_K >> 1$, it corresponds to the free-spin state where the ground

state is either a molecular triplet state ($T_0 = (1, 0, +)$) for $I < 0$ or a molecular singlet state ($S_0 = (0, 0, -)$) for $I > 0$. 2). For small value of $\Delta/T_K << 1$, the competition takes place between Kondo screening T_K and inter-impurity coupling I. For large value of positive I, the ground state is S_0 even for large T_K because of the reduction of total spin, this is in consistence with what happened in Kondo dimer (Fig. 1.8). However if I is small or negative $I < 0$, the S_0 ground state undergoes quantum phase transition (blue dash line) and becomes Kondo singlet $S_2 = (0, 2, -)$. This corresponds to the case where inter-impurity coupling I becomes too weak to reduce total spin and dimer starts to interact with superconducting substrate, leading to a Kondo singlet ground state. 3). For intermediate $\mid I \mid$ and $\Delta \sim T_K$ there is a molecular doublet which correspond to the case where one of the impurity enters Kondo-screened ground state while the other remains unscreened. For non zero $\mathcal{S}$, the hybridization leads to the formation of bonding or anti-bonding state $D_\pm = (1/2, 1, \pm)$.

The excitation spectra of Shiba dimer is shown in Fig. 1.18 (c) that illustrates the evolution of ground state and excited states along the black dashed line in Fig. 1.18 (b) at $I/T_K = 0.58$. At small Δ/T_K the dimer is strongly coupled to the substrate and ground state is S_2, due to the selection rule ($\Delta S = \pm 1/2, \Delta Q = \pm 1$) the excitation can only take place between S_2 and $D_\pm$, in such case we will have two pairs of Shiba states just like a spin-1 Shiba impurity. For $\Delta \sim T_K$, the ground state is bonding molecular doublet state D_+ and excited states are S_2, T_0 and S_0, three pairs of Shiba states could appear in the gap. At large Δ/T_K, T_0 is the ground state and excited states are again $D_\pm$.

Till now we have the conception about the ground state and excited state evolution together with corresponding excitation spectra of an interacting spin-1/2 Shiba dimer. It might not seem difficult to describe it theoretically, however in real experiments the realisation of ideal interacting Shiba dimer that shows potential to develop long range order (Shiba band) is more challenging. Because unlike Kondo resonance which is a many-body phenomena that localizes at Fermi level with a characterized width of T_K, Shiba state is a single quasiparticle excitation, which means Shiba state has a well defined energy level E_b. As we have learnt that E_b depends not only on magnetic exchange coupling with substrate J but also on the impurity environment where local density of states of substrate ρ_0, magnetic anisotropy D and E should be taken into account. Ideal interacting Shiba dimer requires that 1). E_b of each Shiba state are the same. 2). Overlap of Shiba wavefunction of both impurities. 3). Intermediate coupling strength of both I/T_K and Δ/T_K so that the long range order (related to I/T_K) can be developed without significantly suppressing in-gap states formation (related to Δ/T_K). All these requirements indicate that an ideal platform with the potential to build up Shiba band is extremely to find. Many works including this thesis have been dedicated to pursue Shiba band formation, but till the end of this manuscript only Wiesendanger's group [105, 106, 116] had recently given a solid prove of Shiba band formation in interacting Mn atom chain on superconducting Nb(110) surface.

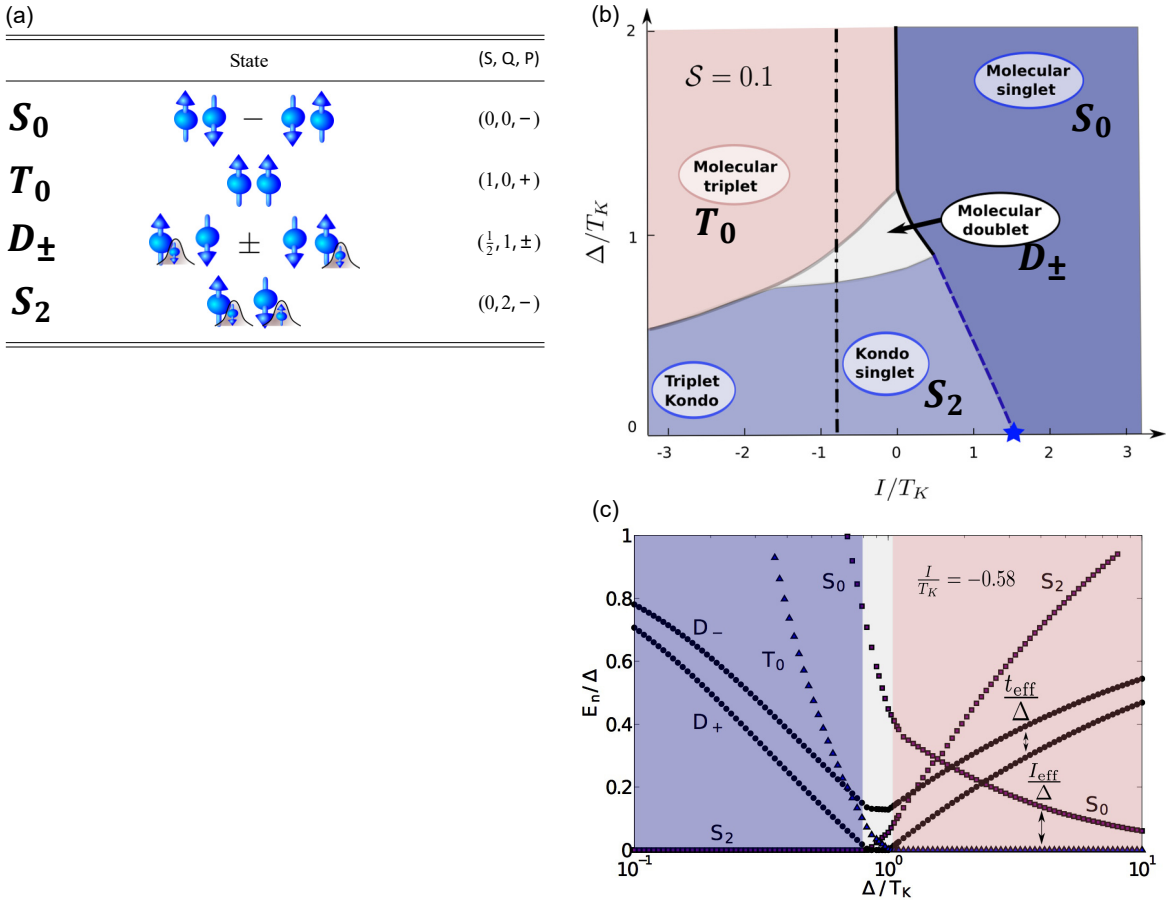

Figure 1.18: Phase diagram and corresponding excitation spectra for spin-1/2 Shiba dimer (a) Shiba dimer states labelled by (S, Q, P) where S denotes the total spin, Q the number of quasiparticles bound to dimer and P the parity. (b) Ground state phase diagram for interacting spin-1/2 Shiba dimer as function of I/T_K and Δ/T_K for overlap parameter $\mathcal{S} = 0.1$. The background colors indicate regions with S = 1 (light maroon), S = 1/2 (white), and S = 0 (blue) ground states. (c) Evolution of states along black dashed line in (a) where $I/T_K = 0.58$. At small Δ/T_K the ground state is Kondo singlet S_2 and the excitation can only occur between S_2 and molecular doublet $D_\pm$ due to selection rule $(\Delta S = \pm 1/2, \Delta Q = \pm 1)$. At intermediate Δ/T_K, the ground state is bonding molecular doublet D_+ and excited states can be Kondo singlet S_2, molecular triplet T_0 and molecular singlet S_0. At large Δ/T_K, the ground state is molecular triplet T_0 and excited states are molecular doublet $D_\pm$. The effective RKKY interaction I_{eff} can be extracted by the splitting between the S_0 and T_0 states and the effective hopping t_{eff} related to the overlap can also be deduced by splitting of $D_\pm$. Image adapted from [122].

1.4 Self-assembled molecules on metal surface

1.4.1 Motivation

For STM study there are two proposals to form Shiba band. The first one is build up 1D interacting impurity chain [113, 123]. This can be realised by artificially made magnetic transition atomic chain using STM tip manipulation technique (see section (2.4) and people have used several magnetic atoms such as Fe, Mn, Co to build up chains on different kinds of superconductor surfaces [106, 124–126]. The second one is to build up 2D interacting impurity lattice [114, 115]. This usually refers to self-assembled magnetic transition metal island on superconductor surface or embed in the superconductor [127–130].

Tip manipulation enables us to control inter-adatom distance r which is related to inter-impurity interaction I but magnetic exchange coupling J (related to atom orbital, substrate and inter-impurity interaction) is not controllable for adatom impurity, this indicates that the only way to control J is to try different impurities atom and substrate superconductor to satisfy the requirements of Shiba band formation. Another important aspect is that tip manipulation is a risky operation hence it is usually used to control small amount of atoms in 1D chain formation.

In view of shortcoming of uncontrollable J for atom impurities and the difficulty of tip manipulation operation, we propose here the investigation of self-assembled magnetic molecule system on superconductor surfaces. In this thesis, supramolecular chemistry and self-assembly concepts will be utilized to create atomically defined systems with controlled and tunable interactions between well-ordered and periodically spaced magnetic centers I and with the superconducting substrate J.

1.4.2 Porphyrin-based molecule

The molecules we propose to use are porphyrin-based molecules that consist of a magnetic transition metal (Mn, Fe) at organic porphyrin molecule center. Porphyrins are a family of organic molecules with a central pi-conjugated aromatic macrocycle ($C_{20}H_{12}N_4$, or usually labelled by "P") consisting of four pyrrole rings. A metal-free porphine molecule ($H_2-C_{20}H_{12}N_4$ or H_2-P) that is the most basic porphyrin molecule is shown in Fig. 1.19 (a) in which pyrrole ring is marked by red circle. The porphine molecule is non magnetic in gas phase, but it is possible to substitute two center hydrogen atoms by magnetic transition metal, forming a magnetic organic molecule ($TM-P$ with TM the transition metal) [131, 132]. Fig. 1.19 (b) shows the metal-free phthalocyanine ($H_2-C_{32}H_{16}N_8$ or H_2-Pc) molecule that is similar to porphine molecule, it is shown here for comparison because people have widely studied Kondo effect of its metal complexes ($TM-Pc$) on various systems (normal metal and superconductor).

The interactions between magnetic molecules I and with substrate J can be indirectly controlled by bonding substituents (or called ligand in this manuscript) to the porphine macrocycle. There are a wide range of organic ligands including phenyl ($-C_6H_5$)(Fig. 1.19 (c)), pyridyl ($-C_5H_4N$)(Fig. 1.19 (d)), and octaethyl ($-CH_3$) groups that can be bound to either β- or meso-positions on macrocycle. For example, the effective coupling with substrate J can be controlled by binding proper ligands: 1). Octaethyl groups can be bound to eight β-position of $Fe-P$ molecule and serve as a spacer that decouples molecule from the superconducting substrate, resulting a zero J so that in-gap Shiba states feature is replaced by above-gap inelastic spin flip excitation [109, 110]. 2). Sulfonyl hydroxide ($-SO_3H$) can be bound to meso-position of macrocycle, due to the strong electron affinity of sulfonyl ground J is expected to be large [133].

The inter-impurity coupling strength I is intimately related to the way the molecules assemble the lattice. In a self-assembled molecular lattice (or chain), unlike atom impurity where inter-atom interaction occurs through exchange coupling (short range) or RKKY coupling (long range), the inter-molecule interaction can occur through different kinds of chemical bonds where molecular orbitals are extended (or expelled) such as Van der Waals interaction, covalent bond,

hydrogen bond, polar bond, $\pi - stacking$, $T - stacking$ bonding, halogen bond ([134–137]). By using proper ligands we expect to control the bonding configuration in molecular assemblies.

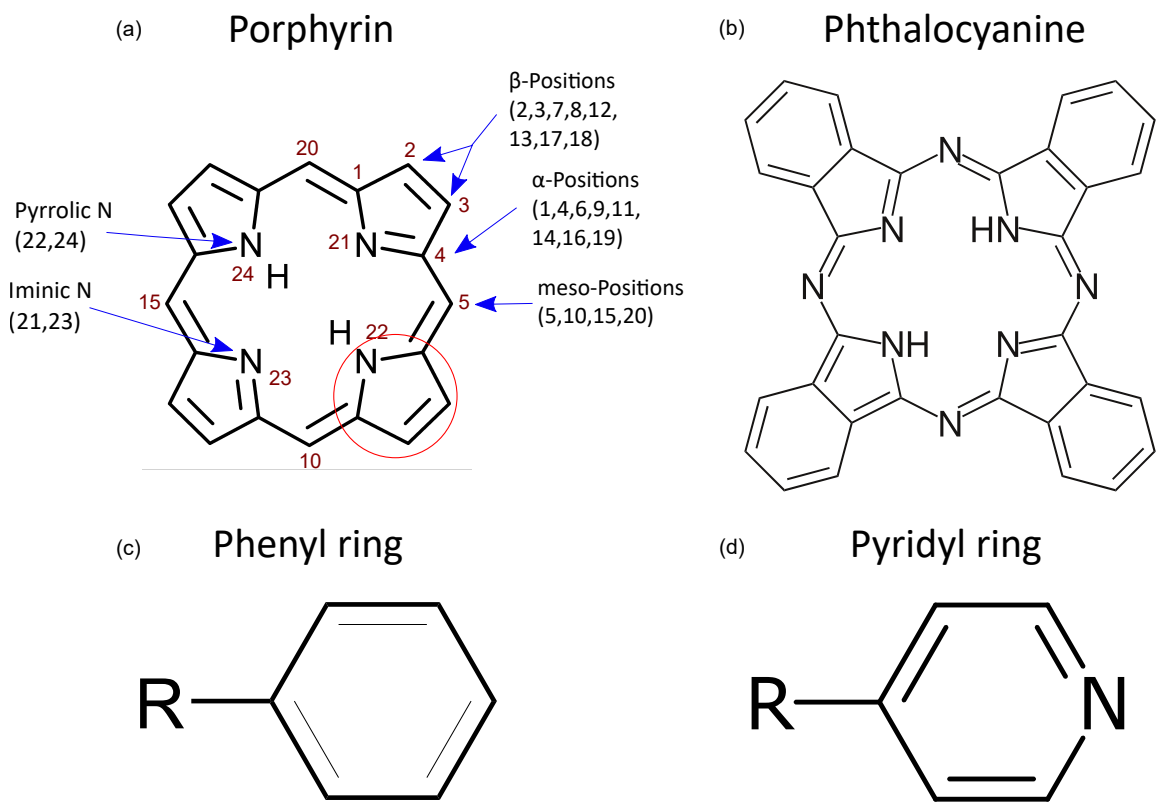

Figure 1.19: Structure of a macrocycle molecule and ligands. (a) Porphine ($H_2 - C_{20}H_{12}N_4$). Hydrogen atoms not shown explicitly, except for those bound to the pyrrolic nitrogen. Image adapted from [138]. (b) Phthalocyanine ($H_2 - C_{32}H_{16}N_8$). (c) Phenyl group ($-C_6H_5$), also called phenyl ring. (c) Pyridyl group ($-C_5H_4N$), also called pyridyl ring.

1.4.3 Molecule network

There are various strategies to realise on-surface bonding of molecules. The one to our interest is covalently bonded molecule chain or lattice through Ullmann reaction [139]. It has been shown that ligands containing labile Br atom can be used, when molecules are thermally activated, they will dissociate Br atom and form covalent bond with other molecule, this process can occur on the metal surface or in the molecule evaporation crucible [66, 138, 140, 141]. For example, four-fold symmetry tetra (4-bromophenyl) porphyrin (H_2Br_4TPP) molecule where four $Br - phenyl$ ligands are bonded to meso-positions of porphyrin macrocycle is shown in Fig. 1.20 (a). Upon heating the molecules are thermally activated and Br atoms are dissociated, then molecules connect with each other by forming covalent bond and stable 2D molecule lattice is formed (Fig. 1.20 (b)). Here 2D lattice is formed because the molecule had four-fold symmetry with $Br - phenyl$ ligands added to (5,10,15,20) meso-positions, if ligands are only added to

opposite position (5,15) or (10,20) one might expect to form 1D molecule chain [138].

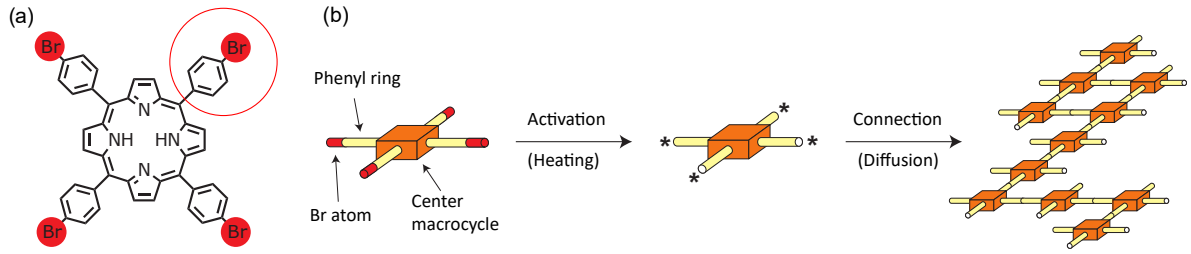

Figure 1.20: Covalently bonded H_2Br_4TPP molecular networks. (a) Chemical structure of H_2Br_4TPP) molecule (ligands are marked by red circle, Br atoms are highlighted in red). (b) Concept of debromination process that gives rise to covalently boned 2D molecule lattice. Image adapted from [140].

This thesis is dedicated to realise self-assembled magnetic molecule lattice/chain through debromination process on normal and superconducting metal, using STM/STS technique to study molecule orders and electronic structures of emerging Kondo/Shiba lattices (if there are) and exploring the recipes of forming Shiba band in molecular architectures.

1.4.4 Discussion

Finally we make a brief discussion concerning molecular system. The inter-molecular interaction is mediated by molecule orbitals (usually refer to π orbital of macrocycle) while the magnetic property are mainly given by center TM metal. The presence of molecular orbital will complicate the physic: 1). The coupling between center magnetic atom and macrocycle π orbital is inevitable which drives the whole molecule magnetic (spin polarized orbital in organic part). This has been confirmed by several studies [142–147] but the consequence of intra-molecule coupling still far from being fully understood. 2). The magnetic molecule conception indicates a non-point-like scatterer, this will result delocalized orbital in the view of center atom [147–150] and new phenomena such as vibration modes [40, 145, 151], single channel spin-1 Kondo effect [40]. 3). Molecular orbital itself can directly couples with substrate that might greatly influence the magnetic behavior of the molecule [152–154]. In some cases a metal-free molecule can acquire magnetism by receiving charge from the substrate and Kondo resonance appears [41, 137, 155, 156] or a magnetic molecule becomes non-magnetic once adsorbed on metal surface [39, 157, 158].

On the other hand, the presence of macrocycle makes molecule system ideal for spin state manipulation studies. For example the stabilized macrocycle allows capturing additional transition atoms to molecular [159, 160], attaching removable ligand directly to center atom [161–165] that can modified the spin state of molecule or using the tip to tune the interaction between molecule with substrate J to study its effect on Kondo or Shiba phenomena [31, 33, 166–169].

Concerning the molecule network formation, there are various kinds of approach such as forming covalent bonds with other substituent ligands from the bromine atoms [170], forming transition atom coordinated network [67, 171–174], forming other bonds like homocoupling

through hydrogenation [175] or using distorted molecules that couples tightly [62]. In this thesis we mainly focus on the effects of phenyl, pyridyl and bromine atoms ligands attached to porphyrin macrocycle.

Chapter 2

Experimental Techniques and Methods

2.1 Introduction

In this chapter we will present the basis concepts and techniques that will be used throughout this thesis.

At the first stage shown in section (2.2), we will first introduce the model of quantum tunneling phenomena in section (2.2.1) and the experimental scanning tunneling microscopy and spectroscopy (STM/STS) techniques in sections (2.2.2) and (2.2.3). The specific cases using normal or superconducting tips, with elastic tunneling or inelastic tunneling will also be involved. Then we will present the simulated spectral lineshape obtained by tunneling through magnetic impurities on metal surface in section (2.3) and tip manipulation process in section (2.4).

At the second stage shown in section (2.5) we will introduce our approach to data analysis, which includes both topographic (section (2.5.1)) and spectroscopic data (section (2.5.2)) which are respectively obtained in STM/STS experiments. After that, in section (2.5.3) we will introduce the deconvolution method in detail which aims to remove the effect of BCS DOS of superconducting tip in SIS STS experiments.

In the last part (section (2.6)) we will detail the characteristics of the laboratory apparatuses which were used for our experimental works.

2.2 Scanning tunneling microscopy and spectroscopy

Scanning tunneling microscopy (STM) and spectroscopy (STS) techniques were used throughout this thesis to study the conformation of the molecules and their electronic properties once adsorbed on various substrates. STM allowed us to image architectures of molecules with atomic scale resolution and STS allowed us to probe local electronic properties of molecules and substrates with a spectral resolution up to 0.1 meV. STM/STS techniques are implemented with a scanning tunneling microscope which was first invented by Binnig and Rohrer, [176–178] in early 1980's and these techniques are based on the concept of quantum tunneling effect. The basic idea of a scanning tunneling experiment is simple: under ultra-high-vacuum (UHV) condi-

tion we consider a fixed conducting sample and a controllable sharp metallic tip above it (Fig. 2.1 (a)). The tip position is finely controlled by three piezoelectrics operating along three different orthogonal spatial directions and a bias voltage is applied between the tip and the sample. When the tip is brought close enough to the sample surface, electrons in the tip extremity can tunnel through the vacuum barrier to the sample or vice versa. Depending on the sign of bias voltage, a net tunneling current occurs between the tip and the sample. The tunneling current which is exponentially dependent on tip-sample distance is then measured. During the tunneling process if an electron tunnel to a final state with same energy as the one of the initial state (e.g. Fig. 2.1 (b)), it is called elastic tunneling. If the energy of the final state is different from the initial one, i.e. an inelastic interaction occurred during the tunneling process, it is called inelastic tunneling (see paragraph (2.2.4)). Both structural information and electronic properties are encoded in tip-sample distance and tunneling current.

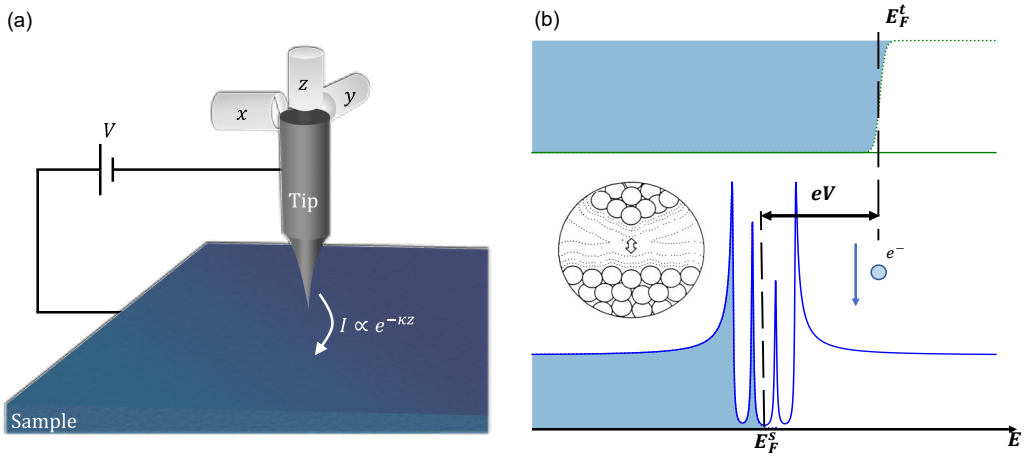

Figure 2.1: Scanning tunneling experiment principle. (a) Illustration of a scanning tunneling microscope. A metallic probe tip controlled by piezoelectrics is stabilized about several angstroms above the sample surface. A bias voltage V is applied between the tip and the sample. A tunneling current I is measured and its amplitude depends on the tip-sample distance z, bias voltage V and decay constant κ. Image adapted from [179]. (b) Illustration of the elastic electron tunneling spectroscopy process. Considering a tunneling current measured between a normal metal tip (up) and a superconducting sample hosting a rigid magnetic impurity (Shiba impurity) (down). A positive bias V is applied to the tip with respect to the sample which moves the chemical potentials of the electrodes relatively to each other. The electrons in the occupied states of the tip will tunnel elastically to the sample's empty states. In this simple picture, the tunneling current I depends only on V, the DOS of tip and sample (solid green and blue lines) and the tip-surface distance. The colored dashed line indicates the occupancy of states due to the Fermi-Dirac distribution. Embed image adapted from [180].

2.2.1 Modeling tunneling current

The tunneling phenomena between two electrodes (tip and sample) can be treated as a metal-insulator-metal (MIM) junction. John Bardeen had applied a transfer Hamiltonian method to solve this MIM tunneling junction problem [181] and his theory was further extended to scanning tunneling microscopy by J. Tersoff and D. R. Hamann [182, 183] while voltage dependent calculation of the scanning tunneling current was later developed [184–186].

Bardeen's tunneling theory

In Bardeen's model, the MIM tunneling junction is described by the following Hamiltonian:

$$H = H_t + H_s + H_b \tag{2.1}$$

where H_t and H_s are Hamiltonian of left and right electrodes. H_b is the transfer Hamiltonian that describes the tunneling electrons through the vacuum barrier. Illustration of this MIM junction is shown in Fig. 2.2, the eigenstates and corresponding energies of H_t and H_s are E^t_μ, ψ^t_μ and E^s_ν, ψ^s_ν respectively. ϕ is the workfunction, V the applied bias between electrodes and z_0 the distance of barrier.

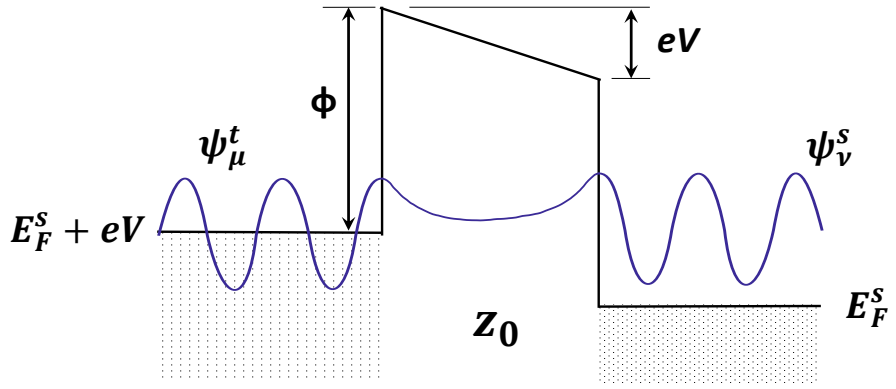

Figure 2.2: Illustration of MIM tunneling junction. The two electrodes are separated by vacuum barrier of width z_0. Tunneling phenomena occur when two electrodes are close enough.

The tunneling current of such MIM junction follows the expression:

$$I = \frac{4\pi e}{\hbar} \sum_{\mu\nu} [f(E^t_\mu - eV) - f(E^s_\nu)] \mid M_{\mu\nu} \mid^2 \delta(E^t_\mu - E^s_\nu + eV) \tag{2.2}$$

$$f(E) = \frac{1}{e^{(E-E_F)/(k_B T)} + 1} \tag{2.3}$$

$M_{\mu\nu}$ is the tunneling matrix element and $f(E)$ the Fermi-Dirac distribution. The tunneling matrix elements $M_{\mu\nu}$ depends on the geometry of both electrodes and can be described by surface integral of the wavefunctions of the two electrodes:

$$M_{\mu\nu} = \frac{\hbar^2}{2m} \int_\Sigma (\psi^t_\mu \nabla \psi^{s*}_\nu - \psi^{s*}_\nu \nabla \psi^t_\mu) d\vec{S} \tag{2.4}$$

Σ is the surface of two electrodes.

The tunneling matrix element describes the effect of potential barrier H_b on the tunneling electrons between states ψ^t_μ and ψ^s_ν. We will see that the evaluation of tunneling matrix element shows important consequences on tunneling properties.

We can also introduce the DOS of both electrodes ρ_t and ρ_s by replacing the summation over

finite states μ, ν by the integral over energies:

$$I \propto \int \rho_t(E - eV)\rho_s(E)[f(E - eV) - f(E)] \mid M \mid^2 dE \tag{2.5}$$

We find that I depends on the electronic structures of both electrodes in a way of convolution between ρ_t and ρ_s, and it depends also on the geometry structures of both electrodes given by tunneling matrix element M.

Model for the tunneling current

To extend Bardeen's tunneling theory to STM setup one has to apply a proper model for describing the geometry of the two electrodes i.e. evaluate the tunneling matrix element $M_{\mu\nu}$ in a sharp tip and flat sample geometry (i.e. Fig. 2.1 (a)). Tersoff and Hamann formulated a simple but widely used model (TH model) where STM tip is considered as a locally spherical potential well and the sample as a plane with periodic potential (Fig. 2.3) [182, 183].

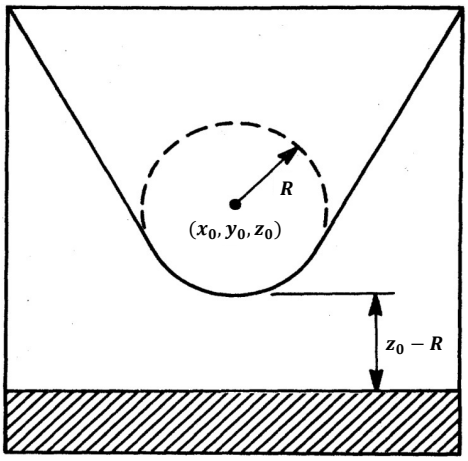

Figure 2.3: Tersoff-Hamann model of STM. The STM tip is modeled as a locally spherical potential well radius of curvature R centered at (x_0, y_0, z_0). In the following discussions we consider R being negligible with respect to tip-sample distance z_0, which means the tip apex is considered as a geometric point. Sample surface is modeled as $z = 0$ plane. Image adapted from [183].

In this assumption, the wavefunction of the tip can be characterized by a spherical evanescent wave propagating from the tip apex located at r_0, and wavefunction of surface by 2D-Bloch wave. So that the wavefunction of the tip can be chosen to be:

$$\psi_\mu^t(\vec{r}) = A_\mu \frac{e^{-\kappa|\vec{r}-\vec{r_0}|}}{\mid \vec{r} - \vec{r_0} \mid} \tag{2.6}$$

with

$$\kappa = \sqrt{2m(\phi - E_\mu^t)}/\hbar \tag{2.7}$$

the decay constant which depends on work function ϕ and energy of electron E_μ^t [1]. r_0 refers to

[1] The energy dependence of κ indicates that tunneling matrix also depends on energy [187]. It will result a more

the tip position (x_0, y_0, z_0), m the electron mass and A_μ the normalisation constant.

The wavefunction of the surface is described by Bloch wave:

$$\psi_\nu^s(\vec{r}) = A_\nu e^{i\vec{k}\vec{r}} u(\vec{r}) \tag{2.8}$$

where $\vec{k}$ denotes the momentum vector, $u(\vec{r})$ the periodic function with the same periodicity as the crystal. A_ν is normalisation constant.

By inserting wavefunction equations (2.6) and (2.8) into the tunneling matrix equation (2.4), we will find the most important dependence of the tunneling matrix element:

$$M_{\mu\nu} \propto \psi_\nu^s(\vec{r_0}) \tag{2.9}$$

This is the central idea of TH model: by considering "s-wave" spherical symmetric tip states at tip apex $\vec{r_0} = (x_0, y_0, z_0)$, the tunneling matrix element is directly proportional to the wavefunction of the sample at the tip apex.

By replacing equation (2.9) in equation (2.5) the tunneling current becomes:

$$I \propto \int \rho_t(E - eV)\rho_s(E, \vec{r_0})T(E, V, \vec{r_0})[f(E - eV) - f(E)]dE \tag{2.10}$$

where $\rho_s(E, \vec{r_0}) \equiv \mid \psi^s(\vec{r_0}) \mid^2 \rho_s(E)$, the local density of states (LDOS) of sample at energy level E at tip apex location. This expression indicates that tunneling current I obtained by the STM tip is related to the LDOS of sample ρ_s at tip apex. T is the transmission factor derived from tunneling matrix element, it is related to decay constant in expression (2.7) and responsible for the exponential dependence of current on tip-sample distance.

When the bias applied is low with respect to the workfunction ϕ, T can be considered as energy independent i.e.:

$$T(E, V << \phi, \vec{r_0}) \approx T(E_F, \vec{r_0}) \tag{2.11}$$

And under the assumption of "s"-wavefunction of tip apex and 2D-Bloch wavefunction of surface proposed in TH model, T can be considered as a variable that depends only on tip-sample distance i.e. $T(E_F, z_0)$, Thus T can be factored out of the integral:

$$I \propto T(E_F, z_0) \int \rho_t(E - eV)\rho_s(E, \vec{r_0})[f(E - eV) - f(E)]dE \tag{2.12}$$

This equation is the basis of the analysis of our data in the following. With small applied bias voltage V and the assumption that both DOS of tip and sample does not vary appreciably near Fermi level at 0 K, then equation (2.12) can be further simplified as:

$$I \propto \rho_t(E_F)\rho_s(E_F, \vec{r_0})Ve^{-2|\kappa z_0|} \tag{2.13}$$

with the last term representing exponential dependence of current on tip-sample distance given

important contribution of tip DOS near Fermi level and sample DOS about eV above Fermi level in equation (2.5).

by transmission factor $T(E_F, z_0)$.

TH model has proven to be effective to explain STM image with low spatial resolution (≥ 0.1 nm) but failed to explain the high resolution image such as corrugation of atomic-scale features. This problem was later addressed by considering the general cases of wavefunction at tip apex (e.g. p and d type) rather than a pure s-wave one [186, 188].

Yet the capabilities of scanning tunneling technique are not limited to measure DOS of sample. For example, spin-polarized scanning tunneling microscopy is sensitive is to the spin orientation of tunneling electrons due to the magnetic atom/molecule decorated tip apex [189, 190], it allows us to measure the spin texture of the sample; Electron spin resonance spectroscopy performed by STM setup in which modulated electric field is applied during tunneling allows us to precisely measure the spin state of magnetic atom or molecules [191]. However these techniques will not be used in this thesis.

2.2.2 Topography mode

The corrugation of a surface, atomic structure, molecular conformations, adsorption sites and structural organisation or assembly can be measured by STM topography image. Topography data can be recorded thanks to two different microscopy modes.

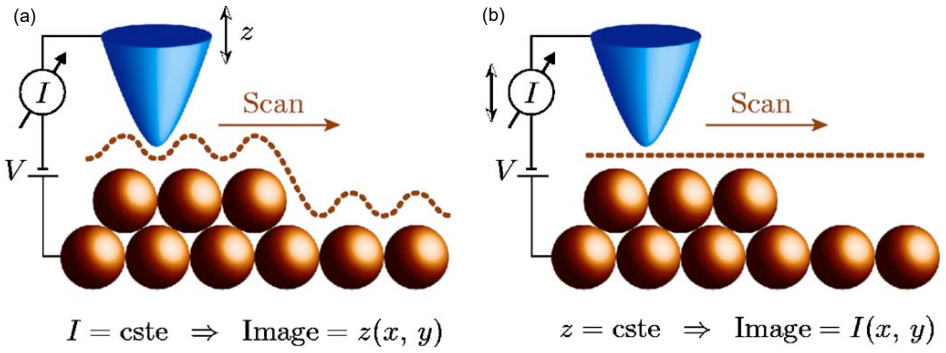

Figure 2.4: Two different modes to make topography image in STM experiments (a) Constant current mode. Tunneling current remains constant during scanning, tip-sample distance does not significantly vary, tip height is used for topography. (b) Constant height mode. Tip height remains constant during scanning, tip-sample distance can significantly vary when tip overpasses a protrusion (depression) of surface, tunneling current is used for topography. Image adapted from [192].

Topography measurement

The first mode is called constant current mode (Fig. 2.4 (a)): a feedback loop maintains the tunneling current at a chosen value I_i when applying constant bias voltage V_i to the tunneling junction. The feedback loop regulates the extension of piezoelectrics in order to keep scanning current equals to I_i when scanning the surface with the tip. The extension of three sets of piezoelectrics define the coordinates of the tip (x, y, z). The topography image is reconstructed by recording $z(x, y)|_{V_i, I_i}$. Due to the exponential dependence of the barrier transmission with the tip distance, the main contribution to this topography is the the surface corrugation which forces

the tip to follow step edges, islands or nanostructures contour lines of height. If the experimental conditions are such as tip-sample height does not significantly vary and that the voltage is low, then transmission factor in equation (2.12) should not significantly vary as well with (x, y) positions. In that case, the topography $z(x, y)|_{V_i,I_i}$ is a direct recording of the sample LDOS $\rho_s(E_F, x, y, z_0)$ at E_F in agreement to TH model, equation (2.13). This is useful to record quasi-particles interference patterns, chemical/defect contrast and atomic resolution (Fig.2.5 (a)). For general case, the constant current topography mode always mixes corrugation and LDOS information. If one wants to get rid of the corrugation signal, one must consider the spectroscopic mode, presented below (section (2.2.3)).

If one wants to get rid of the effect of the LDOS which is inhomogeneous by nature due to quantum interference, the trick is to average the spatial dependence of the LDOS thanks to the energy integral of equation (2.10). This is what is performed with success for metal surfaces where topography images are usually recorded at a large bias voltage (typically a few hundreds of meV) (Fig.2.5 (b)).

When the orbital nature of the sample induces strong variations of the LDOS in space and energy, like in the case of semiconducting surfaces and adsorbed molecules for instance, corrugation and LDOS effects cannot be completely distinguished experimentally. This effect has an impact on the data analysis which does often necessitate theory calculations to be modelled in detail.

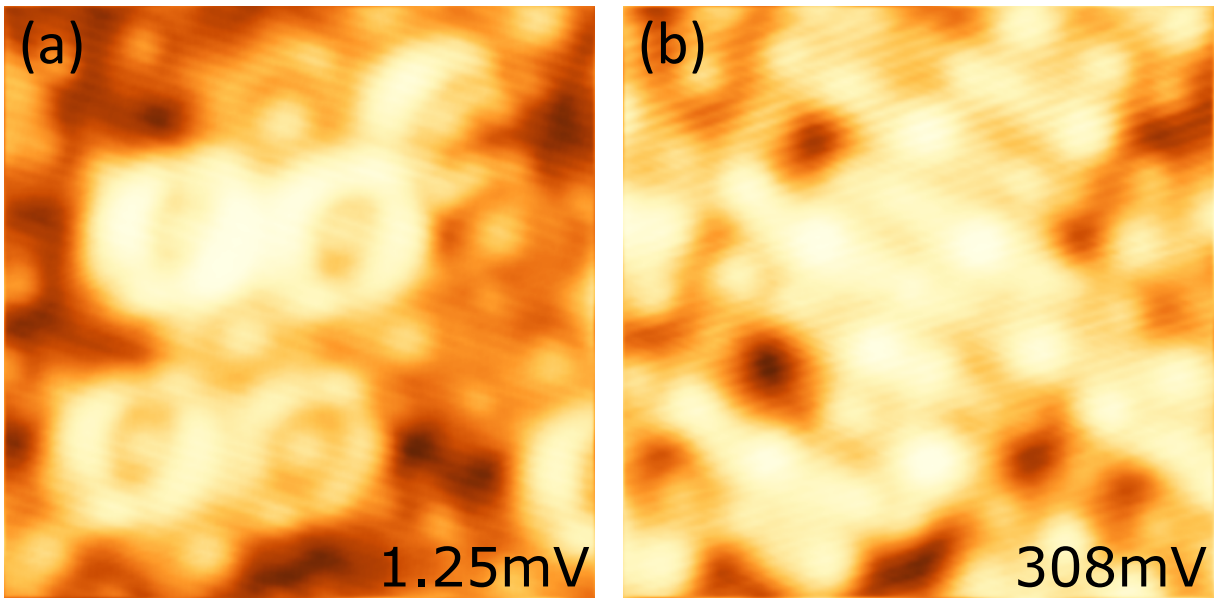

Figure 2.5: Constant current topography images recorded at different setpoint. (a) Constant current topography image ($6\text{x}6\text{nm}^2$) of self-assembled magnetic at setpoint of 1.25 mV, 3 pA. LDOS of molecules at Fermi level ($\rho_s(E_F)$) gives the most contribution to topography. (b) Constant current topography image of same region as (a) but at setpoint of 308 mV, 30 pA. At high setpoint bias voltage, molecular orbital gives the most contribution to the topography.

The second mode is called constant height mode (Fig. 2.4 (b)) in which the feedback loop is turned off. In this case the setpoint consists of a constant height z_i and a constant bias voltage V_i. During scanning process z piezoelectric holds the value z_i and only x, y piezoelectrics extend.

The scanning current $I(x,y)|_{z_i,V_i}$ can be used to reconstruct topography image. Constant height mode is not widely used because disabling feedback loop during scanning process may crash the tip to sample surface. Also, the current is exponentially dependant of tip-sample distance z_0 which might significantly vary, this will make the interpretation of the data quite hazardous because transmission factor is spatial dependent on z_0 and can not be factored out of integral in expression (2.10). However this off-feedback loop technique is essential for spectroscopy experiments and tip manipulation as it will be discussed in the following paragraphs.

2.2.3 Spectroscopy mode

In this paragraph we will introduce the spectroscopy mode and demonstrate that the local density of the quasiparticle states $\rho_s(E,\vec{r}_0)$ of the sample can be deduced from scanning tunneling spectroscopy (STS) experiments where the variation of the current with the voltage is recorded. We consider only elastic processes during the electrons tunneling.

An STS experiment

During STS experiments, the tip-sample distance is kept constant z_0 by turning off feedback loop when the tip is at a specific location above the surface ($\vec{r}_0$). z_0 is determined by the setpoint $V_i, I_i, \Delta z$ where the first two components determine the initial tip height $z|_{V_i,I_i}$ and the third component adjusts the final tip height during STS measurement i.e. $z_0 = z|_{V_i,I_i}+\Delta z$. Once the tip height is setup, $I(V)$ is then measured when the bias voltage is swept linearly with time (the data analysis is more convenient for a linear variation of V). During this process, the tip position $\vec{r}_0$ remains fixed so that bias voltage is the only experimental variable of the spectroscopic measurement.

According to equation (2.12) the electronic properties of the sample ρ_s appears inside the integral and is convoluted with ρ_t. To extract $\rho_s(E,\vec{r}_0)$ we have to first study the differential conductance, i.e. the derivative of the current with respect to the voltage dI/dV which can be obtained either by numerical derivation of the recorded data or directly measured by lock-in technique (see paragraph (2.5.2)). Then we have to know the details of tip ρ_t in order to deduce $\rho_s(E,\vec{r}_0)$.

When using a Normal tip

For a normal metal tip it is generally assumed that its DOS ρ_t is constant with the energy. By chance it is quite always the case when one is interested in small energy windows with respect to the bandwidth of a normal metal (i.e. a few meV as for the case of a superconductor gap energy). This assumption is generally wrong for larger energy windows. However, the STM tip can be experimentally "prepared" for being as close as possible to a constant DOS or at least, to exhibit a monotonous variations with energy which can be easily removed from the data with a simple procedure.

If the tip DOS ρ_t is constant, the derivative of the current with respect to the bias voltage in (2.12) can be written as:

$$dI/dV \propto -\int dE\rho_s(E,\vec{r_0})\frac{\partial f(E-eV)}{\partial E} \tag{2.14}$$

At low temperature the derivative of the Fermi-Dirac distribution function 2.3) with respect to energy tends to a Dirac delta function:

$$\lim_{\text{Temp}\to 0K}\Theta(E) = \lim_{\text{Temp}\to 0K}\frac{\partial f(E-eV)}{\partial E} = \delta(E-eV) \tag{2.15}$$

Thus equation (2.14) becomes:

$$dI/dV(V,\vec{r_0}) \propto \rho_s(eV,\vec{r_0}) \tag{2.16}$$

This result indicates that with a normal metal tip, at T = 0 K, the differential conductance dI/dV is a direct estimate of the LDOS of the sample at the position of the tip $\vec{r_0}$. Thus, in the ideal case there is a direct correspondence between energies and voltages, considering the charge of the electron as a proportional constant. The measure of $dI/dV(V,\vec{r})$ is what is called scanning tunneling spectroscopy. Here, for simplicity but also because it corresponds to our microscope design, the temperature of the tip and the surface are chosen to be the same. The minimum temperature we can reach in our setup is 1.1K. At this temperature the thermal broadening limits spectral resolution to approximately 400 μeV ($\sim 3.5k_B$T).

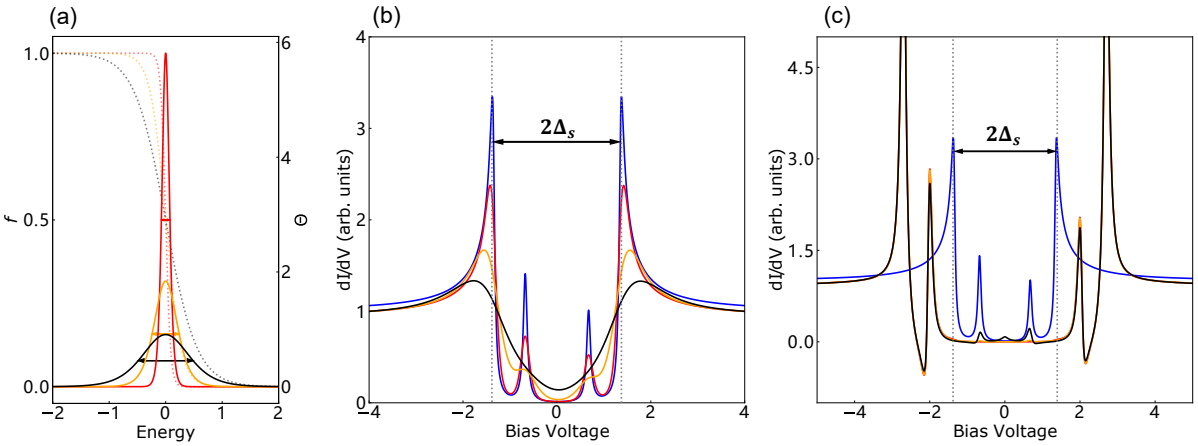

Figure 2.6: Thermal broadening when using normal or superconducting tip when measuring a superconducting sample (a) Fermi-Dirac distribution function $f(E)$ in dashed line and its derivative $\Theta(E)$ in solid line at dimensionless temperatures $T_1 = 0.03$ (red), $T_2 = 0.1$ (orange) and $T_3 = 0.2$ (black). Arrows show FWHM of $\Theta(E)$. (b) Simulated dI/dV spectra of a superconductor showing a superconducting gap (Δ_s) and in-gap quasiparticle states taken with a normal tip. Blur curve represents the standard representative of a perfect measurement with a metallic tip without thermal broadening. Dimensionless simulation temperatures are $T_1 = 0.03\Delta_s$ (red), $T_2 = 0.1\Delta_s$ (orange) and $T_3 = 0.2\Delta_s$ (black). (c) Simulated dI/dV spectra with a superconducting tip ($\Delta_t = \Delta_s$) in the same conditions as for (b). Blue curve represents the standard representative of a perfect measurement with a metallic tip without thermal broadening. Energy and bias voltage are dimensionless.

The effect of thermal broadening with normal tips can be easily estimated by considering the tunneling spectroscopy of a superconducting sample characterized by a superconducting gap Δ_s hosting sharp quasiparticle excitations (e.g. Yu-Shiba-Rusinov states presented in chapter (1)). The broadening can be characterized by full width at half maximum (FWHM) of $\Theta(E)$ function. $\Theta(E)$ is plotted for 3 different temperatures $k_BT_1 = 0.03\Delta_s$, $k_BT_2 = 0.1\Delta_s$ and $k_BT_3 = 0.2\Delta_s$ respectively in (Fig. 2.6 (a)). The effect on the simulated dI/dV spectra is shown in (Fig. 2.6 (b)).

The thermal broadening impacts strongly the the calculated dI/dV spectra. As temperature increases from T_1 to T_2, the width of the superconducting quasiparticle peaks and in-gap quasiparticle excitations broadens and their spectral weight is reduced. At T_3, the thermal broadening is washing out all spectral characteristic and the dip which remains does not does not allow for any reasonable measurement of the the gap amplitude (black arrow in Fig. 2.6 (a)). We chose T_2 as a criterion indicating the crossover where it is becomes difficult to perform any data analysis due to thermal effects. This criterion corresponds to $\frac{T}{T_C} \approx 0.18$ for BCS superconductors (where $k_BT_C \approx 1.764\Delta$). According to this criterion, we should not measure any superconductors with $T_C > 6.8\,\mathrm{K}$ which limits drastically the list of superconductors that can be studied by our microscope. For example, according to our criterion, since Pb which has a critical temperature of 7.2K, the study of its properties should be out of reach. By chance, the spectral resolution due to the thermal broadening can be drastically improved when using a superconducting tip.

When using a Superconducting tip in a SIS junction

To improve the spectral thermal resolution, a superconducting tip can be used during STS experiments. This tunneling configuration is called a "SIS junction" ("S" and "I" stand for superconductor and insulator respectively). To understand the SIS spectral shape, we make a calculation of the tunneling spectrum of a superconducting sample taken with a superconducting tip which gap values are Δ_s and Δ_t respectively (Fig. 2.7 (a)). The transmission coefficient of expression (2.12) is chosen to be equal to 1, and we first neglect the temperature effect as in equation (2.15).

Since the normalised DOS of the tip ρ_t follows the BCS quasiparticle distribution, equation (1.23), SIS spectroscopy is different from that obtained with a normal tip. Because of the absence of DOS near the Fermi level inside the two electrodes, electrons cannot tunnel through the SIS junction at low bias voltage, resulting a zero current in the voltages window $[-(\Delta_t + \Delta_s)/e, +(\Delta_t + \Delta_s)/e]$, see Fig. 2.7 (b-c). When the voltage bias correspond to a larger value than the sum of two gaps $(\Delta_t + \Delta_s)/e$, a current is established in the junction, see Fig. 2.7 (d-e). Thus the differential conductance (Fig. 2.7 (f)) shows two sharp peaks symmetric to zero bias located at the edge of a gap of $\pm(\Delta_t + \Delta_s)/e$; these features are the signature of BCS quasiparticle peaks and gaps in SIS tunneling spectra. The quasiparticle peaks resolved by a superconducting tip show much higher amplitude and much smaller half-width at half maximum than those resolved by normal tip, see Fig. 2.6 (b). This phenomenon originates from the divergence of the quasiparticle DOS at the edge of the superconducting gap which show extremely

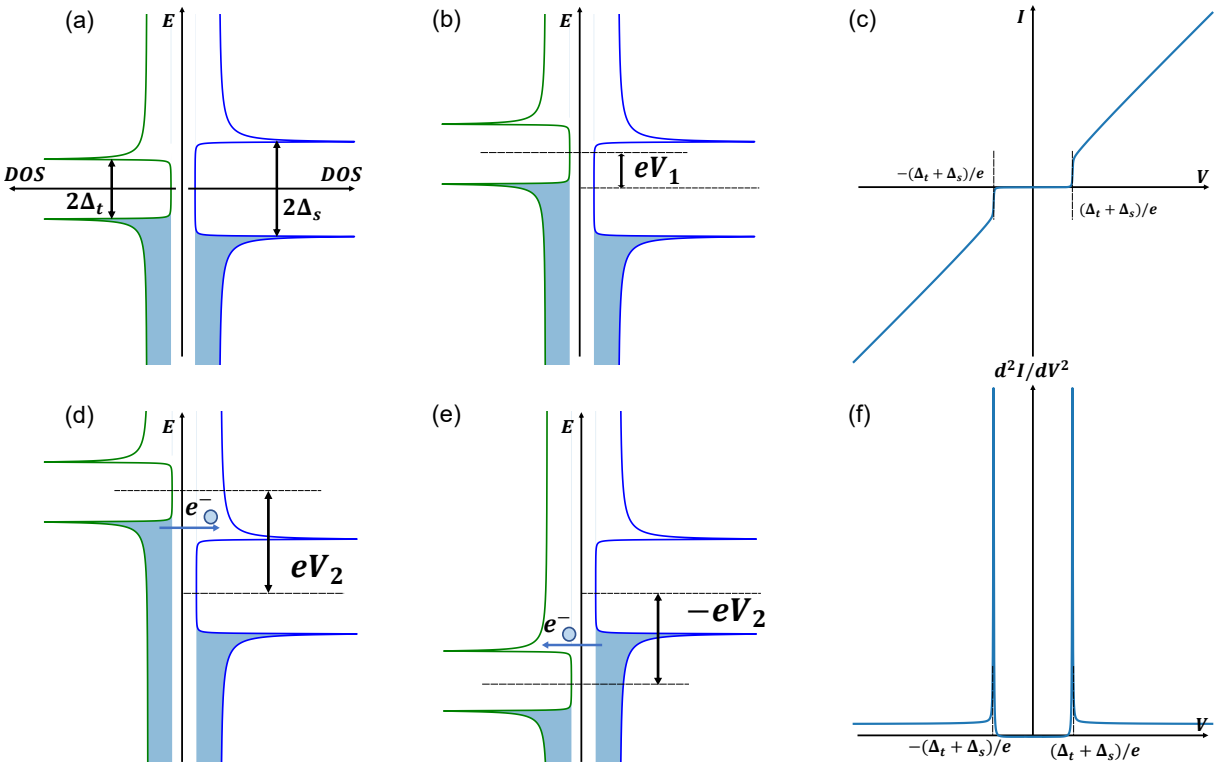

Figure 2.7: Scanning tunneling spectroscopy with superconducting tip at zero temperature. (a) Energy diagram of elastic tunneling between superconducting tip (gap Δ_t, green curve) and superconducting sample (gap Δ_s, blue curve). BCS quasiparticle peaks are partially shown. (b,d,e) With small bias V_1 no tunneling due to the gaps. Tunneling occurs when the absolute value of bias overcomes $(\Delta_t + \Delta_s)/e$. (c) Calculated tunneling current as function of bias. At voltage inferior to $(\Delta_t + \Delta_s)/e$ tunneling current is zero. (f) derivative of current with respect to the bias voltage. Two symmetric sharp peaks are observed at $\pm(\Delta_t + \Delta_s)/e$ which are the signature of BCS peaks.

thin width with respect to the thermal broadening function $\Theta(E)$ described above. It greatly improves the spectral resolution, even for the determination of sharp in-gap states.

Fig. 2.6 (c) presents simulated dI/dV spectra taken with a superconducting tip at temperatures $T1$, $T2$ and $T3$. The chosen case, Δ_t = Δ_s, is experimentally favorable since it gives an "apparent" doubling of the gap voltage with respect to the case of a normal tip and makes easier the understanding of the raw data. The spectra show a modified shape with respect to a perfect measurement with a metallic tip (blue curve). For a normal tip we know that the thermal broadening originates from the non-integer average occupancy of states below and above the Fermi level at finite temperate (Fig. 2.6 (a)) according to Fermi-Dirac distribution function. In the case of superconducting tip there is no state available near Fermi level if the superconducting gap amplitude is well developed, i.e. if the temperature of measurement is much lower than the critical temperature. This provides to the superconductor a natural ability against thermal noise [193]. As one can estimate by comparing the various cases of Fig. 2.6 (b) and (c). Even at relatively high temperature (T_3), sharp spectroscopic features subsist, however the number of peaks has changed and the characteristic voltages have been modified. To understand how the spectrum has been modified with respect to a normal tip, we present, in Fig. 2.8, the calculated SIS spectral with or without in-gap states at various temperatures in the most general general

case where superconducting tip and sample are considered ($\Delta_t = 0.63\Delta_S$).

In the case where there is no in-gap state (Fig. 2.8 (a)), the calculated SIS spectra are shown in Fig. 2.8 (b). At low temperature T_1, thermal effect is not efficient enough to induce a significant population of the occupied states above the gaps Δ_t or Δ_s. Thus the conductance curve (red curve) will be quite similar as the zero temperature case (Fig. 2.7 (f)). At higher temperature T_2 and T_3, the occupied states above the gap will contribute to tunneling current as well (holes below the gap energy will are playing a role). The quasiparticle peak related to ρ_s at $+\Delta_s$ energy gives rise to two spectral features at $(\Delta_s \pm \Delta_t)/e$ in SIS spectra which is explained by the tunneling into the quasiparticle peak of the tip DOS at positive and negative energies. For e-h symmetry reasons, the quasiparticle peak related to the sample DOS at $-\Delta_s$ energy gives rise to two spectral features at $(-\Delta_s \pm \Delta_t)/e$ in SIS spectral.

Hence, at relatively high temperature (fractions of T_C) we observe two new peaks at $\pm(\Delta_s - \Delta_t)/e$ inside the enhanced gap which are the thermally triggered replica of the quasiparticle peaks related to the sample (orange and black curve, quasiparticle peak signature are marked by dashed purple lines). As expected the spectral weight of the replica increases with temperature, witnessing their thermal origin. One should also note that unlike the peaks resolved by a normal tip, in-gap peaks come with a dip of negative differential conductance. This negative differential conductance originates from the divergence of BCS quasiparticle peaks which induces a rapid increase followed with a rapid decrease of the current when when sweeping the voltage.

We now consider the presence of in-gap states. We first consider a zero energy state (e.g. Majorana bound state) inside the gap (Fig. 2.8 (c)). The calculated SIS spectral is shown in (Fig. 2.8 (d)) where the single zero energy peak is resolved as two peaks with same spectral weight located at $\pm\Delta_t/e$ due to the shift by a value of $+(-)\Delta_t/e$ in SIS spectral already observed above. For the typical case of Yu-Shiba-Rusinov states, two sharp spectral features (at electron and hole symmetric energy) subsist inside the superconducting gap at $+(-)E_s$ (Fig. 2.8 (e)). In SIS configuration, Fig. 2.8 (f), the signature of electron and hole in-gap states are two peaks at $+(-)(E_s + \Delta_t)/e$ and $+(-)(E_s - \Delta_t)/e$ respectively. Two first set of spectral signatures at $(\pm(E_s + \Delta_t))$ with the same relative spectral weight correspond to the two genuine electron and hole in-gap states. If the temperature is high enough, the number of spectral features is doubled due to the thermal population of electrons (or holes) of the quasiparticle peaks: two other spectral signatures are measured due to the thermal effect at $\pm(E_s - \Delta_t)/e$ with reverse relative spectral weight, so with reverse relative order with respect to the electron-hole original in-gap states. Thus the electronic properties of in-gap states (energy, spectral weight and width) are encoded in both the 2 sets of measured peaks in SIS configuration.

The use of superconducting tip can indeed greatly improve spectral resolution and the ability against thermal noise, there are still inevitable drawbacks of it. The first one is that the position of peak is shifted by a value of Δ_t which is the gap value of tip and the differential conductance is not readily comparable to the LDOS, for example the existence of negative conductance. The second one is the thermally induced replica located inside energy window of $[-\Delta_t, +\Delta_t]$. These thermal induced replica still contain information about the LDOS of the sample.

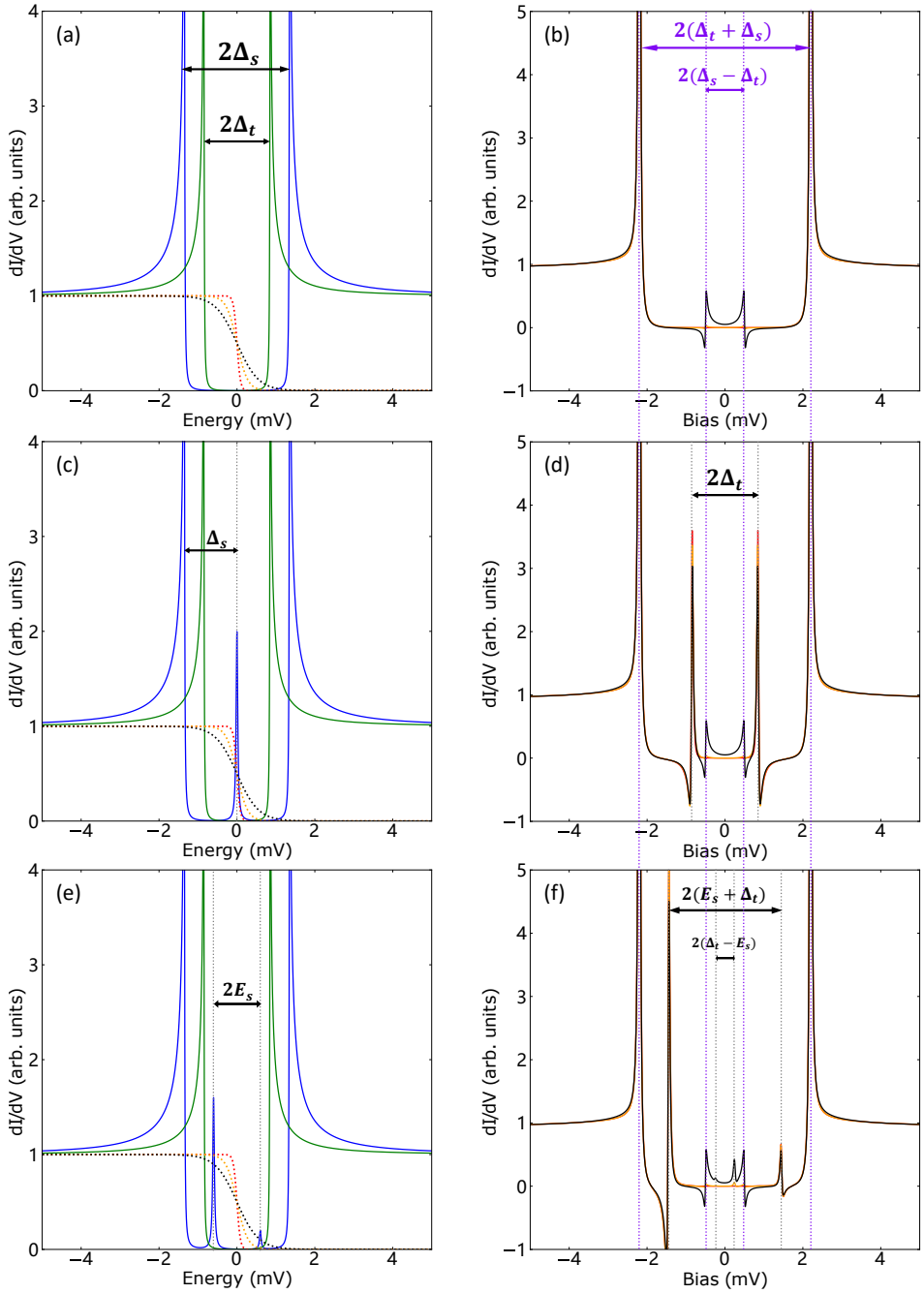

Figure 2.8: Temperature and in-gap states effect on SIS tunneling spectroscopy. (a) LDOS considering a superconducting tip and surface with BCS-like DOS ($\Delta_t = 0.63\Delta_S$) represented by green and blue curve. Red, orange and black dashed lines represent Fermi-Dirac distribution at temperature of $T_1 = 0.03\Delta_s$, $T_2 = 0.1\Delta_s$ and $T_3 = 0.2\Delta_s$. (b) Simulated dI/dV spectra for configurations described in (a). The peaks related to the quasiparticle peaks are marked by dashed purple lines at $(\pm(\Delta_s + \Delta_t)/e)$. If the temperature is high enough, two additional peaks are the result of the thermal population of electrons above the gap energy (and holes below the gap energy) and are also related to the quasiparticle peaks at $(\pm(\Delta_s - \Delta_t)/e)$. (c) LDOS in the case of a zero energy in-gap state in the sample DOS. (d) Simulated dI/dV spectral of configurations described in (c). The spectra show the same spectral features as in (b) plus 2 peaks at $\pm(\Delta_t)/e$ surrounded by negative conductance which are the signature of the zero-energy in-gap state. (e) Case of electron-hole split in-gap states in the sample DOS. (f) Simulated dI/dV spectra for configurations described in (e), The spectra show the same spectral features as in (b) plus 4 peaks : the 2 in-gap DOS features produce two corresponding spectral features at $\pm(E_s - \Delta_t)/e$. If the temperature is high enough, two additional replica with reverse the relative spectral weight are created at $\pm(E_s - \Delta_t)/e$. The in-gap peaks voltages and energies are marked with vertical dashed lines.

In order to remove the effect of non-constant DOS of superconducting tip and thermal effect and recover the genuine LDOS of the sample one will have to apply a deconvolution procedure to the SIS spectra. Our deconvolution procedure will be discussed in paragraph (2.5.3).

Finally, one should also note that when superconducting tip and sample are strongly coupled, the tunneling current is no more related to single electron tunnelling and one can observe the signature of multiple Andreev reflections and Josephson supercurrent in SIS spectra [194]. Andreev reflections will introduce symmetric peaks in SIS spectra and Josephson supercurrent introduces a peak at zero bias. In this thesis we avoid these two effects by choosing a weak coupling between tip and sample.

2.2.4 Inelastic electron tunneling spectroscopy

When using a Normal tip

So far we have considered the elastic tunneling in which electrons conserve energy during tunneling process. While in inelastic tunneling spectroscopy (IETS) the tunneling electrons can lose energy by exciting certain modes (e.g. molecule vibration mode [151], spin excitation [32]), resulting inelastic tunneling current.

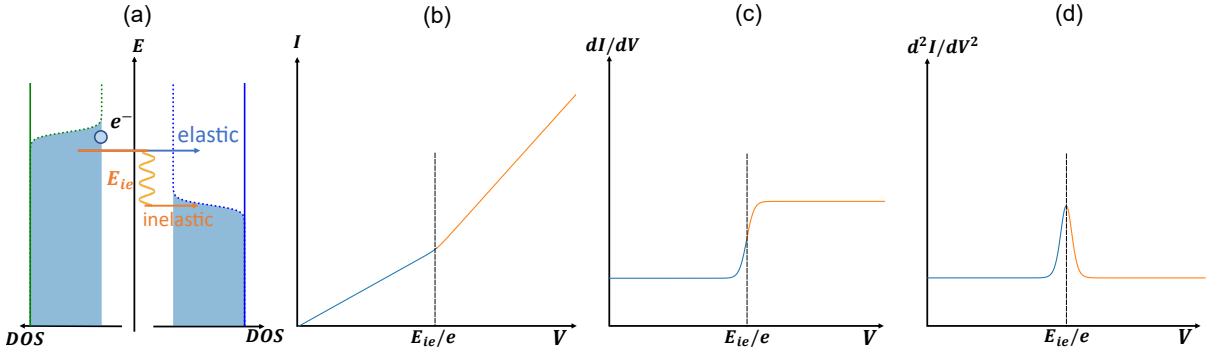

Figure 2.9: Inelastic electron tunneling spectroscopy by normal metal tip. (a) Energy diagram of inelastic tunneling. When electron acquires sufficient energy to induce an inelastic excitation (E>E_{ie}), the electron can tunnel to a final state with energy inferior to the initial one by inducing an inelastic excitation. (b) Calculated tunneling current as function of bias. At small bias we have only elastic current (blue). When bias is above the inelastic excitation energy E_{ie} both elastic and inelastic part contribute to total current (orange), resulting a kink at E_{ie} in current-bias curve. Negative current (not shown here) is central-symmetric to positive current with respect to zero point. (c) Derivative of current with respect to bias. The kink becomes a step signature at inelastic excitation energy. (d) Second derivative of current with respect to bias (shifted for clarity). Step signature becomes a peak (or dip for negative part).

When bias voltage shifts the energy of the electrons (holes) beyond the energy of an excitation mode E_{ie}, electrons will have sufficient energy to excite this mode. This excitation can possibly open a new channel to an unoccupied state of the other electrode which contribute to the tunneling current (Fig. 2.9 (a,b)). In spectroscopic $I(V)$ measurements, the opening of new channel results in a sudden increase rate of tunneling current when sweeping the voltage thought the characteristic voltage threshold. This appears as a kink in $I(V)$ curve. The voltage threshold can easily be measured in derivative of the current with respect to bias, dI/dV, which contains

not only DOS information but also inelastic excitation information. In Fig. 2.9 (c) we observe that a step feature at finite bias is added to a constant background. The step feature is a characterization of inelastic excitation of energy E_{ie} (e.g. spin excitation discussed in section (1.2.5)). The second derivative of current enables a further determination of this inelastic excitation mode. In d^2I/dV^2 relation curve this excitation mode is characterized as a peak located at E_{ie}/e (Fig. 2.9 (d)). Electron-hole symmetry allows us to discriminate excitations from other spectral features because it implies the existence of equivalent peaks located at $\pm E_{ie}/e$ in d^2I/dV^2. By calculating the antisymmetry value of $|\ \frac{d^2I}{dV^2}|_{V>0} - \frac{d^2I}{dV^2}|_{V<0}\ |$ the existence of IETS step feature will be further enhanced, we will see it in our experimental results presented in section (4.6.3).

When using a Superconducting tip in a SIS junction

For a superconducting tip, its BCS DOS is convoluted into current (Fig. 2.10 (a,b)). In I/V relation curve two kinks are observed at Δ_t/e and $(E_{ie} + \Delta_t)/e$. The first one refers to the starting point of elastic current due to superconducting gap as we have seen in previous section. The second one refers to the opening of inelastic tunneling channel, its energy is shifted by Δ_t due to superconducting gap of tip. In dI/dV relation curve a step with a peak appears which is the repetition of BCS peaks due to the convolution of DOS. For second derivative d^2I/dV^2 relation curve, we can still characterize the inelastic excitation mode by a peak at $E_{ie} + \Delta_t$ like the normal tip. If the sample is a superconductor of gap Δ_s with an inelastic excitation mode of energy E_{ie}, the SIS spectrum will be the same as (Fig. 2.10) but replace Δ_t by $\Delta_t + \Delta_s$ which signifies the shift of two gaps.

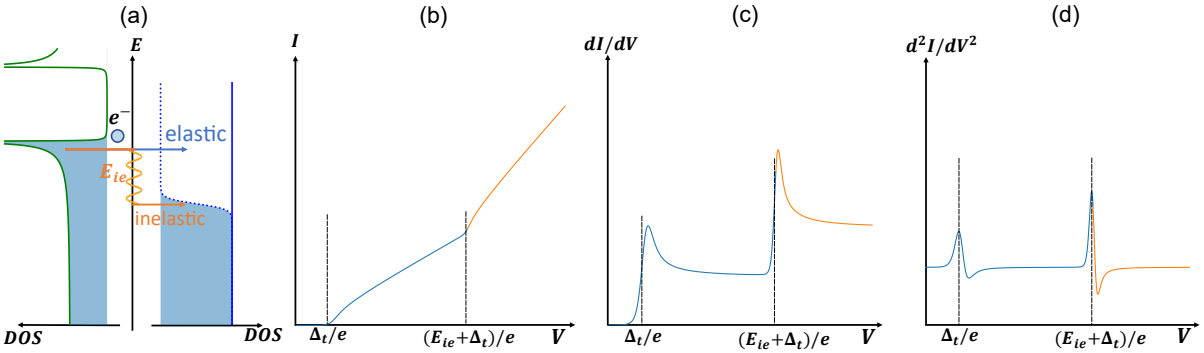

Figure 2.10: Inelastic electron tunneling spectroscopy by superconducting tip. (a) Energy diagram of inelastic tunneling by a superconductor tip with gap value Δ_t. Inelastic excitation energy is E_{ie}. (b) Calculated tunneling current as function of bias. Two kinks at Δ_t and $E_{ie} + \Delta_t$ energy are marked. (c) Derivative of current with respect to bias. Negative current (not shown here) is central-symmetric to positive current with respect to zero point. (c) Derivative of current with respect to bias. (d) Second derivative of current with respect to bias (shifted for clarity).

2.3 Tunneling through impurity

2.3.1 Kondo impurity

Tunneling through an adsorbed adsorbed impurity (atom or molecule) on a metal surface may imply various tunneling paths such as tunneling directly to the continuum states of metal substrate or tunneling through the impurity state (Fig. 2.11). The electron tunneling through different paths may induce quantum interference resulting in an altered $I(V)$ characteristic. This is for instance a well-known effect of Kondo impurities.

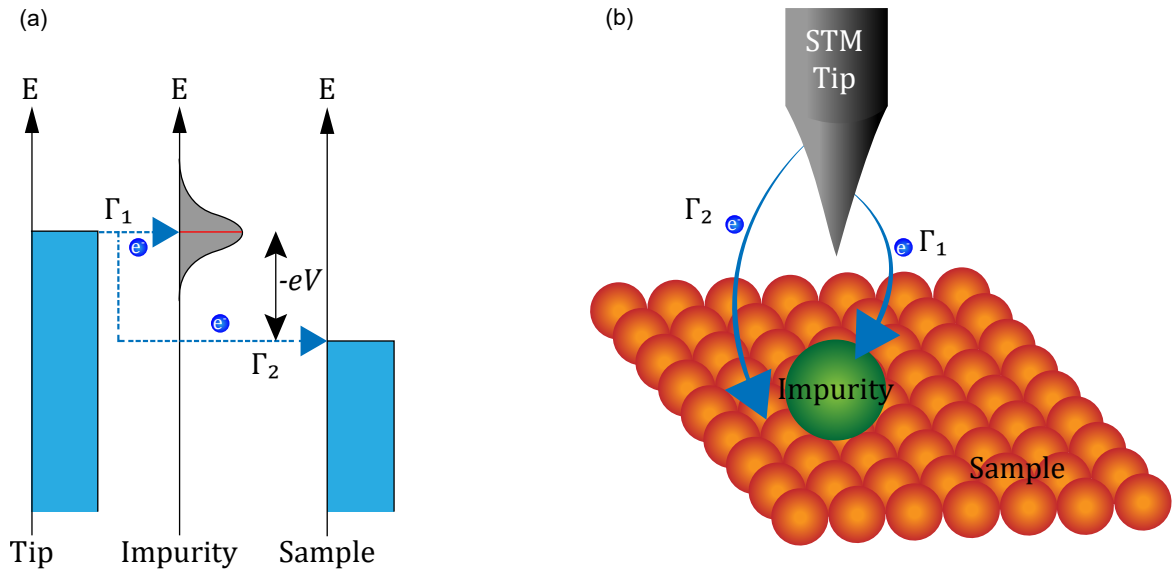

Figure 2.11: Illustration of different tunneling paths with normal tip and substrate. (a) Energy diagram of different tunneling paths. An electron from the tip can directly tunnel into Fermi sea of metal substrate (with hybridization factor Γ_2) or tunnel through the impurity state (with factor hybridization Γ_1). (b) Schematic picture of different tunneling paths. Image adapted from [179].

For a Kondo impurity bearing sharp resonance at Fermi level, the electron can tunnel through interacting orbitals of impurity and directly to the substrate. This might result interference phenomena and the LDOS could not be resolved as a lorentzian peak but rather as an asymmetric lineshape [195] in dI/dV spectra. This asymmetric lineshape is referred as to a Fano resonance [196] or a Fano lineshape (Fig. 2.12 (a)). The Fano lineshape follows the expression:

$$f_{Fano}(V) = A\frac{(q+\epsilon)^2}{\epsilon^2+1} + B \tag{2.17}$$

where A denotes the amplitude, B the background, q controlling the lineshape, $\epsilon = (eV - \omega_0)/\Gamma$ with ω_0, Γ the energy and half-width at half maximum (HWHM) of the resonance, respectively.

It has also been found that Frota lineshape [197, 198] may better describe the Kondo effect in STS experiments [199, 200]. The Frota lineshape follows the expression (2.18) and is illustrated

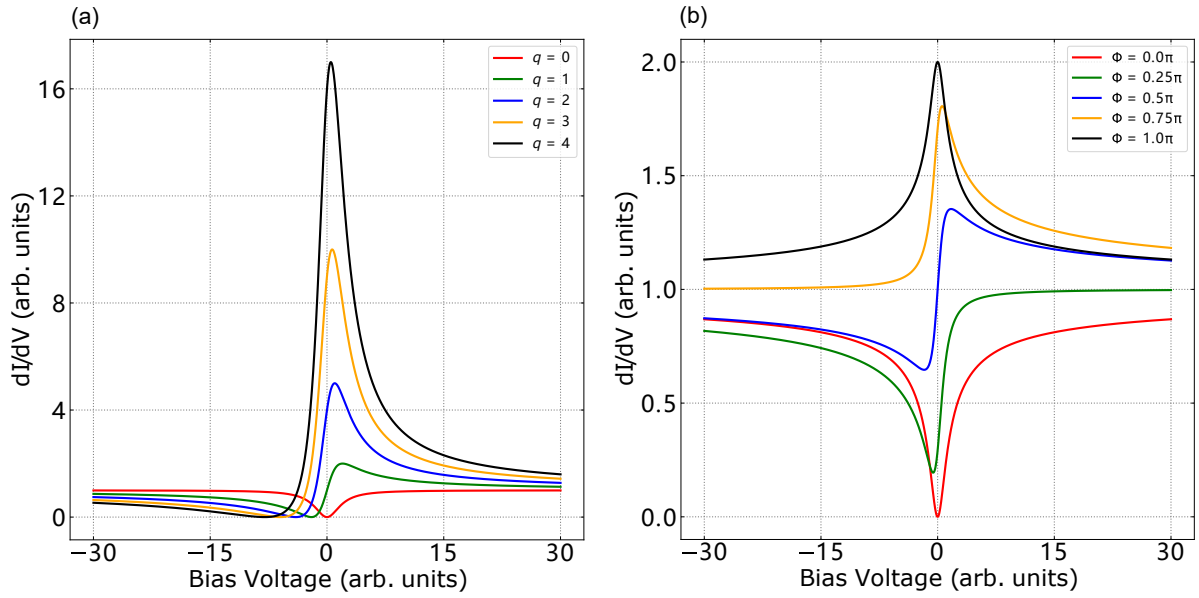

Figure 2.12: Fano lineshape and Frota lineshape for a Kondo impurity. (a) Simulated Fano lineshapes for different values of the parameter q from equation (2.17), A = 1 and B = 0 for all curves. (b) Simulated Frota lineshapes for different values of the parameter ϕ from equation (2.18), A = 1, B = -1 and $\Gamma = 2$ for all curves.

in Fig. 2.12 (b).

$$f_{Frota}(V) = A\mathrm{Re}(e^{i\phi}\sqrt{\frac{i\Gamma}{\epsilon + i\Gamma}}) + B \tag{2.18}$$

where A denotes the amplitude, B the background, ϕ the phase parameter that controls lineshape, Γ the hybridization factor and $\epsilon = (eV - \omega_0)$.

By utilising Fano or Frota function to implement fitting one can obtain the quantitative parameters such as hybridization term Γ (width of resonance peak) which is related to Kondo temperature T_K. The relation between them follows the expression:

$$\Gamma = \frac{1}{2}\sqrt{(\alpha k_B T)^2 + (2k_B T_K)^2} \tag{2.19}$$

where T denotes the experimental temperature, $\alpha = 2\pi$ according to [201], yet α can takes other value depending on different experiment environment [150, 202].

However one has to be cautious when examining the Fano feature to make sure it is Kondo originated because the step feature originated from inelastic excitation can mimic Fano lineshape in presence of charge fluctuation (see section (1.2.5)).

It has also shown that Fano feature in dI/dV spectral is intimately related to the orbital that gives rise to Kondo effect [203], this relation is also valid for the magnetic impurity in atomic limit where magnetic anisotropy dominates the coupling with substrate, which means the shape of inelastic spin-flip step feature is related to the magnetic orbital properties [32].

In presence of superconductivity, it has been reported that interference of tunneling through different orbitals is manifested as asymmetry spectra weight of particle and hole peak of YSR states [98]. This phenomena is common when studying magnetic molecular system where multiple molecular orbitals can contribute to tunneling.

2.3.2 Atomic limit impurity

For IETS step lineshape shown in Fig.2.9 (c) obtained from atomic limit impurity, it can be fitted with following function:

$$F(E) = \frac{1 + (E-1)e^E}{(e^E - 1)^2} \tag{2.20}$$

$$f_{step}(V) = B_1 F(\frac{-eV + E_1}{k_B T_{eff}}) + B_2 F(\frac{eV + E_1}{k_B T_{eff}}) + B_3 F(\frac{-eV + E_2}{k_B T_{eff}}) + B_4 F(\frac{eV + E_2}{k_B T_{eff}}) + C \tag{2.21}$$

where F is the step function for inelastic excitation introduced in [28]. E_1, E_2 the energies of steps, they are related to renormalised magnetic anisotropy of impurity (see section (1.2.5)), T_{eff} the effective temperature which includes both extrinsic and intrinsic broadening of IETS step, B1,B2,B3,B4 the amplitudes and C the background.

2.4 Tip manipulation

In STM/STS experiments tip-substrate interaction is detrimental to the fidelity of signal as it may change local environment. This is particularly significant when we study the flexible organic molecule which is sensitive to tip-substrate force and the electrical field. However the tip-substrate interaction can be utilized for moving atom/molecule on substrate surface which is called tip manipulation. The first tip manipulation experiment on flat surface was implemented in 1989, scientists in IBM lab managed to arrange 35 Xenon atoms on Ni(110) surface forming "IBM" letters (Fig. 2.13) [204, 205].

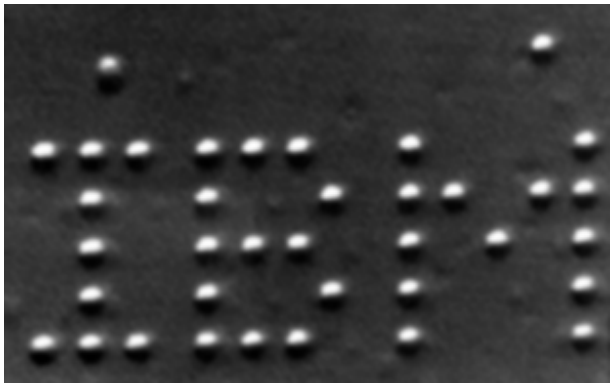

Figure 2.13: Topography image of IBM logo in Xenon atoms. 35 Xenon atoms are artificially rearranged on Ni(110) surface by lateral manipulation, forming "IBM" letters at 4K. Image adapted from [204].

This implies that we can relocate atom/molecule with atomic scale precision by tip. In this thesis we implement tip manipulation to move the molecules in a way called soft lateral manipulation following the process of: 1). Turning off feedback loop and approaching the tip towards atom/molecule in order to increase tip-substrate interaction. 2). Moving the tip towards destination in constant height mode and the atom/molecule will move due to the tip. 3). Retracting

the tip and engaging the feedback loop (Fig. 2.14 (a)). In soft lateral manipulation tip-substrate force is decisive with respect to other parameters such as electric field that is used in vertical manipulation where the molecule is adsorbed at tip apex [206] (Fig. 2.14 (b)).

As discussed before the off-feedback loop operation is already risky for the tip not to mention approaching the tip towards substrate and move the atom/molecule. Thus there are several requirements for a lateral tip manipulation to be implemented successfully: 1). Constant height displacement of tip should be parallel to the substrate which demands us to work in a rather small region and correct the slope of substrate surface. 2). Temperature should be low enough to quench the thermal movement of molecule which may overcome the tip-substrate interaction and make it impossible to put molecule in desired location. 3). Other parameters like the electric field between tip and substrate that depends on the applied bias should be well controlled otherwise they might interfere manipulation or even dissociate molecule [207].

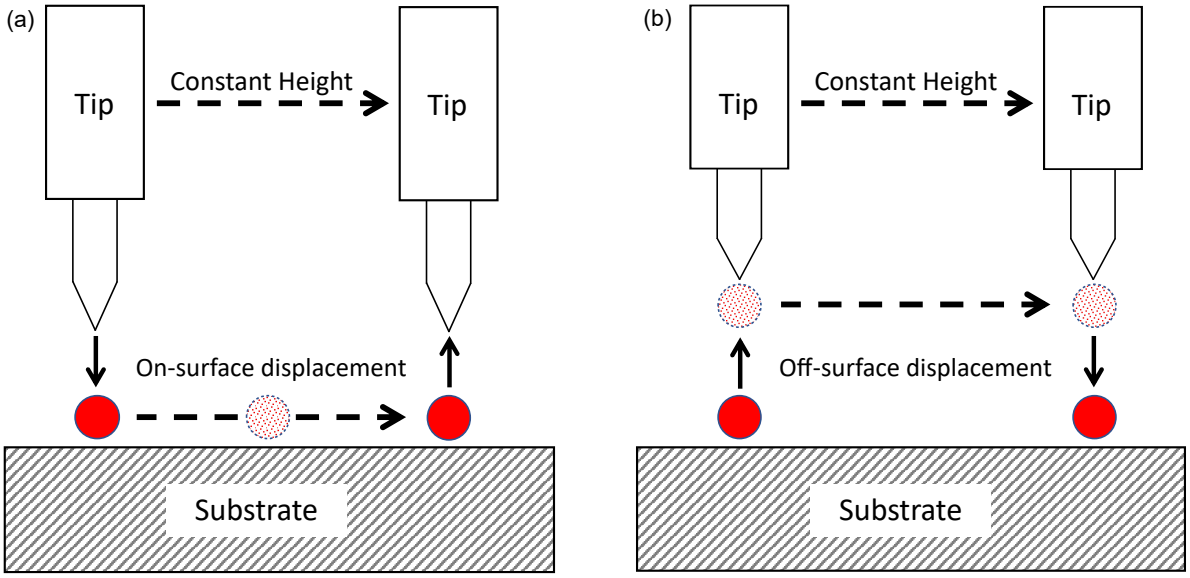

Figure 2.14: Two ways to perform tip manipulation. (a) Lateral manipulation where atom/molecule (red circle) is always on the substrate during displacement. (b) Vertical manipulation where atom/molecule will be picked up by the tip during displacement.

2.5 Data analysis

In this thesis the raw data are recorded by the software provided by Nanonis. They were post-processed first with Mathematica and Matlab programs. Rapidly, we developed a new set of Python procedures for a more powerful and efficient data analysis. Additionally, WSxM [208] and Scilab [209] programs were also used for the topography and spectroscopy analysis.

2.5.1 Topographic data

STM topography data consists of tip height z as function of tunneling position coordinate of surface (x, y) thus it has 2D array data format. The raw topography data usually shows a background slope because of the non-parallel scanning with respect to the surface or thermal drifting of tip in z direction. To correctly understand the structure of sample it is necessary to remove the slope. The slope can be subtracted along every line of topography (along x or y direction) by means of linear fit or a plane fit directly to the 2D array.

Another way to analyse topography is to construct current error image where we use the tunneling current $I(x, y)$ to make image. In constant current mode tunneling current is set to a fix value but current can still vary when tip encounters a sudden change of height. Because piezoelectric takes time to regulate the tip in order to maintain the setpoint current, when tip suddenly encounters a protrusion (dip) on the surface the current will become larger(lower) than the setpoint current before it is regulated. In a current image those parts corresponding to sudden tip height change will be emphasized (usually atomic step terraces and adsorbed particles) and the parts of flat surfaces will be faded (Fig. 2.15 (b)).

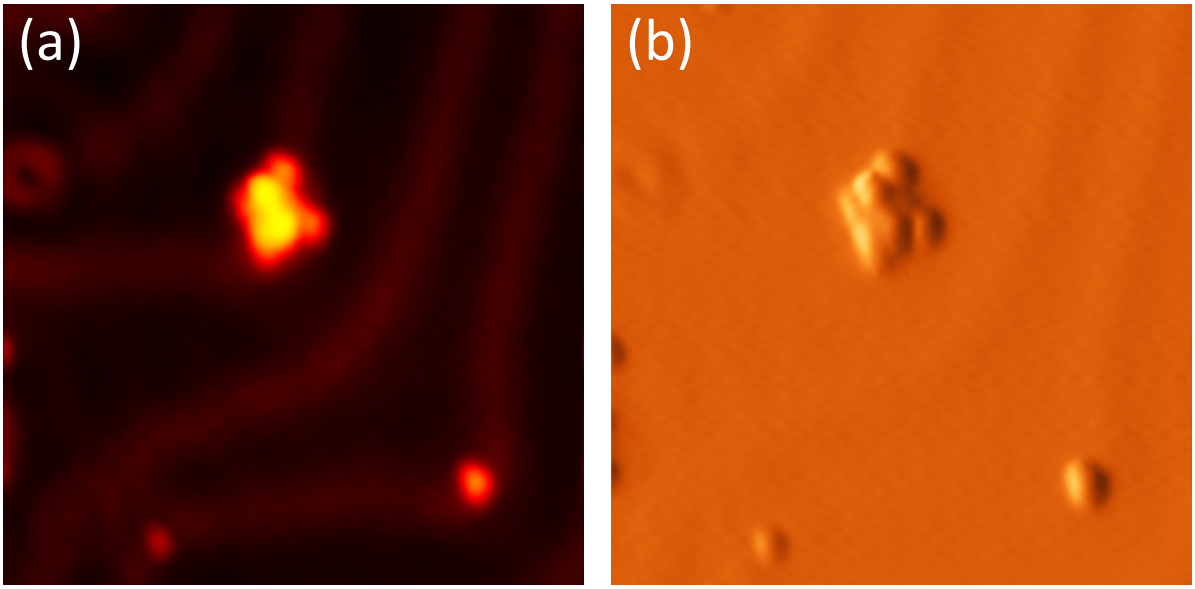

Figure 2.15: Two ways to analyse topography image. (a) Tip height topography image ($15\text{x}15\text{nm}^2$ setpoint: 125 mV, 20 pA) of a molecule on Au(111) surface after linear fit correction and Gaussian smoothing. (b) Current topography image of same region of (a). The reconstruction lines of Au(111) becomes hard to be distinguished in this mode.

After the slope correction the next step is to filter the noise which mainly comes from the vibration of tip. In topography it usually behaves as series of abnormal spots along the lines of scanning. To filter this noise for a 2D array $SciPy$ library [210] provides ready-to-use filters in python such as 2D median filter and 2D Gaussian filter. One can also perform customized band pass filter by manipulating with the Fourier transformation of 2D array.

There are various origins of the noise. The most critical one is the mechanical vibration that comes from the cryostat of the microscope. It shows a resonance frequency around 25Hz de-

pending on the amount of cooling liquid inside. Once the cryostat feels the out-come vibrations like heavy construction works nearby, foot steps upstairs or door closing in the lab it will transfer the vibration to the tip. Other types of noise such as electrical perturbation in alternating current network may also be involved but they show a minor influence with respect to the mechanical one in our system[2].

2.5.2 Spectroscopic data

The basis STS data consists of tunneling current I as function of bias V thus it has 1D array format for each spectral ($I(V)$). The acquisition time for recording one $I(V)$ spectral depends on multiple parameters of STS experiment, the most important one is the number of points which is usually chosen to be 800 points so that it is neither too few to cause insufficient spectral resolution nor too many to cause long acquisition time. For lock-in detection the acquisition time depends not only on number of points but also lock-in parameters that are modulation voltage V_m and modulation frequency f. For large-range measurement the lock-in parameter is usually set to $V_m = 5\,\text{mV}$, $f = 900\,\text{Hz}$ and for low-range measurement it is set to $V_m = 0.2\,\text{mV}$, $f = 750\,\text{Hz}$. The normal period to measure a $I(V)$ spectral is about 4 s while using lock-in detection it could take 7 s.

To extract the information related to LDOS one can make derivative to current I with respect to bias V and obtain 1D conductance relation array $(dI/dV)(V)$. As the tunneling current is exponentially dependent on tip height which is sensitive to vibration. The mechanical noise is inevitably induced into to spectroscopy data and it must be properly handled because derivation amplifies the noise.

In experimental aspect, there are two ways to minimize the noise: 1). Perform repeated measurements for the same spectroscopy $I(V)$ and take the average value of I with respect to the corresponding bias V. 2). Use lock-in technique that allows us to filter the signal in noisy environments and it can directly measure $(dI/dV)(V)$ relation. The ideas of these two methods are the same: improving data quality by increasing acquisition time.

The effect of the noise can also be reduced in post-processing aspect, for example we can apply different filters to suppress the noise or implement fitting to the spectral and completely remove the noise. In this thesis we have used Savitzky-Golay filter [211] and 1D Gaussian filter provided by $SciPy$ library to smooth the spectroscopy data.

We can estimate the effect of taking average, making derivative, smoothing and using lock-in detection on spectroscopy data in the example shown in Fig. 2.16. Blue dots in Fig. 2.16 represent single raw spectrum of 600 points taken on Pb(110) surface by a superconducting tip. Red line is the same as blue one but after 25 times average. $I(V)$ signal measured in STS experiment is shown in Fig. 2.16 (a) and its derivative dI/dV is shown in Fig. 2.16 (b).

The signal to noise ratio (SNR) is characterized by comparing the height of quasiparticle peaks at $\pm 2.7\,\text{mV}$ and oscillation amplitude of noise outside the gap. From the raw data (blue

[2]During the period of this thesis, there were heavy construction works at site of ESPCI, which had some impact on our experiments.

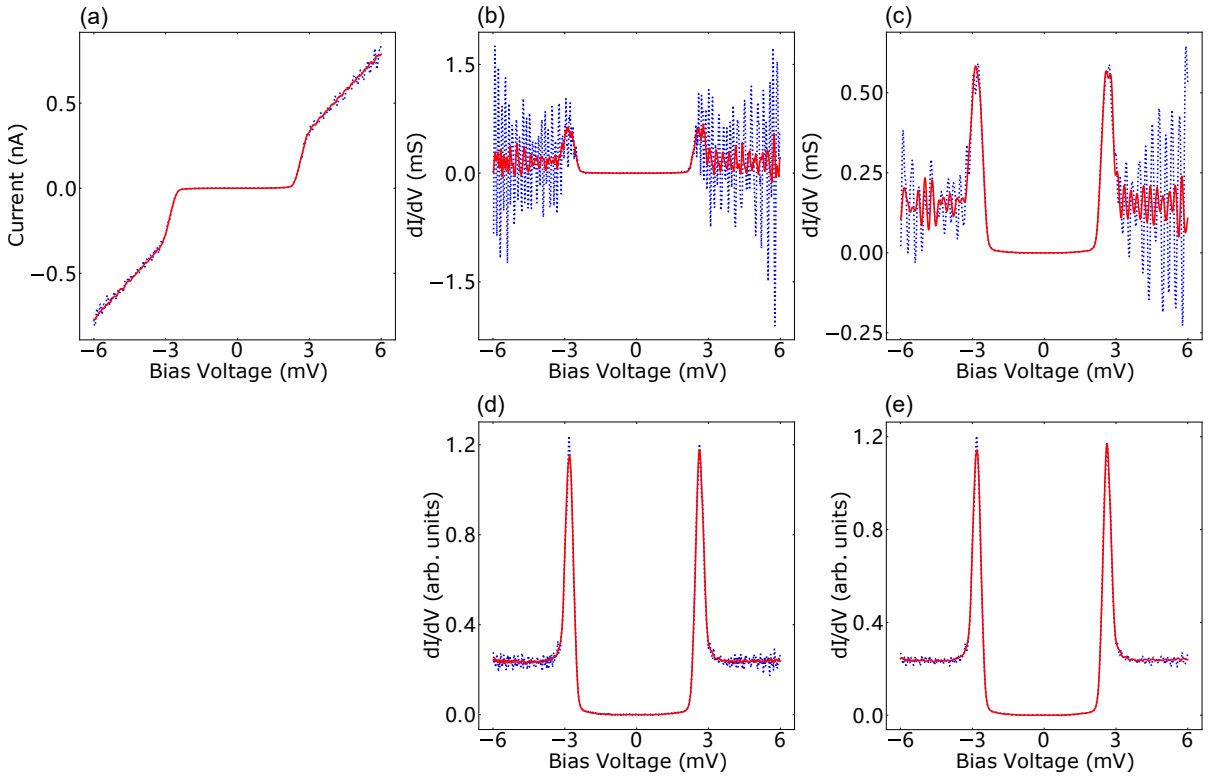

Figure 2.16: Effects of averaging, derivative, smoothing and lock-in detection on spectroscopy. Blue dots represent single spectrum and red curve is after 25 times averaging. (a) $I-V$ relation curve measured on Pb(110) surface. (b) dI/dV of (a). (c) Spectrum of (b) smoothed via 1D Gaussian filter. (d) dI/dV spectrum obtained by lock-in detection. (e) Spectrum of (d) smoothed via 1D Gaussian filter.

dots in (b)) we can hardly distinguish quasiparticle peak from the noise while after averaging (red curve in (b)) the SNR ration is around 2. In Fig. 2.16 (c) we have applied 1D Gaussian filter to smooth the data. We clearly see that SNR increases and we can now distinguish quasiparticle peak even in blue dots. Fig. 2.16 (d) shows the signal acquired by lock-in detection which is directly dI/dV. With lock-in technique we improve our SNR by an order of magnitude and the smoothed data by Gaussian filter are presented in Fig. 2.16 (e) where the effect of smoothing becomes less effective due to the large SNR obtained by lock-in detection. Lock-in technique indeed provides large SNR however it takes more time to measure and may produce artifact in the signals. Thus we must cautiously adjust the lock-in parameter.

Single STS dI/dV spectral allows us to study LDOS of a point while STS dI/dV map allows us to visualize the spatial distribution of states. By taking a specific value of energy V_i we can construct 2D conductance map of target area at this energy with $(dI/dV)(V_i, x, y)$. With a normal tip $(dI/dV)(V_i, x, y)$ represents $\rho_s(eV_i, x, y)$ which is the DOS map at eV_i energy. dI/dV map data consists of spatially arranged dI/dV spectral thus it has 3D array format $I(V, x, y)$. It is obvious that it will take much more time than a single dI/dV spectral to acquire a dI/dV map. For example to measure a well-resolved dI/dV map of 256x256 points, if each dI/dV spectral costs 4 s it will take 72h which almost reaches maximum measurement time allowed by our STM setup (see paragraph (2.6)). Hence for each dI/dV map measurement, we have to balance the spectral resolution (number of points of V) and spatial resolution (number of points

of (x, y)).

The post-processing for dI/dV maps can be realised in two aspects. The first aspect is to smooth the data in energy space where each single $(dI/dV)(V, x_i, y_i)$ spectral at specific position (x_i, y_i) is smoothed independently. However the spike noise (or those types of noise) may still exist in dI/dV map even if every spectral $(dI/dV)(V, x_i, y_i)$ is smoothed because dI/dV spectral is non-coherent with each other in real space (x, y). Hence in second aspect, we smooth dI/dV map in real space where each single $(dI/dV)(V_i, x, y)$ map at specific energy V_i is spatially filtered. We can perform interpolation process to dI/dV spectral and map to increase the spectral and spatial resolution.

2.5.3 Deconvolution

For STS spectral obtained by superconducting tip, the conductance dI/dV does not directly represent the LDOS as BCS DOS of tip is convoluted in it. We have to implement deconvolution process to dI/dV and recover LDOS ρ_s. To do so, we first consider the general expression of conductance calculated from equation (2.12):

$$dI/dV(V, \vec{r_0}) \propto T(E_F, \vec{z_0}) \int dE M_t(V, E) \rho_s(E, \vec{r_0}) \tag{2.22}$$

$$M_t(V, E) = (f(E) - f(E - eV)) \frac{\partial \rho_t(E - eV)}{\partial E} - \frac{\partial f(E - eV)}{\partial E} \rho_t(E - eV) \tag{2.23}$$

where M_t is a global parameter decided by DOS of tip ρ_t. $T(E_F, \vec{r_0})$ is the transmission factor at tunneling point coordinate $\vec{r_0}$.

The conductance dI/dV and LDOS ρ_s has 1D array format and M_t has 2D array format. Thus during data processing the relation (2.22) can be considered as [212]:

$$(dI/dV)(V_i) = M_t(V_i, E_j) \rho_s(E_j) \tag{2.24}$$

This expression has a typical form of:

$$\vec{b} = A\vec{x} \tag{2.25}$$

in linear regression where $\vec{x}$ is undetermined vector while matrix A and vector $\vec{b}$ are known.

Here are two crucial points we have to note: 1). We must know the details of ρ_t that derives M_t then the deconvolution process can be implemented, because information of A and b must be known to calculated $\vec{x}$ in (2.25). 2). Proper algorithm to calculated ρ_s must be used. Because matrix elements of M_t are ill-defined, as we can see from (2.23) M_t depends on bias voltage V and energy E which both are involved in the determination of matrix elements. For a ill-defined matrix one can use ordinary least squares approach to determine the most probable value of $\vec{x}$ in (2.25) rather than applying inverse matrix of M_t.

Determination of tip DOS

Concerning the first point about the determination of M_t, one possible way is to make the assumption that ρ_t follows a nearly BCS DOS with a phenomenological imaginary part $i\Gamma$ added to the energy to get rid of divergence of quasiparticle peak [213]:

$$\rho(E) = Re\frac{\mid E \mid}{\sqrt{(E+i\Gamma)^2 - \Delta_t^2}} \tag{2.26}$$

where Δ_t is superconducting gap of tip.

However this method can only work for a well prepared superconducting tip which is extremely hard to obtain. A common way to prepare superconducting tip is to indent the tip into clean superconductor substrate. Then tip apex will be covered by clusters of superconductor and expected to acquire the superconducting properties ρ_t similar to bulk superconductor substrate ρ_s. In real experiments ρ_t usually shows reduced gap and sometimes deformed quasiparticle peak shape that differs from expression (2.26).

As we have discussed that the SIS spectral signal is mainly contributed from the quasiparticle peak of ρ_t, the mismatch between assumed quasiparticle peak and real one may greatly modify deconvoluted data. Thus in this thesis we propose another approach to deduce ρ_t that can work for both well and less-well prepared tip. Instead of assuming value of ρ_t we assume the value of ρ_s and calculate ρ_t. To do so, we first make transformation of $E \to E + eV$ to equation (2.12) and the calculated conductance expression will become:

$$dI/dV(V, \vec{r_0}) \propto T(E_F, \vec{z_0}) \int dE M_s(V, E, \vec{r_0}) \rho_t(E) \tag{2.27}$$

$$M_s(V, E, \vec{r_0}) = (f(E) - f(E+eV))\frac{\partial \rho_s(E+eV, \vec{r_0})}{\partial E} - \frac{\partial f(E+eV)}{\partial E}\rho_s(E+eV, \vec{r_0}) \tag{2.28}$$

where M_s is a matrix determined by DOS of sample ρ_s at location $\vec{r_0} = (x_0, y_0, z_0)$ of surface. If (x_0, y_0) refers to a place of clean substrate (no magnetic impurities nearby), $\rho_s(\vec{r_0})$ should equal to BCS DOS of bulk superconductor (2.26) ρ_{bulk} which is spatial independent. This assumption is much more reliable than the previous one because DOS of a s-wave bulk superconductor substrate ρ_{bulk} can not quickly vary within coherent length [214] of superconductor. Once we determine M_s, we can determine ρ_t and thus M_t.

nnls approach

Concerning the second point, the algorithm we use to determine ρ_t from M_s and ρ_s from M_t is called non-negative least squares (nnls) approach provided by $SciPy$ library. The idea of nnls is the same as ordinary least square which is used to solve least squares problem but with constrain on under-determined vector $\vec{x}$ to be non-negative (2.29). This choice is reasonable as

under-determined DOS of tip ρ_t and sample ρ_s are non-negative.

$$\vec{x} = argmin_{\vec{x}} \parallel A\vec{x} - \vec{b} \parallel_2^2 \tag{2.29}$$

where $\parallel \ . \ \parallel_2$ denotes Euclidean norm. Each element of under-determined vector $\vec{x}$ is subjected to be non-negative ($x_i \geqslant 0$).

Tikhonov regularization

In practice ρ_s calculated from nnls method contains strong amplified noise due to inverse mapping process. There are two aspects in which we deal with noise. The first aspect is through post-processing methods such as applying filters discussed in section (2.5.2). However the noise level in calculated ρ_s can be rather large and the filtering process may not ensure a good SNR with proper smooth order. Thus the second aspect is intended to reduce the numerical noise by improving algorithm. Here we propose a new way based on Tikhonov regularization [215] in which we still use nnls method but with modified parameters:

$$\vec{x} = argmin_{\vec{x}} \parallel C\vec{x} - \vec{d} \parallel_2^2 \tag{2.30}$$

subject to $x_i \geqslant 0$, matrix C and vector $\vec{d}$ are:

$$C = [A \quad \lambda I] \tag{2.31}$$

$$\vec{d} = \begin{bmatrix} \vec{b} \\ 0 \end{bmatrix} \tag{2.32}$$

where I is the identity matrix of same dimension as A, λ a scalar called ridge parameter and $\vec{d}$ the extended vector which has twice the length of $\vec{b}$.

Ridge parameter plays the role like smooth order (stand deviation) in Gaussian smoothing, it has be carefully chosen so that data will not be neither under- nor over-smoothed. The application of Tikhonov regularization proves to be much more effective than the filtering in post-processing because it can directly suppress the numerical noise generated during deconvolution process. The drawback of this method is obvious: the size of input matrix A and vector $\vec{b}$ are doubled and it will cost more time to compute $\vec{x}$.

For example, to deconvolute a single STS spectral $(dI/dV)(V)$ with a typical size of 600 points, execution time is around 2s and 10s without or with using Tikhonov regularization[3]. To deconvolute a STS map $(dI/dV)(V, x, y)$ consisting of multiple single spectral, for example 100x100 points in real space (x, y), it will cost 5h and a day without or with using Tikhonov regularization, this is clearly not feasible hence we must reduce computation time.

[3]Used CPU: Intel(R) Xeon(R) CPU E5-2620 v4 @ 2.10GHz, Memory: 128G 2133MHz

Parallel processing

As the spectral in STS map are independent on each other, we can implement parallel processing in order to reduce computing time for a STS map deconvolution. In this thesis, we use Ray package [216] which enables us to activate all CPU Kernels to implement parallel deconvolution[4].

One might wonder that the long execution time caused by the extension of matrix and vector size in Tikhonov regularization can be greatly reduced by using algorithm based on GPU Kernels. And the parallel processing should also be implemented in GPU Kernels. Indeed $CuPy$ library [217] has already provided ready-to-use nnls codes based on CUDA cores, the reduction of execution time becomes significant when size of matrix and vector are large as GPU is powerful in large matrix processing. However GPU Kernels based parallel processing algorithm is still not available at the time of writing of this manuscript.

Considering the fact that STS map usually contains multiple single spectral $(dI/dV)(V)$ with relative small size (points), we chose to use CPU Kernels based codes to reduce execution time.

2.6 Langevin STM

q All experimental results presented in this thesis were obtained with "Langevin" AFM-STM microscope at ESPCI (Fig.2.17). This microscope allows us to study conformation and electronic properties of molecules adsorbed on various substrates at controllable temperature where the minimum is 1.1K and under a base pressure of $3\text{x}10^{-11}$ mbar.

The machine is constituted of two main parts: preparation chamber and STM chamber.

The metallic substrate can be introduced into the preparation chamber at a base pressure around $8\text{x}10^{-11}$ mbar via load lock chamber (at base pressure around 10^{-8} mbar). It is then prepared by repeated cycles of ionized argon gas sputtering [218], annealing cycles to get rid of contamination on the surface and ensure that the surface is flat in atomic scale. Annealing can be performed in different ways such as pyrolytic boron nitride (PBN) heating annealing, direct current (DC) heating or electron beam (e-beam) heating depending on the nature of substrate and desired annealing temperature. Molecules are deposited by means of molecular beam epitaxy (MBE) on metallic substrates with controllable temperature. Prepared samples are transferred to STM chamber for measurement without exceeding a pressure over 10^{-10} mbar.

Microscope lies inside STM chamber which is also under UHV. Its inner structure is shown in Fig. 2.18. In order to reach low temperature we have used double stage cooling where two cryostats of cooling liquids are embed inside microscope. The outer shield cryostat (marked by red arrow) contains liquid nitrogen (LN_2) which will cool the system down to 77K and the inner shield cryostat (marked by blue arrow) contains liquid helium (LHe) which will cool down to 4.2K. STM head holding both tip (marked by green arrow) and sample (marked by orange arrow) lies inside LHe shield, it is further cooled down to 1.2K by means of Joule–Thomson

[4]For our CPU with 32 Kernels, the Ray boosted parallel processing decreases computation time by a factor around 12.

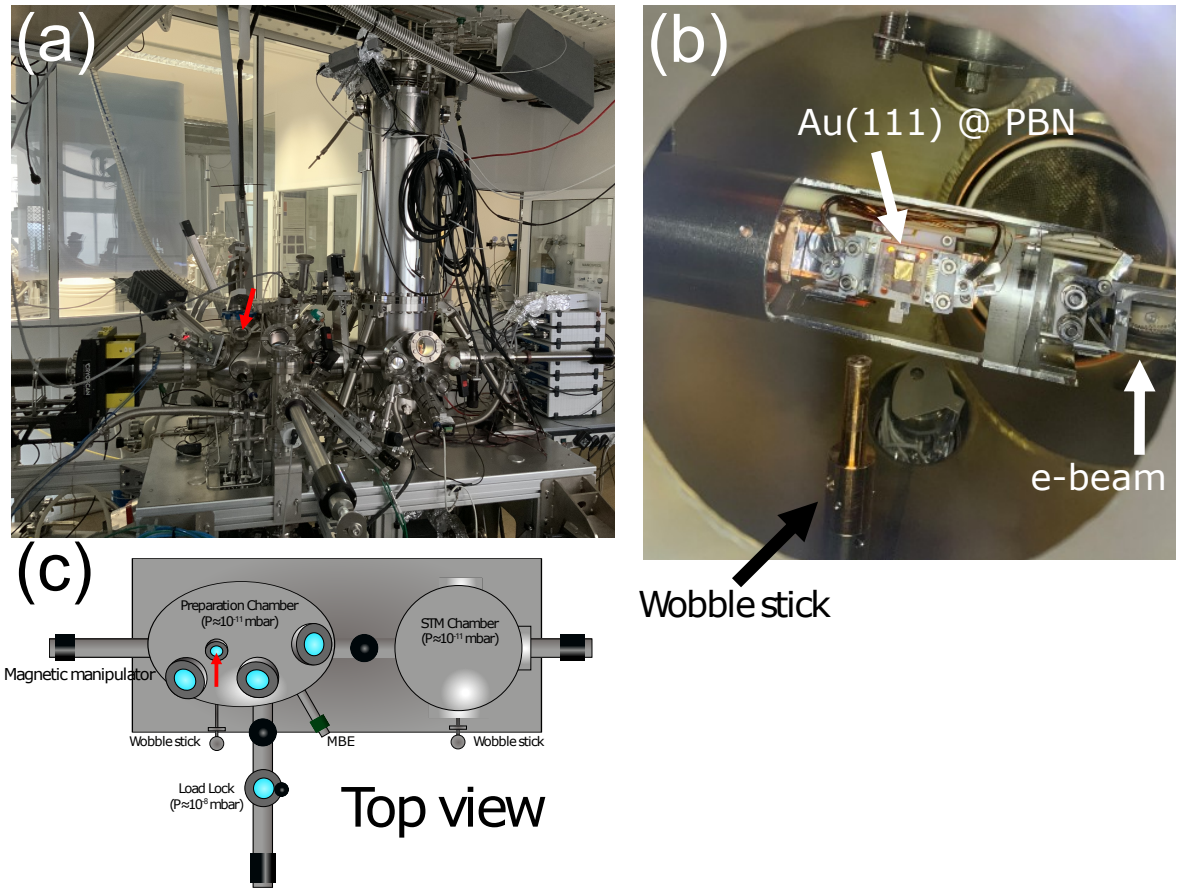

Figure 2.17: "Langevin" AFM-STM microscope on which all the STM/STS measurement are performed in this thesis. (a) Picture of the experimental setup. (b) Picture of head of manipulator on which a Au(111) substrate is being annealed by PBN heating in preparation chamber. Picture photoed through window marked by red arrow. (c) Top-view scheme of the setup.

effect where LHe is injected through a fine needle. The consummation of cooling liquids limit the time to make continuous measurements because we have to refill $\mathrm{LN_2}$ and LHe before the thermal variation becomes significant, and after each refill the tip needs to be re-stabilized. The maximum duration between each refill is around 3-4 days which should be adequate for normal single STS map acquisition.

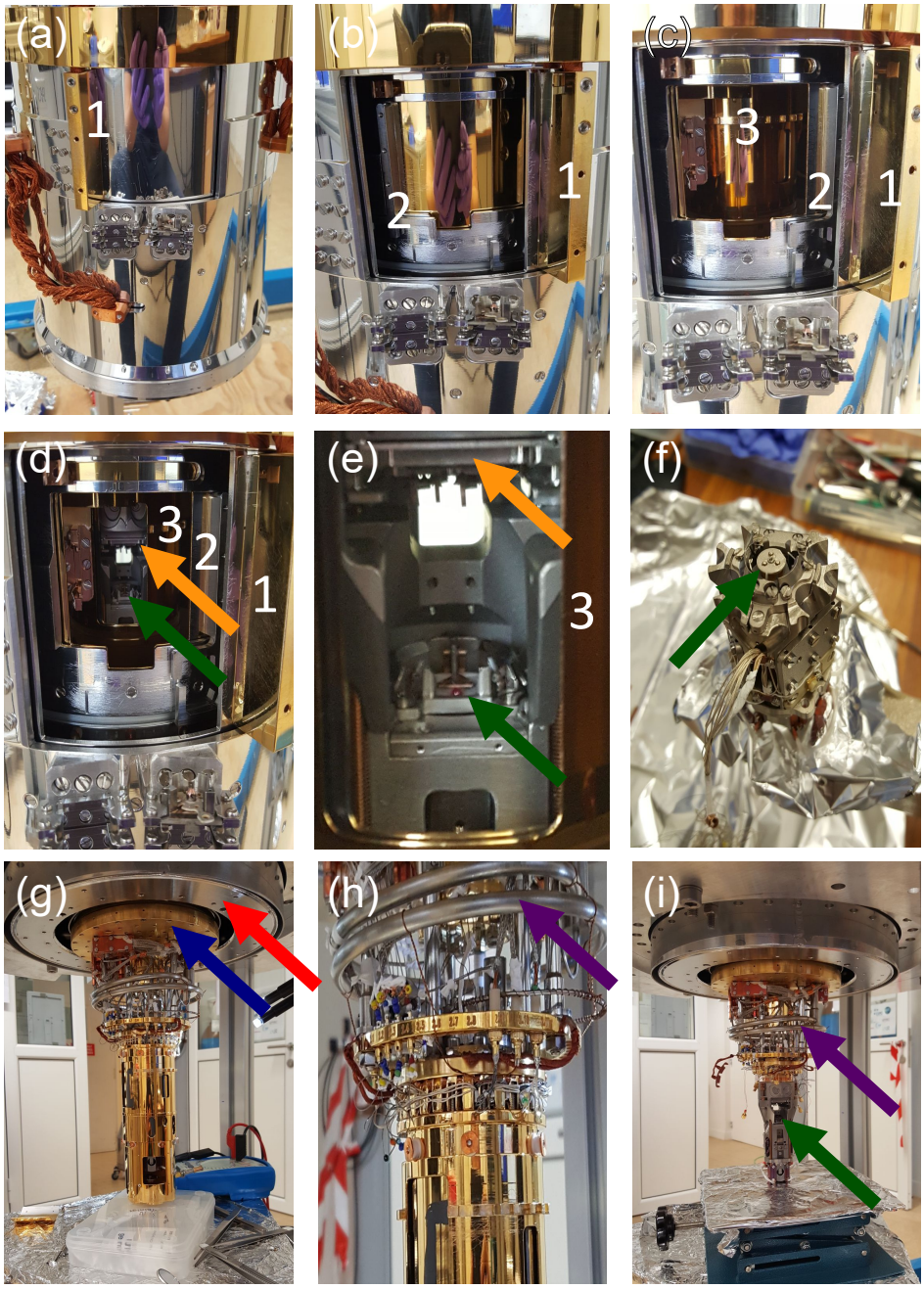

Figure 2.18: Inner structure of STM head. (a)-(i) Structure of STM head from outside to inside. Red and blue arrows mark the cryostat containing LN_2 and LHe respectively, purple arrow mark the tube transferring LHe used for Joule–Thomson effect, green and orange arrows mark tip holder and sample holder. Three thermal barrier from outside to inside are labeled from 3 to 1.

Chapter 3

Structural and Electronic Properties of Porphyrin Magnetic Molecules on Normal Metal Surfaces

3.1 Introduction

Spin state control of molecular species at interfaces for spintronics [44], nanoelectronics [219, 220] and quantum electronics applications has drawn strong interest in recent studies.

In this chapter, we will show our STM/STS results on realisation spin state control in molecular systems consisting of 5,15-dipyridyl-10,20-dibromophenyl porphyrin ($\mathrm{Fe-DPyDBrPP}$) molecules on non-superconducting Au(111) surface.

We have found that depending on the adsorption sites of $\mathrm{Fe-DPyDBrPP}$ on Au(111) surface, $\mathrm{Fe-DPyDBrPP}$ molecule can exhibit inelastic spin-flip (SF) excitation signature which indicates a SF regime (S = 1) or Kondo resonance signature at Fermi level which indicates a Kondo regime. Additionally, we discovered that the behavior of SF or Kondo regimes of $\mathrm{Fe-DPyDBrPP}$ molecule is related to the energies of two different spin polarized molecular frontier orbitals that respectively localize above and below Fermi level.

By utilizing tip manipulation, we have managed to drive $\mathrm{Fe-DPyDBrPP}$ molecule into mixed-valence intermediate spin states that exhibit non-integer valency behavior. We have confirmed that occurrence of intermediate spin state is a consequence of charge fluctuation, which occurs when two molecular frontier orbitals shift close to Fermi level. When two frontier orbitals are tuned to merge at Fermi level and become degenerate, $\mathrm{Fe-DPyDBrPP}$ molecule exhibits a Fano-like lineshape predicted by David Jacob [17] who explained it as SF effect in presence of strong charge fluctuation. Yet, the degenerate molecular orbitals nature could also imply a SU(4) Kondo effect [15] though it is less likely to occur in molecular system [221].

In the first three sections of this chapter, we will introduce the structural and electronic properties of Au(111) surface and its preparation process (section (3.2)), the chemical compositions of $\mathrm{Fe-DPyDBrPP}$ molecule (section (3.3)) and the method to prepare self-assembled

$\mathrm{Fe-DPyDBrPP}$ molecule assemblies on Au(111) surface (section (3.4)).

Then the topographic, spectroscopic and DFT results showing $\mathrm{Fe-DPyDBrPP}$ molecules of high- and low- spin states configuration together with tip manipulation method will be presented in sections (3.5) and (3.6).

Finally we will present the results of crossover between high- and low- spin states where mixed-valence intermediate spin states behavior are observed (section (3.7)) together with the discussion about the spin state crossover phenomena reported in others' works (section (3.7.3)).

3.2 Au(111) surface

Gold surfaces have been widely used as substrates for on surface nanostructure studies during last decades. Among different noble metals surfaces, Au(111) surface is one of most interested one as it exhibits a very peculiar structural reconstruction [222] and extraordinary electronic properties that originates from Shockley type surface states [223, 224]. The Shockley surface states consist of confined electronic states in the first atomic layer of surface near E_F subsisting in the directional band gap of the bulk valence states centered at $\bar{\Gamma}$. Therefore the surface state electrons can be treated as quasi 2D electron gas that provides an ideal platform for STM studies [15, 31, 32, 38, 57, 163].

The topography of the genuine Au(111) surface is shown in Fig. 3.1 (a) where we can observe atomic flat terraces and the famous herringbone reconstruction of Au(111) surface which divides the surface to fcc and hcp regions separated by stacking fault lines (Fig. 3.1 (c-d)). The surface reconstruction patterns generate a weakly modulated potential that acts differently on fcc, hcp and stacking fault regions [224]. This reconstruction produce an attractive potential at the elbow of herringbone reconstruction on which deposited chemical species and adatoms are preferentially adsorbed, chemically bound or buried in the first atomic layer by an exchange with a gold atom [225, 226]. For example in Fig. 3.1 (c-d), the white arrow points to the elbow of herringbone reconstruction where we can clearly distinguish an impurity localized at this site. Later we will show that the adsorption of a Br atom at this location plays an important role in controlling spin states of site-dependent admolecule.

3.2.1 Au(111) surface preparation

We used a gold crystal cut and polished along (111) orientation by Matek company. The clean and atomically flat Au(111) surface was prepared by repeated cycles of Ar ion sputtering (at 1 keV and pressure of 10^{-5} mbar for 30') and annealing (at 900 K for 30') by PBN heating or e-beam heating. A successful Au(111) surface preparation is characterized by large atomically flat terraces (large enough with respect to the nanostructure to study, usually larger than $50\mathrm{x}50\mathrm{nm}^2$) with few impurity contamination and well ordered herringbone reconstruction pattern (Fig. 3.1).

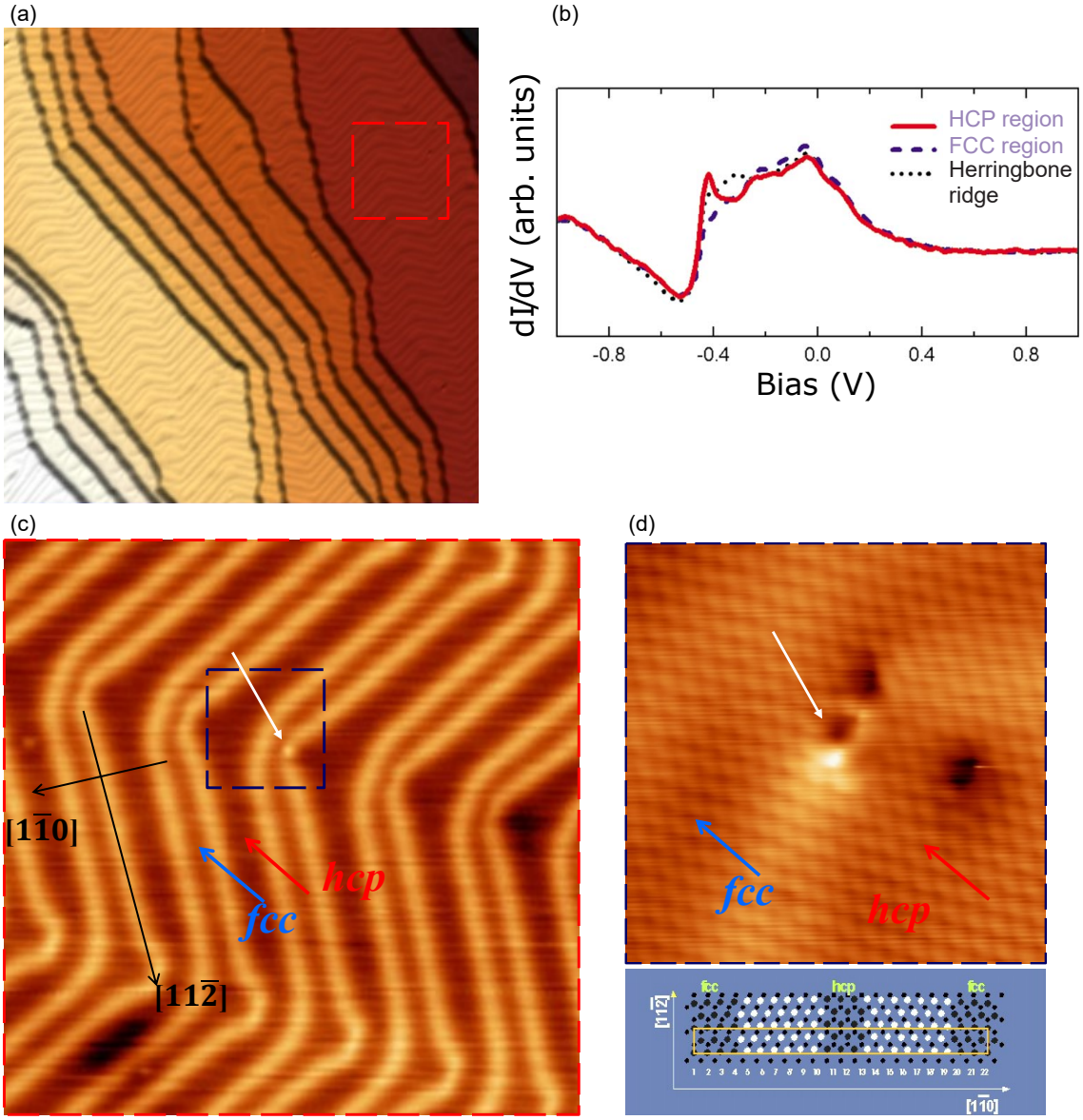

Figure 3.1: Topography and spectroscopy of Au(111) surface. (a) Current topography image ($200\text{x}200\text{nm}^2$) of clean Au(111) surface. (b) dI/dV spectra of Au(111) surface taken on different locations. A step-like upturn around -460 mV reveals the detection of Au(111) surface state. Image adapted from [227]. (c) Topography image of red square region ($40\text{x}40\text{nm}^2$) in (a). Blue and red arrows indicate fcc and hcp region of surface respectively. White arrow aims at elbow of herringbone reconstruction where a defect atom is trapped. (d) High-resolution image of blue square region ($5\text{x}5\text{nm}^2$) in (c).

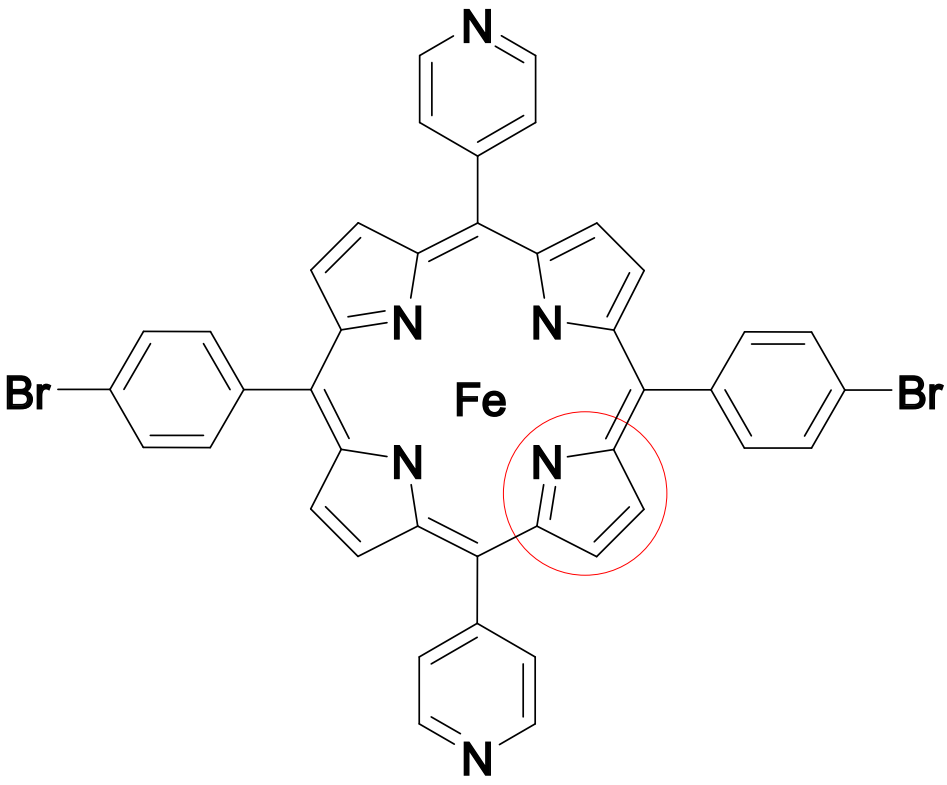

Figure 3.2: Structure of $\mathrm{Fe-DPyDBrPP}$ **molecule.** Two-fold symmetry Fe 5,15-dipyridyl-10,20-dibromophenyl porphyrin ($\mathrm{Fe-DPyDBrPP}$) molecule. The pyrrole ring is marked by red circle, hydrogen atoms not explicitly shown. Figure drawn by Chemydraw.

3.3 $\mathrm{Fe-DPyDBrPP}$ molecule

Fe 5,15-dipyridyl-10,20-dibromophenyl ($\mathrm{Fe-DPyDBrPP}$) molecules were provided by PorphyChem company, its structure is shown in Fig. 3.2 where two bromophenyl ligands are attached to opposite 10,20 meso-positions and pyridyl ring to 5,15 opposite meso-positions. Hence $\mathrm{Fe-DPyDBrPP}$ molecule has two-fold symmetry in gas phase.

3.4 Preparation for STM experiment

$\mathrm{Fe-DPyDBrPP}$ deposition on freshly prepared clean Au(111) surface is done by organic molecular beam epitaxy (OMBE) ($T_{crucible}$ = 575K) when the Au(111) surface is kept at room temperature. During the deposition the pressure in the preparation chamber is temporary increasing up to the 10^{-9} mbar range. After deposition process the $\mathrm{Fe-DPyDBrPP}$/Au(111) sample is usually post-annealed at about 400 K for 10' by PBN heating. This process aims to accelerate the diffusion of $\mathrm{Fe-DPyDBrPP}$ molecules on Au(111) surface and launch thermally activated Au-catalyzed debromination reaction that forms covalently bonded molecular chain.

It was observed that the molecule source is also depositing Br atoms on the surface of gold.

We have attributed this concomitant deposition of Br with $\mathrm{Fe-DPyDBrPP}$ to the stochastic Br detaching from $\mathrm{Fe-DPyDBrPP}$ molecules inside the crucible when heated at evaporation temperature. In-crucible Br detaching form similar molecules was already reported in [140] at 590 K. This implies a sizeable amount of molecules have formed tight bonded clusters in the molecular crucible and become resistant against thermal evaporation. The in-crucible reaction also indicates that unlike atom evaporation it will be impossible to obtain a solid dependence between evaporation temperature, deposition time and covering rate for $\mathrm{Fe-DPyDBrPP}$ molecules. Thus we normally adopt deposition time of 20" and evaporation temperature between 580 K and 610 K in which we should have a moderate covering rate (5% to 20% monolayer).

The debromination reaction inside the crucible or at the gold surface yield the presence of Br at the surface of gold during deposition or post-annealing. In our case, almost all elbow sites of the herringbone reconstruction are occupied by deposited Br atoms.

Once the annealing process is completed we transfer $\mathrm{Fe-DPyDBrPP}$/Au(111) sample to STM chamber for experiment without exceeding a pressure over 10^{-10} mbar.

3.5 Structure of monomer, chain and lattice

Fig. 3.3 (a) shows a large area topography image (current error image) of adsorbed $\mathrm{Fe-DPyDBrPP}$ molecules evaporated at 580 K and after post-annealing at 400 K for 10'. We see that most of molecules are monomers (marked by orange arrow, shown in Fig. 3.3 (c)) while a few molecules form compact lattices (marked by red arrow, shown in Fig. 3.3 (b)) and chain of bonded molecules (marked by blue arrow, shown in Fig. 3.3 (d)).

In large-range topography image Fig. 3.3 (a) we observe that monomers locate preferentially at elbow sites of the herringbone reconstruction (marked by orange arrow) and at the step edges, while chain of bonded molecules can also be found at elbow sites (marked by blue arrow) and the lattices can be mostly found at fcc domains (marked by red lattice).

The high-resolution images Fig. 3.3 (b-c) show the $\mathrm{Fe-DPyDBrPP}$ monomer at elbow site and $\mathrm{Fe-DPyDBrPP}$ lattice at fcc domain. We can clearly distinguish the skeleton of the molecules with the center Fe atom, the porphine macrocycle and the ligands attached to macrocycle. The most intuitive image is that $\mathrm{Fe-DPyDBrPP}$ molecule on Au(111) surface does not show a planar configuration as two opposite-site pyrrole rings (red circle) show enhanced topographic weight than the other two opposite-site pyrrole rings. This indicates a deformation of macrocycle where the enhanced topographic weight pyrrole rings (upper pyrrole rings) bend toward vacuum and couple better with the tip while the other two (downer pyrrole rings) bend towards Au substrate. Such deformation corresponds to the saddling distortion of porphyrin-based molecules [228] which is quite commonly observed [32, 148, 163, 229].

We are also interest in the fate of the ligands when adsorbed on the Au(111) surface. The sketch of the $\mathrm{Fe-DPyDBrPP}$ molecule is placed above the molecules in Fig. 3.3 (b-d) to match the topography as closely as possible. By comparing the difference between the sketch and the topography, we can understand the behavior of the ligand on the Au(111) surface.

From Fig. 3.3 (c), we see $\mathrm{Fe-DPyDBrPP}$ molecule sketch has well fitted with topography while we notice that the bottom bromophenyl ligand ($-\mathrm{C_6H_4Br}$) shows stronger topographic weight than the upper one, this indicates that the upper bromophenyl ligand is debrominized while the bottom one is not. Due to the low molecule coverage, this monomer could not form covalent bond with other molecules during annealing process and remain trapped at elbow site.

Fig. 3.3 (b) shows a $\mathrm{Fe-DPyDBrPP}$ molecular lattice lying on fcc region. In this lattice all bromine atoms of $\mathrm{Fe-DPyDBrPP}$ molecules are preserved and the lattice is supported by Van der Waals interaction, hydrogen bond and possible halogen bond. We understand that by looking at the lattice which can be described as a compact arrangement of rows of $\mathrm{Fe-DPyDBrPP}$ molecules along direction indicated by black dashed arrow. Along this direction, the bromophenyl ligand of a $\mathrm{Fe-DPyDBrPP}$ molecule couples with downer pyrrole ring of neighbor molecule (molecule 1 and 3 with green circles in Fig. 3.3 (b)). Between different rows, the molecule 1 can also couple with lateral molecules 2 and 4 through connecting pyridyl ring ($-\mathrm{C_5H_4N}$) of molecule 1 with upper pyrrole ring of molecule 2 (blue circle) and upper pyrrole ring of molecule 1 with bromophenyl ligand of molecule 4 (yellow circle), respectively. These bonding formations are weak because it is confirmed by tip manipulation that we use the tip to extract $\mathrm{Fe-DPyDBrPP}$ monomer from the lattice (Fig. 3.25), indicating these bonds are not strong with respect to covalent bond.

In Fig. 3.3 (d), we observed a chain of molecules covalently linked with the first molecule 1 adsorbed at the reconstruction elbow. The formation of the covalent bond is strongly evidenced by the tip manipulation in which the trimer of molecule can be moved together on the Au(111) surface (see Fig. 3.10), this behavior differs from what we have by implementing the same manipulation on the hydrogen-bonded lattice where the single monomer is extracted.

By comparing the distribution of different molecular assemblies, we can understand the role of Au(111) surface geometry in diffusion process of $\mathrm{Fe-DPyDBrPP}$ monomer during post-annealing.

The elbow site of the Au(111) reconstruction is a favored nucleation site which exhibits strongly attractive potential. During post-annealing process, monomers are thermally activated and start to diffuse on Au(111) surface, they can be trapped by step edges, elbow sites of the reconstruction and by other molecules on the surface. However a molecule island connected to elbow site can barely be found, this indicates that the bonds that support the lattice are too weak to stabilize it around elbow site as the stacking fault lines of Au(111) surface prevents the its formation during post-annealing, but strongly bonded molecular chain can still locate at elbow sites. While at fcc domains, the formation of weak bonds between monomers is still able to reduce the total kinetic energy and hinder the diffusion process, giving rise to weakly bonded molecular lattice.

Yet a quantitative analysis that requests listing these events to attribute quantitative potential energies and activation energy to produce each molecular configuration and to confront it to the kinetic energies of the molecules in these configurations, for instance Monte Carlo simulation, is needed. However this analysis goes beyond the objective of the structural analysis here.

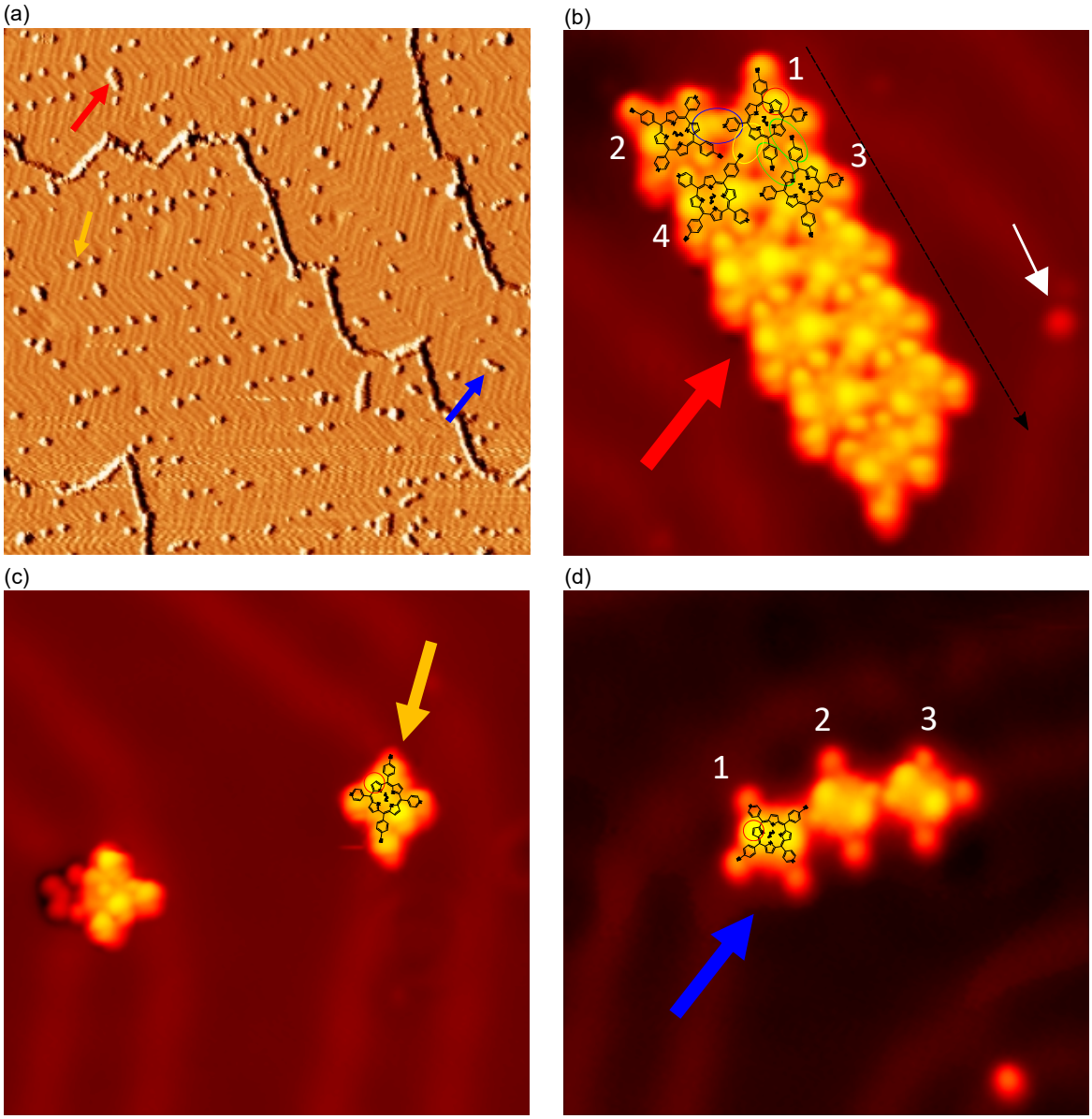

Figure 3.3: Topography image of different $Fe-DPyDBrPP$ **molecule structure on Au(111) surface.** (a) Current topography image ($200x200nm^2$, setpoint: 125 mV, 20 pA) of large area. Red, orange and blue arrows indicate $Fe-DPyDBrPP$ lattice, monomer and bonded chain respectively. (b) Topography image of $Fe-DPyDBrPP$ lattice ($10x10nm^2$, setpoint: 50 mV, 100 pA). Red circle marks the upper pyrrole ring that bends towards vacuum. Blue circle marks the bond between pyridyl ring of molecule 1 and upper pyrrole ring of molecule 2. Green circles mark the bond between debrominized phenyl ring of molecule 1 with downer pyrrole ring of molecule 3 and debrominized phenyl ring of molecule 3 with downer pyrrole ring of molecule 1. Yellow circle marks the bond between debrominized phenyl ring of molecule 4 with upper pyrrole ring of molecule 1. Black dash arrow indicates the direction that molecule in lattice arranges. White arrow aims at adsorbed defect atom at elbow site of herringbone reconstruction of Au(111) surface. (c) Topography image of $Fe-DPyDBrPP$ monomer ($12x12nm^2$, setpoint: 50 mV, 100 pA). (d) Topography image of bonded $Fe-DPyDBrPP$ trimer ($12x12nm^2$, setpoint: 200 mV, 100 pA).

3.6 Spin state switching

We now present the results of the electronic properties of the monomers and $\mathrm{Fe-DPyDBrPP}$ arrays (lattice) on Au(111). Their topographic images and corresponding dI/dV STS spectra are shown in Fig. 3.4. The yellow and red crosses in Fig. 3.4 (a-b) indicate that the STS measurements are taken on the upper pyrrole rings of the isolated monomer $\mathrm{Fe-DPyDBrPP}$ positioned at the elbow site of the reconstruction and the $\mathrm{Fe-DPyDBrPP}$ molecule in the lattice on the fcc region of Au(111), respectively. Fig. 3.4 (c-d) shows the dI/dV STS spectra at large- and low- range bias voltage window. The large voltage range is used to characterize the energy dependence of molecular orbitals which are usually extending far from the Fermi level with respect to the low-energy feature such as inelastic scattering and Kondo resonance. In the following, we assume that the interaction between the molecule and the surface is strong enough so the chemical potential of the molecule is pined to the Fermi level of the gold surface there is a direct correspondence between energy of the molecular states and bias voltages without any Coulomb blockade or field effect induced distortions. This last assumption is later justified by the proposed scenario of the involved physical mechanisms and our DFT calculations.

In Fig. 3.4 (c), the scatter points represent the raw data and the continuous curves with corresponding colors represent the smoothed data. We can clearly see that the red curve (molecule in the lattice) shows a strong peak at bias about $+150\,\mathrm{mV}$ above the Fermi level which corresponds to an unoccupied molecular frontier orbital (frontier orbital B, FOB) of the molecule in the lattice. At a slightly higher bias around $+200\,\mathrm{mV}$ there is also some spectral weight which could signify the presence of other molecular orbitals. Another important feature is that there is a dip at the Fermi level, however it is not well resolved due to the large amplitude of the modulation voltage V_m during Lock-in measurement. There are also some features above $+500\,\mathrm{mV}$ but they are too far from the Fermi level to be of interest here. The orange curve (monomer) behaves differently from the red curve, it seems that the peaks at $+150\,\mathrm{mV}$ of the orange curve shift below zero bias at $-100\,\mathrm{mV}$, leaving a flat signal around $+150\,\mathrm{mV}$. We also notice that the trough feature disappears and instead a small bulge emerges at zero bias while the signature above $+500\,\mathrm{mV}$ remains unchanged.

The high-resolution dI/dV spectra measuring a small voltage window (between gray dashed lines in Figure 3.4 (c)) around the zero bias is shown in Figure 3.4 (d). These spectra allow us to know the low-energy behavior which cannot be well resolved by large scale spectroscopy (c). The orange and red scatter points are raw data for the monomer and lattice molecule, respectively. It is evident that the orange and red signatures near the Fermi level are completely different, the orange signature shows a single peak located at the Fermi level and the red signature shows a symmetric double step feature at the Fermi level.

The red double-stepped feature is the result of inelastic spin excitation of a spin-1 impurity[1] with non-zero uniaxial magnetic anisotropy D and transverse magnetic anisotropy E. From

[1] In fact the spin description for this system is not rigorous[230]. But for molecules exhibiting SF features, they are still in atomic limit so that spin description can still holds.

now, we use the notion of spin-flip (SF) [27, 103] to denote inelastic spin excitation. The single-peak orange feature corresponds to an Abrikosov-Suhl resonance, also called Kondo peak in the following, resulting from Kondo effect. These low-energy behaviors indicate to us that the $\mathrm{Fe-DPyDBrPP}$ molecule retains its magnetic properties on the Au(111) surface.

The orange and red curves are fitted by a simple Frota line shape (equation (2.18)) with a Gaussian background and a step line shape (equation (2.20)) respectively. The fitting results yield coupling strength $\Gamma = 0.8$ meV for the monomer $\mathrm{Fe-DPyDBrPP}$ showing Kondo resonance and renormalized SF excitation energies $E1$, $E2$ = 7 meV, 10 meV for the molecule $\mathrm{Fe-DPyDBrPP}$ in the array showing SF signature. From the expression (2.19), we can estimate the Kondo temperature $T_K = 10$ K for the monomer, which is sufficiently large compared to the temperature in our experiment $T = 1.1$ K, indicating a fully developed Kondo effect. $E1$ and $E2$ can derive the magnetic anisotropy $D = 8.5$ meV and $E = 1.5$ meV which are around the typical value for a Fe-porphyrin-based magnetic molecule [30–33, 231].

It is astonishing that the same molecule on Au(111) surface can show such drastic variation of electronic behavior despite that in topography images they appear not to be so different. There were indeed studies reporting different electronic behaviors for same FePc molecule or FeTPP molecule on Au(111) surface [15, 232, 233], but such obvious switching from SF step feature to Kondo peak behavior is not observed yet on Au(111) surface to our knowledge.

3.6.1 Electronic properties of lattice molecules

To understand the underneath mechanism that makes molecules to behave like a spin-1 impurity showing SF feature or to exhibit Kondo peak, we first investigate dI/dV STS maps and spectra taken on a lattice of molecules in Fig. 3.5 and Fig. 3.6.

Fig. 3.5 shows the dI/dV spectra taken on the same $\mathrm{Fe-DPyDBrPP}$ molecule in a lattice. The red and blue spectra are taken on the upper pyrrole rings while the green spectra are taken at the center Fe atom. In (b) we see that the red and blue spectra have almost the same spectra shape with a strong peak at around $+150$ mV, indicating that we are tunneling through the same molecular orbital that localizes on upper pyrrole rings, in agreement with the molecule symmetry observed in topography Fig. 3.4 (a-b).

The spatial extension of this molecular orbital is probed by in the STS dI/dV map at bias of $+150$ mV shown in Fig. 3.5 (e) where all $\mathrm{Fe-DPyDBrPP}$ molecules in lattice shows two lobes shapes but with variable spectral weight. This two lobes shape orbital localized above and close to the Fermi level correspond to the lowest unoccupied FOB for this molecule. The green spectra measured at the central Fe atom shows mainly 2 features: 1). A small spectral weight corresponding to the weak spatial extension of the FOB on the iron site probably associated with a weak hybridization of the pyrrole states with the iron state; 2). A strong spectral signature at -150 mV which localized on the Fe atom center in STS map in Fig. 3.5 (d). This point-like orbital, localized below and close to Fermi level, correspond to the occupied FOA. All $\mathrm{Fe-DPyDBrPP}$ molecules in the lattice show the same feature but with different spectral weights in dI/dV maps of ± 150 mV.

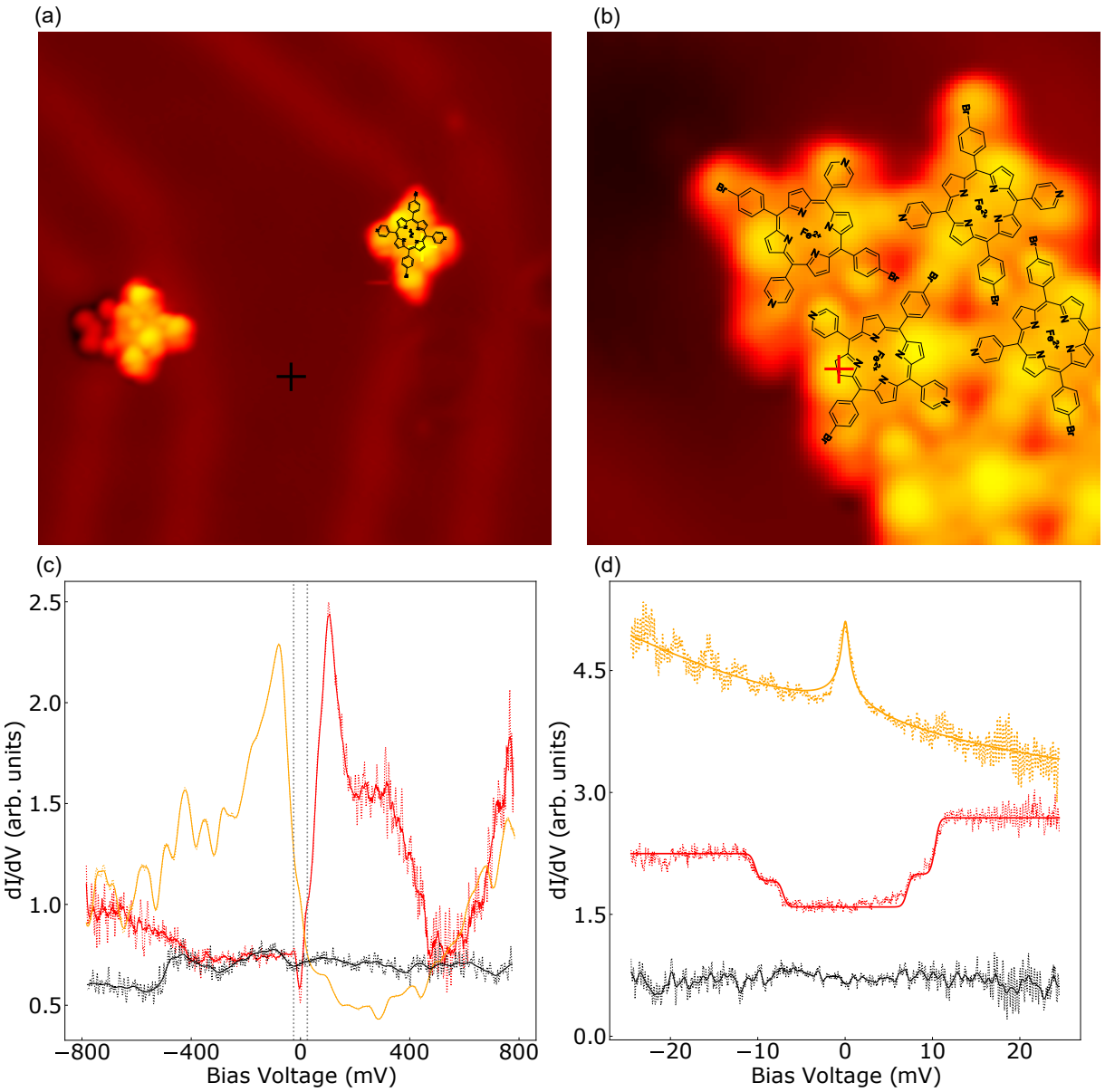

Figure 3.4: Spectroscopy of $\mathrm{Fe-DPyDBrPP}$ **monomer and lattice.** (a) Topography image of $\mathrm{Fe-DPyDBrPP}$ monomer ($12\mathrm{x}12\mathrm{nm}^2$, setpoint: 50 mV, 100 pA). Yellow cross indicates the location where STS spectra is measured. (b) Topography image of $\mathrm{Fe-DPyDBrPP}$ lattice ($5\mathrm{x}5\mathrm{nm}^2$, setpoint: 50 mV, 100 pA). Red cross indicates the location where STS spectra is measured. (c) Large-range dI/dV spectra measured at cross positions of $\mathrm{Fe-DPyDBrPP}$ monomer (orange curve) and $\mathrm{Fe-DPyDBrPP}$ molecule in lattice (red curve) in (a) and (b) respectively. Scatter points are raw data and curves are smoothed data, black curve represents the spectra taken on Au(111) surface. All spectra are normalized. 800 mV, 500 pA. Lock-in parameters: ($V_m = 5$ mV, $f = 900$ Hz). (d) High-resolution dI/dV spectra in a voltage window between gray dashed lines marked in (c). Orange curve and red curve are fitted by single Frota lineshape with a Gaussian background and step lineshape, respectively. All spectra are normalized and shifted vertically for clarity. Setpoint: 30 mV, 200 pA. Lock-in parameters: ($V_m = 0.2$ mV, $f = 750$ Hz).

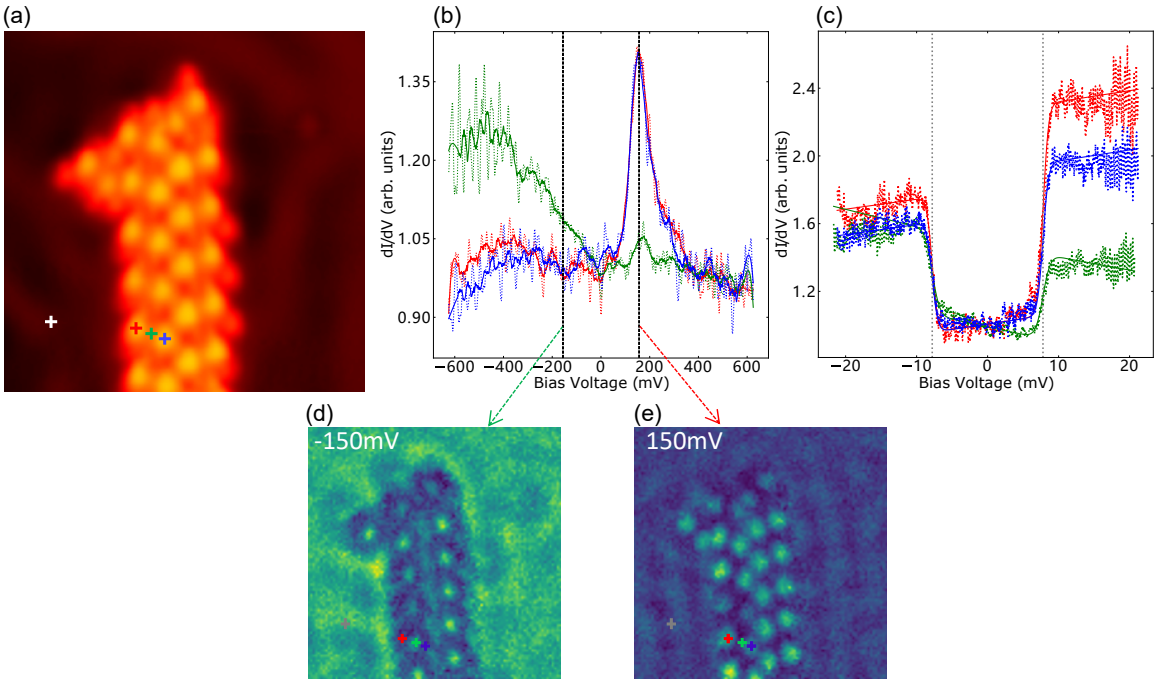

Figure 3.5: Spectroscopy of a single $\mathrm{Fe-DPyDBrPP}$ **molecule in lattice.** (a) Topography image of $\mathrm{Fe-DPyDBrPP}$ lattice ($10\mathrm{x}10\mathrm{nm}^2$, setpoint: 125 mV, 20 pA). Red, blue crosses mark the upper pyrrole rings and green cross marks the center Fe atom of same $\mathrm{Fe-DPyDBrPP}$ molecule. (b) Large-range dI/dV spectra measured at cross positions in (a) with same colors. Scatter points are raw data and curves are smoothed data. All spectra are normalized. Setpoint: 650 mV, 100 pA. Lock-in parameters: $V_m = 5$ mV, $f = 900$ Hz. (c) High-resolution dI/dV spectra in a voltage window of ± 25 mV of (b). Setpoint: 30 mV, 200 pA. Lock-in parameters: $V_m = 0.2$ mV, $f = 750$ Hz. (d) dI/dV map of topography region at bias -150 mV. Curves are fitted by step lineshape. All spectra are normalized. (e) dI/dV map of topography region at bias $+150$ mV.

The corresponding high-resolution dI/dV spectra within the voltage window of ± 25 mV are shown in Fig. 3.5 (c). These spectra, which correspond to different locations on the same molecule, exhibit the SF step feature with similar excitation energy but with a different background slope. The same energy behavior indicates that the inelastic SF excitation measured on different positions of same molecule have the same magnetic origin, while the spectra asymmetry behavior looks related to the background contributed from FOB or FOA. However the asymmetry behavior can be also explained as the potential scattering differs in FOB and FOA when we are tunneling through them to measure SF signature [32, 97, 98, 231].

Fig. 3.6 shows the dI/dV spectra taken on three different $\mathrm{Fe-DPyDBrPP}$ molecules of the lattice where red, green and blue spectra are taken on their upper pyrrole rings respectively. From Fig. 3.6 (b) and (c), depending on the molecules the energy of FOB varies in 50 meV range, accompanied with it, SF energy varies as well. While FOA cannot be probed at the pyrrole location. For the molecule with larger FOB energy (red curve) it exhibits smaller SF energy, while for those with smaller FOB energies (green and blue curves) their SF energies are larger. The dependence between energies of frontier orbitals and magnetic anisotropy energy (SF energy) has been well studied by Meng et. al. [231] who had revealed by DFT calculations that, in atomic limit, the shifting of FOB energy is a result of rearrangement of d-level occupation due to different adsorption sites which can affect on magnetic anisotropy energy [234].[2]

But here in our case, we can not determine yet the origin of this phenomenon whether it is due to different adsorption sites with respect to substrate [231] or to the interaction between neighboring molecules of the lattice [40, 65, 158].

All $\mathrm{Fe-DPyDBrPP}$ molecules in the lattice exhibit SF feature with a double-lobe frontier orbital located on the upper pyrrole rings at about $+150$ meV (FOB) and a dot-shaped frontier orbital located on the central ion at about -150 meV (FOA). The detection of the SF signature on FOB indicates that the macrocycle π orbital hybridizes with the d orbitals of the central Fe atom, which are considered as Fe $3d_{xz/yz}$ (d_π) [142–145] orbitals. The dot shape of the FOA at the central Fe atom is essentially a characterization of the d_{z^2} orbital that is expected to hybridize weakly with the molecular orbital but strongly with the substrate. The lower pyrrole rings show neither the frontier orbital feature nor the SF signature in a small energy window, indicating the absence of molecular states near the Fermi level on the lower pyrrole rings.

The SF feature indicates a spin-1 configuration for all molecules in the $\mathrm{Fe-DPyDBrPP}$ lattice, which means that all molecules in the lattice have a well-defined valence, i.e., they are in the atomic limit. In this case, the inter-impurity spin-spin interaction cannot occur through the RKKY interaction (see section (1.2.6)). The dipolar interaction seems insufficient to couple the spins in the lattice (Fig. 3.6 (c)) as in dI/dV spectra, we do not observe any obvious collective behavior affecting the SF feature [39, 235] where multiple steps should be observed.

But we have found an important feature: the frontier orbitals extend to the Fermi level and induce a background asymmetry to the SF signature (Fig. 3.5 (c)), which may imply that the

[2]Large shifting of frontier orbital level would result charge fluctuation which can strongly renormalise magnetic anisotropy and atomic limit condition breaks down (see paragraph (3.6.4)).

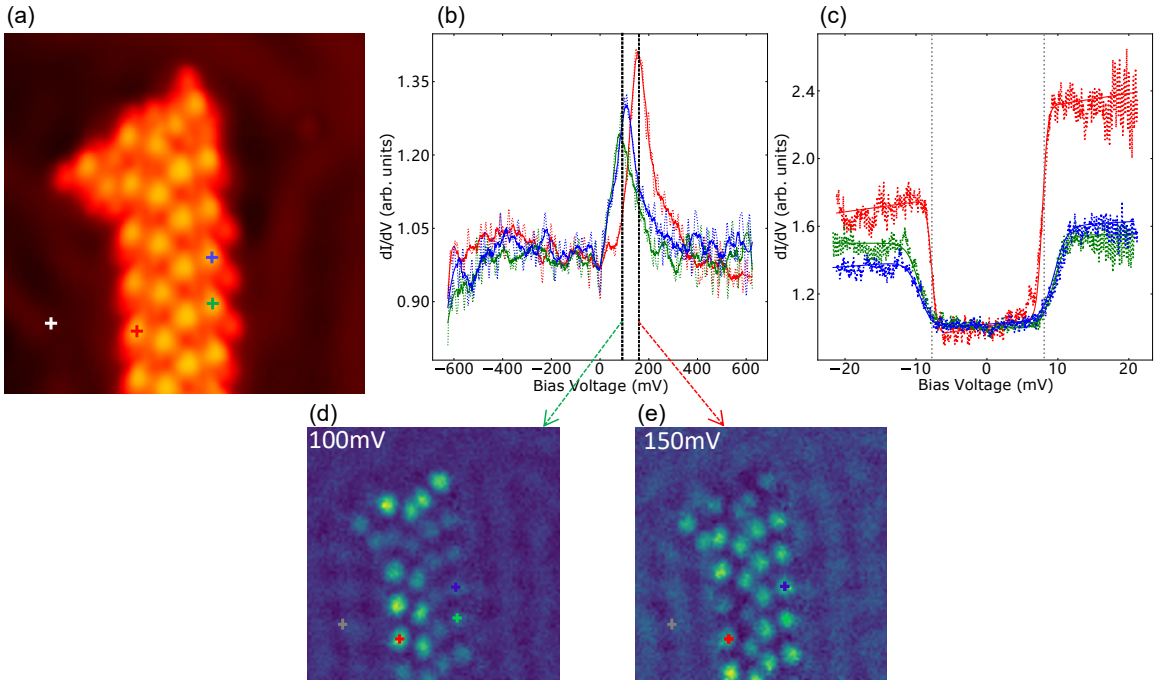

Figure 3.6: Spectroscopy of three different $\mathrm{Fe-DPyDBrPP}$ **molecules in lattice.** (a) Topography image of $\mathrm{Fe-DPyDBrPP}$ lattice ($10\mathrm{x}10\mathrm{nm}^2$, setpoint: 125 mV, 20 pA). Red, green and blue crosses mark the upper pyrrole rings of three different $\mathrm{Fe-DPyDBrPP}$ molecule. (b) Large-range dI/dV spectra measured at cross positions in (a) with same colors. Scatter points are raw data and curves are smoothed data. All spectra are normalized. Setpoint: 650 mV, 100 pA. Lock-in parameters: $V_m = 5$ mV, $f = 900$ Hz. (c) High-resolution dI/dV spectra in a voltage window of ± 25 mV of (b). Setpoint: 30 mV, 200 pA. Lock-in parameters: $V_m = 0.2$ mV, $f = 750$ Hz. (d) dI/dV map of topography region at bias 100 mV. Curves are fitted by step lineshape. All spectra are normalized. (e) dI/dV map of topography region at bias $+150$ mV.

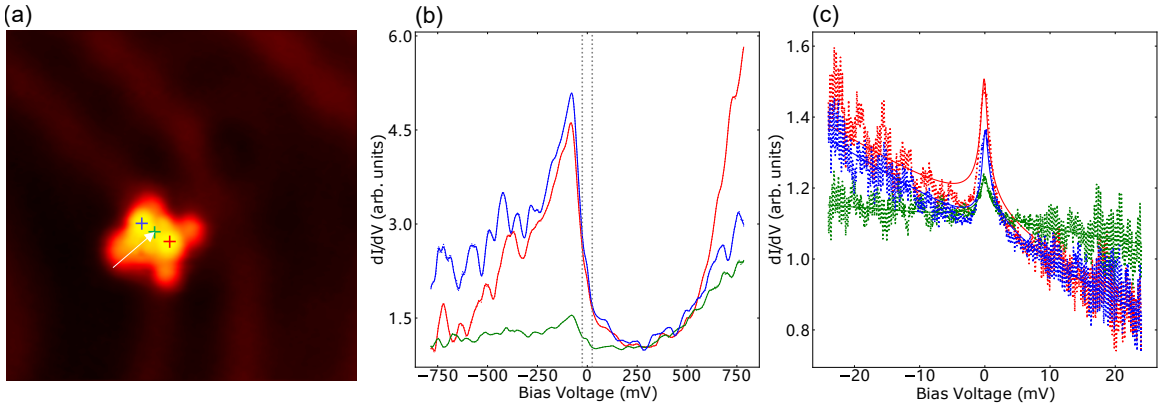

Figure 3.7: Spectroscopy of a $\mathrm{Fe-DPyDBrPP}$ **monomer adsorbed at elbow site.** (a) Topography image of $\mathrm{Fe-DPyDBrPP}$ monomer at elbow site ($10\mathrm{x}10\mathrm{nm}^2$, setpoint: 125 mV, 20 pA). Red, blue crosses mark the upper pyrrole rings and green cross marks the center Fe atom. White arrow aims at the elbow site of herringbone reconstruction of Au(111) surface. (b) Large-range dI/dV spectra measured at cross positions in (a) with same colors. Scatter points are raw data and curves are smoothed data. Setpoint: 800 mV, 200 pA. Lock-in parameters: $V_m = 5\,\mathrm{mV}$, $f = 900\,\mathrm{Hz}$. (c) High-resolution dI/dV spectra in a voltage window between gray dashed lines marked in (b). Setpoint: 30 mV, 200 pA. Lock-in parameters: $V_m = 0.2\,\mathrm{mV}$, $f = 750\,\mathrm{Hz}$. Scatter points are raw data and curves are fitted by single Frota lineshape with a Gaussian background. All spectra are normalized.

$\mathrm{Fe-DPyDBrPP}$ molecule is not far from the mixed-valence regime as we will see below.

3.6.2 Electronic properties of isolated monomer

Now we examine the electronic property of the monomer that exhibits Kondo effect. We start with a monomer trapped at the elbow site of herringbone reconstruction of Au(111) surface in Fig. 3.7. The red and blue spectra are taken on the upper pyrrole rings while the green spectra is taken on the central Fe atom. The white arrow marks the exact position of the elbow site of the chevron reconstruction.

In Fig. 3.7 (b), we see that the red and blue curves measured on upper pyrrole rings always exhibit almost the same spectra lineshape where a strong peak localizes at about -100 mV. This peak corresponds to FOB of the monomer, and it has the same orbital distribution as the FOB of the lattice molecule. The green spectra measured at the central Fe atom shows similar behavior to the red and blue curves, but with reduced spectral weight.

The low-energy excitation feature is shown in Fig. 3.7 (c) where we observe a peak that is the signature of the Abrikosov-Suhl resonance of a Kondo state. The Kondo peaks are fitted using a unique linear Frota shape with a Gaussian background, the resulting Kondo temperature for the red, green, and blue curves are 9.6 K, 10.7 K, and 9.35 K, respectively. Considering the fitting error, we can state that the Kondo temperatures measured in different parts of a single molecule do not vary, which is also the case for the SF signature. It seems that the low-energy excitation feature (SF or Kondo) extends to the molecular states localized on the upper rings of pyrrole, we will study this phenomenon in the section (3.7).

We also want to examine the electronic properties of a monomer in an arbitrary adsorption site. But as illustrated in Fig. 3.3 it is almost impossible to find an isolated monomer. Hence we

develop a protocol for the manipulation of the molecules with the tip that is introduced in section (3.9.1) to move the monomer at elbow site or extract it from the lattices (see section (3.9.2)), to put it in an arbitrary adsorption site.

Fig. 3.8 (b-d) are the topography images showing the $\mathrm{Fe-DPyDBrPP}$ monomer in Fig. 3.7 (a) removed from the elbow site by tip assisted manipulation. Once the molecule is removed from the elbow site, we are able to see the presence of an adatom (indicated by the white arrow) trapped at the elbow site that was underneath the molecule in Fig. 3.7 (a). This is a general observation: the elbow sites of the reconstruction are decorated by the presence of Br adatoms deposited on the surface during the molecular deposition[3].

Fig. 3.8 (b) shows the monomer which has been moved to the fcc region of the Au(111) surface, Fig. 3.8 (c-d) show the case where $\mathrm{Fe-DPyDBrPP}$ monomer is moved to hcp region of Au(111) surface, in (c) one of pyridyl ligands of $\mathrm{Fe-DPyDBrPP}$ monomer is on top of adatom at elbow site while in (d) monomer center is close to elbow site but not on top of it.

Fig. 3.8 (a) shows the dI/dV spectra of $\mathrm{Fe-DPyDBrPP}$ monomer in these 3 conditions presented in (b-d). Intriguingly, all of them do not exhibit Kondo peak anymore but instead the SF step feature emerges. Depending on the adsorption sites, the SF step feature varies the excitation energy and exhibits a double-stepped or single-stepped feature. The fitting results of SF step feature yield that the uniaxial anisotropy D varies between (6.8 meV, 10 meV) and transverse anisotropy E varies between (0 meV, 1.5 meV) (with tens of positions measured).

These behavior indicate that when $\mathrm{Fe-DPyDBrPP}$ monomer center is moved away from elbow site, it behaves as a spin-1 quantum magnet exhibiting inelastic SF excitation feature which magnetic anisotropy depends on the adsorption sites. This can explains the moiré-like patterns of lattice molecules in dI/dV maps shown in Fig. 3.6 (d-e) where FOB energy varies.

The sudden disappearance of Kondo peak feature when $\mathrm{Fe-DPyDBrPP}$ monomer in Fig. 3.7 (a) is moved away from elbow site is very puzzling. To verify that if this drastic change is related to the adatom at elbow site or not, we implement tip manipulation to move monomer in Fig. 3.8 back to the elbow site so that its center lies above adatom at elbow site again.

Fig. 3.9 shows the case when the same monomer in Fig. 3.8 is moved to back to elbow position occupied by a Br adatom monomer center is on top of it. (c-d) corresponds to different orientation of monomer symmetry axis with respect to Au(111) crystallographic orientations. Their dI/dV spectra are shown in Fig. 3.9 (a) where Kondo signature is recovered again. The width of Kondo resonances is similar to the case presented Fig. 3.7 (a) and remain unchanged when rotating the molecule with Kondo temperature estimated to $T_K = 10$ K from fits.

It is surprising that spin-1 SF feature disappears and Kondo effect emerges again when the monomer is moved back to the elbow site. This confirms that Br adatom at elbow site is responsible for the emergence of Kondo effect.

For a spin-1 magnet, when in interaction with an electron reservoir it may exhibit a spin-1 Kondo effect originated from degenerate triplet ground state. However, spin-1 Kondo effect

[3]The elbow site of the reconstruction is also possible to be occupied but by a $\mathrm{Fe-DPyDBrPP}$ molecule itself rather than a Br adatom. In this scenario, $\mathrm{Fe-DPyDBrPP}$ molecule becomes almost impossible to be moved away (see section (3.9.3)).

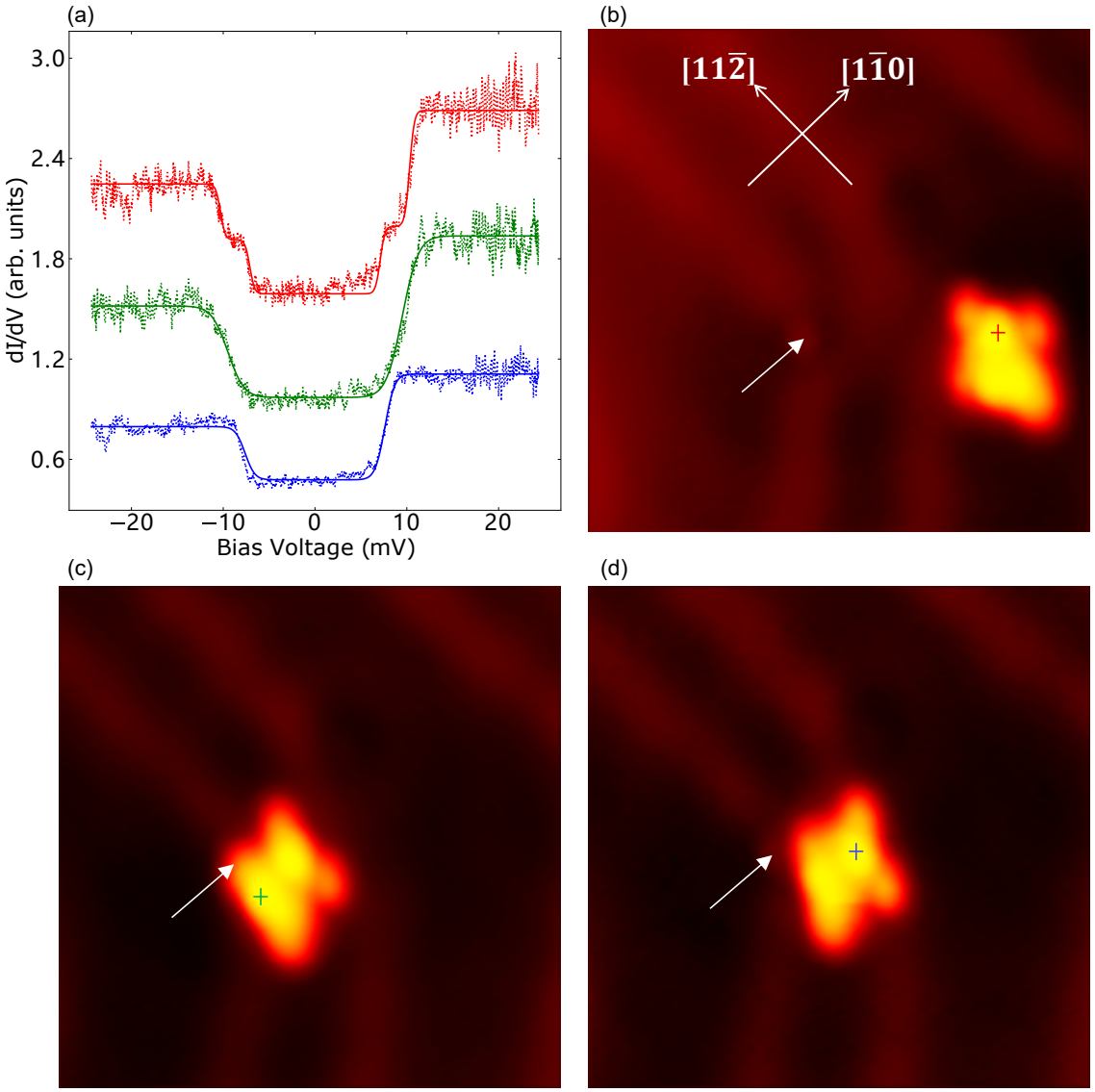

Figure 3.8: Spectroscopy of a $\mathrm{Fe-DPyDBrPP}$ **monomer at different adsorption sites.** (a) dI/dV spectra of $\mathrm{Fe-DPyDBrPP}$ monomer shown in (b)-(d) with different orientation. The spectra are taken on the cross positions with corresponding colors. Setpoint: 30 mV, 200 pA, Lock-in parameters: $V_m = 0.2$ mV, $f = 750$ Hz. Scatter points are raw data and curves are fitted by step lineshape. All spectra are normalized and shifted for clarity. (b)-(d) $\mathrm{Fe-DPyDBrPP}$ monomer at different adsorption sites of Au(111) surface where (b) on hcp region, (c) on fcc region with one of the ligand attracted by elbow site, (d) fcc region, ($10\mathrm{x}10\mathrm{nm}^2$, setpoint: 125 mV, 20 pA). White arrow aims at the elbow site.

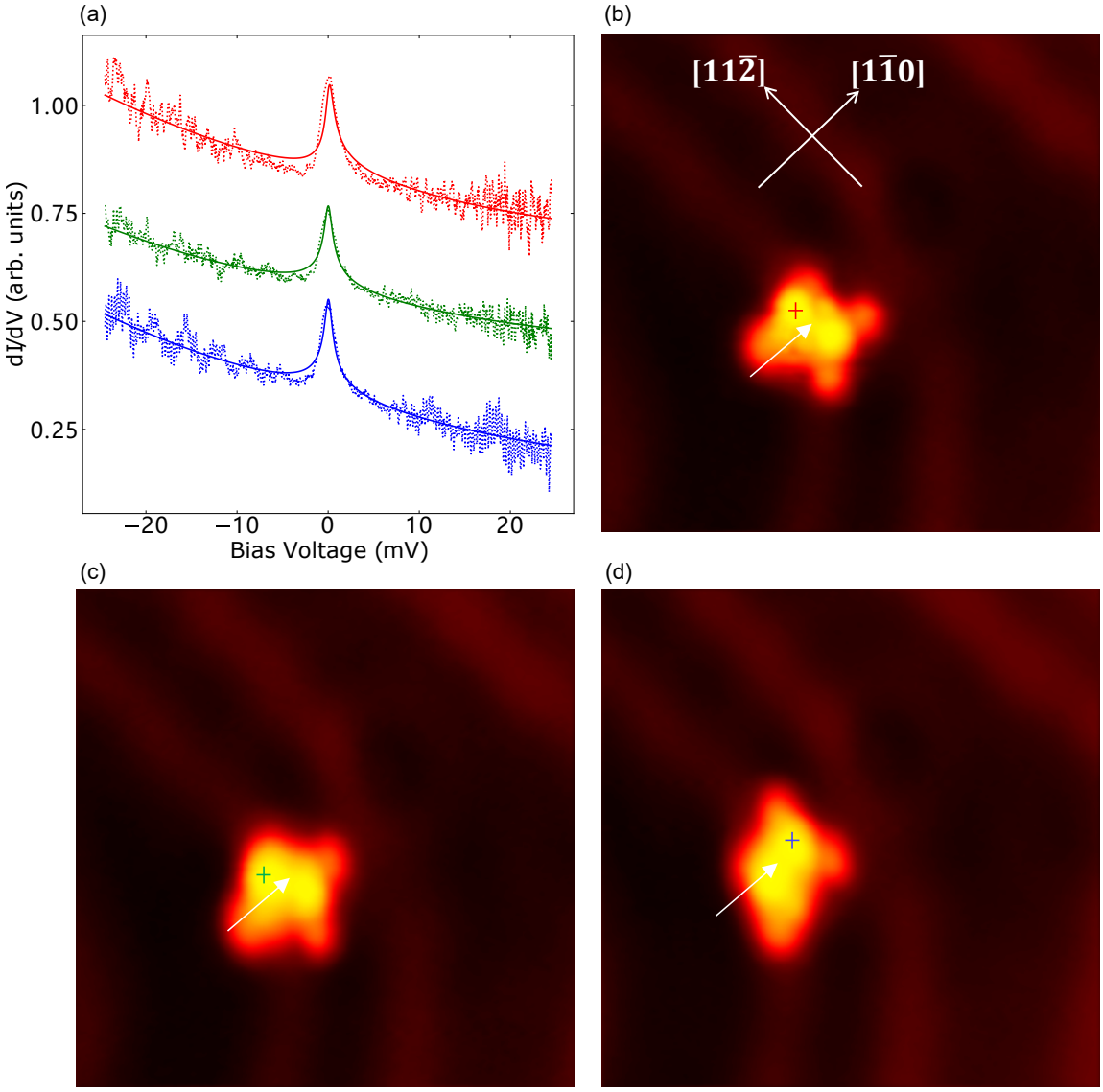

Figure 3.9: Spectroscopy of a $\mathrm{Fe-DPyDBrPP}$ **monomer adsorbed at elbow site of different orientations.** (a) dI/dV spectra of $\mathrm{Fe-DPyDBrPP}$ monomer shown in (b)-(d) with different orientation. The spectra are taken on the cross positions with corresponding colors. Setpoint: 30 mV, 200 pA. Lock-in parameters: ($V_m = 0.2$ mV, $f = 750$ Hz). Scatter points are raw data and curves are fitted by single Frota lineshape with a Gaussian background. All spectra are normalized and shifted for clarity. (b)-(d) $\mathrm{Fe-DPyDBrPP}$ monomer adsorbed on same elbow site but different orientations with respect to Au(111) surface ($10\mathrm{x}10\mathrm{nm}^2$, 125 mV, 20 pA). White arrow aims at the elbow site which is also the rotation center.

is extremely sensitive to magnetic anisotropy which tends to lift the degeneracy [29]. In our experiments, the Kondo resonance does not show any feature which could be related to the magnetic anisotropy as we have managed to rotate the molecule with respect to the surface atomic lattice and the Kondo feature remains unchanged when we expect that the magnetic anisotropy varies.

To explain this anisotropy-resistant behavior of Kondo effect occurring at the elbow site, there are two possibilities: 1). The coupling between molecule with substrate becomes so enormous that magnetic anisotropy is negligible with respect to the amplitude of the Kondo correlations, resulting a spin-1 Kondo effect that occurs in a nearly degenerate triplet ground state. 2). The total spin of the molecule is reduced from S = 1 to S = 1/2 due to a sizeable charge reception, resulting a spin-1/2 Kondo effect which is naturally immune against magnetic anisotropy. 3). The charge fluctuation process results strong renormalisation of magnetic anisotropy and brings system into mixed-valence regime where atomic limit description breaks.

Concerning the first explanation, the estimated Kondo temperature T_K at the elbow site is around $10\,\mathrm{K}$, corresponding to a coupling energy $\Gamma \approx 0.8\,\mathrm{meV}$, this is one order of magnitude smaller than the value of the magnetic anisotropy $D \approx 8\,\mathrm{meV}$ deducted from our experiments (when molecules are at other locations). In the meantime, the simulations (see section (1.2.5)) tell us that the renormalisation of the anisotropy energy requires an overwhelming coupling strength. Hence we believe the first origin of the Kondo effect is less probable for a porphyrin-based molecule at the surface of gold.

For the second and third explanations, they suggest the occurrence of charge effect (change of occupation and polarisation of impurity levels) when monomer is moved to the elbow site[4].

We will prove that the third explanation is correct through DFT calculation (3.6.4) and experimental observation (3.7). Before that, we first demonstrate that the observation of spin state switching is solid, reproducible and reversible for any $\mathrm{Fe-DPyDBrPP}$ molecule.

3.6.3 Electronic properties of a molecular trimer

Till now we know the spin state switching can happen for a $\mathrm{Fe-DPyDBrPP}$ monomer that changes its low-energy excitation behavior between Kondo or SF signature when it is located at the elbow site or somewhere else. But could such behavior be a special case that only occurs in $\mathrm{Fe-DPyDBrPP}$ monomer shown in Fig. 3.7 ? Here we show that the spin state switching phenomena can occur for any $\mathrm{Fe-DPyDBrPP}$ molecule.

Fig. 3.10 shows a covalently bonded $\mathrm{Fe-DPyDBrPP}$ trimer on Au(111) surface and the dI/dV spectra of this trimer in different configurations. Three $\mathrm{Fe-DPyDBrPP}$ molecules are marked by red, green and blue crosses respectively (now labeled red, green and blue molecules for simplicity), the adatom at elbow site is aimed by white arrow. Fig. 3.10 (b) shows the dI/dV spectra of $\mathrm{Fe-DPyDBrPP}$ trimer in corresponding configurations.

[4]Tip-induced charge fluctuations mechanism has been ruled out as measured tip-distance dependence of the spectra for reasonable of z values is irrelevant in the physics (see section (3.9.5)).

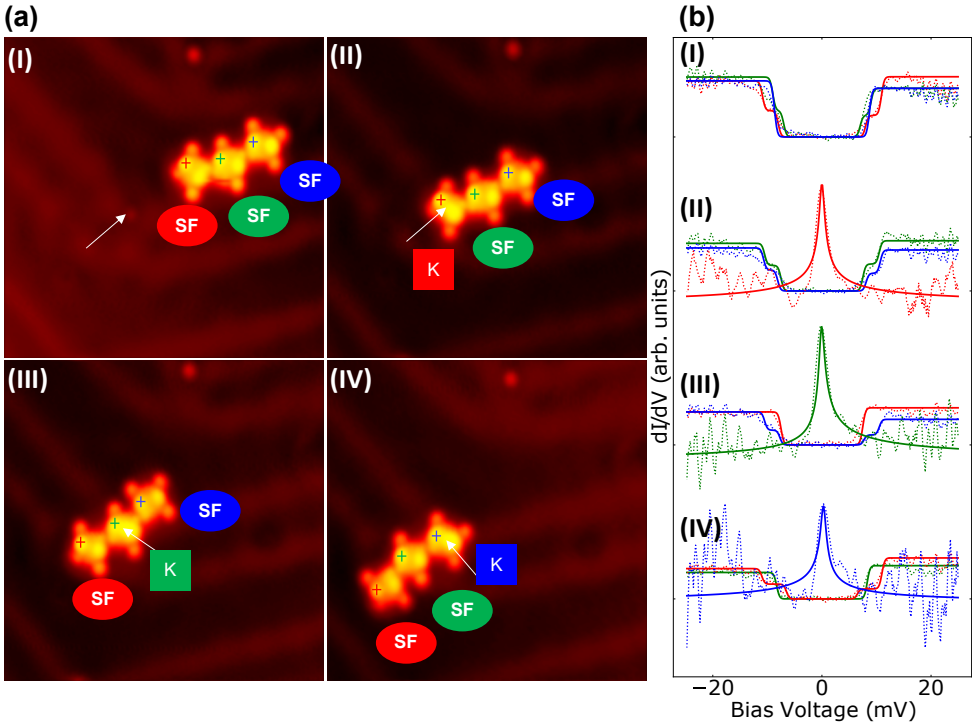

Figure 3.10: Reversible Kondo-SF switching in $\mathrm{Fe-DPyDBrPP}$ **trimer molecules.** (a) Topography image ($15\mathrm{x}15\mathrm{nm}^2$, setpoint: 125 mV, 20 pA) of a covalently bonded trimer of $\mathrm{Fe-DPyDBrPP}$ molecules in different configurations labeled from (I) to (IV) on Au(111) surface. The 3 bonded molecules are marked by red, green, and blue crosses respectively, the adatom at elbow site is marked by white arrow. In (I) none of molecules is at elbow site, in (II)-(IV) red, green, and blue marked molecule is on specific site respectively. K or SF indicate that the corresponding molecule shows Kondo or SF signature. (b) dI/dV spectra of trimer molecules in different configurations shown in (a). Each spectra is taken is taken at cross position in (a) with same color. Scatter points are raw data after background removal. Peak feature and step feature are fitted by single Frota lineshape and step lineshape, respectively. All spectra are normalized and shifted vertically for clarity. Setpoint: 30 mV, 200 pA. Lock-in parameters: $V_m = 0.2$ mV, $f = 750$ Hz.

There are four configurations labelled by (I) to (IV) in Fig. 3.10 (a). In (I) none of the $\mathrm{Fe-DPyDBrPP}$ molecules of the trimer is located at elbow site and as expected their dI/dV spectra are all presenting SF features ((I) in Fig. 3.10 (b)). In (II) the trimer is moved by tip manipulation so that the red $\mathrm{Fe-DPyDBrPP}$ molecule is at the elbow site, just like what we have observed for monomers before, the red molecule is now showing a Kondo peak while the other two $\mathrm{Fe-DPyDBrPP}$ molecules (green and blue) are still showing SF signatures ((II) in Fig. 3.10 (b)). In (III) the red molecule is moved away from elbow site and the green one is placed on top of it; interestingly now the red molecule has recovered the SF behavior and green one is showing Kondo effect while the blue one is still showing SF. Similarly in (IV) we place the blue molecule at the elbow site and it is now exhibiting a Kondo feature ((IV) in Fig. 3.10 (b)). Moreover, the spectroscopic features are following the expected temperature dependence for inelastic spin-flips and Kondo physics as measured in section (3.9.4).

The Kondo temperature obtained from fitting results for red, green and blue molecule are respectively 10.4 K, 11 K and 11 K which are almost identical. Hence we have confirmed that spin state switching that changes Kondo and SF feature can occur reversibly for any $\mathrm{Fe-DPyDBrPP}$ molecules which depend only on adsorption site on Au(111) surface. Another important point

is that, we do not observe any obvious evidence indicating the inter-molecular spin-spin interaction in the tightly bonded trimer molecule, which is just like what we have seen in the lattice (Fig. 3.5). This could possible imply that for spin-1 molecules in atomic limit, the covalent bond that connects macrocycle is still not enough efficient to correlate spins in different molecules.

3.6.4 DFT Calculation

Density-functional theory (DFT) calculations is useful for determination of structural and orbital configuration of molecules adsorbed on metal surfaces, it can also calculate hybridization strength, spin polarization of orbitals and charge transfer. Although DFT calculation fails to describe the correlation between electrons that gives rise to Kondo effect or renormalisation of magnetic anisotropy due to coupling in low-energy scale and the inter-molecular interaction (e.g. hydrogen bonds) calculation is hard to be modeled, it can rationalize the occurrence of high- and low- spin states as a result of charge fluctuation, moreover DFT predicted orbital evolution tendency under charge fluctuation is in consistent with our experimental observation of intermediate spin states.

DFT calculations were performed by Tommaso Gorni and Luca De' Medici at ESPCI. The spin state switching between SF and Kondo regimes is also rationalized by density functional theory (DFT) simulations which are carried out with v. 6.8 of the QUANTUM ESPRESSO package [236, 237] within the Projector Augmented-Wave (PAW) scheme [238] and using the Perdew-Burke-Ernzerhof (PBE) functional [239]. The main idea of our DFT calculation is correctly understand the effect of adatom at elbow site on electronic properties of $\mathrm{Fe-DPyDBrPP}$ molecule that changes the spin state when adsorbed on it.

As we have experimentally proved that adatom at elbow site is the only essential role that drives the spins state switching, thus we can simplify our model by utilising the following assumptions: 1). Omitting surface reconstruction and Au(111) surface is modelled by a finite slab consisting of 3 gold layers with 15Å of vacuum between periodic replicas along the z direction. The Au-Au nearest-neighbor distance has been set to 2.93Å, the PBE equilibrium distance of the corresponding fcc bulk structure. 2). Adatom at elbow site is modelled by an impurity adsorbed on Au(111) surface. 3). Interaction between adatom with $\mathrm{Fe-DPyDBrPP}$ molecule can only occur between adatom and center Fe atom because of assumption 2). where π orbital of macrocycle can not hybridize with Au(111) surface due to large distance.

The adsorption geometry of $\mathrm{Fe-DPyDBrPP}$ molecule on Au(111) surface with an underneath adatom is illustrated in Fig. 3.11. The non-planar saddling distortion of porphine macrocycle is also produced in DFT simulation shown in Fig. 3.11 (b) which is in agreement with the experimental topography images. We also observe that the center Fe atom in the macrocycle (big red sphere) is attracted by the adatom on Au(111) surface (Br atom in Fig. 3.11 (b)), this is also in coordinate with the attractive potential at elbow site.

To understand the effect of underneath adatom on electronic properties of $\mathrm{Fe-DPyDBrPP}$ molecule, we first present the total charge and magnetic moment of Fe(3d) atom as a function of the distance from the substrate for three different substrates: 1). No adatom (Bare Au(111)).

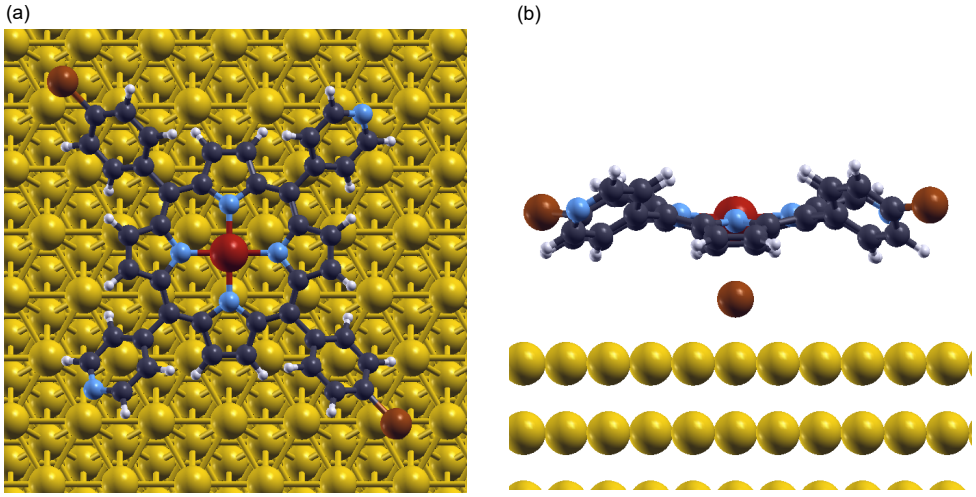

Figure 3.11: Adsorption geometry of $\mathrm{Fe-DPyDBrPP}$ **monomer on adatom at elbow site obtained by DFT.** (a) Top view of $\mathrm{Fe-DPyDBrPP}$ monomer on Au(111) surface. Sphere of different colors and sizes represent different atoms with Red: Fe, Blue: N, Black: C, White: H, Brown: Br, Yellow: Au. (b) Side view of $\mathrm{Fe-DPyDBrPP}$, the adatom at elbow site is chosen as Br atom that lies between surface Au atom and center Fe atom.

2). Au adatom. 3). Br adatom. Au and Br adatom are respectively at 2.16Å and 2.23Å from the Au(111) surface. The calculated results by DFT are shown in Fig. 3.12.

Fig. 3.12 (a) shows the total occupation of Fe 3d levels that refers to the amount of charge that Fe 3d levels posses. Here we see that as distance decreases, the charge transfers to Fe atom, if there exists an underneath adatom (Au or Br) the charge transfer effect can be more efficient. This can be easily understood that if Fe-Au(111) distance decreases the hybridization becomes stronger there would be more charge transferred to Fe levels, if with the help of additional adatom that connects Fe and substrate Au atom the hybridization would be stronger.

Fig. 3.12 (b) shows the orbital polarization of Fe 3d orbital, it shows the magnetic moment of the molecule. As the distance decreases the polarization decreases as well, indicating that the charge transferred to molecule reduces the total magnetic moment. In presence of adatom, the polarization decreases faster than non-adatom case, this has the same explanation as occupation scenario where hybridization is stronger.

When molecule is far from the adatom site, i.e. on clean Au(111) surface, the total occupation and polarization are plotted in purple curves in Fig. 3.12. No matter at small or large distance from the Au(111) substrate the occupation and polarization are about $6.4e^{-}$ and $2.3\mu_B$ respectively, indicating that $\mathrm{Fe-DPyDBrPP}$ interacts poorly with Au(111) substrate and S = 1 (Fe^{2+}) spin state (SF regime) is preserved. This is in agreement with our experimental observation that $\mathrm{Fe-DPyDBrPP}$ molecules in fcc or hcp regions all show spin-1 SF feature.

When the molecule is on top of the adatom (elbow site in experiment), total charge and polarization become sensitive to the distance between molecule with substrate. At 5Å the occupation and polarization is almost the same as on clean Au(111) surface, by moving Fe of 1Å closer to the surface, it accepts around $0.4e^{-}$ charge from the substrate, and the total magnetic moment suddenly decreases to $1.5\mu_B$ and $0.8\mu_B$ for Au and Br adatom respectively. The latter one corre-

spond to the Kondo regime we found in experiment. This can explain the Kondo effect occurring for $\mathrm{Fe-DPyDBrPP}$ on top of adatom: when $\mathrm{Fe-DPyDBrPP}$ is moved to the elbow site, it feels the attractive potential and center Fe atom moves closer to the Au(111) surface, with the help of Br-adatom at the elbow site, Fe atom strongly couples with Au(111) substrate, resulting spin state switching from SF regime to Kondo regime.

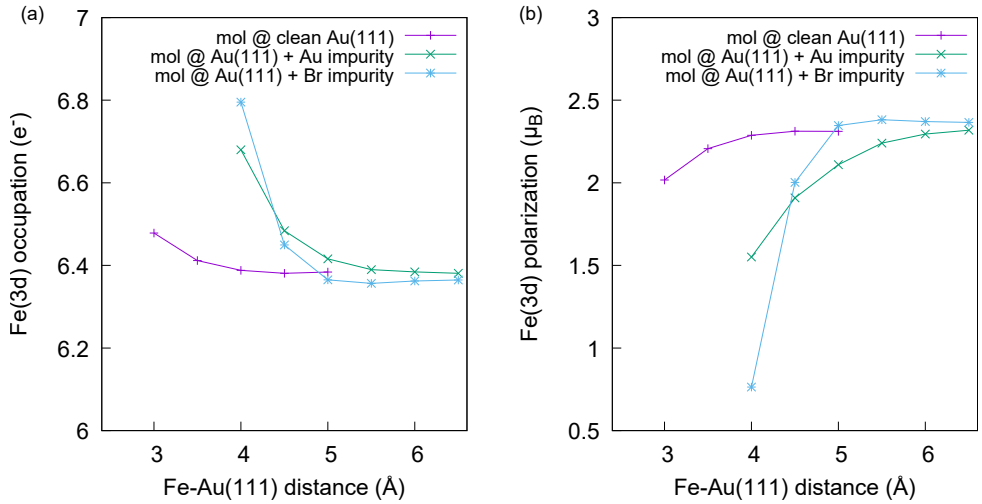

Figure 3.12: Total charge and magnetic moment of center Fe atom. (a) Total Fe(3d) charge as function of distance from the substrate, computed for three different substrates where Purple: flat Au(111) surface without adatom, Green: Au(111) surface with Au adatom beneath Fe atom, Blue: Au(111) surface with Br adatom beneath Fe atom. (b) Magnetic moment of center Fe atom as function of distance in these three cases. The charge and magnetization values have been obtained via a Mulliken analysis projecting the Kohn-Sham orbitals over atomic states of the Fe pseudopotential.

Interestingly in Fig. 3.12 (b), it appears that a spin reduction of 1/2 happens, however Fig. 3.12 (a) suggests that $\mathrm{Fe-DPyDBrPP}$ molecule receive only an amount of charge around $0.4e^{-}$, which is not enough to result a spin 1/2 reduction. This indicates that the Kondo effect occurs in our system is a mixed-valence behavior due to charge fluctuation.

To better understand the charge fluctuation effect, we present the DFT results showing occupation and polarization for different 3d orbitals of Fe atom in Fig. 3.13. We observe the total magnetic moment is mainly shared between d_π ($d_{xz/yz}$), d_{z^2} and $d_{x^2-y^2}$ states while d_{xy} are almost fully occupied. As Fe-Au(111) distance decreases, the occupation of d_{z^2} decreases and the occupation of d_π increases. While the other two orbitals almost not change their occupation. Such behavior is related to the orbital geometry property as d_{z^2} or d_π show better z direction extension and should have better hybridization with substrate with respect to d_{xy} and $d_{x^2-y^2}$.

What is important here is the tendency of the reorganization of orbital occupation in d_π and d_{z^2} orbitals. As we have introduced in previous sections that FOA and FOB respectively exhibit the orbital character of d_{z^2} and d_π. The decrease (increase) of occupation of d_{z^2} (d_π) would imply that FOA (FOB) should move towards positive (negative) energy with respect to Fermi level which can also be visualized in projected density of states (PDOS) figure Fig. 3.14 where (a) and (b) respectively illustrate the Kondo and SF case. Furthermore, we will see in the following sections that such shifting of FOA and FOB are experimentally observed in large-range dI/dV spectra.

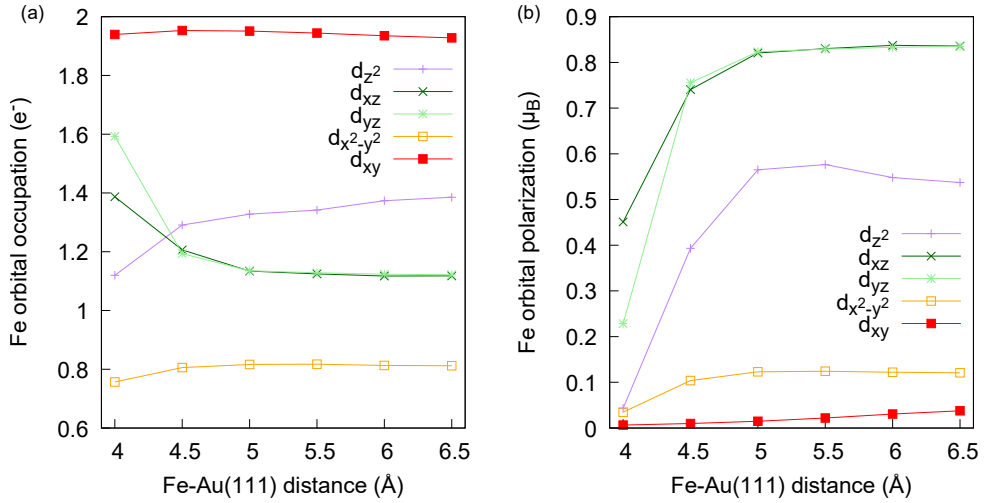

Figure 3.13: Orbital occupation and polarization of center Fe atom on Br-adatom. (a) Orbital occupation of Fe atom as function of distance from the substrate with Br-adatom on Au(111) surface. (b) Orbital polarization of Fe atom as function of distance from the substrate. Occupation and polarization values calculated via same Mulliken analysis as in Fig. 3.12.

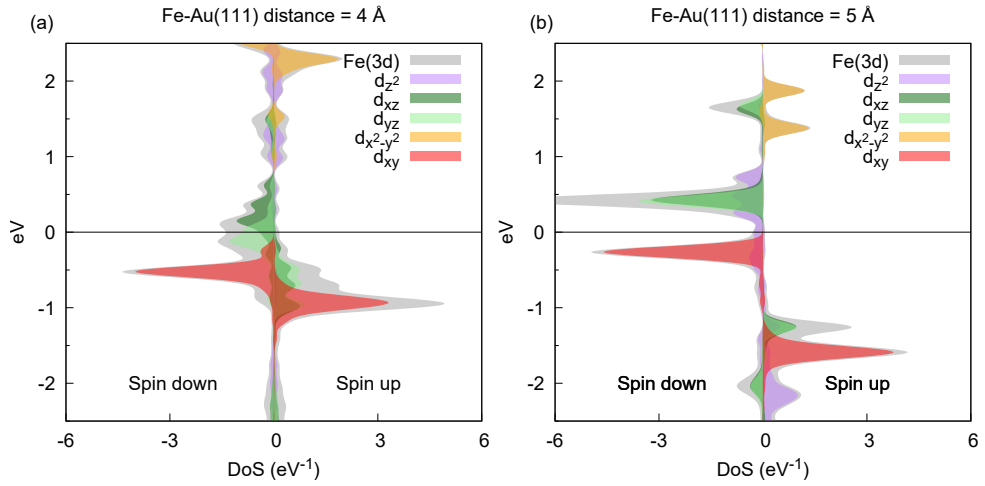

Figure 3.14: PDOS over atomic states of Fe pseudopotential in Kondo and SF cases. (a) PDOS over the atomic states of Fe pseudopotential in the Kondo case where Fe-Au(111) distance is $4\mathring{A}$ with a Br adatom. (a) PDOS over the atomic states of Fe pseudopotential in the SF case where Fe-Au(111) distance is $5\mathring{A}$ with a Br adatom.

We have also calculated non-zero square hopping between Fe(3d) with Br(4s,4p) states in Kondo and SF cases shown in Fig. 3.15. It is shown that the hybridization between Fe states and Br states are mainly contributed from $3d_{z^2} \leftrightarrow 4s$, $3d_{z^2} \leftrightarrow 4p_z$, $3d_{xz} \leftrightarrow 4p_x$ and $3d_{xy} \leftrightarrow 4p_y$ orbitals. In SF regime, the hybridization is weak while in Kondo regime, the hybridization between these orbitals greatly increase among which $3d_{z^2}$ offers the most contribution ($3d_{z^2} \leftrightarrow 4s$ and $3d_{z^2} \leftrightarrow 4p_z$). This result is in agreement that Kondo peak in is invariant against rotation shown in Fig. 3.9 as $3d_{z^2}$ possesses rotation symmetry.

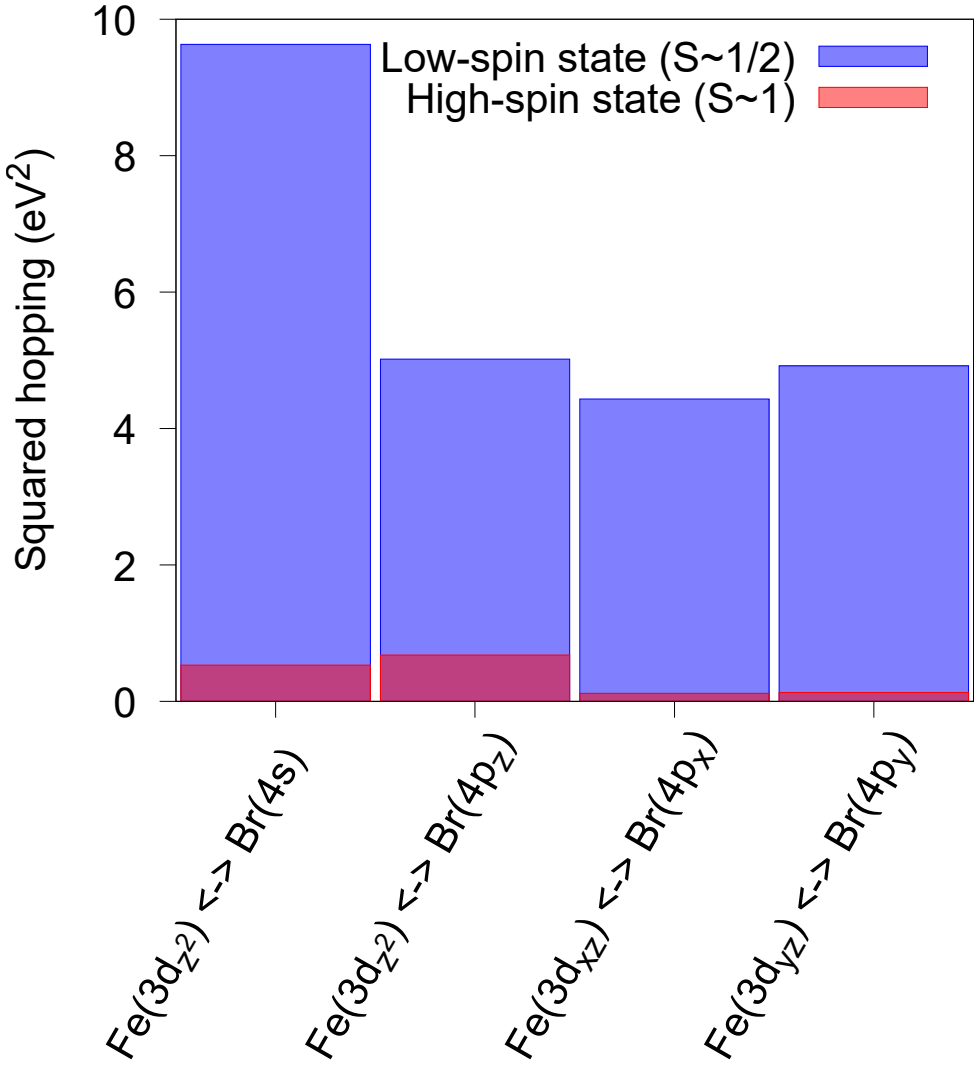

Figure 3.15: Calculated non-zero square hopping between Fe(3d) with Br(4s,4p) states in Kondo and SF cases. Calculated non-zero squared hopping between the Fe(3d) and the Br(4s,4p) states in the Kondo (Fe-Au(111) distance = 4.0Å, in blue) and SF (Fe-Au(111) distance = 5.0Å, in red) case. Only the squared average of the spin-up and spin-down hopping is reported, since no significant difference has been found in the two channels.

3.7 Crossover

In this section we will study the detail of spin state switching by examining the configurations of $\mathrm{Fe-DPyDBrPP}$ trimer in the regimes between spin-1 SF and Kondo regime where we can clearly see that the SF step feature evolves to a Fano-like feature as predicted by David Jacob (see section (1.2.5)) due to the charge fluctuation effect and finally to a Kondo peak as a result of complete quench of magnetic anisotropy. Accompanied with the low-energy excitation spectra evolution, the frontier molecular orbitals (FOB and FOA) also shift in energy simultaneously just as predicted by DFT calculations.

Fig. 3.16 shows a $\mathrm{Fe-DPyDBrPP}$ trimer on Au(111) surface where Fig. 3.16 (a) and (d) are SF (red curve) and Kondo (orange curve) regimes molecule as we have seen before. Fig. 3.16 (b) and (c) shows two intermediate regimes where the left $\mathrm{Fe-DPyDBrPP}$ molecule is close to the adatom at elbow site but the center Fe atom is not exactly on top of it. From Fig. 3.16

(a) to (d), the complete scenario of the transition from a SF regime (S = 1) to Kondo regime is portrayed. The large-range and low-range dI/dV spectra measured on the bright pyrrole location of the left-most molecule in these four regimes are shown in Fig. 3.16 (e) and (f).

Molecule in Fig. 3.16 (a) reproduces the SF regime where we observe FOB at $+150$ meV and SF step feature near Fermi level of energy ± 10 meV (red curve in Fig. 3.16 (e-f)), so that molecule has spin-1 spin state.

Fig. 3.16 (b) shows the case where the upper pyrrole of left molecule is on top of the elbow site, in dI/dV spectra (green curve) we observe the FOB that was at $+150$ meV for red curve moves to around 30 meV which is slightly above Fermi level. Accompanied with the decrease of FOB energy the low-range spectra shows a deformed shape of SF step feature where the right step shifts towards zero bias at 5 mV and a bulge emerges at -5 mV that breaks the symmetric step shape. This shape is theoretically predicted by David Jacob (see section (1.2.5) and ref. [240]), indicating the charge fluctuation begins to occur to S = 1 system and the decreasing of FOB's energy also verifies that. We call this regime intermediate regime 1 (IR1).

In Fig. 3.16 (c) we have moved the left-most molecule even closer to the elbow site. The dI/dV spectra for this case is plotted as blue curves in Fig. 3.16 (e-f), interestingly, the original FOB that was above Fermi level now moves to around -10 meV that is just beneath Fermi level. In this case we expect a strong charge fluctuation and the low-range spectra shows a Fano-like line shape, which is usually regarded as the hallmark of Kondo effect nevertheless, here we still believe it has SF origin but with a strong charge fluctuation. We call this intermediate regime 2 (IR2).

Fig. 3.16 (d) reproduces the Kondo regimes that we have already seen where FOB locates at -100 meV with an obvious low-energy Kondo feature (orange curves).

dI/dV spectra presented until now are measured on bright pyrrole rings where the pyrrole states show a dominant spectral weight and we might not distinguish the evolution of the central point-like FOA observed in Fig. 3.5 (d). Hence we plot the dI/dV spectra measured at the Fe atom of the left-most molecule in Fig. 3.17 and compare them with the spectra measured at the upper pyrrole rings presented in Fig. 3.16.

In large-range dI/dV spectra illustrated in Fig. 3.17 (e), we can distinguish the peak at negative bias that corresponds to the FOA of the molecule. For SF regime, the FOA peak locates at -150 meV (red curve) as observed before. When the molecule is moved closer to elbow site and enters IR1 regime, FOA shifts towards Fermi level as well just like FOB does (green curve). When molecule enters IR2 (blue curve), both FOA and FOB arrive at Fermi level and merge with each other. For Kondo regime case (orange curve), the spectrum is similar to that measured on pyrrole ring, indicating that FOA contribution is suppressed.

For the low-range spectra measured at center Fe atom shown in Fig. 3.17 (f), the SF (red curve) and Kondo (orange curve) have been studied already, in which we observe same excitation energy (SF energy and Kondo width) over single molecule but with asymmetric lineshape for measurements taken on upper pyrrole ring. The asymmetric lineshape is explained by the different background contribution of FOB and FOA. For intermediate regimes IR1 (green curve)

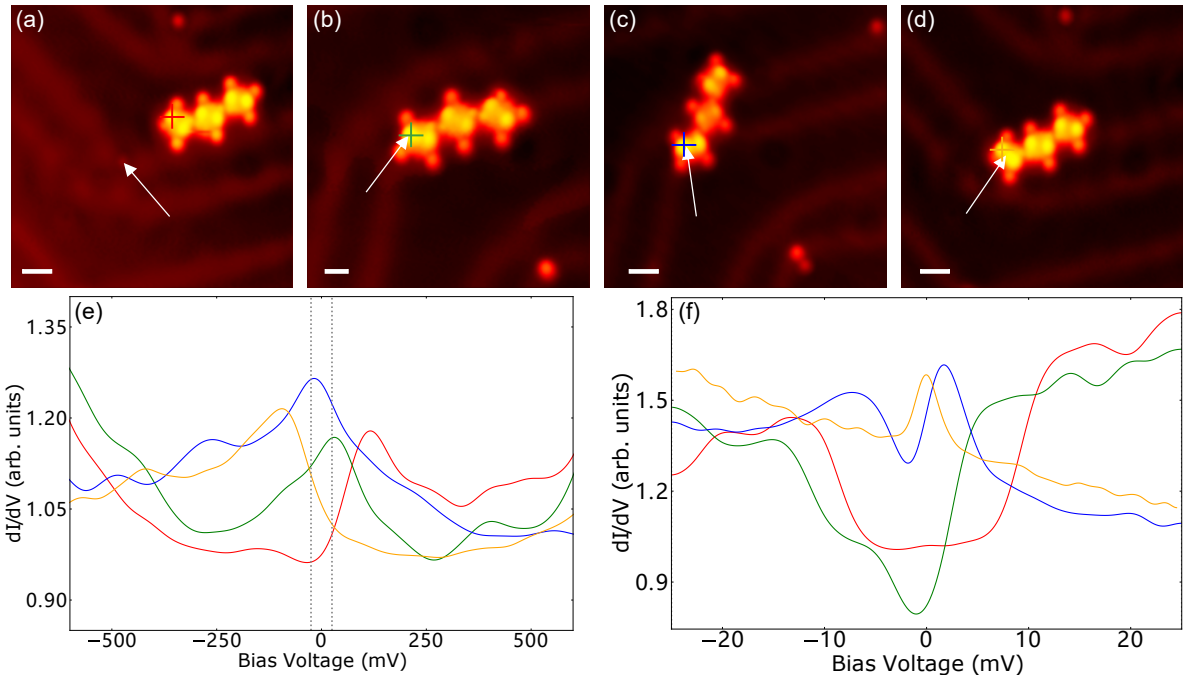

Figure 3.16: Intermediate regimes of $\mathrm{Fe-DPyDBrPP}$ **molecule.** (a-d) Topography image (bar represents $2nm$, setpoint: 125 mV, 20 pA for (a)(d), 200 mV, 100 pA for (b)(c)) of a covalently bonded trimer of $\mathrm{Fe-DPyDBrPP}$ molecules in different configurations on Au(111) surface. (a), (d) are SF and Kondo regimes. (b), (c) are intermediate regimes where charge fluctuation occurs. Crosses mark the upper pyrrole rings of left molecule where dI/dV spectra are taken, white arrow aims at adatom at elbow site of herringbone reconstruction of Au(111) surface. (e) Large-range dI/dV spectra of marked $\mathrm{Fe-DPyDBrPP}$ molecule with same colors in (a)-(d) (Setpoint: 800 mV, 500 pA. Lock-in parameters: $V_m = 5$ mV, $f = 900$ Hz). (f) High-resolution dI/dV spectra in voltage window between gray dashed lines marked in (e). Setpoint: 30 mV, 200 pA. Lock-in parameters: $V_m = 0.2$ mV, $f = 750$ Hz. All data are smoothed, normalised and plotted by continuum curves.

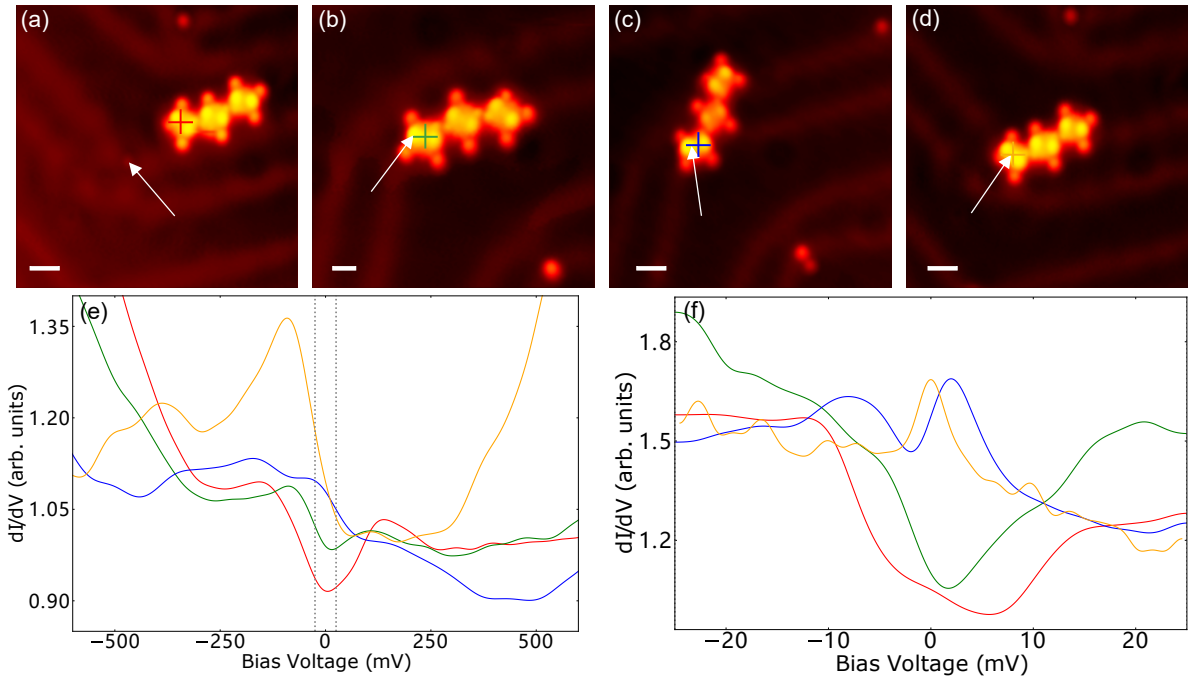

Figure 3.17: Intermediate regimes of $\mathrm{Fe-DPyDBrPP}$ **molecule.** (a-d) Topography image (bar represents $2nm$, setpoint: 125 mV, 20 pA for (a)(d), 200 mV, 100 pA for (b)(c)) of a covalently bonded trimer of $\mathrm{Fe-DPyDBrPP}$ molecules in different configurations on Au(111) surface. (a), (d) are SF and Kondo regimes. (b), (c) are intermediate regimes where charge fluctuation occurs. Crosses mark the center Fe atom of left molecule where dI/dV spectra are taken, white arrow aims at adatom at elbow site of herringbone reconstruction of Au(111) surface. (e) Large-range dI/dV spectra of marked $\mathrm{Fe-DPyDBrPP}$ molecule with same colors in (a)-(d) (Setpoint: 800 mV, 500 pA. Lock-in parameters: $V_m = 5$ mV, $f = 900$ Hz). (f) High-resolution dI/dV spectra in voltage window between gray dashed lines marked in (e). Setpoint: 30 mV, 200 pA. Lock-in parameters: $V_m = 0.2$ mV, $f = 750$ Hz. All data are smoothed, normalised and plotted by continuum curves.

and IR2 (blue curve), IR1 shows a strong variation depending on the measurement location while IR2 seems to be less effected. For IR1, this is in agreement that FOB and FOA are very close to Fermi level for IR1, leading to a strong asymmetric background to the low-range spectra. While for IR2 we can only observe two lobes shape FOB beneath Fermi level that contributes to background.

By comparing large-range and low-range spectral shape in Fig. 3.16 (e-f) and Fig. 3.17 (e-f), we also notice that the low-energy excitation spectra appear to be intimately related to the energy and spectral weight of both FOB and FOA. Their relation will be discussed in detail in following sections.

So far we have introduced two intermediate regimes (IR1 and IR2) that exhibit mixed-valence excitation feature of $\mathrm{Fe-DPyDBrPP}$ molecule between well defined spin-1 SF regime and Kondo regime. All these four regimes together describe a spin crossover phenomena for $\mathrm{Fe-DPyDBrPP}$ molecule on Au(111) surface.

3.7.1 Spin-Flip Regime and Intermediate Regime 1

To better understand the interplay between molecular orbital and low-energy excitation spectra in mixed-valence regimes, we will study dI/dV maps which allows us to directly visualise the

molecular orbital for both large-range and low-range spectra.

We start with the dI/dV map of $\mathrm{Fe-DPyDBrPP}$ trimer molecule shown in Fig. 3.16 (b) where the left molecule is in IR1 regime and two molecules on the right are in SF regime.

Fig. 3.18 compares the large-range dI/dV map between SF and IR1 molecules where we can distinguish the evolution of two lobes shape FOB and point-like FOA. While Fig. 3.19 shows the low-range dI/dV map where we can distinguish the molecule orbitals that give rise to SF and bulge feature that we have observed in Fig. 3.16 (f).

Fig. 3.18 (b) shows spatial variation of dI/dV along the purple arrow crossing SF molecule shown in (a). The dI/dV spectra measured on red, green and blue crosses points are marked in (b) by dashed lines and plotted in (c) with the corresponding colors. The vertical black dashed lines in (b) and (c) indicate following the voltage : $-200\,\mathrm{mV}$, $-100\,\mathrm{mV}$, $100\,\mathrm{mV}$ and $200\,\mathrm{mV}$, the dI/dV maps corresponding to these voltages are shown in (g-j). While (d-f) are the same as (a-c) but for the IR1 molecule on the left.

From Fig. 3.18 (b) we can easily observe that for SF molecule, FOB is mainly spanning on upper pyrrole rings (red and blue dashed lines) at around $+100\,\mathrm{meV}$ while FOA is mainly spanning on the Fe atom (green line) at energy around $-100\,\mathrm{meV}$. Their spatial distribution can be directly observed in (h) and (i) in red dashed SF molecule outline where FOB has two lobes shape and FOA has point-like shape. (e) shows dI/dV spectra across the IR1 molecule in which both FOB and FOA shift toward Fermi level. FOB shifts to $+50\,\mathrm{meV}$ while FOA to $-50\,\mathrm{meV}$.

Fig. 3.19 shows the low-energy cases. (g) is the dI/dV map measured at $0\,\mathrm{mV}$, i.e. inside SF gap, corresponding to energies lower to the spin-flip excitation energies. (h-m) show composite artificial dI/dV maps made by subtracting the dI/dV map taken at $0\,\mathrm{mV}$ from their original contrast. The subtraction process reveals only the inelastic channels opened by the spin-flipping processes and thus allows to identify the spatial distribution of the inelastic effects in order to associate the involved orbitals.

We first study the low-range spectra for SF molecule marked red dashed outline. At voltage window between $\pm 9.3\,\mathrm{mV}$ (Fig. 3.19 (j)(k)), the region marked with a red dashed line shows no features because we are inside the SF gap and therefore no spin-flip channel exists. At energy of $\pm 9.3\,\mathrm{mV}$ (Fig. 3.19 (i)(l)) and $\pm 15\,\mathrm{mV}$ (Fig. 3.19 (h)(m)), we see the two lobes shape at upper pyrrole rings for positive and negative energy with absolute value larger than $9.3\,\mathrm{mV}$. The point feature at center exhibits strong spectral weight at negative energies smaller than $-9.3\,\mathrm{mV}$ while at positive energy it shows a rather weak feature.

Comparing what we have observed with the large-range data shown in Fig. 3.18 (g-j), the two lobes shape and point-like shape correspond to FOB and FOA that locate on upper pyrrole rings and Fe center respectively. This means that FOB and FOA are responsible for inelastic spin excitation at low-energy. Interestingly, both two lobes shape FOB located at $100\,\mathrm{meV}$ and point-like FOA located at $-100\,\mathrm{meV}$ extend through Fermi level. This indicates the existence of mixed-valence property.

Then we start to analyze the IR1 molecule in green dashed outline in the same way. In large-range spectra we observe that FOB and FOA both shift closer to Fermi level and locate at

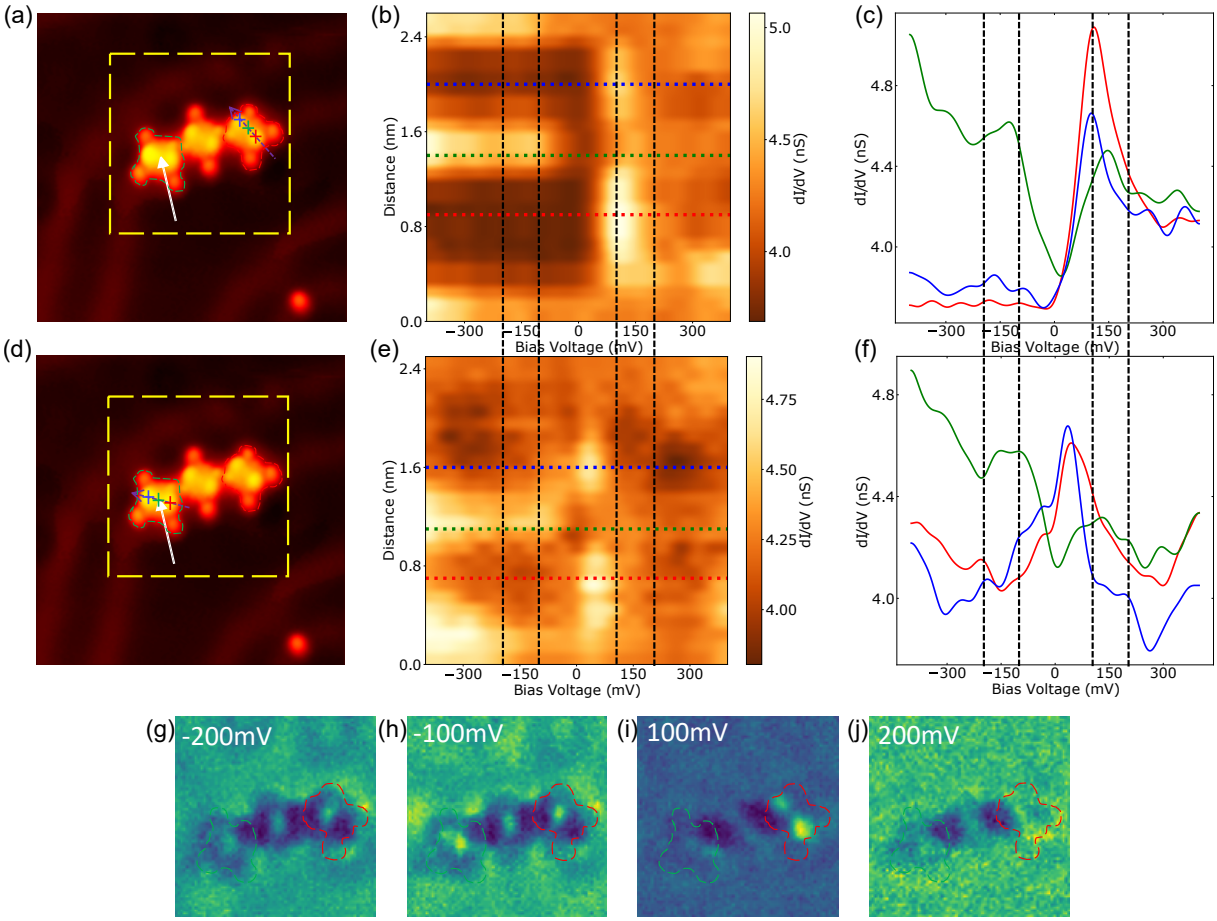

Figure 3.18: Large-range dI/dV map of $\mathrm{Fe-DPyDBrPP}$ molecule in IR1 and SF regimes. (a)(d) Topography image ($12\mathrm{x}12\mathrm{nm}^2$, setpoint: 200 mV, 100 pA) of a covalently bonded trimer of $\mathrm{Fe-DPyDBrPP}$ molecules on Au(111) surface where the left molecule is in IR1 regime while two others are in SF regime. Outline of IR1 and SF molecule are marked by dashed green and red lines respectively. White arrow aims at adatom at elbow site of herringbone reconstruction of Au(111) surface. (b)(e) Stacking plot of point dI/dV spectra (Setpoint: 800 mV, 500 pA. Lock-in parameters: $V_m = 5$ mV, $f = 900$ Hz.) along the purple dashed arrows over $\mathrm{Fe-DPyDBrPP}$ molecule in (a)(d). Red, green and blue dash lines mark the positions with crosses of same colors in (a)(d). (c)(f) Large-range dI/dV spectra measured at crosses position with same colors in (a)(d). (g-j) dI/dV maps of yellow dashed square region in (a)(d) at voltage of ± 200 mV and ± 100 mV labeled by vertical black dashed lines in (b), (c), (e), (f).

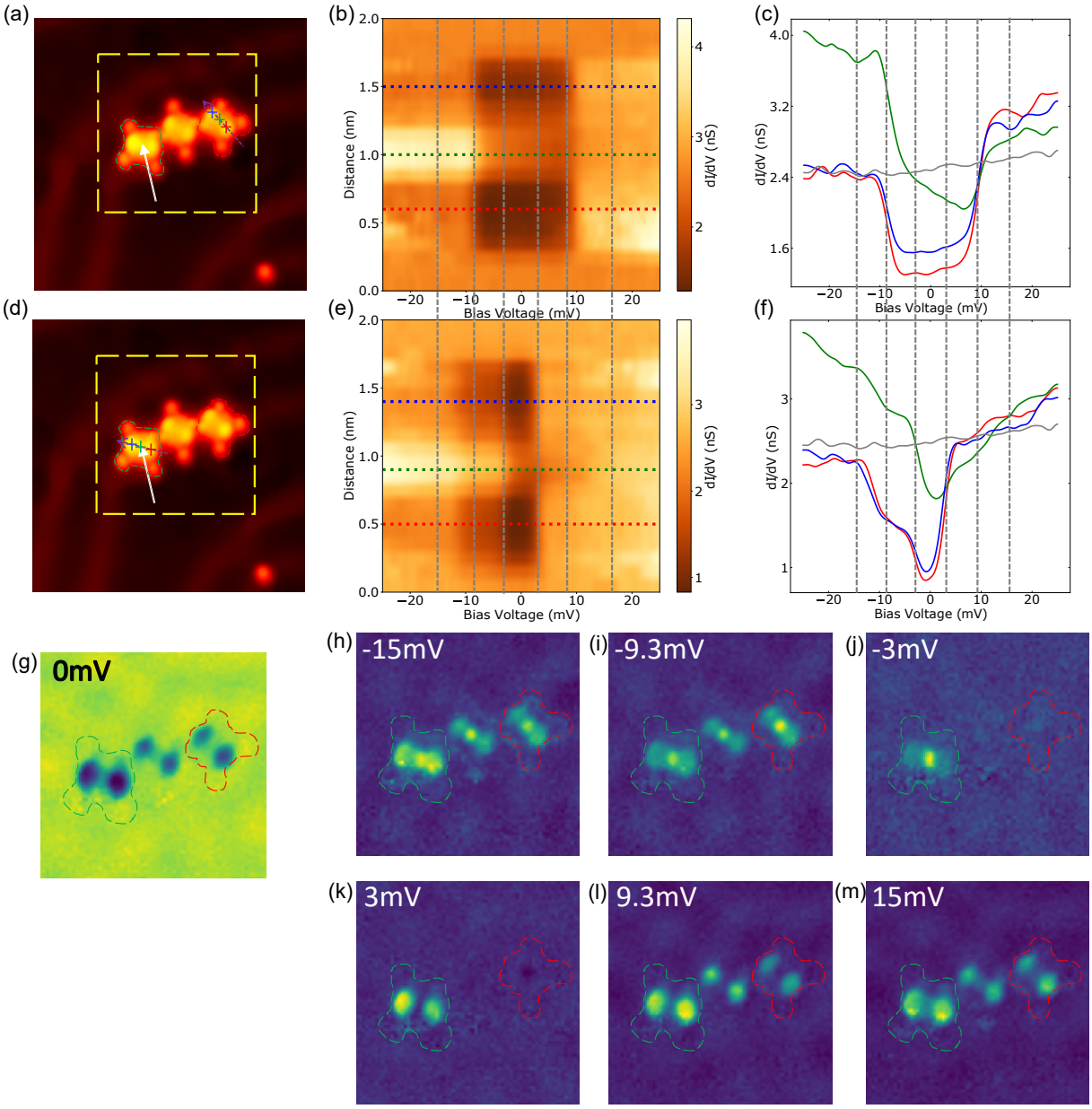

Figure 3.19: Low-range dI/dV map of $\mathrm{Fe-DPyDBrPP}$ molecule in IR1 and SF regimes. (a)(d) Topography image ($12\mathrm{x}12\mathrm{nm}^2$, setpoint: 200 mV, 100 pA) of a covalently bonded trimer of $\mathrm{Fe-DPyDBrPP}$ molecules on Au(111) surface where the left molecule is in IR1 regime while two others are in SF regime. Outline of IR1 and SF molecule are marked by dashed green and red lines respectively. White arrow aims at adatom at elbow site of herringbone reconstruction of Au(111) surface. (b)(e) Stacking plot of point dI/dV spectra, setpoint: 30 mV, 200 pA. Lock-in parameters: ($V_m = 0.2$ mV, $f = 750$ Hz.)) along the purple dashed arrows over $\mathrm{Fe-DPyDBrPP}$ molecule in (a)(d). Red, green and blue dash lines mark the positions with crosses of same colors in (a)(d). (c)(f) Low-range dI/dV spectra measured at crosses position with same colors in (a)(d). Gray line denotes the background. (g) dI/dV map of yellow dashed square region in (a)(d) at 0 mV. (h-m) Composite artificial dI/dV maps made by subtracting dI/dV map (g) from their original contrast. The voltages are labeled inside the images and are also marked by vertical gray dashed lines in (b), (c), (e), (f).

50 meV and -50 meV approximately. Along with the closing of FOA-FOB gap, the SF gap that is related to magnetic anisotropy is reduced as well so that we have non-null signal at energy ± 3 mV with the same pattern as for the SF molecules in red dashed outline but with much lower characteristic energy. The bulge inside SF gap at -5 mV shows a strong point-like feature (Fig. 3.19 (j)), while at gap edge and outside the gap (Fig. 3.19 (i)(h)) the feature is similar to SF molecule in red dashed outline.

The shifting of FOB and FOA energies, the reduction of magnetic anisotropy and deformed SF lineshape are in agreement with David Jacob's work [240] and our DFT calculation (see section (3.6.4)). The decreasing/increasing of orbital occupancy on d_{z^2} (FOA)/d_π (FOB) which is initially below/above Fermi level shifts towards Fermi level. As a consequence, charge fluctuation becomes more important. Charge fluctuation also renormalises magnetic anisotropy that is responsible for a smaller SF gap and results asymmetric SF feature in low-range spectra as the IR1 lineshape shown in Fig. 3.19 (f).

Hence the low-range spectral feature (SF and IR1) can be understood in such way: Two spin polarized molecular frontier orbitals with energies closest to the Fermi level in positive (FOB) and negative (FOA) energy extend through the Fermi level and energetically "overlap" with each other. As a result of such overlap, the low-energy excitation feature that succeeds their orbital shapes is generated. Depending on their position with respect to Fermi level the low-energy excitation feature can behave differently. In other words, the molecular orbitals position controls charge fluctuation between them, which further determine the magnetic properties.

3.7.2 Intermediate Regime 2

Now we begin the study on $\mathrm{Fe-DPyDBrPP}$ molecule in IR2 regime where two molecular frontier orbitals merge at Fermi level and low-range spectra shows no more step shape. We will adopt the same manner of investigation as IR1 to study IR2 molecule.

Fig. 3.20 (a) shows a $\mathrm{Fe-DPyDBrPP}$ molecule in IR2 regime, as we have demonstrated that the monomer and trimer electronic properties are the same, the results obtained from monomer will not contradict what we have observed in trimer case shown in Fig. 3.16 and Fig. 3.17.

In Fig. 3.20 (b), we observe two strong peaks located at upper pyrrole rings (blue and red dash lines) close to zero bias, as we have seen before, this is the two lobes shape FOB which is shown in dI/dV maps (d-h). FOB was above Fermi level for SF and IR1 regime molecule (Fig. 3.18 (b)(e)) but now it shifts slightly beneath Fermi level. By following the green dashed line that shows the dI/dV spectra measured at center Fe site in (a), we observed that point-like FOA is no longer observable neither in dI/dV spectra (c) nor in dI/dV map (d-h).

Fig. 3.21 is dedicated to the low-energy case of IR2 molecule. Along with molecular orbital behavior where two lobes shape orbital shifts to Fermi level and point-like shape orbital vanishes, the low-range spectra exhibits Fano-like lineshape where we see a dip at -2 mV and a peak at 2 mV. (d) presents the dI/dV map measured at -2 mV which is related to the dip of Fano-like feature in (c). (e-j) are composite artificial dI/dV maps made by subtracting dI/dV map at -2 mV from their original contrast.

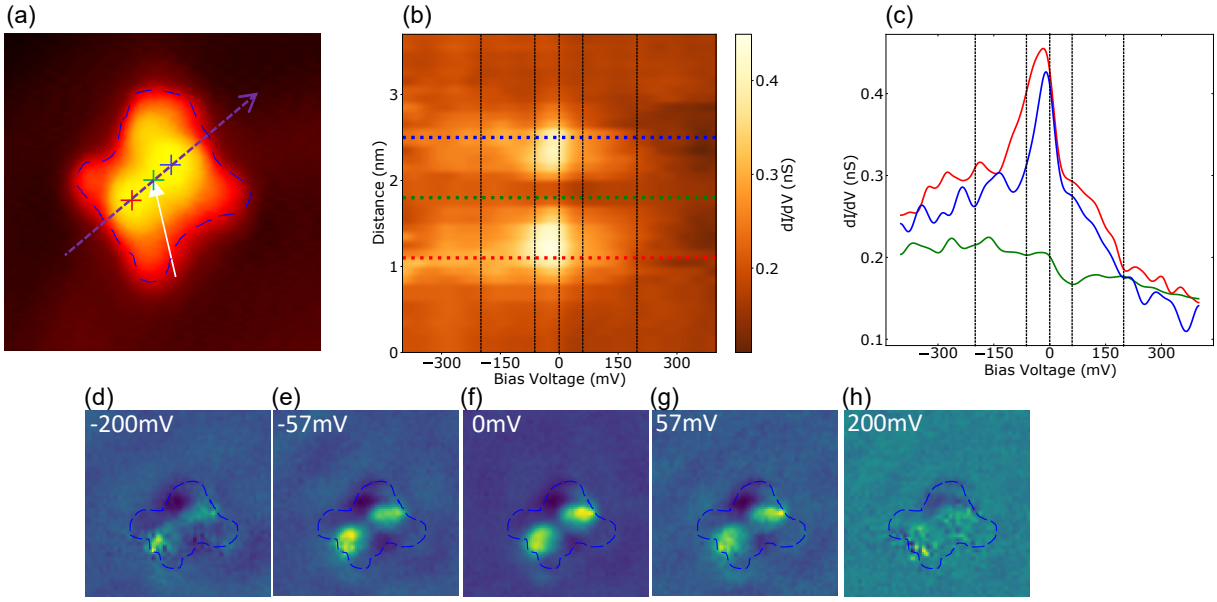

Figure 3.20: Large-range dI/dV map of $\mathrm{Fe-DPyDBrPP}$ monomer in IR2. (a) Topography image ($5\mathrm{x}5\mathrm{nm}^2$, setpoint: 500 mV, 2 pA) of a IR2 $\mathrm{Fe-DPyDBrPP}$ monomer on Au(111) surface. (b) Stacking plot of point dI/dV spectra (Setpoint: 800 mV, 30 pA. Lock-in parameters: $V_m = 5$ mV, $f = 900$ Hz.) along the purple dashed arrow over IR2 $\mathrm{Fe-DPyDBrPP}$ molecule in (a). Red, green and blue dash lines mark the positions with crosses of same colors in (a). (c) Large-range dI/dV spectra measured at crosses position with same colors in (a). (d-h) dI/dV maps of IR2 $\mathrm{Fe-DPyDBrPP}$ monomer in (a) at energies of ± 200 mV, ± 58 mV and 0 mV labeled by vertical black dashed lines in (b)(c).

In these dI/dV maps (e-j), the two lobes pattern that is very similar to two lobes molecular orbital shown in Fig. 3.20 (d-h). But we notice that at positive voltages (2 mV, 5 mV) the solid two lobes shape become hollow at the center. We have also observed this kind of hollowing for IR1 molecule at positive energy (green dashed outline in Fig. 3.19 (m)) as well. The emerging of vacancy at the center of pyrrole rings is very puzzling. Its origin could be a derivative effect in STS experiments i.e. an artifact, or due to quantum interference that creates a hole in the dI/dV map or other reasons. The first one is less possible because in Fig. 3.19 (m) the SF molecule (red dashed outline) does not exhibit such behavior while IR1 molecule (green dashed outline) does.

By comparing the Fano-like lineshape with low-range spectra in other regimes with same orbital characterization, we can extract more information about the charge fluctuation driven spin state crossover. The peak of Fano-like shape at 2 mV shows two lobes shape in Fig. 3.21 (i), which has the same shape as SF steps or IR1 steps (Fig. 3.19), we might say that this peak is evolved from the right step of IR1 feature (Fig. 3.19). While the dip of Fano-like shape at -2 mV seems to be evolved from the SF gap. If such statement about evolution is true, we could have found a very interesting discovery that the effect of charge fluctuation is to reduce the SF gap width and "push" it to negative energy while the SF step at positive energy evolves to the peak feature which finally becomes Kondo peak. We can verify this tendency by reviewing Kondo regime molecule where charge fluctuation is further developed than IR2. In the Kondo resonance feature shown before (Fig. 3.4 (d), Fig. 3.7 (c), Fig. 3.9 (a) and Fig. 3.10 (b)), there seems always exists a small dip at negative energy side (left side) of Kondo peak. This dip

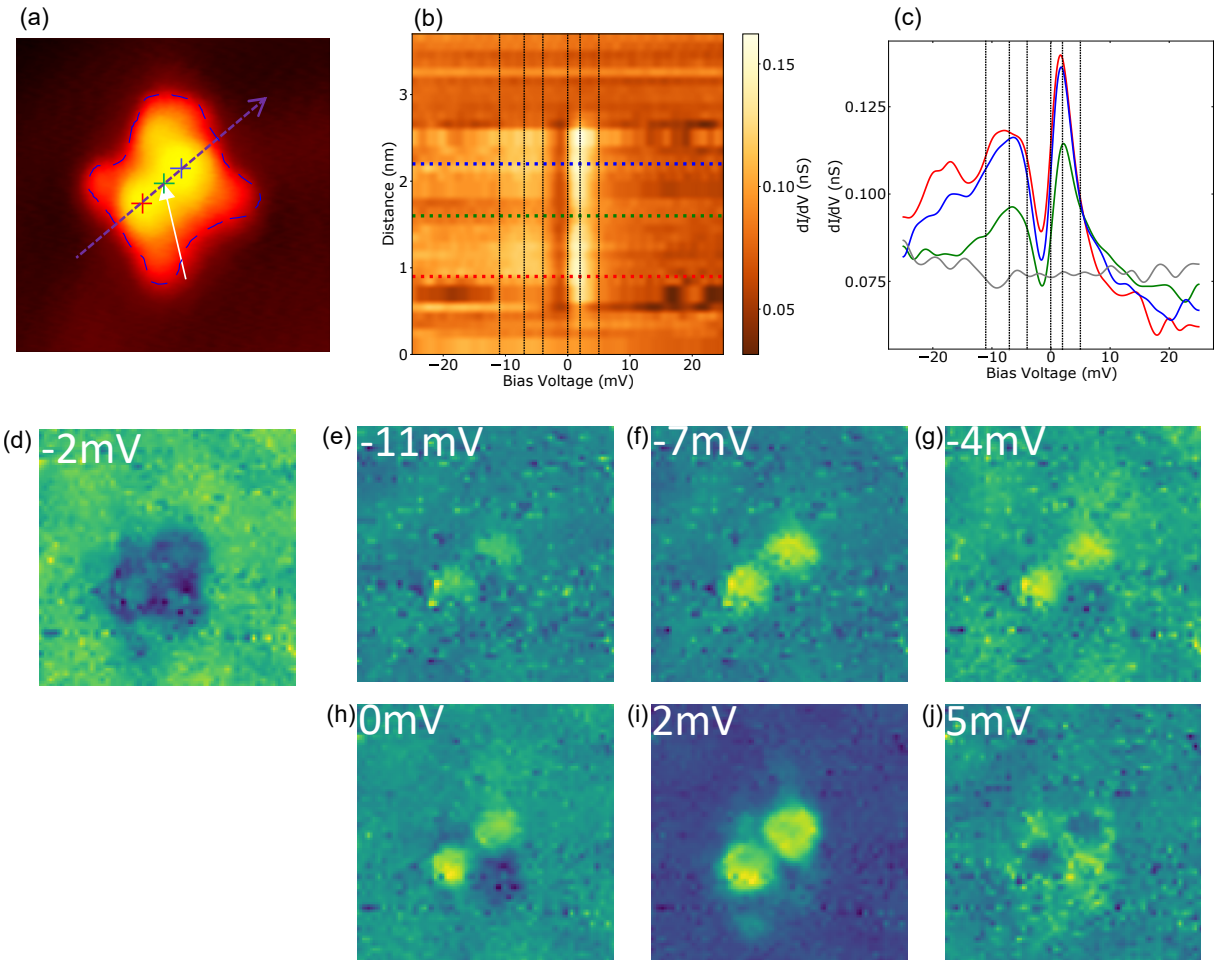

Figure 3.21: Low-range dI/dV map of $\mathrm{Fe-DPyDBrPP}$ monomer in IR2. (a) Topography image ($5\mathrm{x}5\mathrm{nm}^2$, setpoint: 500 mV, 2 pA) of a IR2 $\mathrm{Fe-DPyDBrPP}$ monomer on Au(111) surface. (b) Stacking plot of point dI/dV spectra (Setpoint: 30 mV, 5 pA. Lock-in parameters: $V_m = 0.5$ mV, $f = 750$ Hz.) along the purple dashed arrows over IR2 $\mathrm{Fe-DPyDBrPP}$ molecule in (a). Red, green and blue dash lines mark the positions with crosses of same colors in (a). (c) Low-range dI/dV spectra measured at crosses position with same colors in (a). Gray line denotes the background. (d) dI/dV map of IR2 monomer in (a) at -2 mV. (e-j) Composite artificial dI/dV maps made by subtracting dI/dV map (d) from their original contrast. The bias voltage are labeled inside the images and are also indicated by vertical gray dashed lines in (b)(c).

should be the residual feature of SF gap and the Kondo peak is the result of evolution of peak at 2 mV of Fano-like feature. One can image this evolution process by reviewing the low-energy spectra from red (SF) to green (IR1), blue (IR2) and finally orange (Kondo) curves in Fig. 3.16 (f) again.

3.7.3 Spin state crossover in other systems

It worth mentioning here the studies of FePc molecule deposited on Au(111) surface. FePc molecule is a Phthalocyanine-based molecule introduced in Fig. 1.19, its chemical composition is not too much different from our porphyrin-based molecule. On Au(111) surface, FePc can exhibit a sharp dip feature that lies slightly below Fermi level, which feature has been widely reported in many works, but has been attributed to different kinds of origin explanations. It can be explained as SU (4) Kondo effect [15], as a result of valence fluctuation regime [241], due to the double channel screening [31, 33], as non-Landau Fermi liquid [242] etc...

People have also managed to tune the interaction between FePc with Au(111) surface by tip potential [31], dehydrogenation [33] or FePc orientation with respect to Au(111) [168], and found that the dip feature is evolved from SF step feature when interaction with substrate is stronger (Fig. 3.22). The large-range spectra also reveals a molecular orbital at Fermi surface [172]. All these behavior are in analogues to our results when porphyrin-based molecule is driven from SF to intermediate regimes due to charge fluctuation. But we are not sure whether the dip feature for FePc reflects charge fluctuation driven mixed-valence behavior or not.

In 2017 Ormaza et. al. [166] succeeded in reversibly switching spin of nickelocene (Ni(C5H5)2, Nc) molecule between S = 1 and S = 1/2. They have attached a S = 1 Nc molecule to the STM tip apex and formed an electrode-electrode junction with Cu(100) surface. By tuning the displacement of tip (z) the distance between Nc molecule and Cu(100) surface can be finely controlled. When Nc molecule changes from tunneling to contact regime, a sudden change of low-energy spectra signature from SF to Kondo behavior is observed (Fig. 3.23). Such observation indicates that when contacting with Cu surface, magnetic anisotropy is strongly reduced. The DFT calculation suggests that in contact regime the molecule-surface interaction is enhanced and intra-orbital Coulomb repulsion is reduced. Both effects result a charge reorganization that leads to a reduction of total magnetic moment, which, is responsible for S = 1/2 Kondo behavior. Their findings are in good agreement with our experimental but we believe the Kondo effect is a mixed-valence behavior rather than a S = 1/2 Kondo that is described in atomic limit(3.6).

A recent study of adsorbed Fe atoms on monolayer MoS_2 island on Au(111) [243] has shown that depending on the adsorption sites of Fe atoms, they exhibit the low-energy excitation spectra ranging from inelastic spin excitations (SF), characteristic of negligible exchange and dominant single-ion anisotropy, to a fully developed Kondo resonance, indicating strong exchange and negligible single-ion anisotropy. The evolution of low-energy dI/dV spectra is shown in Fig. 3.24 where the triangular yellow feature is the adsorbed Fe atom, bright part and dark part are respectively maximum and minimum of moiré structure of MoS_2 island. When Fe atom is absorbed at minimum of moiré structure (Fig. 3.24 (a)), the lineshape can be easily understood as mag-

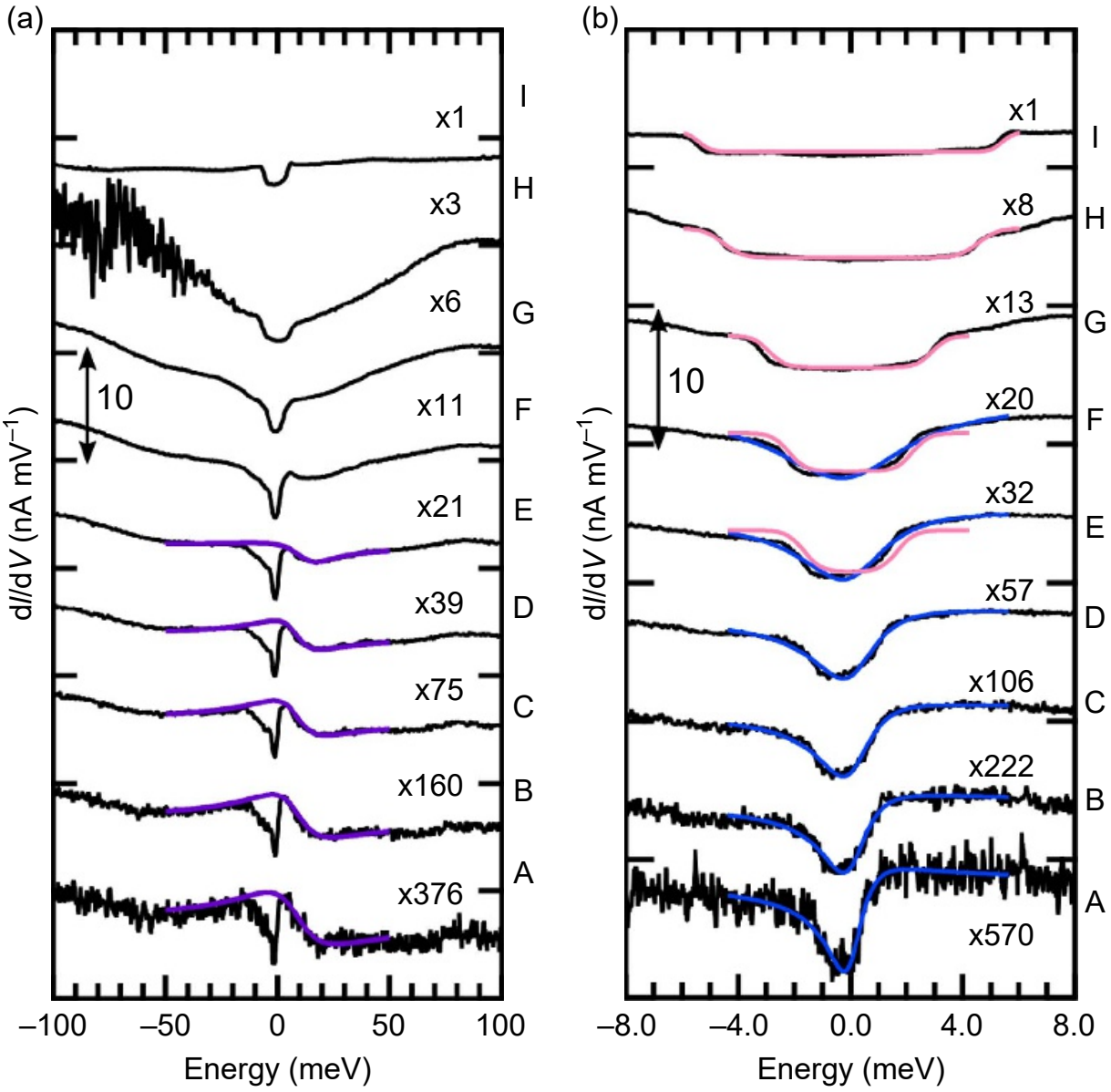

Figure 3.22: Experimental Kondo simulation with approaching an STM tip. (a)(b) Evolution of tunnelling spectra in wide and narrow energy ranges measured at 0.4 K with approaching the STM tip to the center Fe atom of FePc molecule adsorbed on Au(111) surface. The tip positions for each spectra are specified with letters A–I from far to near. When tip is close, a clear SF step lineshape is observed, when tip moves away, SF step feature evolves to dip feature. Pink and blue lineshape are respective calculated by step lineshape and Fano lineshape. Image adapted from [31].

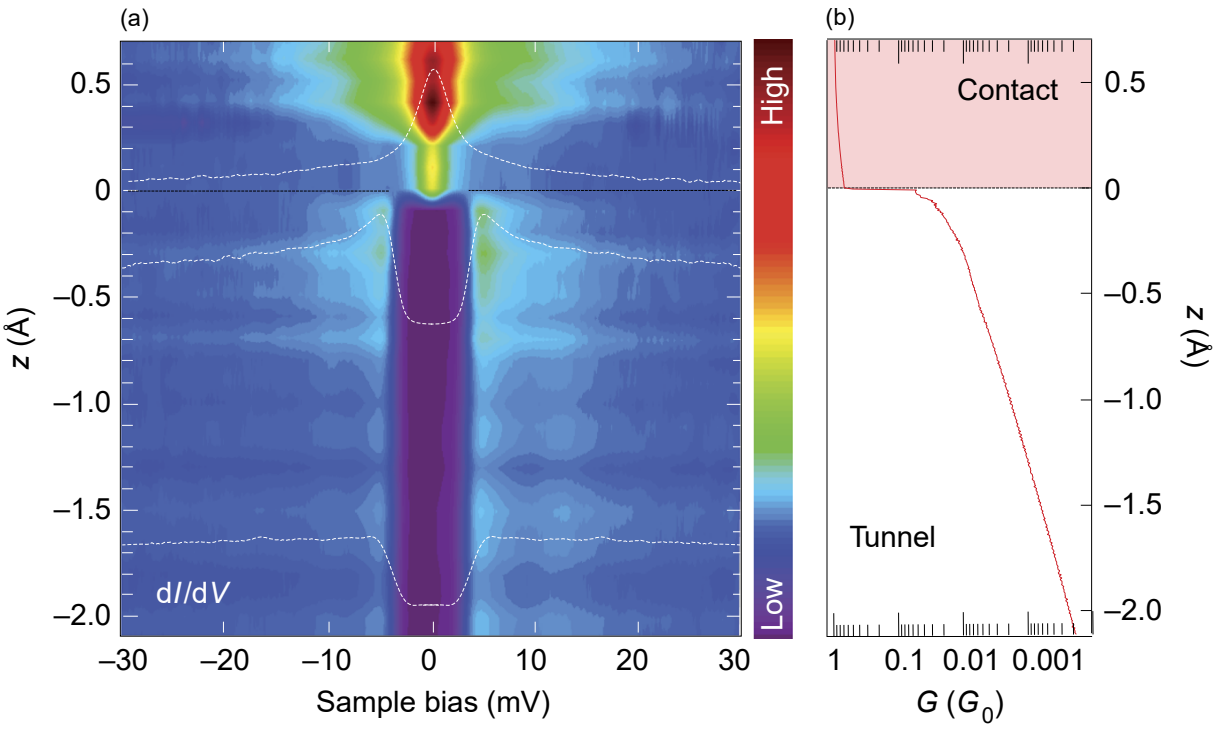

Figure 3.23: Spin state control in metallocene molecular junction. (a) 2D intensity plot of dI/dV spectra acquired with a Nc-tip at increasing z. The intensity of the spectra has been normalized by the opening conductance value (at 30 mV) of the spectrum at z = 0Å. As a guideline to identify the differences, three characteristic spectra (white dashed lines) are superimposed. (b) Conductance (G) vs. tip displacement (z) curve measured at 2 mV for a Nc-tip approaching the Cu(100) surface. The boundary between the tunnel and the contact regime occurs at z = 0 pm and is indicated with a dashed line. Image adapted from [166].

netic anisotropy dominated SF step feature. When adsorption site shifts closer and finally to the maximum of moiré structure (Fig. 3.24 (b-f)), the spectra evolves to a peak feature at Fermi level which is characterized as Kondo resonance. The author contributed the spectra evolution when moving from minimum to maximum site to the increase of exchange coupling ρJ (ρ is the LDOS at adsorption site) and reduction of anisotropy D due to renormalisation. While the asymmetric lineshape behavior is explained as the result of potential scattering of different orbitals when making STS spectra. If it is the case, the lineshape shown in Fig. 3.24 (d)(e) that look similar to our IR1 and IR2 regimes are not mixed-valence behavior and the Kondo feature in Fig. 3.24 (f) could be spin-1 Kondo effect.

3.8 Conclusion

In this chapter we have studied $\mathrm{Fe-DPyDBrPP}$ molecules on Au(111) surface. We have observed different kinds of molecular assemblies including monomers, covalently bonded molecular chain and lattices on different adsorption sites depending on the geometry of Au(111) surface. STS experiments have shown that most of the $\mathrm{Fe-DPyDBrPP}$ shows spin-1 inelastic spin flip excitation dominated by magnetic anisotropy induced by surface, indicating a S = 1 magnetic state. There is no obvious evidence in low-energy excitation spectra that proves the existence of inter-molecular spin-spin interaction occurring between spin-1 $\mathrm{Fe-DPyDBrPP}$ molecules

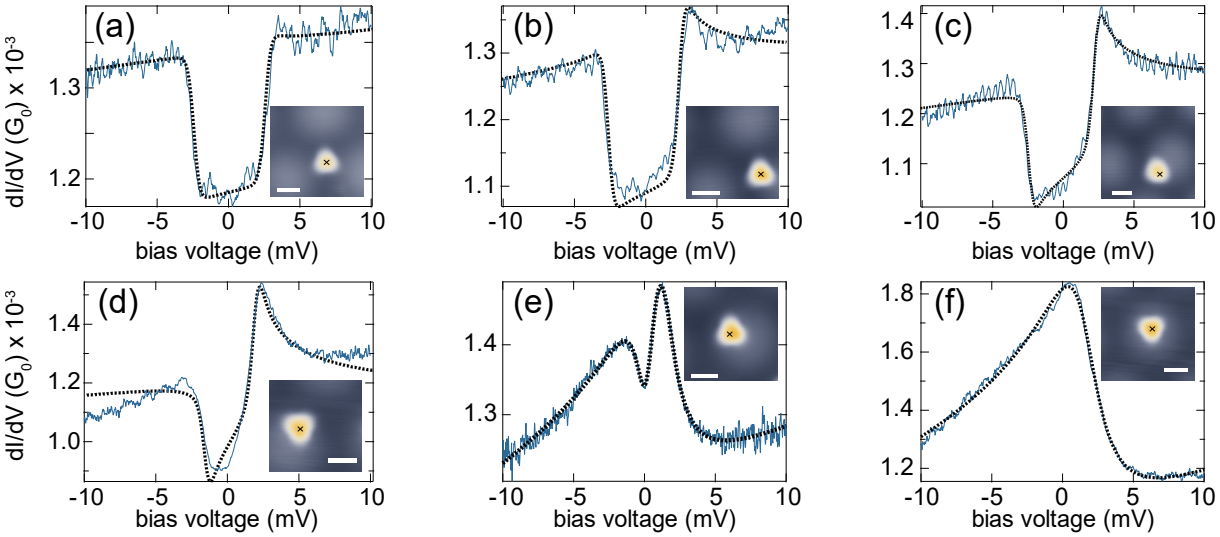

Figure 3.24: Evolution of low-range spectra depending on Fe adsorption site on monolayer MoS_2 island on Au(111) surface. (a)-(f) Low-energy dI/dV spectra measured at center of Fe adatoms in different moiré environments as indicated by the STM topographies in the insets (scale bars are 1 nm, crosses mark the location of the spectra). The Fe atoms are located on islands with different orientations with respect to the Au(111) lattice. Blue curves denote measured spectra, black dashed lines are fitted curves. Image adapted from [243].

neither in strongly bonded chain nor in lattice.

We have also realised tip-manipulation controlled reversible spin state switching between S = 1 SF regime and Kondo regime when $\mathrm{Fe-DPyDBrPP}$ molecule is adsorbed away from or on top of adatom at elbow site of herringbone reconstruction of Au(111) surface. We have revealed that the spin state switching is driven by the charge fluctuation effect which is confirmed by our DFT calculations when molecule is on top of Br-adatom at elbow site.

The charge fluctuation effect is also confirmed experimentally where mixed-valence states induced by charge fluctuation are observed in $\mathrm{Fe-DPyDBrPP}$ molecule when it is adsorbed near elbow site. We have observed that charge fluctuation occurs between two molecular frontier orbitals which are respectively closest to the Fermi level in positive and negative energies. We believe these two frontier orbitals are responsible for the low-energy spin excitation that occurs near Fermi level. When two frontier orbitals are far from Fermi level, the molecule has a well defined S = 1 spin state and shows step feature in low-range spectra. When two orbitals shift closer to Fermi level and finally merge at Fermi level, charge fluctuation develops and results the intermediate states and the low-range spectra shows deformed step feature which lineshape is in agreement with theoretical work. When two orbitals cross each other at Fermi level, charge fluctuation becomes strong enough to completely renormalise the magnetic anisotropy, resulting Kondo peak feature in the low-range spectra.

3.9 Supplementary Materials

3.9.1 Manipulation protocol

The manipulation protocol used in this thesis is as follows:

1. We first set the tunneling set point to ($V = 200\,\mathrm{mV}$, $I = 100\,\mathrm{pA}$), this is the value we normally use to manipulate $\mathrm{Fe-DPyDBrPP}$ molecules on the Au(111) surface.

2. Implement the scan plane slope correction process on a region that contains the target molecule and on the target location we want the target molecule to move to. This process will allow the tip to move parallel to the sample surface so that it does not crash into the surface during the manipulation operation.

3. Move the tunneling position to the bare Au(111) surface around the target molecule (typically a few nanometers away).

4. Disengage the feedback control and approach the tip toward the Au(111) surface by a distance $\Delta z = -200\,\mathrm{pm}$ (typical value we used for the set point of ($V = 200\,\mathrm{mV}$, $I = 100\,\mathrm{pA}$), it can be modified). As the tip approaches the sample surface, we observe an increase in current that reaches a new value (from $100\,\mathrm{pA}$ to about $500\,\mathrm{pA}$).

5. Approach the tip towards the molecule, when the tip is almost in contact with the target molecule, we can observe a jump of the current (above $1nA$ which is the saturation limit of the preamplifier at the usual gain), if this is the case the target molecule has been successfully attracted by the tip.

6. Once the molecule bounds to the tip, we move slowly (usually less than $0.5nm/s$) towards target location, during the movement the current should remain high, if the current suddenly drops this indicates that the molecule is decoupled from the tip apex, we will need to relocate the molecule and perform a new manipulation. If the molecule has trouble being attracted to the tip, we can use different setpoints, a different distance $Deltaz$, try to push the molecule or even use vertical manipulation.

7. When we have successfully moved the molecule to the target location, we engage the feedback loop and the tip moves away from the sample surface, this process is usually fast enough that the molecule immediately decouples from the tip and remains at the target location.

3.9.2 Dissociation of a $\mathrm{Fe-DPyDBrPP}$ lattice

If the lattice does not consist of covalently bonded $\mathrm{Fe-DPyDBrPP}$ molecules, a monomer can be extracted by tip manipulation which detail. Fig. 3.25 (a) shows a $\mathrm{Fe-DPyDBrPP}$ lattice in which weak bonds between $\mathrm{Fe-DPyDBrPP}$ monomers construct the lattice like the case of

Fig. 3.3 (b). Fig. 3.25 (b-d) show the images that $\mathrm{Fe-DPyDBrPP}$ monomers marked by 1 and 3 are extracted from lattice.

3.9.3 $\mathrm{Fe-DPyDBrPP}$ with one ligand trapped at elbow site

The manipulation for $\mathrm{Fe-DPyDBrPP}$ near elbow site is not always possible because the attractive potential at this site could be so huge that molecule can not be moved away, this usually corresponds to the case where $\mathrm{Fe-DPyDBrPP}$ itself is catch by the elbow site due to attractive potential during deposition. Fig. 3.26 shows a $\mathrm{Fe-DPyDBrPP}$ monomer with one of its ligand strongly trapped by the elbow site. We can not remove this monomer from the elbow site but can only rotate it along the axis of the ligand. When the molecule change its orientation with respect to Au(111) surface, the uniaxial and transverse magnetic anisotropy D and E can slightly vary. Interestingly only the configuration marked by red cross shows an observable transverse anisotropy E that shows double step feature.

3.9.4 Temperature dependence of SF and Kondo feature

The temperature dependence of SF and Kondo feature are shown in Fig. 3.27. We have measured the $\mathrm{Fe-DPyDBrPP}$ trimer shown in Fig. 3.10 (a) configuration (III) where center molecule shows Kondo feature while two side molecules show SF feature. We have measured at different temperatures (T) of $1.2\,\mathrm{K}$, $4\,\mathrm{K}$, $8\,\mathrm{K}$, $12\,\mathrm{K}$ and $16\,\mathrm{K}$. The width of Kondo peak (Γ) at these temperatures are $0.9\,\mathrm{meV}$, $1.5\,\mathrm{meV}$, $2\,\mathrm{meV}$, $2.5\,\mathrm{meV}$ and $3\,\mathrm{meV}$ respectively. Applying the Γ and T dependence to equation (2.19), it yields a Kondo temperature of $12\,\mathrm{K}$ which is basically the same as our previous measurements.

3.9.5 Tip distance dependence of SF and Kondo feature

We have learnt that the tip can tune the interaction between molecule with substrate for FePc molecule on Au(111) surface (Fig. 3.22). We have implemented the same experiment to Kondo and SF molecule. Fig. 3.28 (a) shows a covalently bonded $\mathrm{Fe-DPyDBrPP}$ dimer where the upper molecule is in SF regime, bottom molecule in Kondo regime where an adatom aimed by white arrow lies beneath it. The dI/dV spectra of SF and Kondo molecules measured at different tip distances are respectively plotted in Fig. 3.28 (b) and (c). Red, green, blue and orange scatter points represent the raw data acquired for tip relative distance $\Delta z = -150\,\mathrm{pm}$, $-200\,\mathrm{pm}$, $-250\,\mathrm{pm}$ and $-300\,\mathrm{pm}$ with setpoint $25\,\mathrm{mV}$, $20\,\mathrm{pA}$. Purple lines are fitted curves by step lineshape and Frota lineshape with a Gaussian background for SF and Kondo feature respectively. The starting setpoint of $25\,\mathrm{mV}$, $20\,\mathrm{pA}$ corresponds to a rather far tip-sample distance, during experiments we have examined the tip distance till $-350\,\mathrm{pm}$ where the tip is extremely close to molecule and spikes appear in the spectra (not shown here). Nevertheless the SF and Kondo feature at Fermi level does not change excitation energy or peak width as illustrated in Fig. 3.28

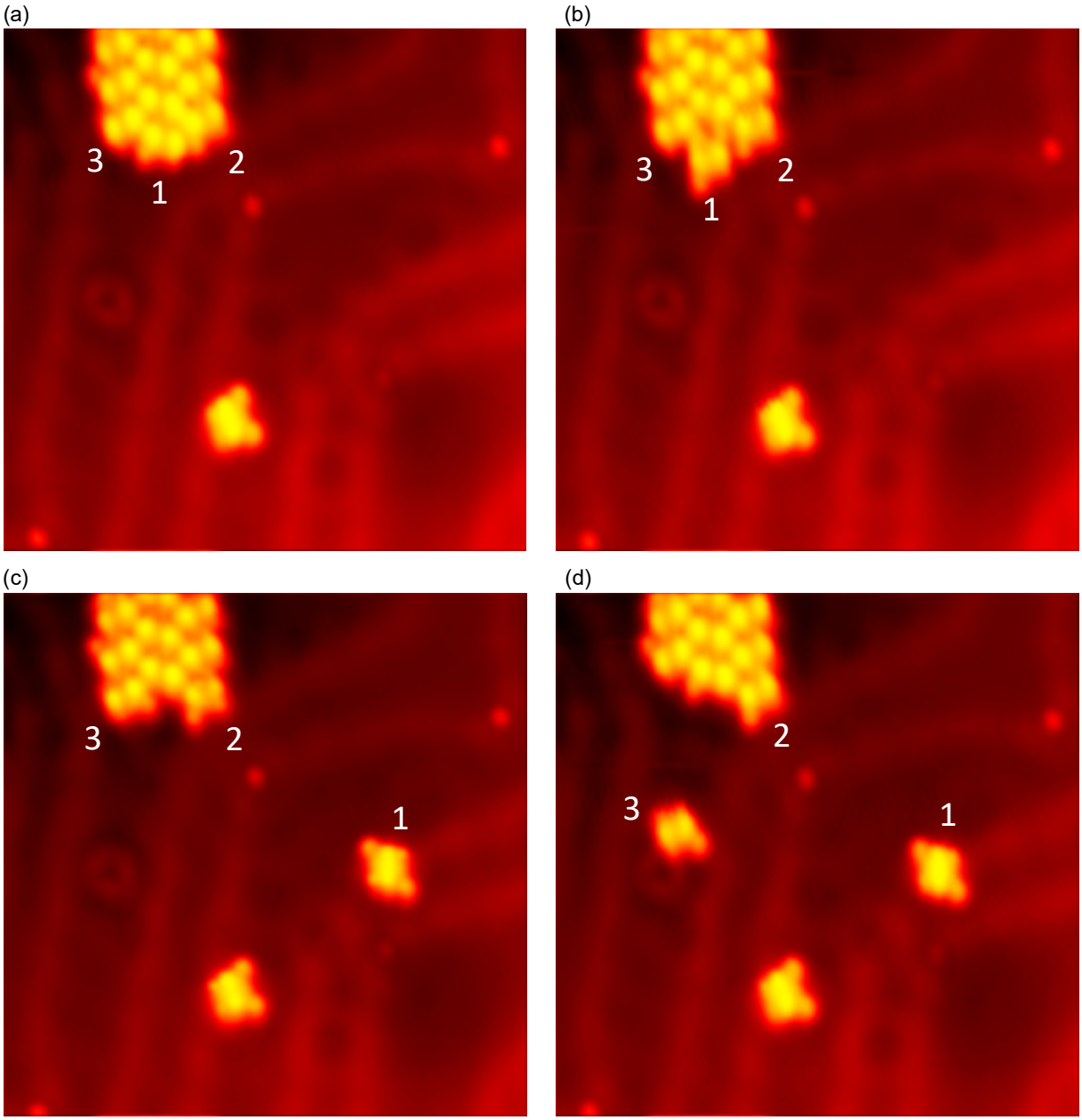

Figure 3.25: Dissociation of $\mathrm{Fe-DPyDBrPP}$ **lattice by tip manipulation.** (a)-(d) Topography images ($20\mathrm{x}20\mathrm{nm}^2$, setpoint: 125 mV, 20 pA) showing the process where $\mathrm{Fe-DPyDBrPP}$ monomers are extracted from the lattice by tip manipulation.

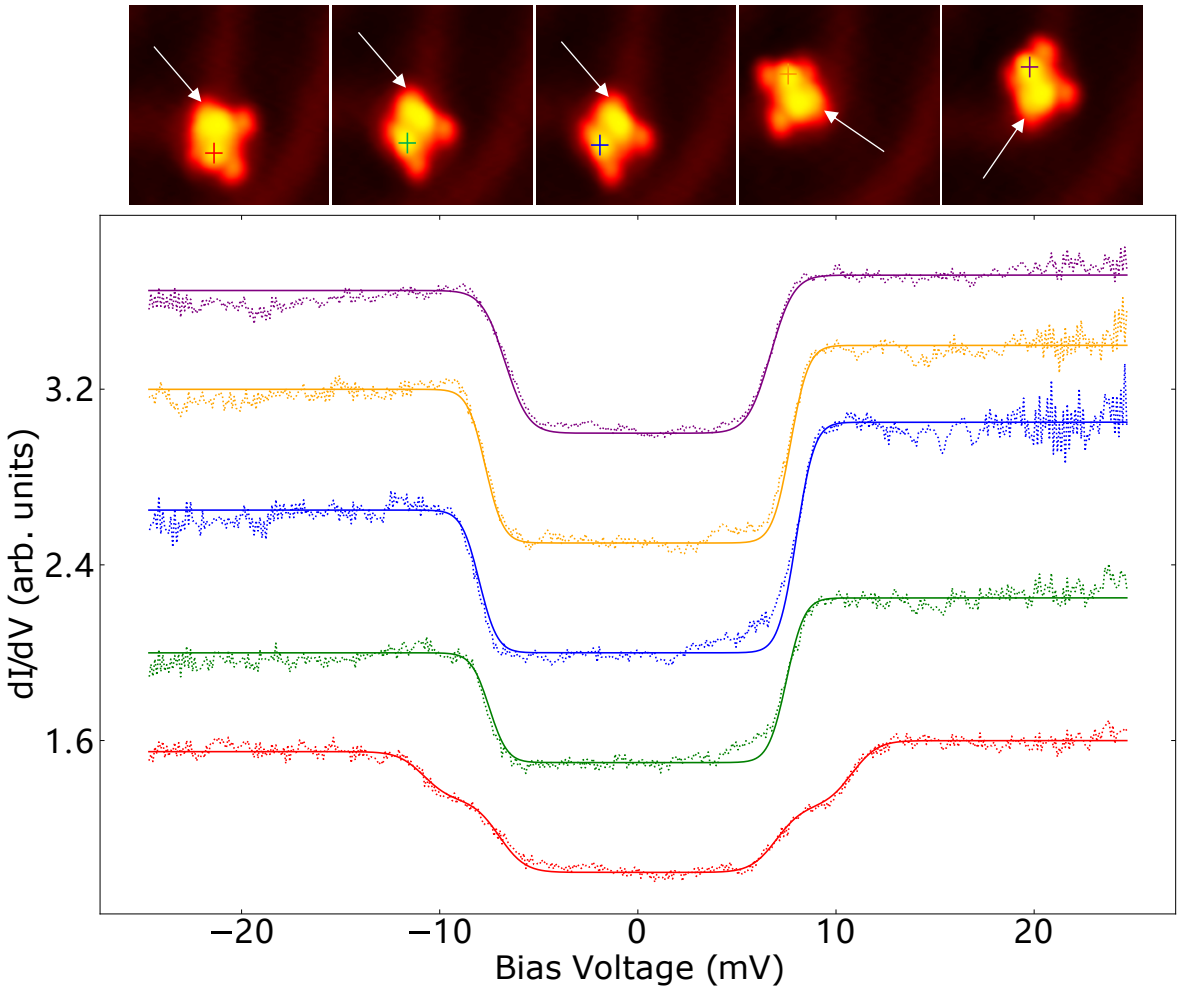

Figure 3.26: Spectroscopy of a $\mathrm{Fe-DPyDBrPP}$ **monomer with one ligand trapped by elbow site.** dI/dV spectra of $\mathrm{Fe-DPyDBrPP}$ monomer with one of the ligands strongly bonded to elbow site that tip manipulation can only rotate it on vertical axis of elbow site marked by white arrow in top topography images. spectra measured at cross positions with corresponding colors shown in the top (topography images: $6\mathrm{x}6\mathrm{nm}^2$, setpoint: 125 mV, 20 pA). spectra setpoint: 30 mV, 200 pA. Lock-in parameters: $V_m = 0.2$ mV, $f = 750$ Hz. Scatter points are raw data and curves are fitted by step lineshape. All spectra are normalized and shifted for clarity.

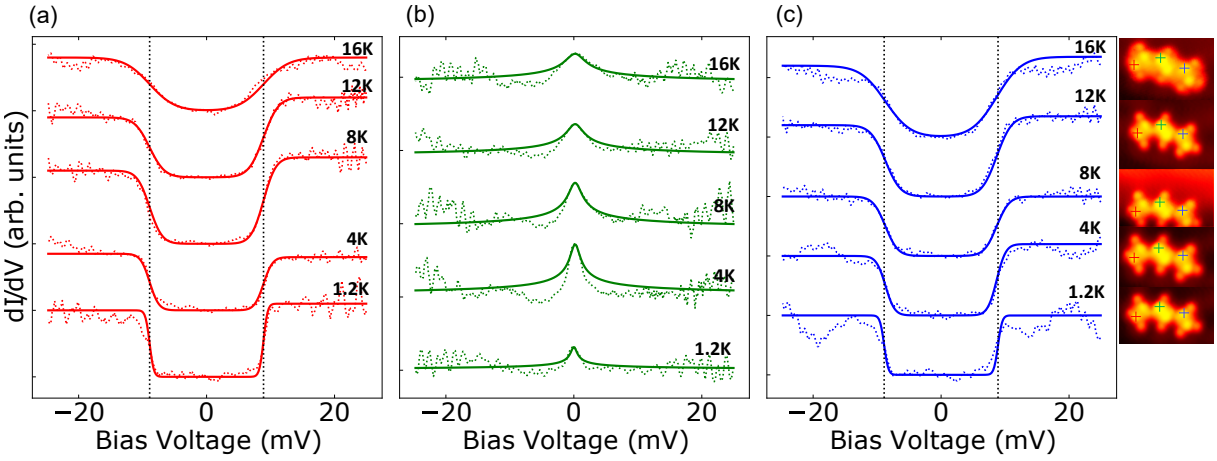

Figure 3.27: Temperature dependence of SF and Kondo feature. (a)(b)(c) dI/dV spectra measured at crosses positions with same colors at different temperatures for three $\mathrm{Fe-DPyDBrPP}$ molecule in trimer shown in the right images. Topography images of trimer are taken at corresponding temperatures. Scatter points are raw data after background removal, curves are fitted by step lineshape (red and blue) and Frota lineshape (green). All spectra are normalized and shifted for clarity.

(b)(c). This means the coupling with substrate can not be modified by tip distance, probably due to the covalent bond formation that stabilizes molecule.

3.9.6 Molecular orbital located in covalent bonds

When the covalently bonded molecular chain is formed we expected to observe collective behavior of magnetic molecules. Although for low-range spectra we do not observe anything that evidences the collective behavior, we have found the orbitals that localize at covalent bond at higher energy. Fig. 3.29 shows the large-range dI/dV map of covalently bonded trimer that we have seen in Fig. 3.18. We observe that the molecular orbitals localized at covalent bond lies at high energy ($+800$ meV). These orbitals show delocalized feature that does not exhibit distinguishable $3d$ orbital shape. If we can bring such orbitals closer to Fermi level we could probably observe delocalized spin excitation signature in such orbitals. To achieve this, the molecules and substrates may have to be properly designed and chosen.

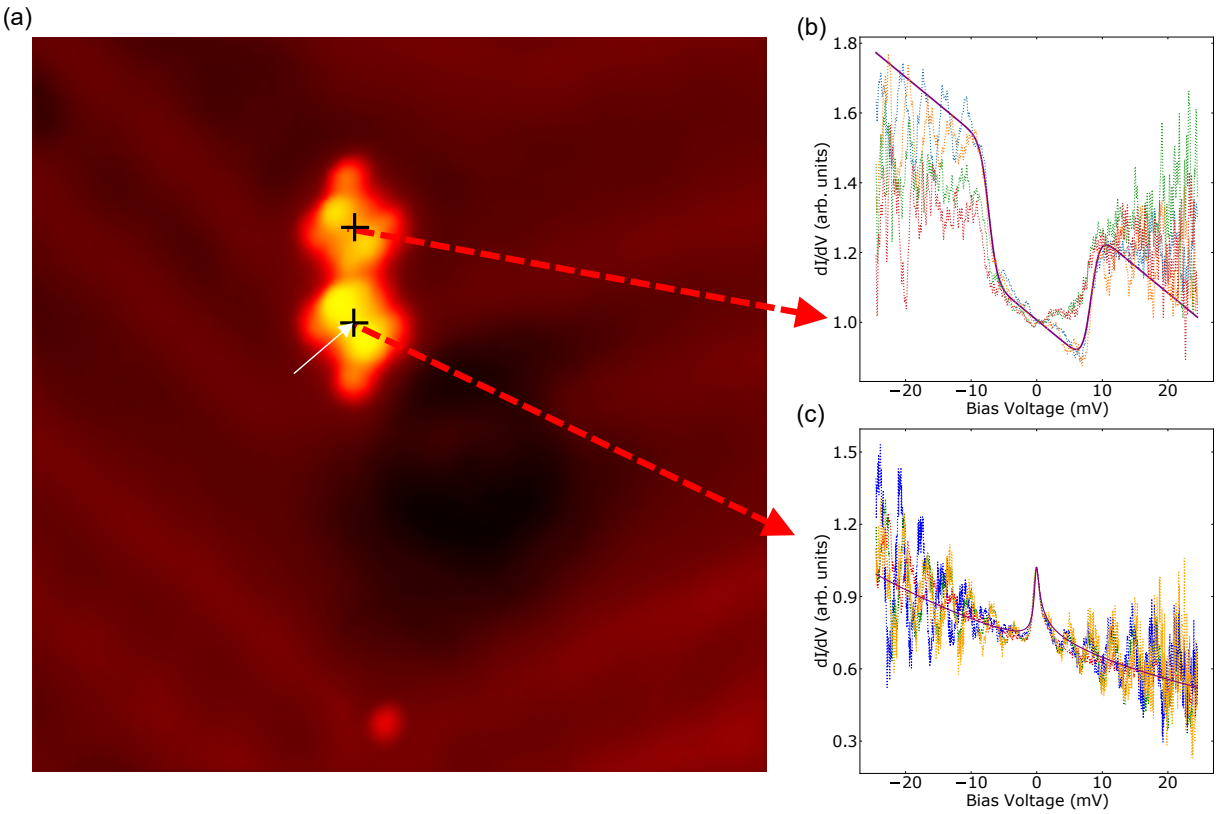

Figure 3.28: Temperature dependence of SF and Kondo feature. (a) Topography image ($15\mathrm{x}15\mathrm{nm}^2$, setpoint: 125 mV, 20 pA) of covalently bonded $\mathrm{Fe-DPyDBrPP}$ dimer on Au(111) surface. Upper molecule shows SF regime and bottom molecule shows Kondo regime. White arrow aims at the adatom at elbow site that lies beneath bottom molecule. Black crosses mark the positions where the dI/dV spectra are measured. (b-c) dI/dV spectra for upper and bottom molecules shown in (a). Scatter points of red, green, blue and orange colors represent the raw date measured for relative tip distance $\Delta z = -150$ pm, -200 pm, -250 pm and -300 pm respectively. Initial setpoint is 25 mV, 20 pA. Purple lines are fitted curves by step lineshape and Frota lineshape with a Gaussian background for SF and Kondo feature respectively. All spectra are normalized.

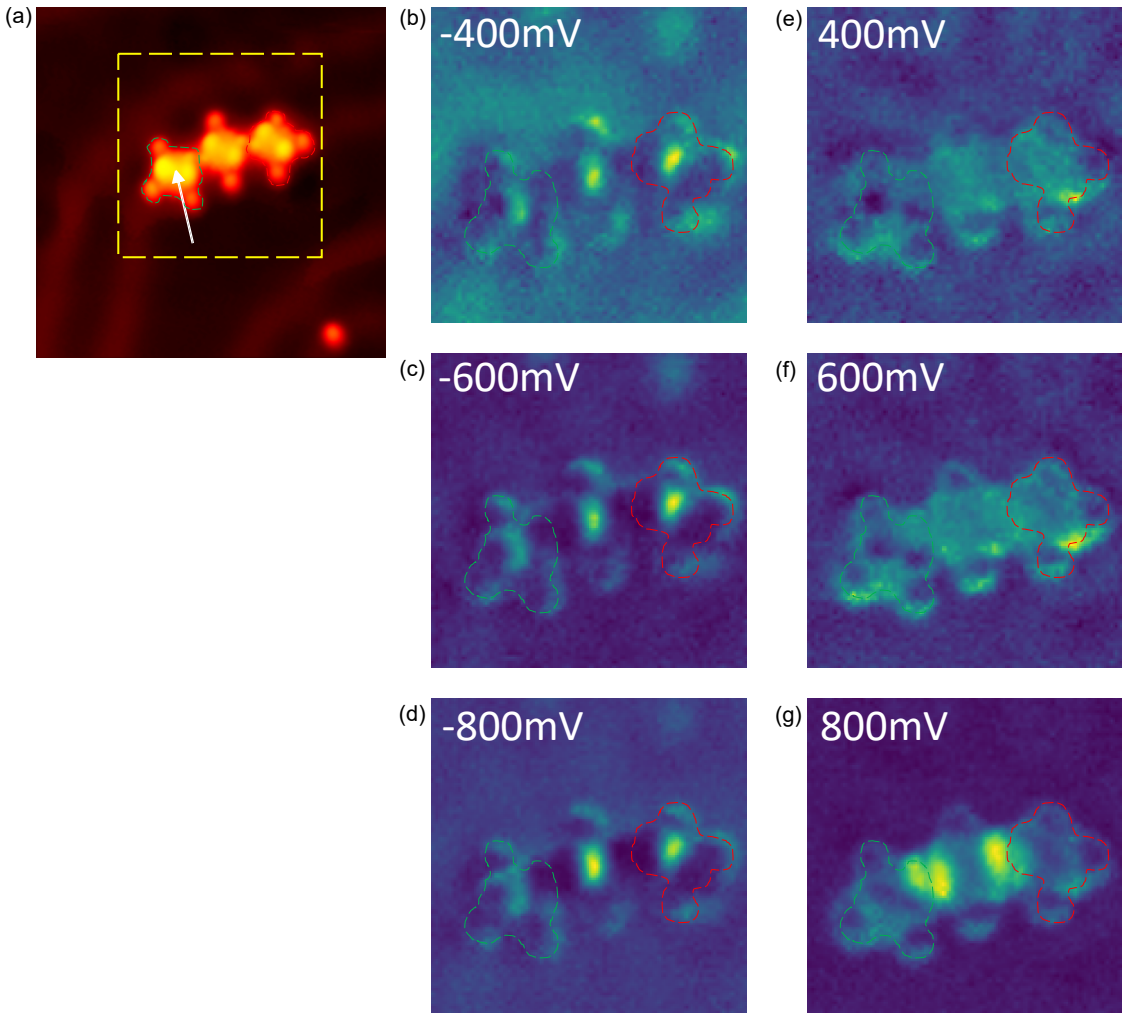

Figure 3.29: Large-range dI/dV maps of covalently bonded $\mathrm{Fe-DPyDBrPP}$ trimer. (a) Topography image ($12\mathrm{x}12\mathrm{nm}^2$, setpoint: 200 mV, 100 pA) of a covalently bonded trimer of $\mathrm{Fe-DPyDBrPP}$ molecules on Au(111) surface, same as IR1 case shown in Fig. 3.18. (b-g) dI/dV maps of yellow dashed square region in (a) at bias voltages marked inside the images. Setpoint: 800 mV, 500 pA. Lock-in parameters: $V_m = 5$ mV, $f = 900$ Hz.

Chapter 4

Structural and Electronic Properties of Porphyrin Magnetic Molecules on Pb Surfaces

4.1 Introduction

In this chapter we will present STM/STS results of self-assembled Fe 5,15-dibromo-10,20-diphenyl porphyrin ($\mathrm{Fe-DBrDPP}$) molecule supramolecular lattices deposited on superconducting Pb(110) surface. Unlike normal metal surface which can be described as non-interacting electron gas, superconductor substrate possesses pairing interaction which would make electronic system become even more complicated.

On Pb(110) surface $\mathrm{Fe-DBrDPP}$ molecules always form compact supramolecular lattices because of high molecule mobility. In $\mathrm{Fe-DBrDPP}$ supramolecular lattices almost all $\mathrm{Fe-DBrDPP}$ molecules exhibit S = 1 spin state through detection of out-gap SF feature or two in-gap Shiba states feature. Both SF excitation and Shiba state originate from FOA and FOB of $\mathrm{Fe-DBrDPP}$ molecule where the former one represents a weak coupling regime and the latter one the strong coupling regime.

Furthermore we have also discovered that the local geometry of molecule also plays an important role in molecule's electronic properties. Lattice mismatch can induce charge fluctuation, resulting Type2 "1B" molecule which molecular orbital localizes at center become quenched and low-energy excitation can no more be observed. Inter-molecular interaction can make "0B" molecule extremely sensitive to local environment, especially the presence of tip, thanks to which we are able to observe the evolution of out-gap SF feature to in-gap Shiba feature under tip interaction. Impressively the evolution process resolved in spectroscopic maps behave as continuous opening/closing of bubble shape and we also observed an intermediate regime where both in-gap and out-gap feature coexists, such exotic behavior has also been reported in a S = 3/2 molecular system [103].

At the beginning of this chapter, we start by introducing the preparation of Pb(110) surface

together with the description of the structural and electronic properties of different Pb surfaces in order to explain why we chose to study the (110) surface of Pb in section (4.2). Then we will introduce the structure of the assemblies of $\mathrm{Fe-DBrDPP}$ molecule on the surface in section (4.3).

After the introduction section, there will be three main parts corresponding to different $\mathrm{Fe-DBrDPP}$/Pb(110) sample preparation processes which are respectively called disordered (4.4), low temperature (4.5) and high temperature phases (4.6). In each of them, we adopt the same narrative structure as for chapter (3): sample preparation, topography results, spectroscopy results and exotic electronic properties (if there are).

In the first part presented in section (4.4), $\mathrm{Fe-DBrDPP}$ supramolecular lattices on Pb(110) surface are not post-annealed, thus this case is also called disordered phase. The structure and electronic properties of $\mathrm{Fe-DBrDPP}$ supramolecular lattices are studied in sections (4.4.2) and (4.4.3) from which we will acquire the basic understandings of $\mathrm{Fe-DBrDPP}$/Pb(110) system.

In the second part presented in section (4.5), $\mathrm{Fe-DBrDPP}$ supramolecular lattices on Pb(110) are post-annealed for producing an ordered structure that we call the low temperature phase. The structure properties of $\mathrm{Fe-DBrDPP}$ supramolecular lattices are studied in section (4.5.2) in which we observe two types of supramolecular domains (A- and B- types). A-type domains exhibit unusual topographic character with double periodicity feature which differs greatly differs from B-type domains where single $\mathrm{Fe-DBrDPP}$ molecule remains well distinguishable. Their electronic properties are studied in section (4.5.3) where we find two Shiba states with different molecular orbital characters, the double periodicity topographic character of A-type domain is explained by the strong electron-like component delocalization of channel 1 Shiba state possibly due to lattice mismatch or the charge effect on $\mathrm{Br}\cdots\pi$ halogen bond. Additionally in section (4.5.3), we find that molecules exhibiting exotic electronic properties tend to localize near the perimeter of A-type domain.

In the third part presented in section (4.6) $\mathrm{Fe-DBrDPP}$ supramolecular lattices on Pb(110) are post-annealed at higher temperature to produce what we call the high temperature phase. The high temperature is the most interesting situation in which we have demonstrated the intimate relation between electronic properties and geometry of molecule which is determined by molecule's conformation, lattice mismatch and inter-molecular interaction. In high temperature phase we observe three basic molecular structure (orderings) labeled by "4mer", "1B", "0B" and various composite supramolecular lattice shown in section (4.6.2). The electronic properties of standard "4mer", "1B" and "0B" molecules are successively studied in section (4.6.3) where "4mer" exhibits only SF feature, representing weak coupling with substrate while "0B" and "1B" molecules exhibit Shiba feature, representing strong coupling with substrate. Then we have studied exotic "0B" molecules that localize near the interface between lattices with different orderings under tip interaction. After that in analysis section (4.6.4) we have analyzed the data obtained in high temperature phase. We have determined the orbital origin and ground state (and excited state) nature of channel 1, 2 Shiba states. We have also discussed about the

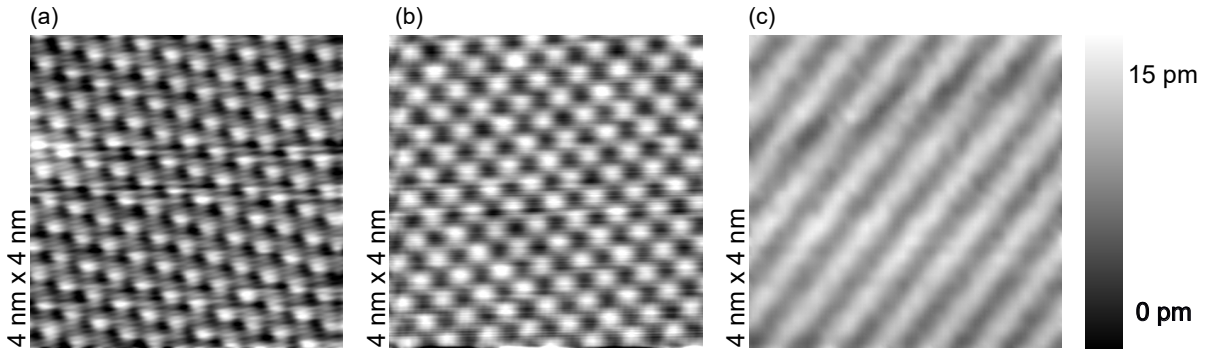

Figure 4.1: Topography images of Pb surfaces of different orientations. (a)-(c) Topography images ($4\text{x}4\text{nm}^2$) of Pb(111), (100), and (110) single crystal surfaces. Setpoint: 50, -50 and 5 mV, 50 50 and 400 pA respectively. Image adapted from [245].

geometry effect and tip effect and made a classification of $\mathrm{Fe-DBrDPP}$ molecules obtained in high temperature phase in section.

At the end of this chapter a section consisting of supplementary information is presented (4.7).

4.2 Pb surface

4.2.1 Structure properties

In this thesis, we focused our study on self-assembled molecular supramolecular lattices on superconducting Pb surfaces of (111), (100) and (110). Lead is a Type I superconductor with relatively high critical temperature of 7.2 K. Thus the superconducting gap is fully developed at the measurement temperature, 1.1 K. Pb surfaces are moreover expected to exhibit sizeable Rashba spin-orbit coupling (SOC) [244] due to the large atomic mass of Pb. A superconductor with SOC is one of the key ingredient to realise topological order in Shiba supramolecular lattice created by molecule supramolecular lattice.

The topography images showing the atomic structure of Pb(111), (100), and (110) surfaces are presented in Fig. 4.1. Pb(110) surface is resolved as rows of atoms parallel to [110] direction, indicating that Pb atoms arrange more compact in [110] direction. Different crystallographic surface ordering could have important influence on supramolecular lattice arrangement that could lead to different electronic properties. One of our first objectives was to study rows of molecules so we have chosen the anisotropic Pb(110) surface as a template with idea to favor one-dimensional assembly.

4.2.2 Electronic properties

Pb is a strong-coupling superconductor [246, 247] which can be accurately described by Eliashberg theory [248]. For a strong-coupling superconductor, the phonon-mediated pairing interac-

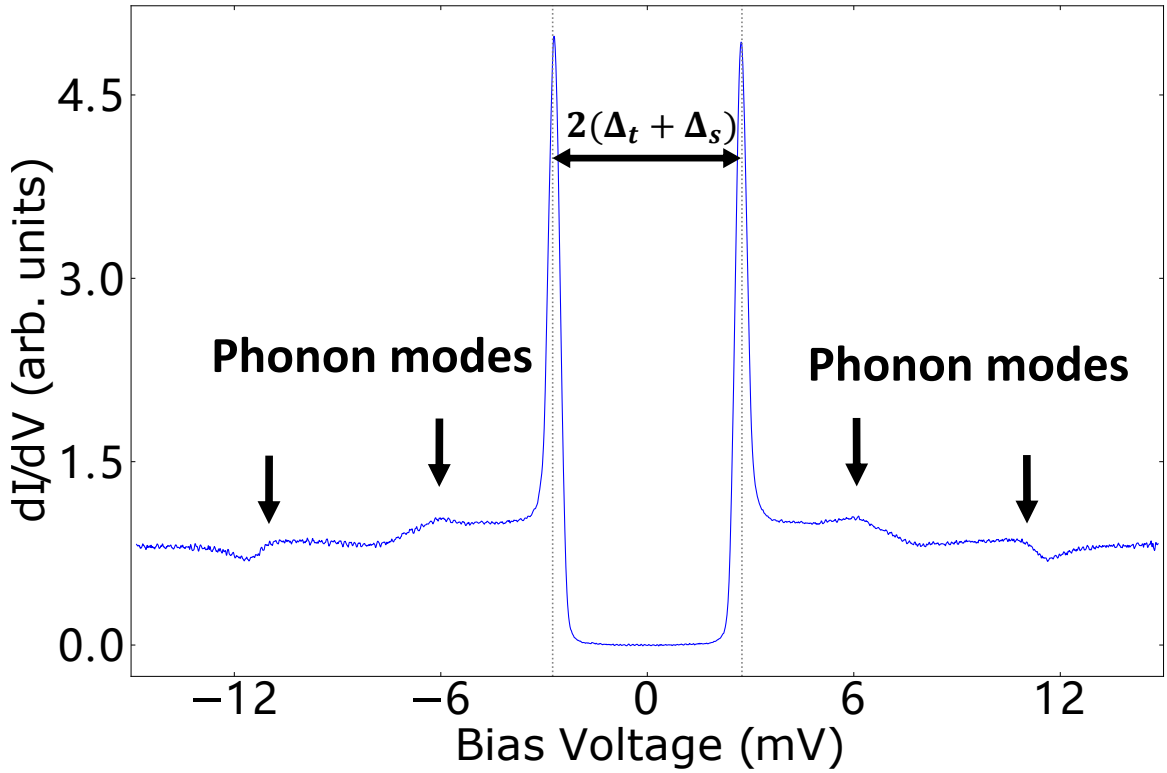

Figure 4.2: SIS dI/dV spectra on clean Pb(110) surface. SIS dI/dV spectra taken on clean Pb(110) surface. Bulk Pb cover superconducting tip of gap $\Delta_t = \Delta_s = 1.35$ meV is used, "t" and "s" stand for tip and substrate (Pb). Vertical dashed lines mark the bias voltage of ± 2.7 mV which are the enhanced gap value for Pb in SIS spectra. Two steps outside the gap at around 6 mV and 11 mV are found ascribed to the phonon mode. Setpoint: 20 mV, 100 pA, 200 pm, Lock-in parameters: $V_m = 0.2$ mV, $f = 750$ Hz.

tion is so strong that the energy scale of the superconducting order (Δ) and inelastic phonon excitation become comparable [249]. In the conductance spectrum measuring the DOS of Pb (Fig. 4.2), in addition to the superconducting gap ($\Delta_s = 1.35$ meV) described by BCS theory, there are two conductance steps outside the gap that can be attributed to van Hove singularities of the phonon modes [250].

Pb is also a two-bands superconductor,[251], so the BCS quasiparticle peaks at $+(-)2.7$ mV are splitted in two peaks in the spectroscopy measurements with a very narrow separation. The splitting can be resolved by high-resolution STS experiments with well prepared superconducting tip. It has been shown that the splitting is around 150μeV and depending on different surface orientations of Pb the relative weight of two peaks can vary as a result of different tunneling rate to two Fermi surfaces [245] (Fig. 4.3)

4.2.3 Pb surface preparation

We have used a lead crystal cut and polished along (100), (110) and (111) orientations by Surface Prep Lab. The clean and atomically flat Pb surfaces were prepared by repeated cycles of Ar ion sputtering (at 1 keV and pressure of 10^{-5} mbar for 30') and annealing (at 390 K for 90') by radiative heating. It usually requires tens of cycles to acquire a well prepared Pb substrate.

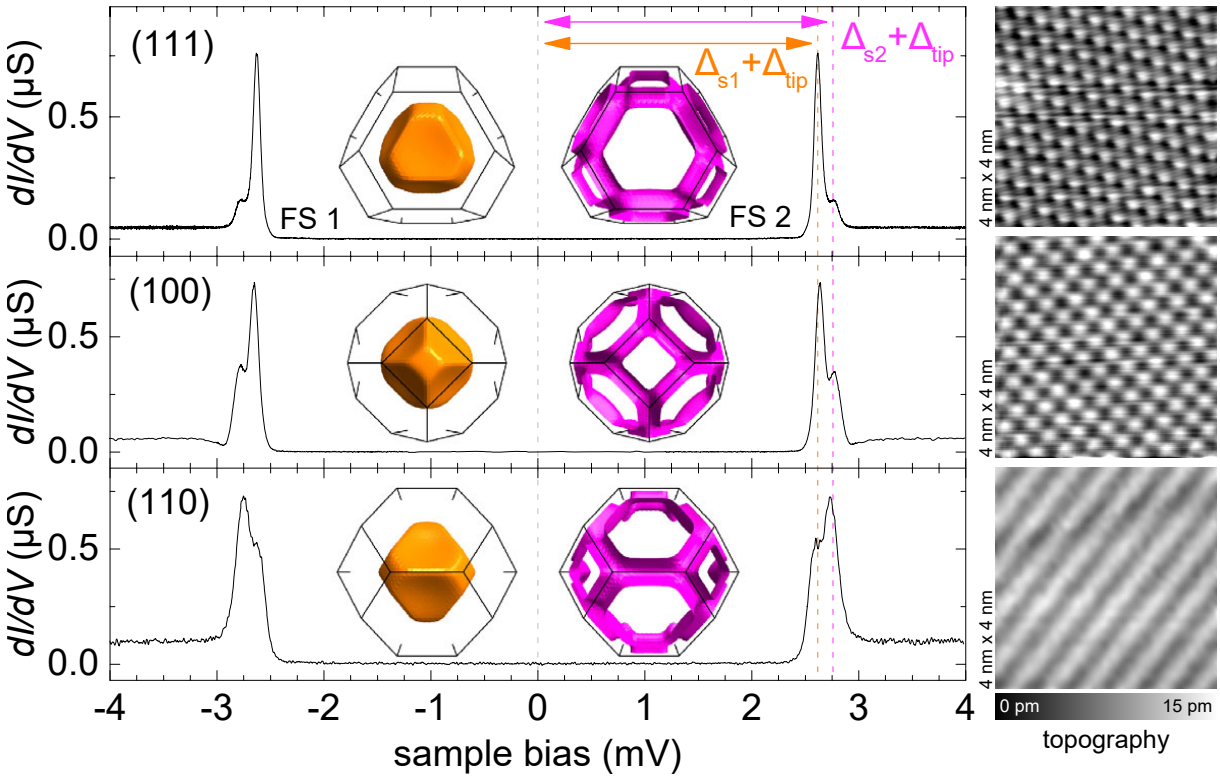

Figure 4.3: SIS dI/dV spectra of different clean Pb surfaces. From top to bottom: SIS dI/dV spectra measured on clean terraces of Pb(111), (100), and (110) single crystal surfaces. Bulk Pb covered superconducting tip of gap Δ_{tip} is used. Two pairs of BCS peaks locate at around $\approx \pm 2.7$ mV splitted by $\approx 150\mu$eV, indicating two-band superconducting state for Pb sample with gap of Δ_{s1} and Δ_{s2}. Setpoint: 5 mV, 250 pA, Lock-in parameters: $V_m = 15\mu$V, $f = 912$ Hz. Image adapted from [245].

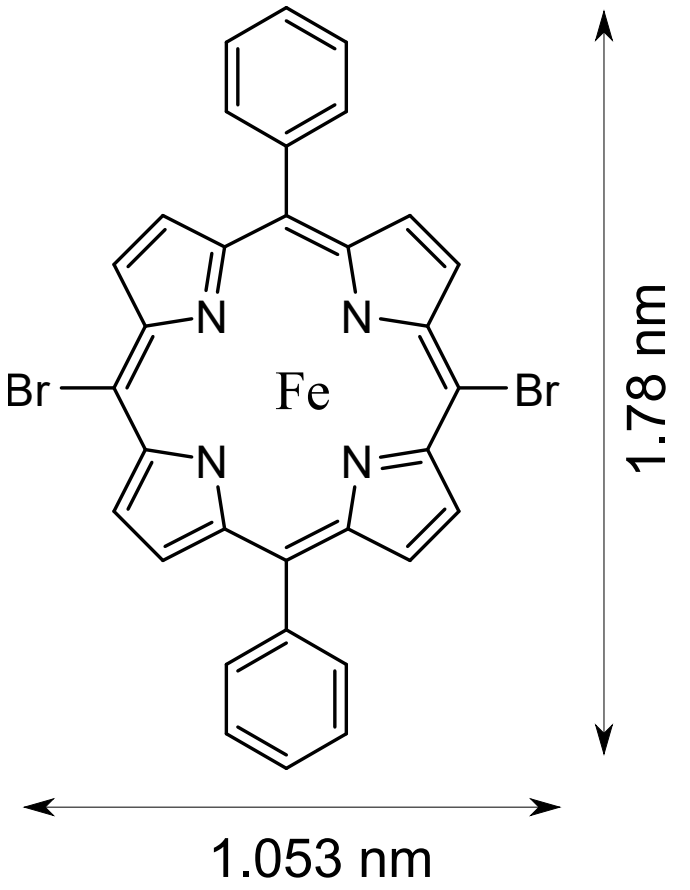

Figure 4.4: Structure of $\mathrm{Fe-DBrDPP}$ **molecule.** Two-fold symmetry Fe 5,15-dibromo-10,20-diphenyl porphyrin ($\mathrm{Fe-DBrDPP}$) molecule. Hydrogen atoms not explicitly shown. Figure drawn by Chemydraw.

Successful Pb surface preparation is characterized by large atomically flat terraces (large enough with respect to the nanostructure to study, usually larger than $50\mathrm{x}50\mathrm{nm}^2$) with few impurity (especially gas molecule) contamination.

4.3 $\mathrm{Fe-DBrDPP}$ molecule

The Fe 5,15-dibromo-10,20-diphenyl porphyrin ($\mathrm{Fe-DBrDPP}$) molecules used in our experiments were provided by Alpha Aesar company. Their structure is shown in Fig. 4.4 where two bromine atoms are attached to opposite 10,20 meso-positions and two phenyl rings to 5,15 opposite meso-positions, hence $\mathrm{Fe-DBrDPP}$ molecule has two-fold symmetry in gas phase.

Such choice of ligands was first proposed in [138] where $\mathrm{Ni-DBrDPP}$ molecules can form covalently bonded molecule chains via debromination process on noble metal surface. Fig. 4.5 (a) shows two types of self-assembled $\mathrm{Ni-DBrDPP}$ molecule supramolecular lattice formed on room temperature Au(111) surface without post-annealing. Fig. 4.5 (b) shows the case when $\mathrm{Ni-DBrDPP/Au(111)}$ sample is post-annealed at 170°C that forms covalently bonded molecule chain on Au(111) surface. These results inspired our initial purpose which was

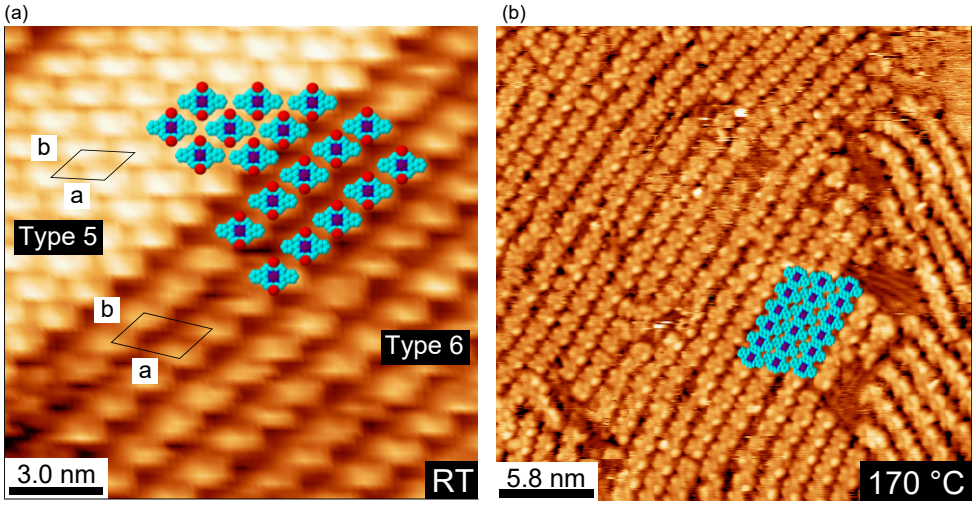

Figure 4.5: $\mathrm{Ni-DBrDPP}$ **molecule network on Au(111) surface.** (a) Topography image (setpoint: 950 mV, 250 pA) of $\mathrm{Ni-DBrDPP}$ molecule on Au(111) surface without post-annealing. Molecule sketch is marked inside the image where purple, cyan and red colors respectively represent Ni, C and Br atoms. (b) Topography image (setpoint: $1.24V$, 310 pA) of $\mathrm{Ni-DBrDPP}$ molecule on Au(111) surface after post-annealing at 170°C. Covalently bonded molecule chain is obtained via debromination process. Image adapted from [138].

to use $\mathrm{Fe-DBrDPP}$ to realise covalently bonded $\mathrm{Fe-DBrDPP}$ chain on superconductor.

4.4 $\mathrm{Fe-DBrDPP}$ on Pb(110) - "Disordered" configuration

4.4.1 Preparation for STM experiment

The calibration of the evaporator was performed by measuring the $\mathrm{Fe-DBrDPP}$ deposition on Au(111). Then, we first study the $\mathrm{Fe-DBrDPP}$ adsorption configuration on Pb(110) surface without post-annealing. $\mathrm{Fe-DBrDPP}$ molecules are evaporated at 500 K and then deposited for 1' by means of OMBE on freshly prepared clean Pb(110) surface at room temperature. During the deposition the pressure of preparation chamber can temporary increase up to 10^{-9} mbar range. It is worth mentioning that evaporation at 500 K for $\mathrm{Fe-DBrDPP}$ molecule can be repeated for many times, indicating that in-crucible debromination reaction hardly occurs for $\mathrm{Fe-DBrDPP}$ molecule. Once the deposition process is completed we transfer $\mathrm{Fe-DBrDPP}$/Pb(110) sample to STM chamber for experiment without exceeding a pressure over 10^{-10} mbar.

4.4.2 Structural properties of $\mathrm{Fe-DBrDPP}$ disordered supramolecular assembly

Fig. 4.6 is the topography image showing a large surface of $\mathrm{Fe-DBrDPP}$/Pb(110) sample without post-annealing. We can find assembled $\mathrm{Fe-DBrDPP}$ molecules into a single layer island on Pb(110) surface on the left part of the image. On the right part, we can distinguish the atomic resolution of Pb(110) surface as parallel lines along [110] direction. We find that

$Fe-DBrDPP$ molecule on Pb(110) surface always form large supramolecular lattice and we do not observe any isolated $Fe-DBrDPP$ monomer or small molecular assemblies like dimer. This implies that even at room temperature $Fe-DBrDPP$ molecule has a high mobility on Pb(110) surface.

Fig. 4.7 (a) shows the small-scale topography image ($12.3x12.3nm^2$) of a monolayer self-assembled $Fe-DBrDPP$ supramolecular lattice on Pb(110) surface without post-annealing. The supramolecular lattice is more or less organized in a way where $Fe-DBrDPP$ molecule arranges along two directions marked by white dashed arrows 1 and 2. Along these rows, molecules seem to be arranged by Van der Waals interaction and hydrogen bonds where the phenyl ring and pyrrole ring of different molecules are bonded together.

We can clearly distinguish the shape of most $Fe-DBrDPP$ molecules where the central Fe atom is resolved as a bright spot surrounded by two phenyl rings which are identifiable as two lighter spots. In the same way as for $Ni-DBrDPP$ on Au(111) the two bromine atoms are not topographically resolved due to the lack of a molecular orbital available for tunneling (Fig. 4.5 (a)). Such two-fold symmetric topographic characterization should correspond to a planar conformation where two bromine atoms are preserved, a porphine macrocycle and two phenyl rings lie parallel with respect to the surface. In the following, we call this arrangement **"0B"** configuration (ordering, phase or conformation), indicating that two Br atoms are preserved.

However not all $Fe-DBrDPP$ molecules show "0B" ordering. $Fe-DBrDPP$ molecules can show an exceptional strong spectral weight at one Br site (marked by red arrow), breaking the two-fold symmetric shape. This could indicate that one bromine atom is dissociated and forms a chemical bond with a Pb atom of Pb(110) surface. This configuration where the molecules have dissociated one of Br atom is called **"1B"** ordering in the following.

There also exist other kinds of ordering such as the compact arrangement of $Fe-DBrDPP$ molecules inside the green circle for which conformation is difficult to be recognized by topography image and the molecules showing distorted orientations marked by blue arrows, etc.

It is not surprising $Fe-DBrDPP$ molecules deposited on metal surface can show various ordering, because they are easy to deform and form different kinds of bonds with neighbor molecules that stabilize them in a stable/meso-stable ordering depending on the annealing temperature. We will see in the following sections how post-annealing affects on the ordering of molecules.

4.4.3 Electronic properties of $Fe-DBrDPP$ disordered supramolecular assembly

In this section we will examine the electronic properties of disordered phases supramolecular lattices by studying spectroscopy results.

As we have discussed in the section (2.2.3), we usually use a superconducting tip to perform tunneling experiments on a superconducting substrate. Here, we use Nb tip coated with Pb cluster, which shows a BCS DOS similar to that of bulk Pb (gap value of about 1.35 meV).

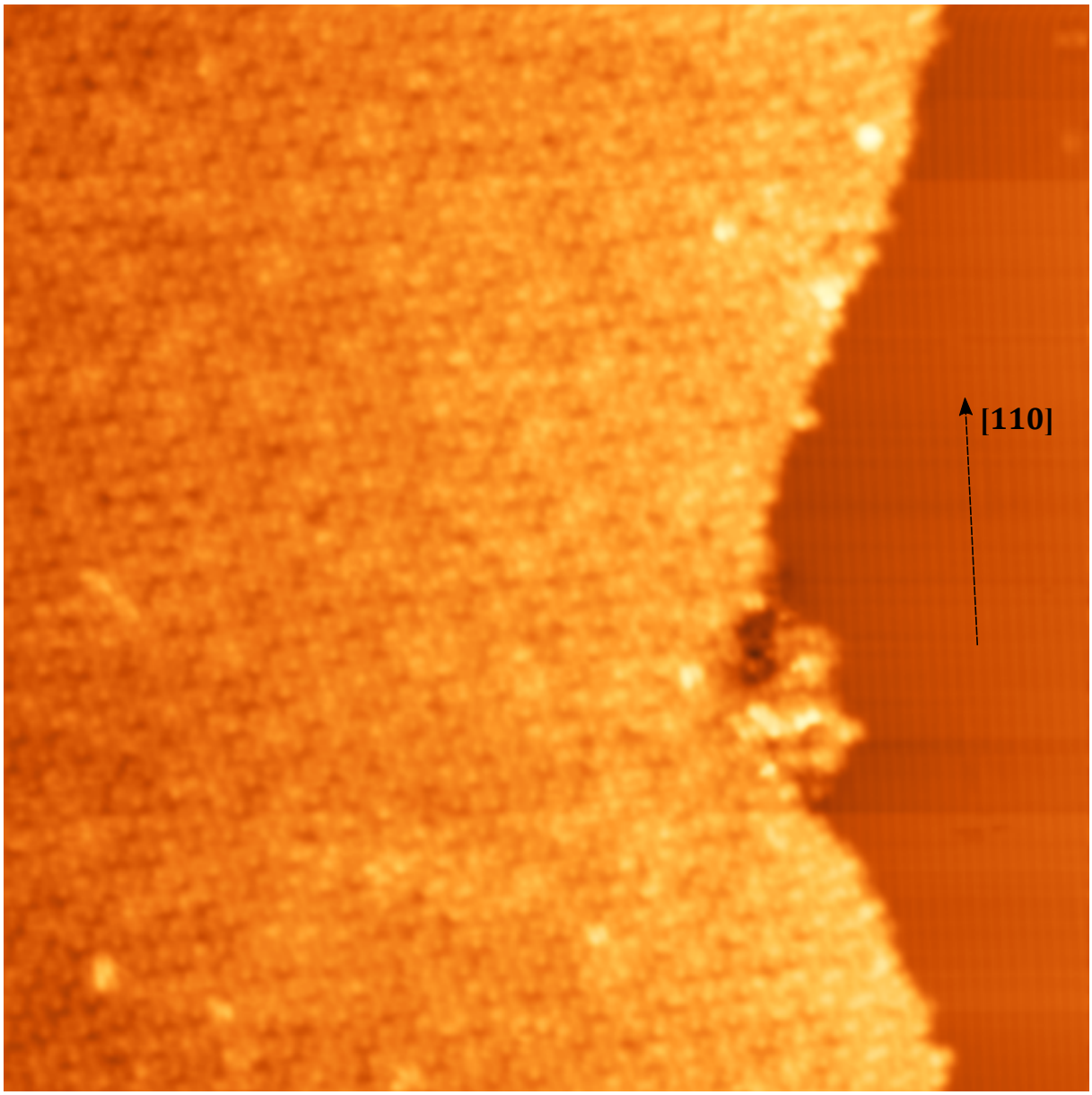

Figure 4.6: Large-range topography image of $\mathrm{Fe-DBrDPP}$ **molecules on Pb(110) surface without post-annealing.** Topography image ($45\mathrm{x}45\mathrm{nm}^2$, setpoint: $1.2V, 30$ pA) of self-assembled $\mathrm{Fe-DBrDPP}$ molecule supramolecular lattice on Pb(110) surface without post-annealing. Black dashed arrow indicates [110] direction of Pb(110) surface.

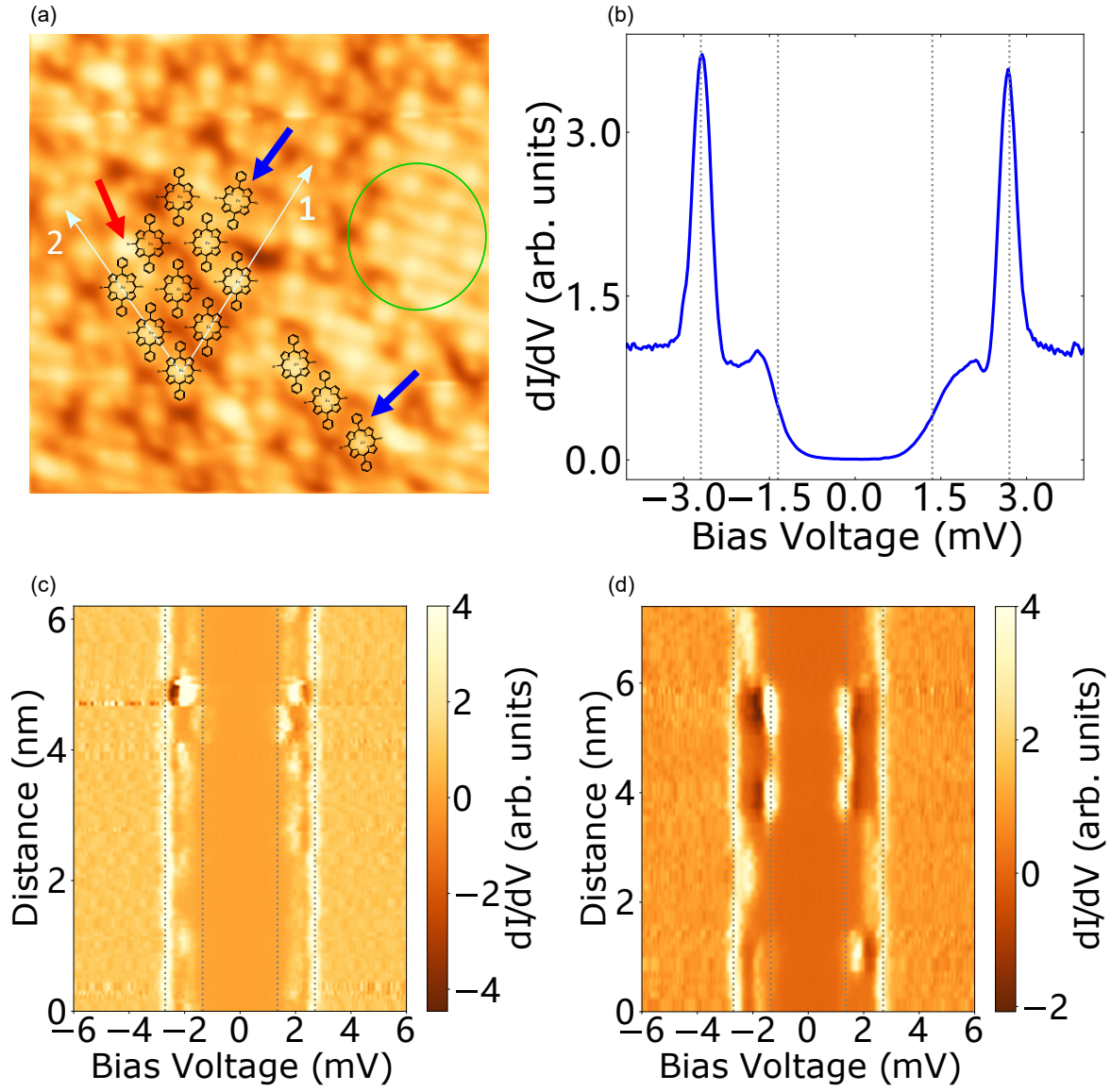

Figure 4.7: $\mathrm{Fe-DBrDPP}$ **molecules on Pb(110) surface without post-annealing.** (a) Topography image ($12.3\mathrm{x}12.3\mathrm{nm}^2$, setpoint: 8 mV, 22 pA) of $\mathrm{Fe-DBrDPP}$ molecules on Au(111) surface without post-annealing. White dashed arrows 1 and 2 indicate the direction that molecule in supramolecular lattice arranges, blue arrows mark the distorted molecule, red arrow aims at the bromine atom of one molecule and green circle marks t. Certain $\mathrm{Fe-DBrDPP}$ molecules are marked by sketch. (b) Averaged SIS dI/dV spectra of the area in (a). Gray dashed lines mark the energy of ± 1.35 meV and ± 2.7 meV. Setpoint: 8 mV, $22pA$, 300 pm. (c)(d) dI/dV spectra consisting of stacking plot of points along black arrows 2 and 1 in (a) respectively.

Fig. 4.7 (b) shows the SIS dI/dV spectra, the gray dashed lines marks the bias voltage of ± 1.35 mV and ± 2.7 mV. The spectra are averaged over the whole area of the supramolecular assembly shown in Fig. 4.7 (a). We observe that non-zero in-gap feature at voltages comprised between the window $\pm[1.35$ mV, 2.7 mV], indicating the existence of Shiba states which energies varies between [0 meV, 1.35 meV].

Fig. 4.7 (c) & (d) show spatial variation of the tunneling conductance along trajectories (white arrows) 2 and 1 presented in (a), respectively. We observe that all molecules examined here show only a pair of Shiba states which energies varies, probably depending on adsorption site of molecules.

Fig. 4.8 shows the SIS dI/dV maps of $\mathrm{Fe-DBrDPP}$ disordered supramolecular assembly on Pb(110) without post-annealing. Fig. 4.8 (c-d) and Fig. 4.8 (e-f) illustrate the distribution of Shiba states at ± 1.65 mV and ± 2.38 mV respectively. Shiba states at ± 1.65 mV have a pattern which is localized around $\mathrm{Fe-DBrDPP}$ molecule on the lead surface while Shiba states at 2.38 mV are localized mainly on the macrocycle.

4.4.4 Conclusion

We have observed that $\mathrm{Fe-DBrDPP}$ molecules tend to form more or less well arranged supramolecular assemblies even without post-annealing, indicating a high molecule mobility on Pb(110) surface. Most of $\mathrm{Fe-DBrDPP}$ molecules exhibit easily identifiable topography shape which is called "0B" ordering. While some of them can adopt other ordering via dissociating bromine atoms or forming various kinds of bonds with neighbor molecules. We have examined the electronic properties of $\mathrm{Fe-DBrDPP}$ supramolecular lattice on Pb(110). We find that all $\mathrm{Fe-DBrDPP}$ molecules shows in-gap Shiba states which energy can be different. This implies that $\mathrm{Fe-DBrDPP}$ molecule remains magnetic on Pb(110) and has rather strong interaction with substrate that gives rise to Shiba state formation. However, we do not find a solid relation between molecular ordering with the corresponding Shiba state's energy and spatial distribution, probably due to distortion of lattice because of the lack of post-annealing.

4.5 $\mathrm{Fe-DBrDPP}$ assemblies on Pb(110): Low-temperature configuration

4.5.1 Preparation for STM experiments

We have learnt from the previous section that $\mathrm{Fe-DBrDPP}$ molecules on Pb(110) surface show high mobility even at room temperature and form supramolecular lattices. In this section we will study the case where the deposition is done at higher temperature followed by a post-annealing (also called low-temperature phase).

$\mathrm{Fe-DBrDPP}$ molecules are still evaporated at 500 K and deposited for 15" by means of OMBE on freshly prepared clean Pb(110) surface which is held at 360 K by radiative heating

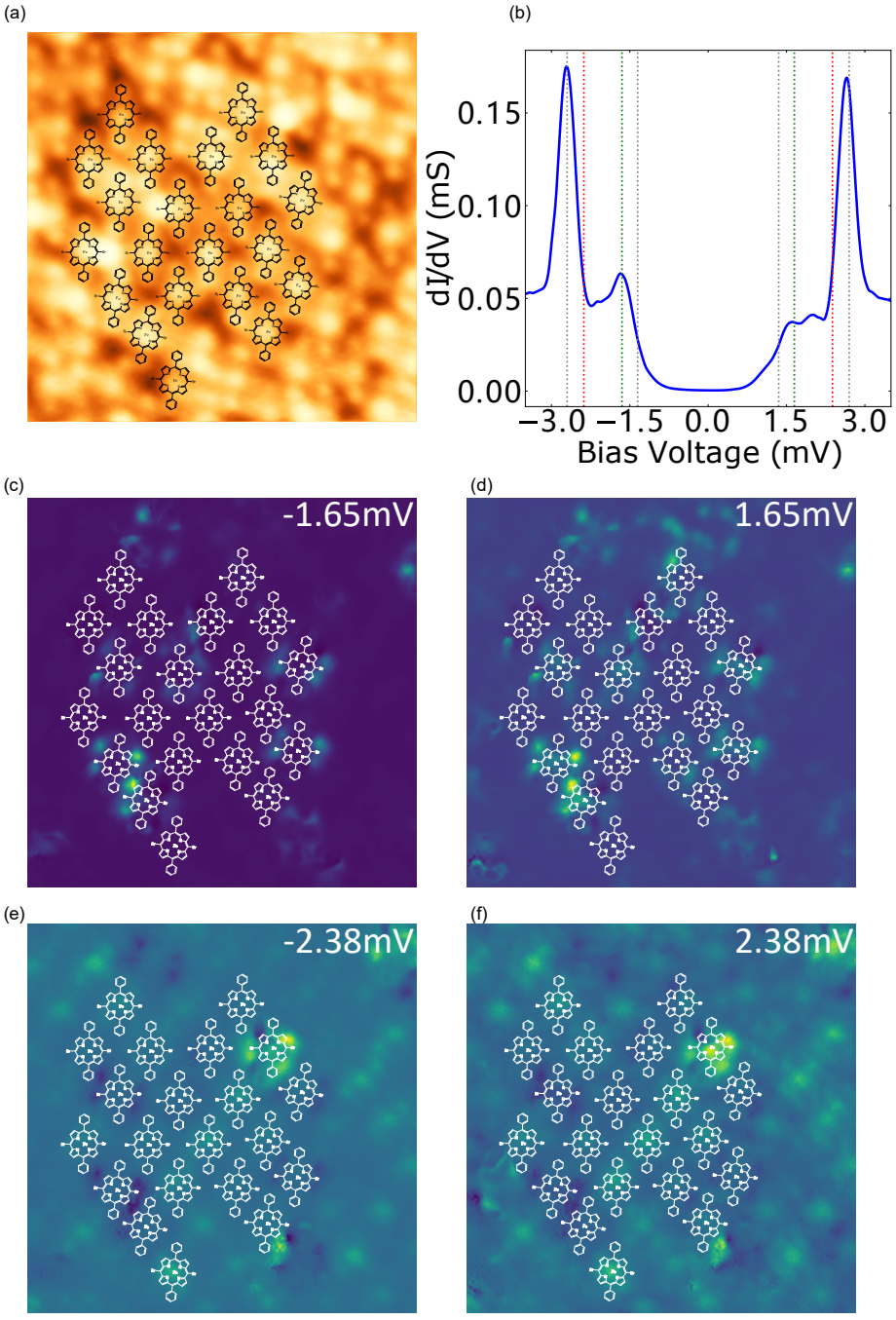

Figure 4.8: $\mathrm{Fe-DBrDPP}$ **molecules on Pb(110) surface without post-annealing.** (a) Topography image ($10\mathrm{x}10\mathrm{nm}^2$, setpoint: 8 mV, 22 pA) of $\mathrm{Fe-DBrDPP}$ molecules on Au(111) surface without post-annealing. Certain $\mathrm{Fe-DBrDPP}$ molecules are marked by sketch. (b) Averaged SIS dI/dV spectra of the area in (a). Gray dashed lines mark the bias voltage of ± 1.35 meV and ± 2.7 meV. Red and green dashed lines mark ± 2.38 meV and ± 1.65 meV. Setpoint: 8 mV, 22 pA, 300 pm. (c-d)(e-f) SIS dI/dV maps of $\mathrm{Fe-DBrDPP}$ supramolecular lattice in (a) at bias voltage ± 1.65 mV and ± 2.38 mV respectively.

during deposition. After the deposition the $\mathrm{Fe-DBrDPP}$/Pb(110) sample is further annealed at 360 K for 20'. This post-annealing process aims to initiate the debromination reaction to form covalently bonded chains of molecules and aims to allow the molecule to adopt a stable conformation.

Once the annealing process is completed we transfer $\mathrm{Fe-DBrDPP}$/Pb(110) sample to STM chamber, then to the cryogenic microscope, without exceeding a pressure over 10^{-10} mbar.

4.5.2 Structural properties of annealed $\mathrm{Fe-DBrDPP}$ supramolecular lattice

Fig. 4.9 shows a large scale topography image of $\mathrm{Fe-DBrDPP}$/Pb(110) sample with post-annealing at 360 K for 20'. We observe large atomically flat terraces of the size around 100 nm and also observe various monolayer supramolecular islands on Pb(110) surface. There are two types of supramolecular lattices marked by red and green solid arrows with different molecular orderings. Both supramolecular structures can be characterized as compact arrangement of rows of $\mathrm{Fe-DBrDPP}$ molecules where the red and green arrows are indicating their orientations. The black arrow indicates the [110] crystal direction.

Most of the supramolecular lattices are of the type marked by red arrows, now labelled **A-type** domains, indicating that such ordering is more energetically favorable than the ones labelled by green arrows, now labelled **B-type** domains. For A-type of lattice, we observe two possible chiral molecular domains which orientation of rows are symmetric to each other with respect to [110] direction. Since both $\mathrm{Fe-DBrDPP}$ molecule (see Fig. 4.4) and Pb(110) surface (see Fig. 4.1 (c)) exhibit two-fold symmetry, such observation indicates that the structure domains break two-fold symmetry due to either unit cell structure or Bravais lattice.

Structural properties of A-type domain

The high-resolution topography image of A-type domains is shown in Fig. 4.10 in which the parallel molecule rows of the supramolecular assemblies are indicated by red dashed lines. The [110] direction of the Pb(110) surface is specified by a black arrow and corrugation of Pb atoms are marked by black dashed lines. The sketch of the $\mathrm{Fe-DBrDPP}$ molecule is placed to best match the topography measured in the STM and STS experiments (method introduced in section (4.7.1), Fig. 4.32). This structural model shows that the molecules do not form covalent bonds in A-type domains. There are multiple reasons for the absence of covalently bonded network e.g. post-annealing temperature of 360 K is not sufficient, Pb(110) surface is not favorable for covalently bonded network formation or halogen bond formation inhibits covalent bond formation [252].

In Fig. 4.10 (a), the most intuitive observation is that besides the molecules in row 1' which are tightly attached to the edge of a Pb monolayer terrace, the rest of A-type assembly exhibits a double periodicity laterally to the molecule rows 2,1,2,1 from left to right (along the blue arrow).

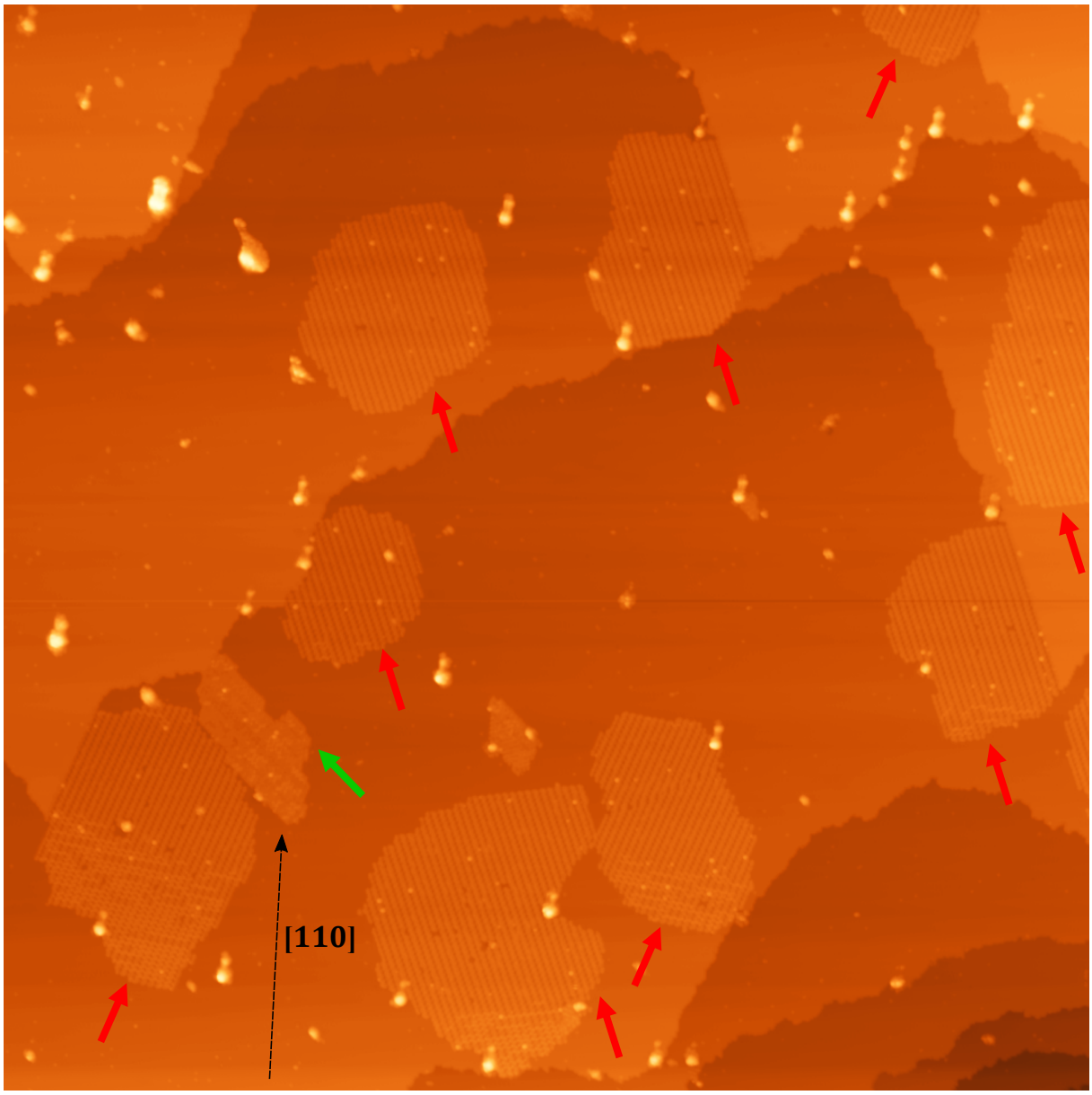

Figure 4.9: Large-range topography image of $\mathrm{Fe-DBrDPP}$ molecules on Pb(110) surface with post-annealing at 360 K. Topography image ($300\mathrm{x}300\mathrm{nm}^2$, setpoint: 512 mV, 9 pA) of self-assembled $\mathrm{Fe-DBrDPP}$ molecule supramolecular lattice on Pb(110) surface with post-annealing at 360 K for 20'. Black dashed arrow indicates [110] direction of Pb(110) surface. Red and green arrows mark the different $\mathrm{Fe-DBrDPP}$ supramolecular lattices.

First let's focus on the molecules in row 1' in which they are tightly bonded to the edge of a monolayer Pb terrace. This observation may indicate that the molecules can bound to free Pb adatoms which surface density is expected to be quite important at the surface preparation temperature, resulting in metal-organic structural assemblies[1]. However the presence of Pb atoms in the structural phases was neither proven in our topography or spectroscopy measurements. For this reason, we consider in the following that supramolecular orderings of A and B-types do not contain Pb adatoms and metal-organic bonds. Moreover, we will see in the next section that molecules in row 1' exhibit similar electronic properties as those in rows 1 that are inside the domain.

According to structural model of $\mathrm{Fe-DBrDPP}$ molecules shown in Fig. 4.10 (a), along each row, including 1', a substantial phenyl-phenyl (now labeled **phenyl-phenyl** bond or π bond, marked by black dashed line in (b)) interaction can be anticipated which is due to the proximity and parallel orientation of the adjacent phenyl-rings. These interactions results a regular arrangement of molecules along the row with a periodicity of about 1.4 nm (marked by vector $\vec{a}$).

Between successive rows 2,1 or 1,2 of molecules, pyrrole-pyrrole hydrogen bonds (now labeled **pyrrole-pyrrole** bond, marked by blue dashed line in (b)) and $\mathrm{Br}\cdots\pi$ halogen bonds (marked by purple dashed lines in (b)) interactions can occur. The structural model of molecules in Fig. 4.10 suggests that molecules should form a supramolecular lattice with periodicity described by vector $\vec{a}$ and $\vec{c}$ which lengths are 1.4 nm and 1.3 nm respectively. However, this can not explain the double periodicity behavior laterally to the rows 2,1,2,1... where the unit cell should be a dimer $\mathrm{Fe-DBrDPP}$ molecules with lattice vector $\vec{a}$ and $\vec{b}$ which lengths are 1.4 nm and 2.2 nm.

The high contrast between rows 2 and 1 in topography image suggests that there is a significant density probability between these successive rows which could be related to inter-molecular orbitals hybridization or localized Pb electronic states at these locations. We will see in the next section that the double periodicity behavior is a feature of delocalized Shiba state i.e. topographic spectral weight is mostly contributed from DOS near Fermi level rather than molecular orbital that is related to molecule's structure.

There are two factors that may be related to the double periodicity behavior:

1. By studying together the structure of $\mathrm{Fe-DBrDPP}$ molecules in A-type domains and the arrangement of Pb atoms in (110) surface which corrugation pattern is marked by parallel black dashed lines in Fig. 4.10 (a). The axes of all $\mathrm{Fe-DBrDPP}$ molecules are following the [110] orientation in A-type domains and the molecules in rows 1 are siting almost perfectly on the upper rows of Pb atoms of the substrate while molecules in rows 2 are mostly sitting in hollow sites of the Pb(110) reconstruction. Thus the double periodicity behavior in A-type domain might originate from the different adsorption site of molecules in rows 1 and 2.

[1]The nature of such bonding is unknown, it could be the result of a debromination of the molecules.

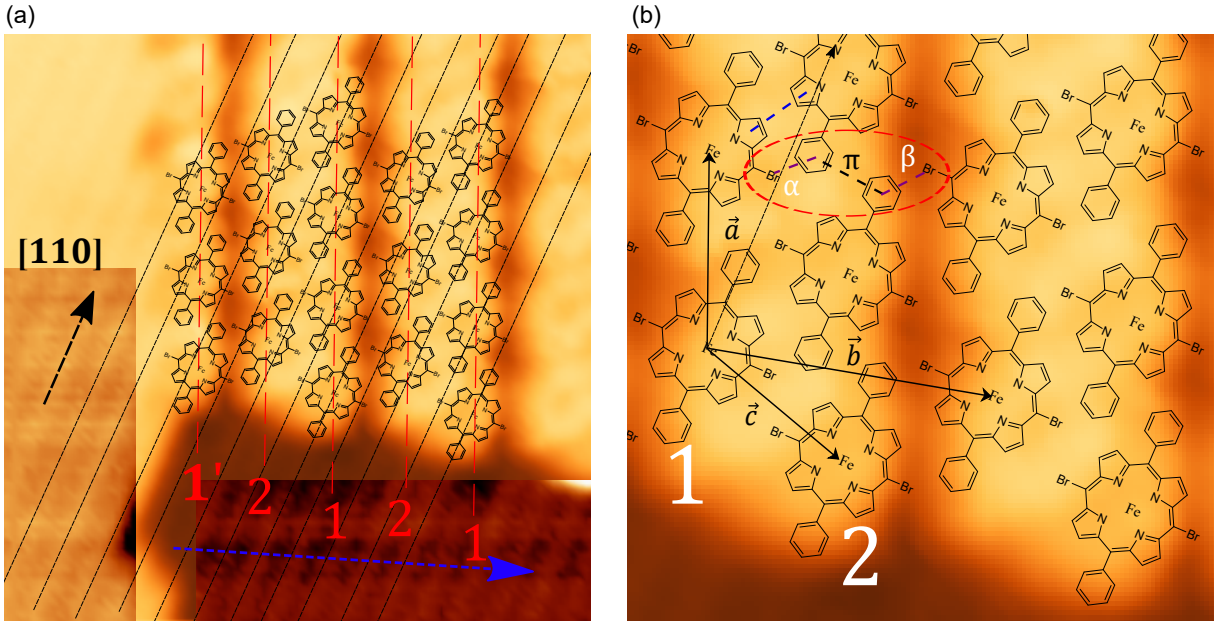

Figure 4.10: Small-scale topography images of A-type $\mathrm{Fe-DBrDPP}$ molecules domain on Pb(110) surface with post-annealing at 360 K. (a) Topography image ($9\mathrm{x}9\mathrm{nm}^2$, setpoint 8 mV, 150 pA) of A-type self-assembled supramolecular lattice of $\mathrm{Fe-DBrDPP}$ molecules and a single row of molecules attached to a step edge of Pb. Red lines mark the rows of molecules which is also the supramolecular lattice orientation, blue dashed arrow indicates the direction of crossing different molecular rows, black dashed arrow marks the [110] direction of Pb(110) surface and black dashed lines mark the corrugation of Pb atoms in (110) surface. (b) Molecules' sketch illustrating unit cell, lattice vector and bonding types of A-type domain. $\mathrm{Fe-DBrDPP}$ molecules labelled 1, 2 form the unit cell of A-type domain. $\vec{a}$, $\vec{b}$ denote the lattice vectors and $\vec{c}$ describes the dimer unit cell of A-type domain, their lengths are respectively 1.4 nm, 2.2 nm and 1.3 nm. Pyrrole-pyrrole hydrogen bond, π bond and Br$\cdots\pi$ halogen bond are respectively marked by blue, black and purple dashed lines. Two Br$\cdots\pi$ halogen bonds with different nature are labeled by α and β respectively.

2. In red circle marked region in Fig. 4.10 (b), from left to right we observe a successive bonds of α Br$\cdots\pi$ halogen bond, π bond and β Br$\cdots\pi$ halogen bond. In such sandwich bonding configuration, α and β halogen bonds could adapt different electronic behavior due to charge effect[2].

Structural properties of B-type domains

Fig. 4.11 shows the boundary between two antiphase B-type domains in which we can easily recognize the shape of $\mathrm{Fe-DBrDPP}$ molecules with its two phenyl rings and macrocycle center and the $\mathrm{Fe-DBrDPP}$ molecule's sketch fits well with topographic character in (b).

B-type domain also consists of parallel rows of $\mathrm{Fe-DBrDPP}$ molecules. According to structural model in Fig. 4.11 (b). The orientation of axes of all $\mathrm{Fe-DBrDPP}$ molecules in B-type domains are about 30° with respect to [110] direction, and like A-type case molecules in rows 1 (and 1') are siting almost perfectly on the upper rows of Pb atoms of the substrate while molecules in rows 2 (and 2') are mostly sitting in hollow sites of the Pb(110) reconstruction. As

[2]From [135] it appears that if there exists two halogen elements on opposite-sites of π bond, the formation of halogen$\cdots\pi$ bond with only one of them is more energetically favorable, which could explain the occurrence of α and β halogen bonds.

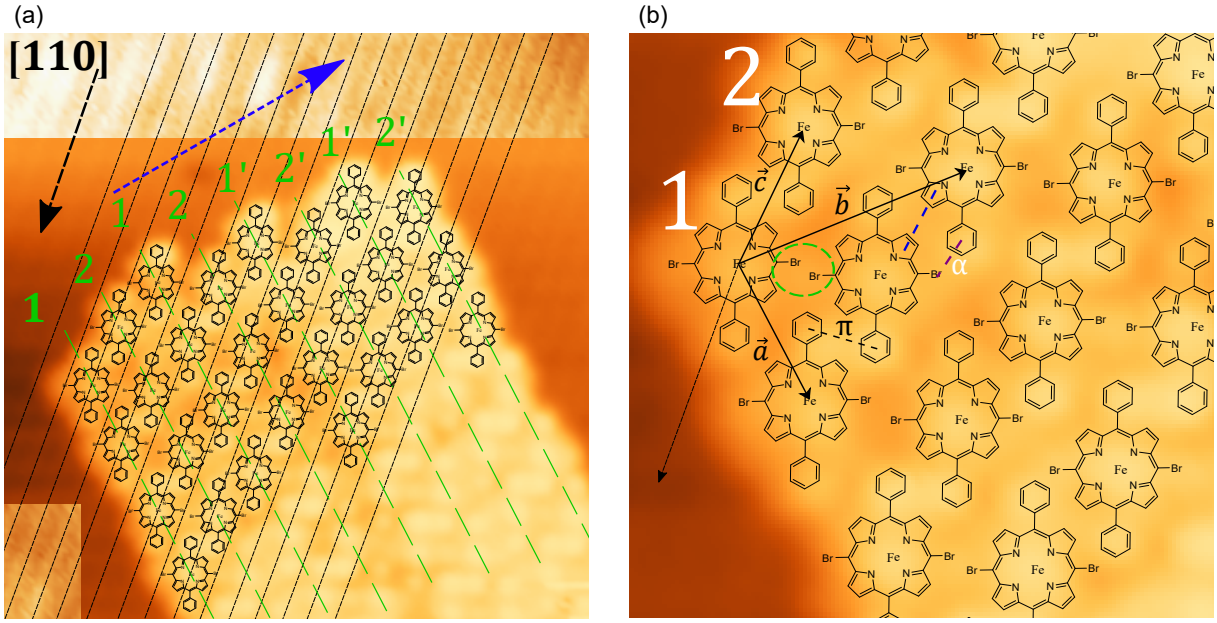

Figure 4.11: Small-scale topography images of B-type $Fe-DBrDPP$ molecules domain on Pb(110) surface with post-annealing at 360 K. (a) Topography image ($12x12nm^2$, setpoint 8 mV, 60 pA) of boundary between two antiphase B-type domains. Green lines mark the lines of molecules which is also the supramolecular lattice orientation, blue dashed arrow indicates the direction of crossing different molecular rows, black dashed arrow marks the [110] direction of Pb(110) surface and black dashed lines mark the corrugation of Pb atoms in (110) surface. (b) Molecules' sketch illustrating unit cell, lattice vector and bonding types of B-type domain. $Fe-DBrDPP$ molecules labelled 1, 2 form the unit cell of B-type domain. $\vec{a}$, $\vec{b}$ denote the lattice vectors and $\vec{c}$ describes the dimer unit cell of B-type domain, their lengths are respectively 1.4 nm, 2.2 nm and 1.3 nm. Pyrrole-pyrrole hydrogen bond, π bond, α Br$\cdots\pi$ halogen bond are respectively marked by blue, black and purple dashed lines. Br$\cdots$Br halogen bond is marked by green circle.

a consequence, the unit cell is a dimer consisting of two $Fe-DBrDPP$ molecules in successive rows 1,2 (molecules labeled 1,2 in (b)). Between these rows the molecules appear to be bonded by π bond (marked by black dashed line) and halogen bond (Br$\cdots$Br, marked by green dashed circle). While between rows 2,1, α Br$\cdots\pi$ halogen bond (marked by purple dashed line) and π bonds occur. The lattice vectors $\vec{a}$, $\vec{b}$ are 1.4 nm and 2.2 nm while the vector $\vec{c}$ describing dimer is about 1.3 nm. These values are almost the same as A-type case, but their orientations with respect to [110] direction are different.

Compared to A-type structure, the orientation of $Fe-DBrDPP$ molecules and inter-rows bonding mechanism are different. For B-type structure, between rows 1,2 there ares halogen-halogen bonds between adjacent Br atoms and π bonds between adjacent phenyl rings, the resolved topography image shows relative weak spectral weight on halogen bond sites which is a result of low DOS [134]. Between rows 2,1 there are α Br$\cdots\pi$ halogen bonds and pyrrole-pyrrole bonds that show relatively strong spectral weight like A-type case.

4.5.3 Electronic properties of annealed $\mathrm{Fe-DBrDPP}$ supramolecular lattices

In this section we will study the spectroscopy data of A-type ordering lattices and try to find out the relation between its structure and spectroscopic (electronic) properties. The B-type domains exhibit similar electronic behavior as A-type, its data are presented in supplementary section (4.7.1).

We have introduced before that the SIS dI/dV spectra obtained by a superconducting tip are not directly proportional to the DOS, there exist bias shift and negative conductance features that can yield disturbing features in conductance maps. To correctly understand the electronic properties, our studies will also include deconvoluted DOS data.

In our work, we mainly focus on the spatial dependence of energies and distribution of Shiba states in large-scale supramolecular lattices, these data are usually obtained by studying two-dimensional deconvoluted DOS maps and DOS stacking plot along the linecuts rather than single spectrum, thus the tip DOS imperfections would be suppressed from the final results. Yet we should keep in mind that the confidence of deconvoluted data relies on the parameters we have used in deconvolution process (see section (2.5.3)), sometimes the deconvoluted data may be nonphysical. Hence for each experiment we should compare the raw SIS dI/dV data with deconvoluted DOS to ensure that calculated DOS is reliable.

Two-channel spin-1 Shiba states

We first study the deconvoluted DOS and original SIS dI/dV spectra of A-type domains shown in topography image Fig. 4.12 (a). The spatial variation of SIS dI/dV spectra along the molecular row marked by red arrow in (a) is plotted in (b). Red, green and blue dashed lines refers to the centres of three successive $\mathrm{Fe-DBrDPP}$ molecules in this line which marked by points with same color in (a), their SIS dI/dV spectra are plotted in (c). The corresponding deconvoluted DOS data are plotted in (d) and (e) which horizontal axis become energy (meV) instead of bias voltage (mV). (f)-(i) show the SIS dI/dV maps of A-type domains shown in (a) of bias voltage ± 2.0 mV and ± 2.49 mV indicated in the figure, the corresponding deconvoluted DOS maps are plotted successively in (j)-(m) of energies ± 0.66 meV and ± 1.14 meV.

By comparing the original SIS dI/dV spectra with corresponding deconvoluted DOS respectively shown in (c) and (e), the effect of deconvolution on spectra can be estimated. The features in window of tip's gap energy [-1.35 meV, 1.35 meV] in (c) is removed and the negative conductance signature is eliminated. The effect of deconvolution on maps can be visualized by comparing upper SIS dI/dV (f)-(i) figures and lower DOS (j)-(m) figures. We observe similar feature in the upper and lower sets of maps which energies are shifted by 1.35 meV. In the upper sets of figures showing SIS dI/dV maps, we can clearly see the negative conductance caused dark feature in maps (g)(h) of bias ± 2 mV. In lower sets of figures of deconvoluted DOS maps (k)(l), such dark feature is removed and the non-negative DOS is recovered.

From both SIS dI/dV data and deconvoluted DOS data we find two pairs of Shiba states, one

locates at about $\pm E_1 = \pm 0.66$ meV that can be easily distinguished in stacking plots ((b) and (d)). The other one locates at $\pm E_2 = \pm 1.14$ meV which energy is close to gap edge ($\delta = \pm 1.35$ meV) and is difficult to be observed in the stacking plots, however they can be distinguished in maps (f)(i) and (j)(m). The existence of two pairs of Shiba states indicates that $\mathrm{Fe-DBrDPP}$ molecule has S = 1 magnetic state related to two channels for Shiba states. For simplicity we call the Shiba states of low energy (closer to Fermi level) **channel 1 Shiba states (CS1)** and the Shiba states with high energy (closer to gap edge) **channel 2 Shiba states (CS2)**.

In (d) we observe that the energy of CS1 varies depending on adsorption sites. The red, green and blue dashed lines in (d) respectively correspond to the DOS measured on red, green and blue points on red solid arrow in (a), which are the centers of three successive molecules in the same row. Their energies increase monotonously in real space, indicating an monotonous change of coupling strength with substrate which determines the Shiba energy (see equation 1.29). More importantly, electron-like components vary in a continuously way along the plot line regardless of molecule distribution. Such continuous variation of Shiba energy could be related to tip effect which tunes the interaction between molecule and substrate (Tip effect will be discussed in detail in section (4.6.3)).

For spectra measured on the macrocycle of molecules (location marked by dashed lines in (b) and points in (a) of same color) shown in (e), the hole-like component peak always exhibit stronger spectral weight than the electron one while for those spectra measured on positions between macrocycles (i.e. on phenyl-phenyl π bonds) the electron-like component is stronger than hole-like one. The reverse relative spectral weight behavior in molecular system has already been reported in [97, 98] where the spectral weight flips when tunneling through different molecular orbitals, however the orbitals do not delocalize outside the molecule and Shiba energy does not vary on each molecule.

Here the observation of Shiba feature between molecules and the continuous variation of Shiba energy could imply that the spin-polarized orbital that gives rise to CS1 may distribute along the molecular row, i.e. there might exist hybridized molecular orbital along molecular rows, probably due to strong inter-molecular coupling.

Orbital properties of Shiba states

Thanks to the DOS maps, we can directly visualise the distribution of Shiba states and the corresponding molecular orbitals that give rise to them[3].

Fig. 4.12 (k) shows the DOS map at -0.66 meV that illustrates the distribution of hole-like component signature of CS1. We observe a well-ordered Shiba supramolecular lattice which unit cell exhibits rectangular shape that locates on the macrocycle of each $\mathrm{Fe-DBrDPP}$ molecule, excepts two molecules marked by cyan arrows which do not show any feature. The corresponding electron-like component map at 0.66 meV is shown in Fig. 4.12 (l) in which CS1 delocalizes

[3]It has been introduced in section (1.3.3) that distribution of Shiba states is just related to the distribution of orbitals as Shiba states exhibit spatial dephasing.

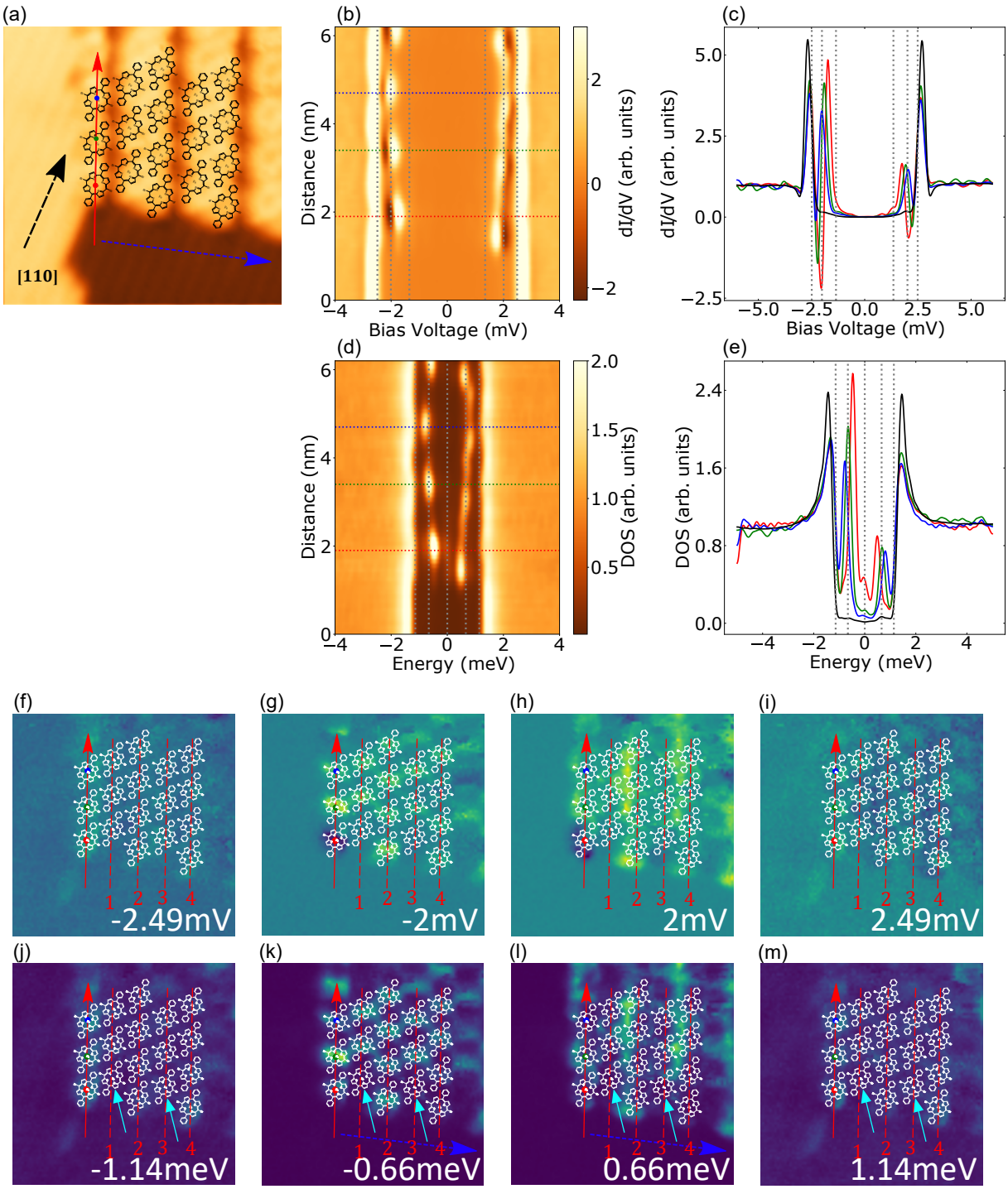

Figure 4.12: Spectroscopic data of A-type self-assembled supramolecular lattice of $\mathrm{Fe-DBrDPP}$ **molecules on Pb(110) surface.** (a) Same topography image as Fig. 4.10 (a), red solid arrow marks the stacking plot line, red dashed lines labeled from 1 to 4 refer to four successive molecular rows, blue arrow indicates the direction crossing different molecular rows. (b) Stacking plot of point SIS dI/dV spectra (setpoint: 8 mV, 150 pA) along the molecular row represented by red arrow in (a). Horizontal red, green and blue dashed lines mark the positions of points of same colors in (a) which are the center of different $\mathrm{Fe-DBrDPP}$ molecules. Vertical gray dashed lines mark the bias voltage of ± 1.35 mV, ± 2.0 mV and ± 2.49 mV. (c) SIS dI/dV spectra measured at crosses position with same colors in (a). Black curve measured on Pb(110) surface with position far from the supramolecular lattice. (d)(e) Deconvoluted DOS from SIS data of (b)(c). Vertical gray dashed lines mark the energies of 0 meV, ± 0.66 meV and ± 1.14 meV. (f)-(i) SIS dI/dV maps of bias ± 2.0 mV and ± 2.49 mV of same region of (a). (j)-(m) Deconvoluted DOS maps of energies ± 0.66 meV and ± 1.14 meV of same region of (a). All spectra are smoothed and normalized.

from the macrocycle and distributes between the molecules[4]. The strongest delocalized feature is found between rows 1,2 and 3,4, this feature explains the double periodicity behavior in topography (Fig. 4.10) as the corresponding setpoint is 8 mV, 150 pA, i.e. the electron-like component of CS1 have important contribution to the topographic weight.

By comparing the location of delocalized pattern in Fig. 4.12 (l) with topography image Fig. 4.10, we find that the electron-like component of CS1 locates on pyrrole-pyrrole hydrogen bonds and α Br$\cdots\pi$ halogen bonds, a similar behavior is also observed in B-type domains (see Fig. 4.33 (c) and Fig. 4.11). This implies that inter-molecular interaction that affects molecule's electronic properties can occur in these supramolecular lattices. Thus we attribute the delocalized pattern that distributes between molecules to the hybridized inter-molecular orbitals due to inter-molecular coupling.

Fig. 4.12 (j) and (m) respectively show the DOS maps at -1.14 meV and 1.14 meV in which the shape of hole-like and electron-like components of CS2 are visualized. Almost all molecules exhibit CS2 feature around ± 1.14 meV on their macrocycles excepts the exotic molecule at extremity of rows 1 marked cyan arrow show neither CS2 feature at ± 1.14 meV nor CS1 feature in ± 0.66 meV. The reason why CS1 and CS2 show different distribution and why CS2 feature can disappear are related to corresponding molecular orbitals of Shiba states and the ground state nature of Shiba states, they will be discussed in details in sections (4.6.4).

Exotic molecules at perimeters of supramolecular lattice

In this section we will focus on the exotic molecules marked by cyan arrows in Fig. 4.12 (k-l). The variation of DOS along four successive molecular rows marked by red arrows labeled from 1 to 4 are shown in Fig. 4.13 (b)(c)(e)(f). (d) shows the DOS map of 0 meV.

In (b) we have observed a zero-energy Shiba state feature on cyan arrow marked molecule's macrocycle (red point on arrow 1 in (a)) while other molecules exhibit ± 0.66 meV CS1. In (c), along arrow 2, we can also find the zero-energy state feature between green and red point marked molecules in arrow 2, but all molecules in arrow 2 (red, green, blue and yellow points) show ± 0.66 meV Shiba states, which implies that such zero-energy feature is not generated from molecules in arrow 2. From zero-energy DOS map shown in (d) we observe that zero-energy feature on arrow 1 and 2 are just a part of large zero-energy feature which most intense part locates between row 1 and 2. Thus we believe the zero energy Shiba state originates from the molecule locating at the extremity of arrow 1. This zero-energy Shiba state localizes on pyrrole-pyrrole and α Br$\cdots\pi$ halogen bonds.

Similarly in Fig. 4.13 (d)(e)(f), the molecule at the extremity of arrow 3 also shows a Shiba state locating on pyrrole-pyrrole and α Br$\cdots\pi$ halogen bonds that exhibits signature in arrow 4. The energy of this Shiba state is slightly higher than 0 meV and it behaves like CS1 by showing energy variation in (e). This implies that the low-energy states between arrows 1,2 and 3,4 are

[4]Here we use word "delocalize" rather than "dephase" to describe the hole-like and electron-like components mismatch because spatial dephasing of Shiba states has been well understood in treating point-like atomic scatterer, here in the case of delocalized inter-molecular orbital scatterer the dephase notion might not be suitable.

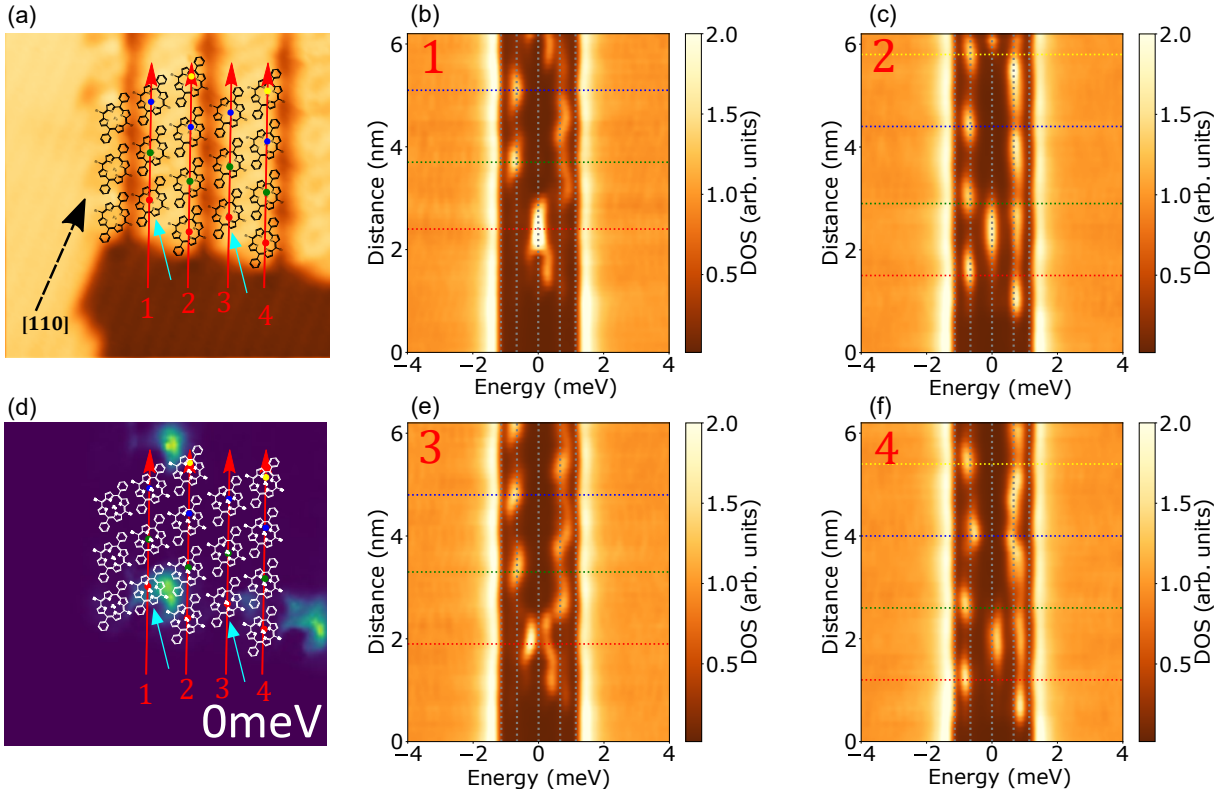

Figure 4.13: (a) Same topography image as Fig. 4.10 (a), red solid arrows are the stacking plot lines labeled from 1 to 4. Two cyan arrows mark the exotic molecule showing zero-energy CS1. (b)(c)(e)(f) Stacking plot of point DOS along the red arrows in (a) with the same label. Horizontal red, green and blue dashed lines mark the positions of points of same colors on corresponding arrow. Vertical gray dashed lines mark the energies of 0 meV, ± 0.66 meV and ± 1.14 meV. (d) DOS map at zero energy.

CS1.

In previous section we attributed the slight energy variation of CS1 to tip effect which varies the coupling strength between molecule with substrate. Here the low-energy behavior of molecules at extremities of rows 1,3 can not be simply explained by the interaction of tip as the Shiba energy has changed a lot. We notice that these exotic molecules appear to be found at extremities of oddly labeled arrows (e.g. 1, 3, 5) while the molecules at extremities of evenly labeled arrows (e.g. 2, 4, 6) behave just like those inside the domains. Hence we believe the geometry effect[5] plays an important role of low-energy behavior Shiba energy.

To verify the geometry origin, we present the energies of Shiba states for all molecules at perimeter of A-type domain in Fig. 4.14 in which oddly labeled rows from 1 to 9 are marked by colored dashed lines.

The DOS maps at -0.66 meV and 0 meV illustrating CS1 of a large region are shown in (b) and (c). Apart from the molecules at perimeter of the domain almost all molecules exhibit -0.66 meV CS1 feature. The low or zero energy Shiba states tend to localize at the perimeter of the domain. The stacking plot of DOS along red arrow which crosses the molecules at perimeter

[5]Term "geometry" is usually used to for single molecules, especially for those lie in unusual environment such as molecules near interface, it consists of molecules' conformation, supramolecular lattice mismatch and intermolecular interaction. For molecules in well-ordered supramolecular lattices the term "ordering" is usually used. Nevertheless, in this thesis they can be substituted for each other.

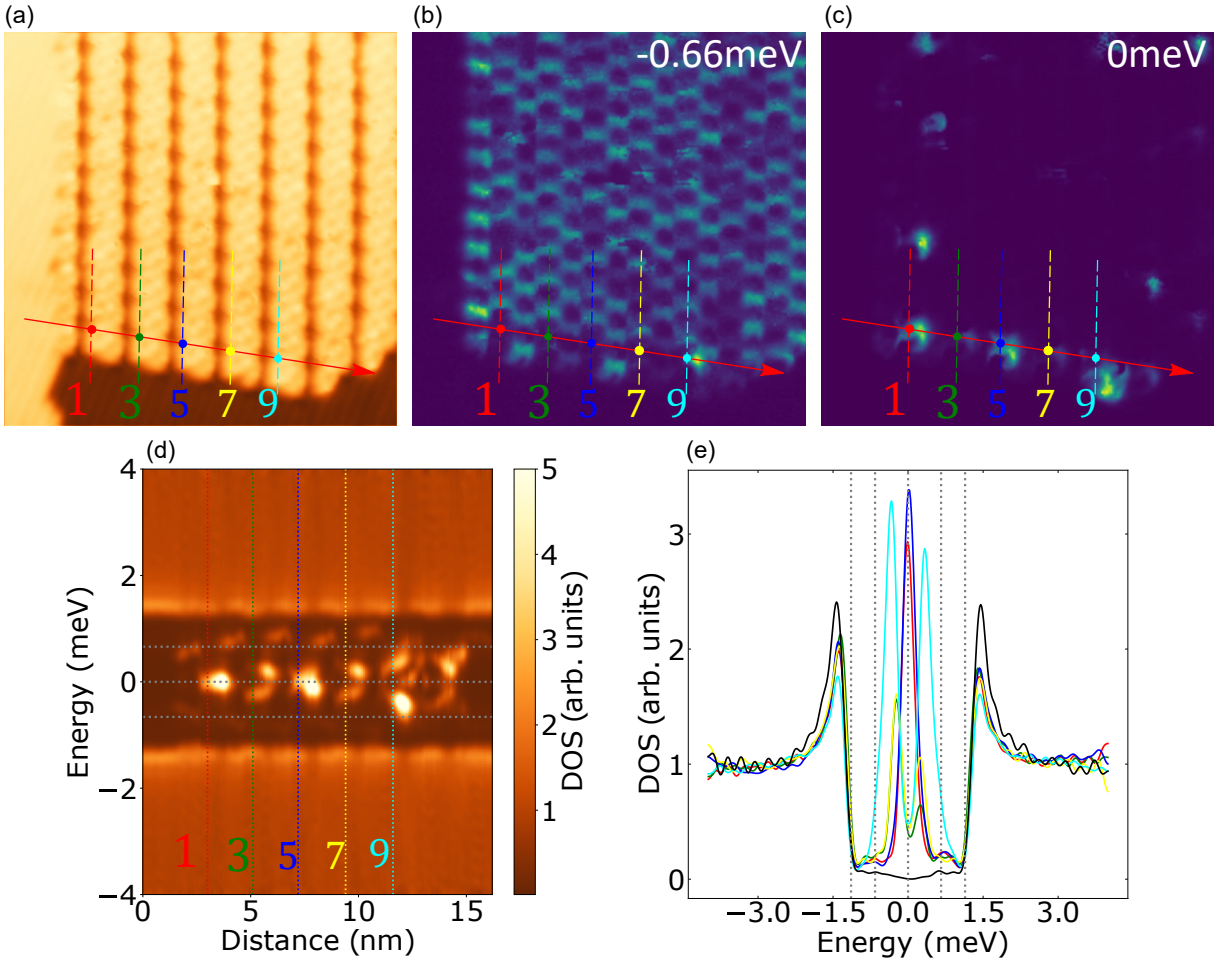

Figure 4.14: Procedure to determine molecular ordering. (a) Topography image ($18\text{x}18\text{nm}^2$, setpoint: 8 mV, 150 pA) of A-type self-assembled supramolecular lattice of $\text{Fe}-\text{DBrDPP}$ molecules on Pb(110) surface after 360 K post-annealing. Oddly labeled molecular rows are marked by dashed lines with different colors. Red arrow indicate the stacking plot line, the intersections between red arrow and molecules lines are marked by points with different colors, which are the centers of $\text{Fe}-\text{DBrDPP}$ molecules at the extremities of corresponding molecular rows. (b)(c) DOS maps at -0.66 meV and 0 meV. (d) Stacking plot of point DOS along the red arrows in (a), colored dashed lines indicates the point positions of same colors. (e) DOS measured on the points with same color shown in (a).

(extremities of rows) is presented in (d). It is obvious that CS1 in oddly labeled rows (1, 3, 5, 7, 9) lie closer to Fermi level compared to the standard CS1 which energy is around 0.66 meV. This can be understood as that the molecules at the perimeter of the domain can have different geometry environment which result a different coupling strength with the substrate comparing with the molecules inside the domain.

4.5.4 Conclusion

To summarize, by implementing a post-annealing of 360 K for 20', $\text{Fe}-\text{DBrDPP}$ molecules form self-assembled supramolecular lattices on Pb(110) surface. Depending on the orientation of the molecule respect the [110] direction of Pb(110) surface, two kinds of supramolecular lattice named A-type domains and B-type domains can be formed. None of these two types of ordering includes covalent bonding network but only hydrogen bonds and halogen bonds.

Most of the supramolecular lattices adopt A-type ordering, indicating a more favorable molecule self-organisation than in B-type domains in such post-annealing configuration. $\mathrm{Fe-DBrDPP}$ molecules in A-type domains could adopt an unknown conformation due to inter-molecular interaction that leads to a double periodicity feature in topography where $\mathrm{Fe-DBrDPP}$ molecule dimer becomes the unit cell to proper describe the doubled periodic supramolecular lattice. The $\mathrm{Fe-DBrDPP}$ molecules in B-type domains adopt a relative flat lying conformation where inter-molecular interaction should be lower, resulting a well distinguishable single molecule feature in topography.

The spectroscopic studies have revealed that $\mathrm{Fe-DBrDPP}$ molecules in both A-type domains or B-type domains exhibit S = 1 magnetic state and there almost always exist two channels for Shiba states formation. Shiba states originated from different channels show completely different behavior. The Shiba states originated from channel 1 are closer to Fermi level and always show a strong spatial delocalization behavior where the electron-like component state distributes between successive rows of molecules. This delocalized signature is related to energy of CS1 and also related to conformation of molecule. In A-type domains the delocalization is so strong that it results a double periodicity feature in topography while in B-type domains the delocalization is not strong enough to induce double periodicity characterization. Shiba states originate from channel 2 are closer to gap edge and do not exhibit obvious spatial delocalization.

We discover that due to different inter-molecular interaction strength, the molecules at the perimeter of A-type supramolecular lattice shows a significantly lower Shiba energy than most of CS1, where the delocalization is strong enough that both hole-like and electron-like components state localize outside the molecule, which further evidences the intimate relation between geometry and Shiba states' properties. We also find that CS1 can vary its energy in a continuous way along the molecular row which is probably due to tip interaction, such behavior could imply the existence of spin-polarized hybridized molecular orbitals that give rise to Shiba state, yet we do not observe any obvious behavior indicating the existence of spin-spin interaction between neighbor $\mathrm{Fe-DBrDPP}$ molecules in spectroscopy.

4.6 $\mathrm{Fe-DBrDPP}$ assemblies on Pb(110) high-temperature configuration

In last section, we have studied the self-assembled $\mathrm{Fe-DBrDPP}$ molecule supramolecular lattice on Pb(110) surface with post-annealing temperature of 360 K and period of 20' where we do not find covalently bonded molecular network.

In this section, we will study the high-temperature phase self-assembled $\mathrm{Fe-DBrDPP}$ molecule supramolecular lattices on Pb(110) surface with the post-annealing temperature of 400 K. By increasing annealing temperature, we hope to observe a more stable molecular ordering, where perhaps covalent bonds are present for supramolecular lattice formation.

4.6.1 Preparation for STM experiments

$Fe-DBrDPP$ molecules are evaporated at 500 K and deposited for 70" by means of OMBE on freshly prepared clean Pb(110) surface which is held at 400 K during deposition by radiative heating. When deposition is complete $Fe-DBrDPP$/Pb(110) sample is further annealed at 400 K for 10'.

Once the annealing process is completed we transfer $Fe-DBrDPP$/Pb(110) sample to STM chamber for experiment without exceeding a pressure over 10^{-10} mbar.

4.6.2 Structural properties of $Fe-DBrDPP$ supramolecular lattice

Fig. 4.15 shows a large scale topography image of $Fe-DBrDPP$/Pb(110) sample with post-annealing at 400 K for 20'. Compared to the low-temperature phase lattices shown in Fig. 4.9, the ordering of supramolecular lattices are more abundant. Although it may look complicated, all $Fe-DBrDPP$ supramolecular lattices can still be characterized as compact arrangement of parallel rows of $Fe-DBrDPP$ molecules just as what we have learnt before.

According to the topographic character and the orientation of molecular row (marked by colored dashed lines) with respect to [110] direction of surface (marked by black dashed arrow), there are three basic types (ordering) of molecular rows shown in Fig. 4.15.

The first one is what we call "1B" (ordering) whose topographic character exhibits a strong bright spot. The orientation "1B" molecular row (red lines) is about 60° with respect to [110] direction of Pb(110) surface.

The second one is called "4mer" phase or for simplicity "4mer". The orientation of "4mer" molecular rows are about 80° with respect to [110] direction. There exists two types of "4mer" phases with different topographic character where "4mer-A" molecules exhibit bright lines feature parallel to "4mer" line (green lines) while "4mer-B" molecules exhibit a well distinguishable $Fe-DBrDPP$ molecule's shape in topography.

The last one, called "0B", that also exhibits easily distinguished $Fe-DBrDPP$ molecule's shape like "4mer-B" molecule. "0B" molecular row (blue line) is parallel to "1B" molecular row and adapts the same periodicity as "1B" row.

Because of Pb(110) surface symmetry, for each ordering, there are always two possible chiral molecular domains which orientation of rows are symmetric to each other with respect to [110] direction. For example, in Fig. 4.15 the white dashed line is parallel to [110] direction, it marks the interface between two supramolecular lattices with symmetric orientation where the right one is a pristine "1B" supramolecular lattice, left one is a "1B+0B" composite supramolecular lattice.

"4mer" structure

To better understand molecules' conformation in "1B", "0B" and "4mer" ordering, Fig. 4.16 shows a zoom-in of Fig. 4.15 which contains three basic sub-supramolecular lattices shown in

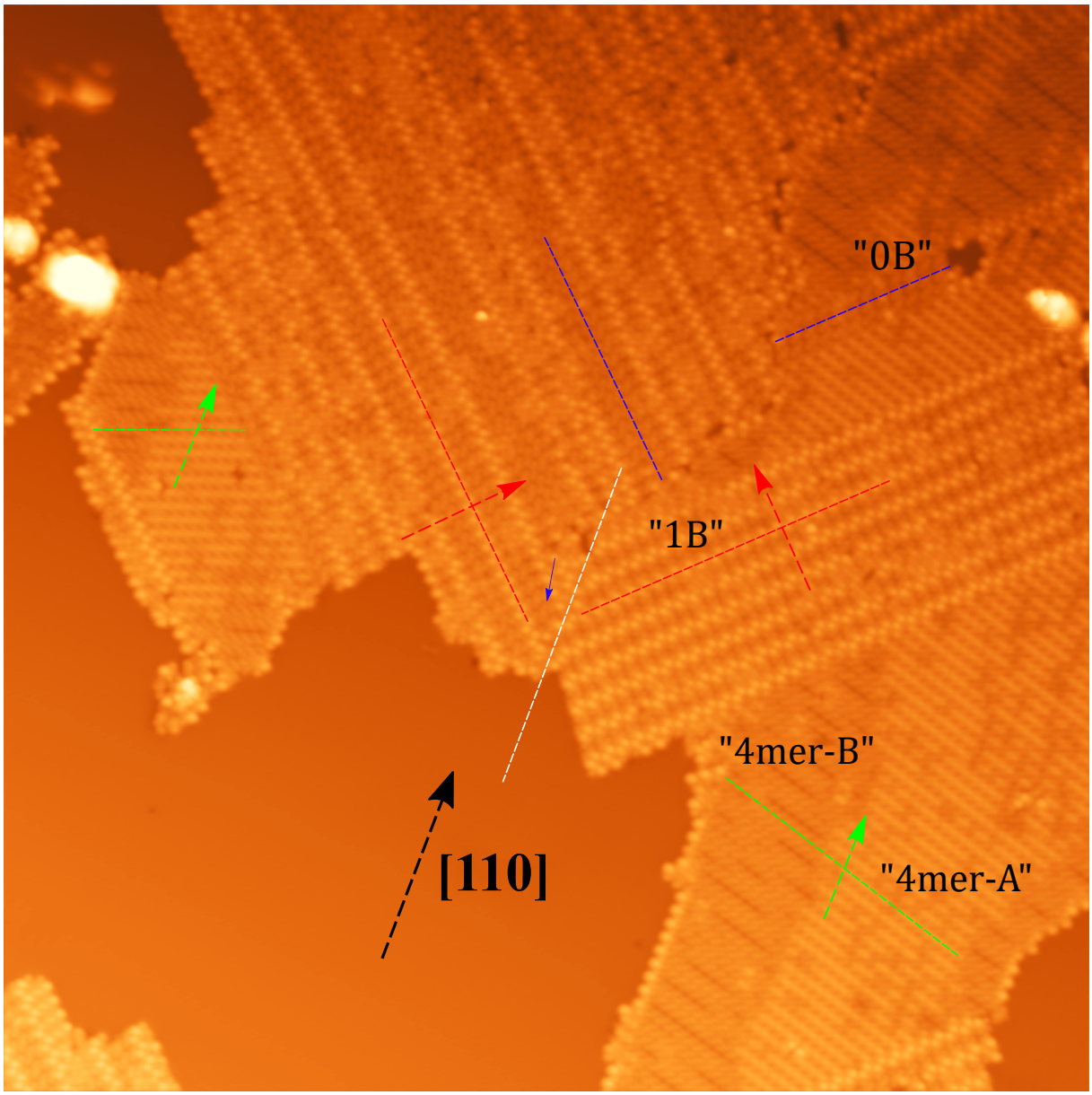

Figure 4.15: Large scale topography images of $\mathrm{Fe-DBrDPP}$ **supramolecular lattices on Pb(110) surface with post-annealing at 400 K.** Large scale topography image ($100\mathrm{x}100\mathrm{nm}^2$, setpoint: 510 mV, 20 pA) of self-assembled $\mathrm{Fe-DBrDPP}$ molecule supramolecular lattice on Pb(110) surface with post-annealing at 400 K. Different supramolecular lattices can be described by compact arrangement of parallel rows of molecules which exhibit different topography characters. Three different molecules rows labeled by "1B", "4mer" and "0B" are respectively marked by red, green and blue dashed lines. Colored dashed arrows indicate the direction crossing adjacent molecules rows along which supramolecular lattice is formed. Blue solid arrow marks one "0B" molecule. Black and white dashed arrow marks the [110] direction of Pb(110) surface.

(b), (c) and (d).

We start with studying the structure of "4mer" molecules. The electronic properties of "4mer-A" and "4mer-B" molecules are identical (see section (4.7), Fig. 4.34), from now on we treat them together as "4mer" molecule. From (b), "4mer" molecules adopt saddling conformation where two bright pyrrole rings, Fe center and phenyl rings exhibit bright features that can be easily distinguished topographically, the Br atoms are resolved as depression in topography image, indicating the absence of molecular orbital near Fermi level on Br site.

Along each "4mer" molecular row (green dashed line), molecules are bonded by halogen bond (Br$\cdots$Br bond, marked by green dashed circle) while between successive rows pyrrole-pyrrole (π) bonds occur. The orientation of axes of all $\mathrm{Fe-DBrDPP}$ molecules in "4mer" lattice are about 30° with respect to [110] direction. "4mer" lattice can be described by a monomer unit cell with lattice vectors $\vec{a}$, $\vec{b}$ which lengths are respectively 1.1 nm and 1.3 nm.

The ordering of "4mer" lattice is similar to B-type lattice shown in Fig. 4.11 but for "4mer" ordering it is clearly more compact.

"1B" and "0B" structure

The notion of "1B" or "0B" has been introduced in section (4.4.2) that it refers to number of bromine atom that $\mathrm{Fe-DBrDPP}$ molecule has dissociated. For "1B" molecules, they dissociate one of the bromine atoms and forms a chemical bond that bonds strongly with Pb atom of Pb(110) surface, resulting a bright spot in topography (Fig. 4.16 (d)). For "0B" molecules, they preserve two bromine atoms and exhibit a clear three spots shape in topography.

In (c), along "1B" molecular row, neighbor $\mathrm{Fe-DBrDPP}$ molecules appear to be bonded by a γ bond (marked by purple dashed circle). While along "0B" molecular row, neighbor molecules appear not to be directly bonded together. Between successive "1B" (and "0B") molecular rows the adjacent $\mathrm{Fe-DBrDPP}$ molecules are bonded by α Br$\cdots\pi$ halogen bonds (marked by purple dashed circle) between their preserved Br atom and phenyl ring.

Hence "1B" molecules can be considered as variant of "0B" molecules, they exhibit same periodicity along each row or laterally to the rows and the orientation of axes of "1B" and "0B" molecules are almost parallel to [110] direction (within $\pm$ 10°). They can be described by lattice vectors $\vec{a}$, $\vec{b}$ which lengths are respectively 1.2 nm and 1.1 nm.

The inter-molecular bonding mechanism and orientation of "1B" and "0B" molecules are very similar to low-temperature phase A-type ordering shown in Fig. 4.10, but here "1B" and "0B" lattices are more compact.

As we have seen in large scale topography image (Fig. 4.15) that whatever the molecular ordering inside the supramolecular lattice there almost always exist bright spot features at the edges. These spot features could be due to "1B" molecule formation at edges by debromination. This could imply that the "1B" molecule is very stable and has the strongest coupling with substrate, once the molecules at the edges of supramolecular lattice become "1B" molecules that bond to the surface, they block the growing of supramolecular lattices.

There are two types of "1B" molecules of different topographic character in (d). Type1

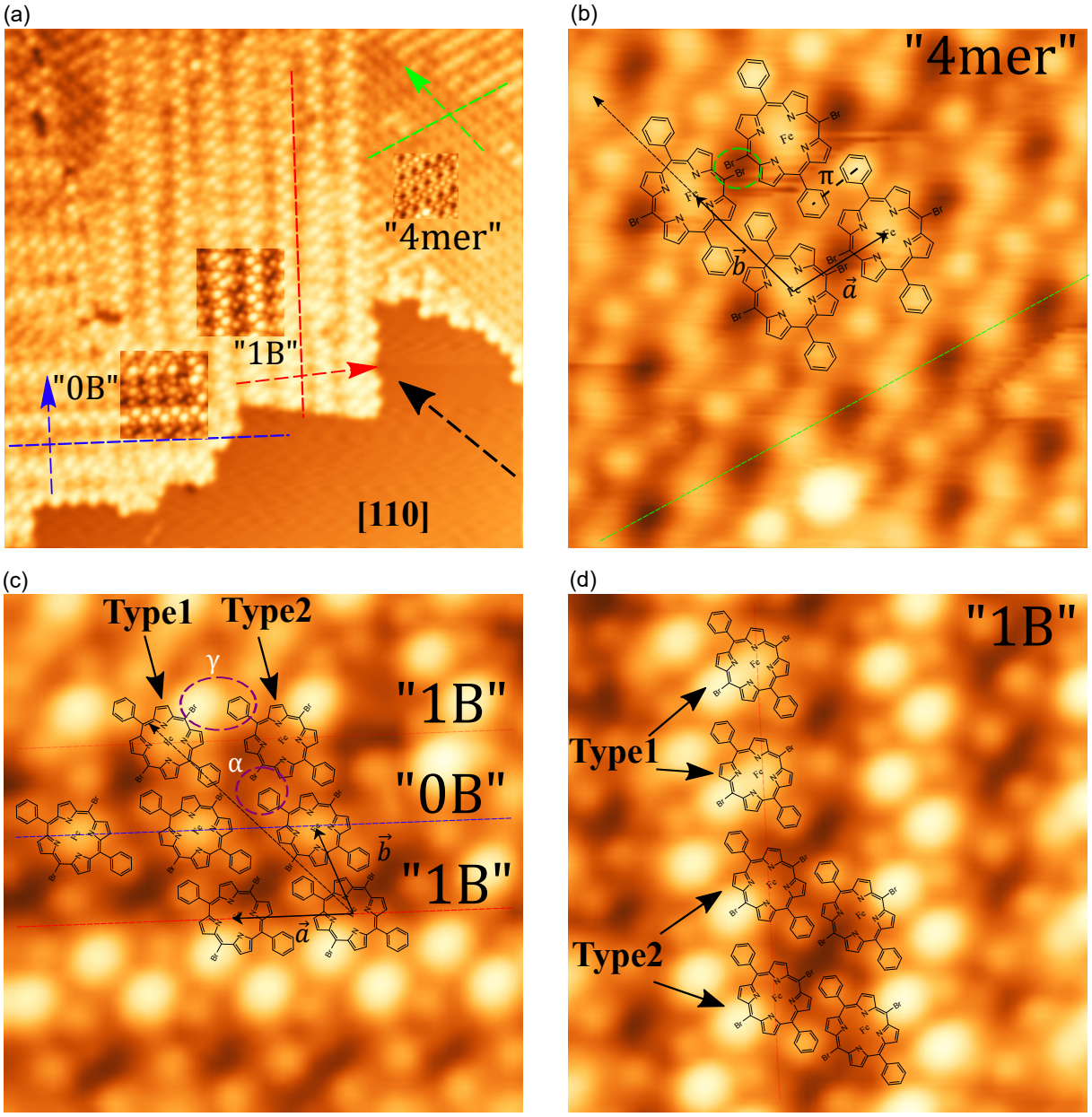

Figure 4.16: Topography images showing three basic $\mathrm{Fe-DBrDPP}$ **conformations in supramolecular lattices on Pb(110) surface with post-annealing at 400 K.** (a) Topography image ($40\mathrm{x}40\mathrm{nm}^2$, setpoint: 8 mV, 50 pA) of self-assembled $\mathrm{Fe-DBrDPP}$ molecule supramolecular lattice consisting of three basic molecule conformations (orderings) labeled by "1B", "0B" and "4mer". molecular rows consisting of "1B", "0B" and "4mer" molecules are marked by red, blue and green dashed lines respectively, arrows of same color indicate the direction crossing adjacent molecules rows along which supramolecular lattice is formed, black dashed arrow marks the [110] direction of Pb(110) surface. Inset images of "4mer", "0B" and "1B" ordering are shown in (b)-(d). (b) Topography image ($5\mathrm{x}5\mathrm{nm}^2$, setpoint: 20 mV, 100 pA) showing "4mer" ordering supramolecular lattice. $\vec{a}$, $\vec{b}$ denote the lattice vectors of lengths 1.1 nm and 1.3 nm respectively. (c) Topography image ($6.6\mathrm{x}6.6\mathrm{nm}^2$, setpoint: 8 mV, 50 pA) showing "0B" ordering molecular row between "1B" ordering molecular rows. $\vec{a}$, $\vec{b}$ denote the lattice vectors of lengths 1.2 nm and 1.1 nm respectively. halogen bonds, π bond is marked by black dashed line. $\mathrm{Br}\cdots\pi$ and $\mathrm{Br}\cdots\mathrm{Br}$ halogen bonds are marked by purple and green circles respectively. (d) Topography image ($6.6\mathrm{x}6.6\mathrm{nm}^2$, setpoint: 8 mV, 50 pA) showing "1B" ordering supramolecular lattice. Two types of "1B" molecules are marked.

"1B" molecules exhibits bright feature at center Fe site while Type2 "1B" exhibits a depression feature at center Fe site. Such different of contrast is related to the coupling between tip states with center Fe orbitals near Fermi level (usually refers to orbitals extends towards vacuum i.e. d_{z^2} and d_π) [25, 253]. There are two possible explanations for such behavior: 1). The center Fe atoms in Type2 "1B" molecules are dissociated. 2). The molecular orbital that gives rise to center spot features is shifted away due to charge fluctuation [254] (or other reasons) and can no longer contribute at the chosen setpoint bias (8 mV here). In the following section we will see that the second explanation is more reasonable.

There is still no strong evidence of existence of covalent bond formation in high-temperature phase $\mathrm{Fe-DBrDPP}$ molecules supramolecular lattices on Pb(110) surface. Once the molecules dissociate Br atoms, they tend to form a chemical bond with the Pb substrate and become "1B" molecules instead of forming covalent bond with other molecules, this might imply that on-surface debromination reaction can not form covalently bonded molecular network on Pb(110) surface as Pb atoms can not serve as catalyst for such process.

"0B-4mer" composite supramolecular lattice

Besides the basic supramolecular lattices with well defined supramolecular lattice periodicity, there also exist composite supramolecular lattices which are more complex. Fig. 4.17 shows two composite supramolecular lattices on Pb(110) constituted of "4mer" and "0B" $\mathrm{Fe-DBrDPP}$ molecules.

(a) shows a "0B"-like sub-lattice (marked by blue dashed circle) embed inside "4mer" ordering supramolecular lattices. We will see later that the "0B" molecules near interface (on blue dashed line) exhibit exotic electronic properties due to unusual geometry caused by intermolecular interaction with "4mer" molecules.

(b) shows a "0B" lattice consisting of three parallel "0B" lines embed inside "4mer" supramolecular lattice. The most interesting point for embed "0B" lattice is that unlike most of the supramolecular lattice that shows bright spot features at the edges, the molecules at left edge stay in "0B" regime by preserving the bromine atoms, this implies that the "0B" molecule might be in a meso-stable geometry.

Yet there still exists many complex composite supramolecular lattices, such as "4mer-0B-1B" supramolecular lattices (not shown here), in this thesis we will present only the basic supramolecular lattices and "0B-4mer" composite supramolecular lattices.

4.6.3 Spectroscopy

In this section we will first study the relation between molecules' ordering with their electronic properties through investigation of spectroscopic data of pristine "4mer", "1B" supramolecular lattices and "0B" molecular row inside "1B" rows. After that we will study more complicated composite supramolecular lattices consisting of "0B" sub-supramolecular lattice embed inside "4mer" supramolecular lattice shown in Fig. 4.16 and Fig. 4.17.

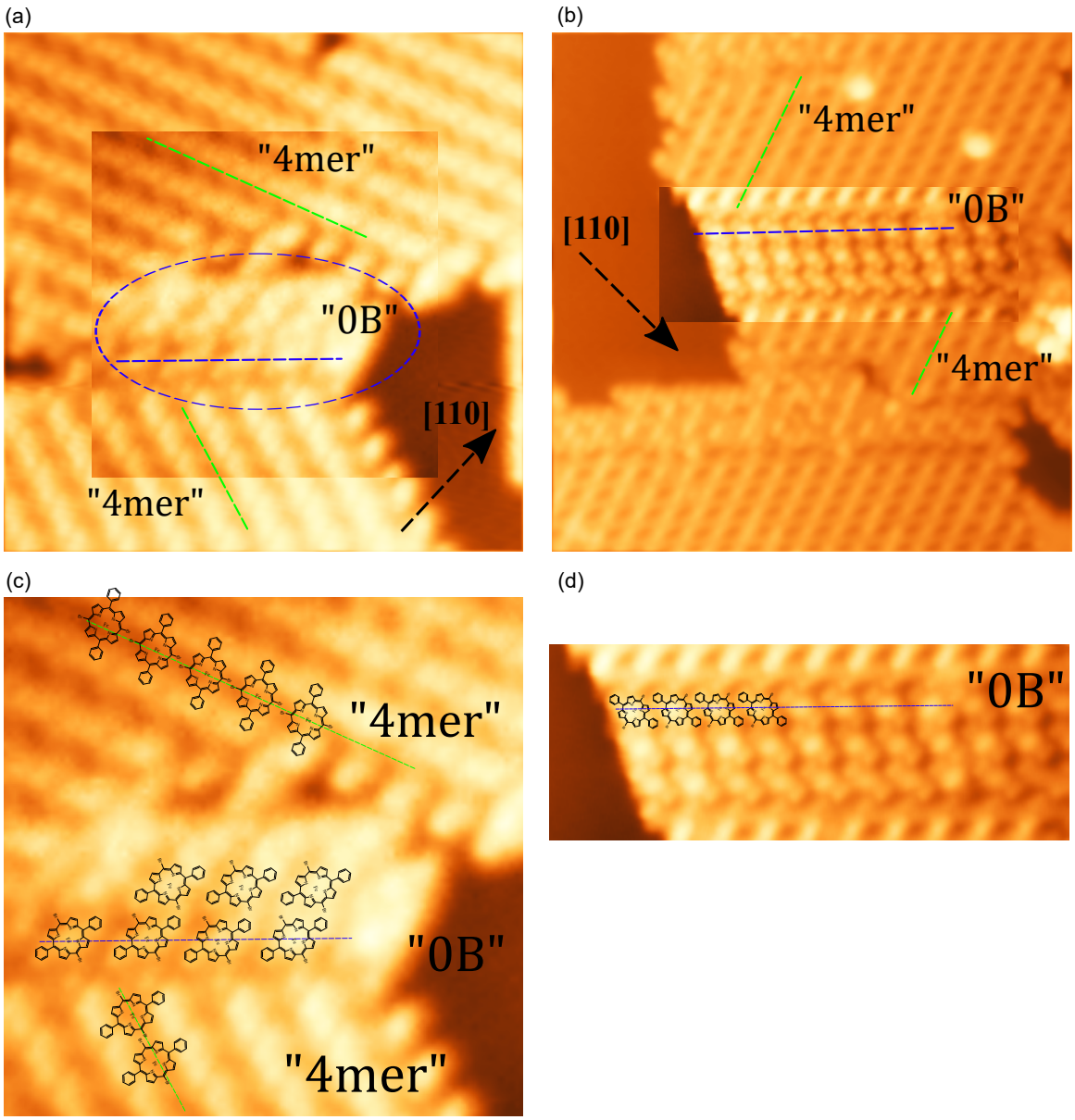

Figure 4.17: "0B" ordering $Fe-DBrDPP$ **molecule supramolecular lattice embed inside "4mer" ordering supramolecular lattice.** (a) Topography image ($15x15nm^2$, setpoint: 100 mV, 100 pA) showing a less-ordered "0B" supramolecular lattice embed inside "4mer" supramolecular lattice which is marked by blue dashed circle. Inset image ($10x10nm^2$, setpoint: 200 mV, 100 pA, 20 pm) is also shown in (c) with $Fe-DBrDPP$ molecule sketch. (b) Topography image ($25x25nm^2$, setpoint: 150 mV, 100 pA) showing a well-ordered "0B" supramolecular lattice consisting of three rows of "0B" molecules embed inside "4mer" supramolecular lattice. Inset image ($17.2x6.4nm^2$, setpoint: 150 mV, 100 pA, 150 pm) is also shown in (d) with $Fe-DBrDPP$ molecule sketch.

It worth mentioning here the spectroscopy data of "4mer", "1B" and "0B" molecules that will be presented in the following sections represent the standard behavior of "4mer", "1B" and "0B" molecules. Because the molecular supramolecular lattice can be easily distorted and there always exist exotic molecules for any ordering (even the most stable "1B" molecules) that exhibit abnormal electronic properties, not all exotic molecules will be discussed in this thesis.

As in previous experiments, the spectroscopic data are recorded with bulk Pb covered superconducting tip ($\Delta_t = 1.35$ meV).

"4mer" ordering: Spin-flip

Fig. 4.17 (c) shows a supramolecular lattice consisting of both "4mer" part and "0B" part, in this section we focus only on the electronic properties of "4mer" molecule supramolecular lattice, the "0B" sub-supramolecular lattice will be discussed later.

A high-resolution SIS dI/dV spectra is shown in the inset image of Fig. 4.18 (a) in which "4mer" molecule exhibits no in-gap feature but instead two pairs of peaks symmetric to Fermi level outside the gap. This is the signature of inelastic spin-flip (SF) excitation in SIS spectra (see section (2.2.4)), it indicates that the "4mer" $\mathrm{Fe-DBrDPP}$ has S = 1 magnetic state and the coupling with substrate is dominated by uniaxial and transverse magnetic anisotropy D and E.

Along trajectory of green arrow in Fig. 4.18 (a), the stacking plot of point antisymmetry value

$$| \ (d^2I/dV^2|_{V>0} - d^2I/dV^2|_{V<0}) \ | \tag{4.1}$$

is shown in (b), this value calculates the absolute value of antisymmetry value of derivative of dI/dV spectra, it will enhance the non-flat signature in dI/dV curve, this is especially useful when studying weak signature outside the gap. For example in SIS dI/dV spectra in (c), the steps feature of phonon modes at bias of ± 7 mV and ± 11 mV marked by vertical gray dashed lines are enhanced in (b), which shows a clear feature that exists at any point on the arrow, this is reasonable because phonon mode is a property of Pb substrate. We also observe the SF feature at bias of ± 9.5 mV and ± 15.5 mV marked by purple dashed lines that exist only on "4mer" molecules. This means the "4mer" molecules inside the supramolecular lattice have S = 1 triplet ground state which degeneracy is splitted by uniaxial magnetic anisotropy $D \approx 9.8$ meV and transverse anisotropy $E \approx 3$ meV.

The spatial variation of SF energy is also observed in stacking plot, as explained before this is due to tip interaction that varies the magnetic anisotropy [109, 110]. The interaction strength depends on tip-molecule distance, in STS experiments tip-molecule distance normally should not significantly vary unless there is a strong derivation of molecular orbital that drastically change tip-molecule distance locally, however this origin can be easily examined by studying topography image constructed by tip height.

The spatial distribution of orbitals that give rise to SF feature can be visualized in SIS dI/dV maps shown in Fig. 4.18 (d)-(g) at corresponding SF energies. In map (d) of bias -9.5 mV, ex-

cept the red dashed circle marked region, we observe point feature locates at center Fe atom of "4mer" $\mathrm{Fe-DBrDPP}$ molecules while for positive bias map at 9.5 mV the SF feature locates near the upper opposite-site pyrrole rings of $\mathrm{Fe-DBrDPP}$ molecule but delocalized a bit outside the molecule. Such pattern is similar to the orbital character of FOA and FOB in $\mathrm{Fe-DPyDBrPP/Au(111)}$ system (see section (3.6.1)) where $\mathrm{Fe-DPyDBrPP}$ molecule also adopts a saddling conformation as "4mer" $\mathrm{Fe-DBrDPP}$ molecules. But the delocalization of SF feature is not expected, this indicates that FOB (d_π derived, located on upper pyrrole rings) for "4mer" $\mathrm{Fe-DBrDPP}$ delocalizes from each single molecule and distributes between them, which could be possibly due to hybridized molecular orbital distributing between molecules[6]. The distribution of higher bias excitation (± 15.5 mV) feature shown in (f)(g) looks similar to (d)(e) but with less spectral weight.

Hence the electronic properties of standard "4mer" molecules are understood: They exhibit obvious inelastic SF feature, indicating a S = 1 magnetic state and the coupling with substrate is dominated by magnetic anisotropy i.e. "4mer" molecules are in atomic limit.

For exotic "4mer" molecules marked inside red dashed circle, their spectroscopic data are shown in supplementary figures (Fig. 4.35) where they exhibit different spectral feature from the standard "4mer" molecules.

Pristine "1B" supramolecular lattices

Now we turn our attention to the spectroscopic data of supramolecular lattice that consists of "1B" $\mathrm{Fe-DBrDPP}$ molecules shown in Fig. 4.19.

(a) is the same typography image as Fig. 4.16 (d) that shows the topography of two "1B" molecular rows in which we observe both Type1 and Type2 "1B" molecules. The variation of SIS dI/dV spectra along the red arrow in (a) is shown in (b) where four horizontal dashed lines correspond to the centers of four "1B" molecules indicated in (a).

It is obvious that red and green molecules (red and green points marked molecule) exhibit no in-gap feature while blue and yellow ones exhibit in-gap features. In topography image (a) the red and green molecules correspond to Type2 molecule while blue and yellow ones correspond to Type1.

For two Type1 "1B" molecules exhibiting in-gap states, we observe a similar behavior to low annealing temperature case (Fig. 4.12) where we find two pairs of Shiba states characterized as CS1 and CS2. CS1 have lower energy (closer to Fermi level), for electron-like component it spatially delocalizes ((e-f), (i-j)) and distributes outside macrocycle of molecules. Interestingly, the electron-like component of CS1 of "1B" molecules distributes around the molecule in a way that it avoids all the ligands (phenyl rings and Br atoms). This behavior is valid for almost all CS1 at 0.6 meV of Type1 "1B" molecules (see Fig. 4.20 (c)). CS2 have higher energy (closer to gap edge) and spatially localize on the macrocycle of the molecules for both hole-like and electron-like components (Fig. 4.12 (h)(k) and Fig. 4.20 (d)). These behaviors of CS1 and

[6]However in spectroscopic data, besides the delocalization excitation pattern we do not observe obvious spectral feature showing inter-molecular spin-spin interaction [39, 235].

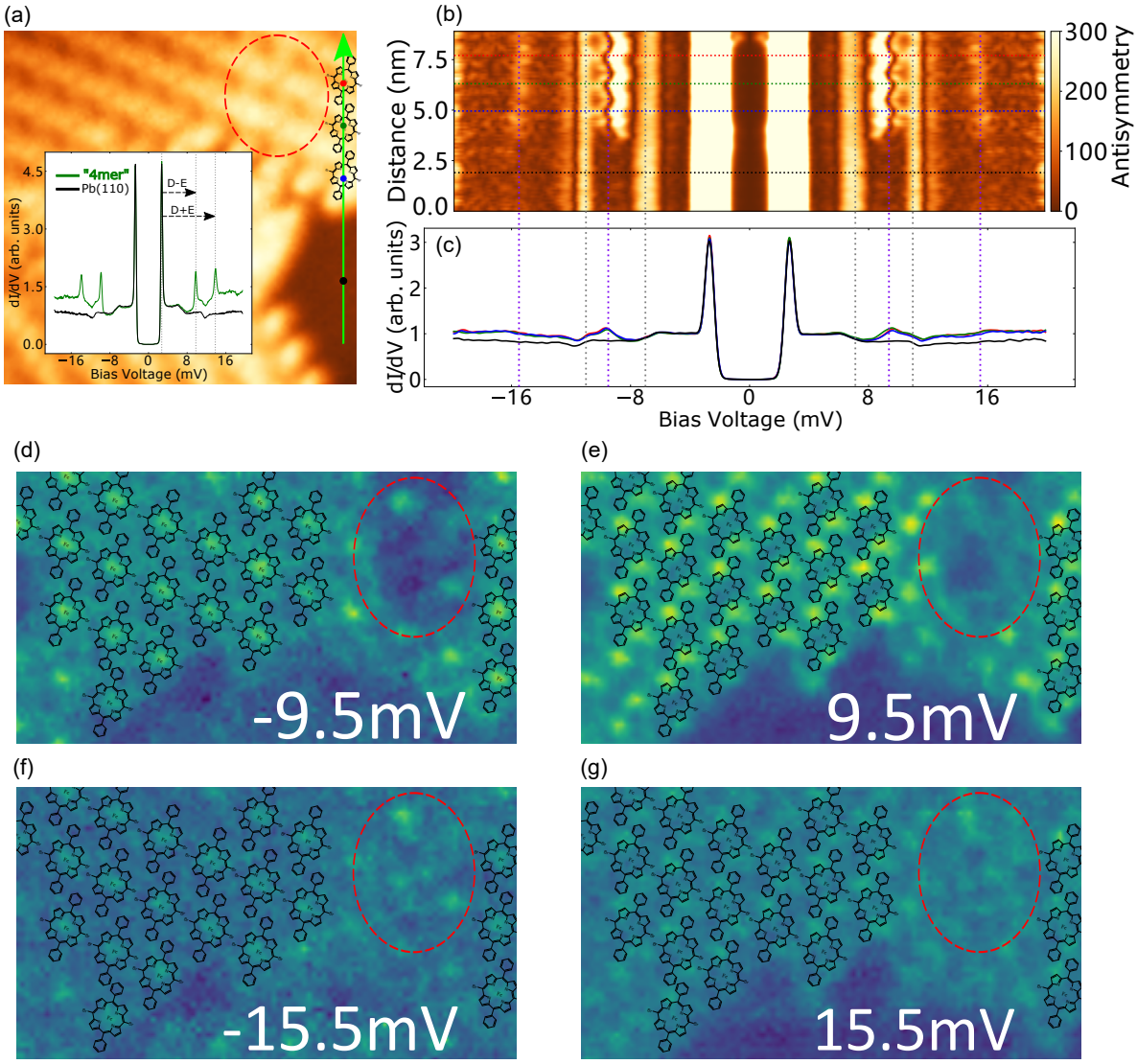

Figure 4.18: Spectroscopic data of "4mer" ordering $\mathrm{Fe-DBrDPP}$ **supramolecular lattice.** (a) Topographic image ($10\mathrm{x}10\mathrm{nm}^2$, setpoint: 200 mV, 100 pA, 20 pm) showing "4mer" ordering $\mathrm{Fe-DBrDPP}$ supramolecular lattice. Inset SIS dI/dV spectra measured at center of a "4mer" $\mathrm{Fe-DBrDPP}$ molecule exhibiting inelastic spin-flip excitation feature (Setpoint: 20 mV, 100 pA, -200 pm, Lock-in parameters: $V_m = 0.2$ mV, $f = 750$ Hz.). Red dashed circle marks the exotic "4mer" molecules that exhibit no SF feature at ± 9.5 mV. (b) Stacking plot of point value of expression (4.1) along the green arrow in (a)(Setpoint: 100 mV, 100 pA, -250 pm, Lock-in parameters: $V_m = 0.2$ mV, $f = 750$ Hz). Horizontal red, green and blue dashed lines mark the positions of points of same colors in (a) which are the center of different $\mathrm{Fe-DBrDPP}$ molecules, black line (point) measured on Pb(110) surface. Vertical gray dashed lines mark the bias voltage of ± 7 mV and ± 11 mV that are energies of phonon modes, vertical purple dashed lines mark the bias voltage of ± 9.5 mV and ± 15.5 mV that corresponds to the SF energies. (c) SIS dI/dV spectra measured at crosses position with same colors in (a). All spectra are smoothed and normalized. (d)-(g) SIS dI/dV map at bias voltage of -9.5 mV, 9.5 mV, -15.5 mV and 15.5 mV of "4mer" supramolecular lattice.

CS2 are now recognized as standard behaviors because they are valid for most of "1B" and "0B" $\mathrm{Fe-DBrDPP}$ molecules inside the lattice (molecules at the edges of lattice will be discussed separately).

For Type2 "1B" molecules, to figure out the origin of their occurrence, we examine supramolecular lattices in Fig. 4.20 where (a) is the topography image, (b) the integrated DOS map over in-gap energy. The yellow indicates where the area in-gap states exist. (c) and (d) are the DOS maps at energies of 0.6 meV and 1.16 meV, corresponding to energies of electron-like component of standard CS1 and CS2. The Red grid follows the arrangement of "1B" molecules, the intersections correspond to the centers of "1B" molecules. By comparing (a) and (b), we can see that Type1 molecules exhibit in-gap states while the area exhibiting no in-gap feature are covered by Type2 molecules (or bare Pb surface).

It is also obvious that the distribution of Type1 and Type2 molecules inside the lattice shows a regular arrangement. This suggests that the difference of two types of "1B" molecules is not due to the dissociation of center Fe atoms, otherwise they should distribute randomly. We also observed that Type1 "1B" molecules in DOS map shows a moiré pattern at different energies, implying that lattice mismatch results an alternating coupling strength with substrate depending on the adsorption sites. This could explain the spatial distribution of Type1 and Type2 "1B" molecules[7].

We have also examined the topography images of Type1 and Type2 "1B" molecules measured at 8 mV, 158 mV and 510 mV shown in Fig. 4.21 (a)-(c) respectively. In high bias topography image the contribution of in-gap feature is negligible and molecular orbital contributes most, we find that the absence of bright spot features at Fe site for Type2 "1B" molecules is still observable in high bias topography. Such observation indicates that the depression feature is not a result of absence of in-gap state but the absence of molecular orbital at positive energy.

Hence the presence of Type2 "1B" molecules is possible due to the induced charge fluctuation that shifts the frontier molecular orbital away from the Fermi level, resulting a depression center in topography and zero in-gap feature in spectroscopy.

"0B" inside "1B" lines

The spectroscopic data of "0B" molecules which preserve both bromine atoms and exhibit a clear topography shape is presented in Fig. 4.22. The variation of SIS dI/dV spectra along the blue arrow crossing three successive "0B" molecules is shown in (b). The spectra measured on macrocycles of these three molecules are plotted in (c) by red, green and blue curves, for simplicity these three molecules are for now called red, green and blue "0B" molecules. The SIS dI/dV and DOS maps are respectively presented in (d)-(g) and (h)-(k).

Red and green "0B" molecules exhibit standard CS1 and CS2 features while the blue "0B" molecule behaves differently. For the spectrum taken on blue "0B" molecule in (c), we observe only one Shiba state of at energy of 0.85 meV that exhibits stronger spectral weight than red and green curves in (c). In DOS maps the electron-like component of this state mainly locates on

[7]The lattice mismatch of "1B" molecules has been studied in supplementary section (4.7.2), Fig. 4.36

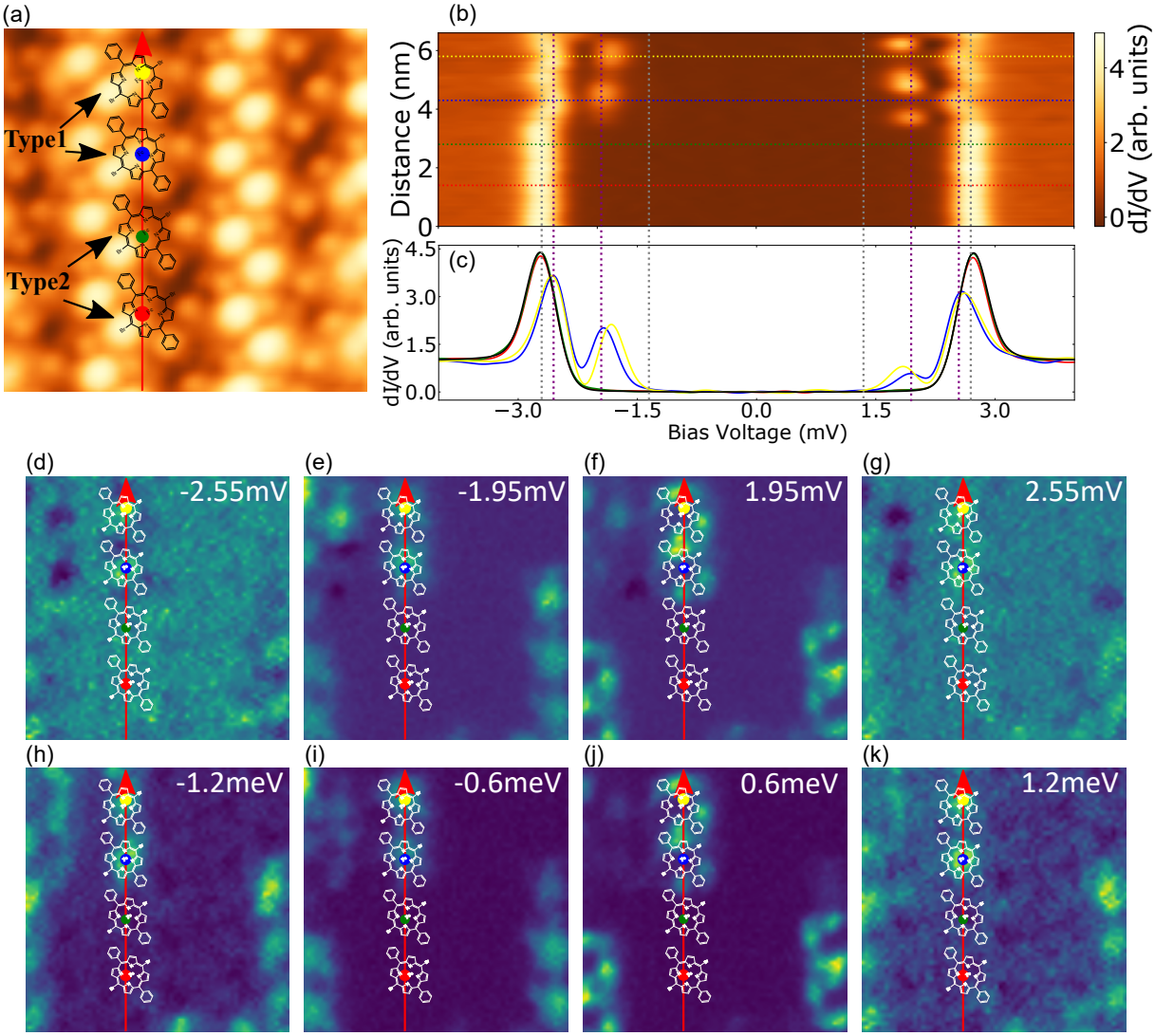

Figure 4.19: Spectroscopic data of "1B" ordering $\mathrm{Fe-DBrDPP}$ **supramolecular lattice.** (a) Same topography image as Fig. 4.16 (d), red arrow marks one "1B" molecular row on which two upper $\mathrm{Fe-DBrDPP}$ molecules are of Type1, two bottom ones are Type2. (b) Stacking plot of point SIS spectra along red arrow in (a)(Setpoint: 8 mV, 50 pA). Horizontal red, green, blue and yellow dashed lines mark the positions of points of same colors in (a) which are the center of different "1B" $\mathrm{Fe-DBrDPP}$ molecules. Vertical gray dashed lines mark the bias voltage of ± 1.35 mV and ± 2.7 mV, purple dashed lines mark the bias voltage of ± 2.55 mV and ± 1.95 mV. (c) SIS dI/dV spectra measured at crosses position with same colors in (a). Black curve measured on Pb(110) surface. (d)-(g) SIS dI/d maps of bias voltage ± 2.55 mV and ± 1.95 mV of same region of (a). (h)-(k) Deconvoluted DOS maps of energies ± 1.2 meV and ± 0.6 meV of same region of (a). All spectra are smoothed and normalized.

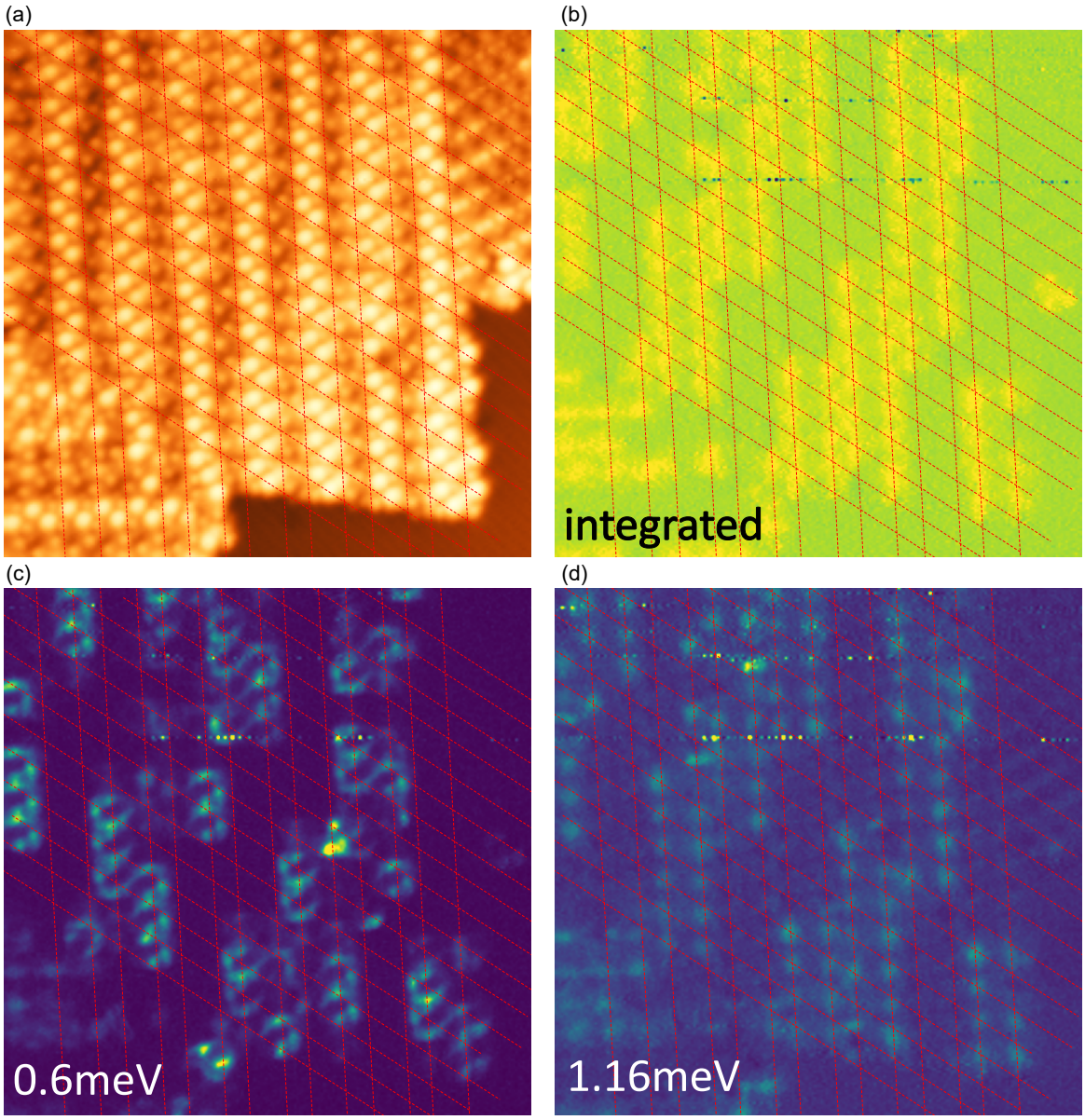

Figure 4.20: Distribution of Type1 and Type2 "1B" $\mathrm{Fe-DBrDPP}$ **molecules.** (a) Topography image ($22\mathrm{x}22\mathrm{nm}^2$, setpoint: 8 mV, 50 pA) of $\mathrm{Fe-DBrDPP}$ "1B" supramolecular lattice. Red grid roughly represents the arrangement of "1B" supramolecular lattice where the intersections correspond to the center of "1B" molecules inside the supramolecular lattice. (b) Integrated deconvoluted DOS map over in-gap energy of same region of (a). (c)(d) DOS maps at energies of $+0.6$ meV and $+1.16$ meV.

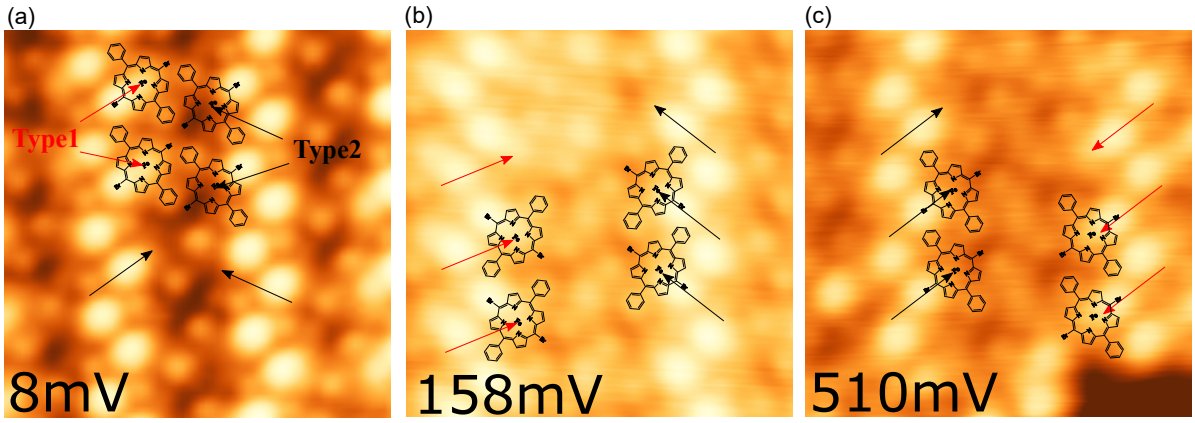

Figure 4.21: Topographic characterization of center orbitals of "1B" molecules. (a)-(c) Topography images of Type1 and Type2 "1B" molecules measured at setpoints of: 8 mV, 50 pA, 158 mV, 50 pA and 510 mV, 100 pA. Type1 and Type2 molecules which center Fe site exhibit bright spot and depression feature are marked by red and black arrows respectively.

macrocycle but also extend to nearby Type2 "1B" molecule (marked by red circle) at standard CS1's energy of ± 0.65 meV, while at standard CS2's energy of ± 1.2 meV there is no spectral weight on the blue molecule.

All these observations show that for blue "0B" molecule, CS1 and CS2 become degenerate at energy of 0.85 meV. The exotic behavior of blue "0B" molecule is within our expectation, because this molecule locates near the interface between two chiral domains (see Fig. 4.15 in which blue molecule marked by blue solid arrow, interface marked by white dashed line).

At the edge of supramolecular lattices or near the interfaces between supramolecular lattices of different orderings the translation symmetry is broken, the molecules nearby will feel different geometry environment (inter-molecular interaction, conformation change etc.) with respect to the molecules inside the supramolecular lattice. It is reasonable to find exotic behaviors at edges of interfaces. We will see later in section (4.6.3) that it is indeed due to geometry effect which leads to a degenerate CS1 and CS2.

For a brief conclusion, "4mer" $\mathrm{Fe-DBrDPP}$ molecules have the weakest coupling with substrate and exhibit only out-gap SF signatures, indicating a magnetic anisotropy dominant weak coupling regime. We attribute the weak coupling to the compact arrangement of "4mer" lattices where the inter-molecular interaction decouples "4mer" molecules from the substrate. The spatial distribution of SF feature exhibits similar pattern of FOB and FOA studied in section (3.7), but d_π derived FOB delocalize from upper pyrrole rings location, indicating the existence of hybridized inter-molecular orbitals.

"0B" and "1B" $\mathrm{Fe-DBrDPP}$ molecules represent the strong coupling limit where most of them exhibit two Shiba states characterized as CS1 and CS2. Like low-temperature phase the electron-like component of CS1 spreads around the molecule while CS2 localizes on macrocycle of $\mathrm{Fe-DBrDPP}$ molecules. Some "1B" molecules exhibit depression center in topography image and show no in-gap state, which is the result of quench of frontier molecular orbital near Fermi level. According to our analysis, the most probable origin is the charge fluctuation induced

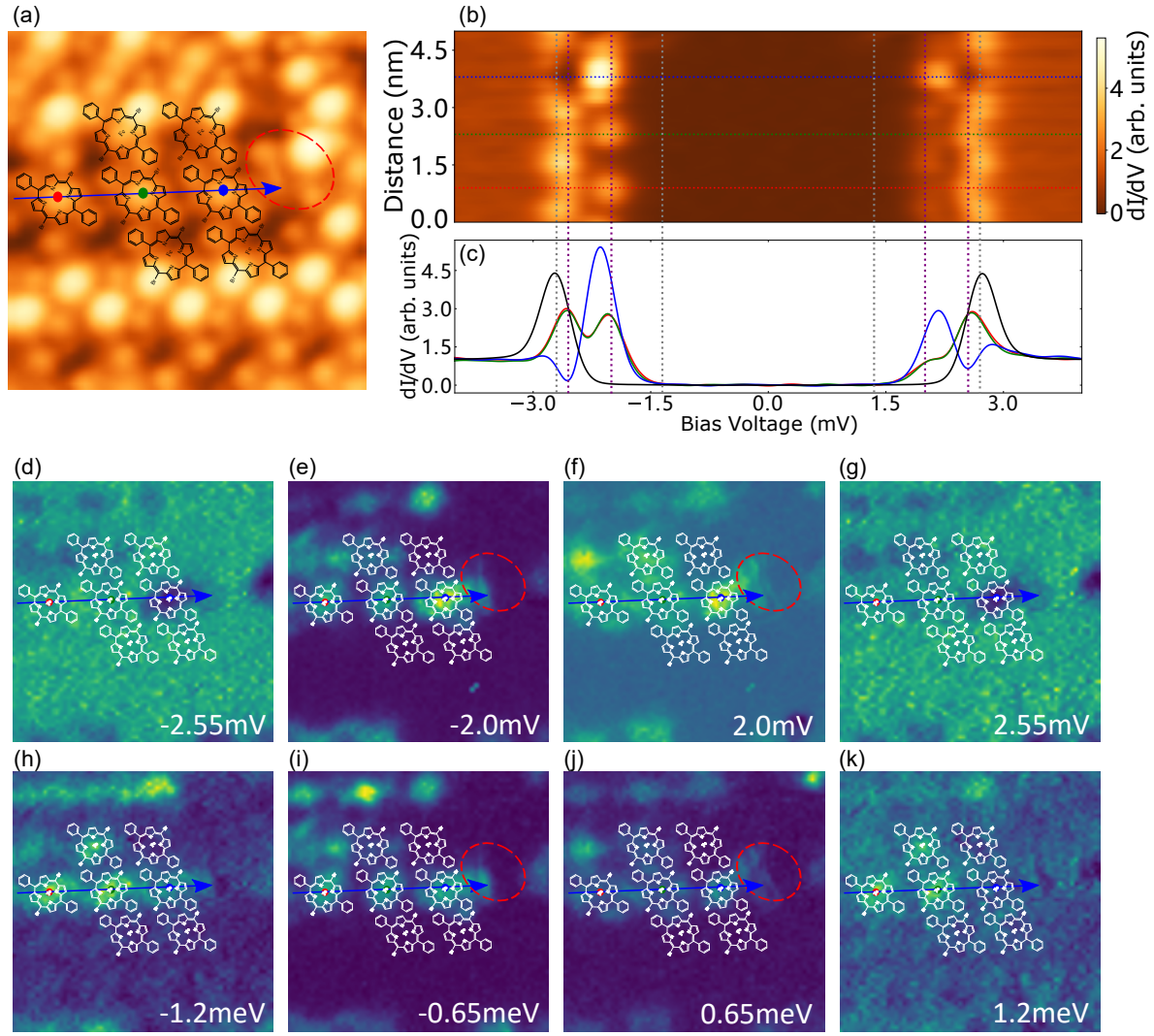

Figure 4.22: Spectroscopic data of "0B" $\mathrm{Fe-DBrDPP}$ **molecules embed in "1B"** $\mathrm{Fe-DBrDPP}$ **molecular rows.** (a) Same topography image as Fig. 4.16 (c), blue arrow marks one "0B" molecular row on which three "0B" molecule whose centers are marked by red, green and blue points. Red dashed circle marks a Type2 "1B" molecule near blue point marked "0B" molecule. (b) Stacking plot of point SIS spectra along blue arrow in (a)(Setpoint: 8 mV, 50 pA). Horizontal red, green, blue and yellow dashed lines mark the positions of points of same colors in (a) which are the center of different "1B" $\mathrm{Fe-DBrDPP}$ molecules. Vertical gray dashed lines mark the bias voltage of ± 1.35 mV and ± 2.7 mV, purple dashed lines mark the bias voltage of ± 2.55 mV and ± 2.0 mV. (c) SIS dI/dV spectra measured at crosses position with same colors in (a). Black curve measured on Pb(110) surface. (d)-(g) SIS dI/dV maps of bias voltage ± 2.55 mV and ± 2.0 mV of same region of (a). (h)-(k) Deconvoluted DOS maps of energies ± 1.2 meV and ± 0.65 meV of same region of (a). All spectra are smoothed and normalized.

by a lattice mismatch.

"0B-4mer" interfaces

So far we have studied the standard molecules and learnt that "1B" and "0B" molecules exhibit two channel Shiba states, indicating a S = 1 configuration. However the ground state (weak coupling free-spin regime or strong coupling Kondo-screened regime) and orbital origin of Shiba states are not determined yet.

In the following two sections, including this one, we will study the "0B" molecules near the interface between supramolecular lattices of different orderings. Because they may very well exhibit unusual electronic properties due to different environment condition. We will see that due to geometric effect, "0B" molecules near interface could suffer from orbital reorganization due to inter-molecular interaction that greatly modifies the properties of frontier molecular orbital. Thanks to this observation, we are able to determine the ground state nature and orbital origin of Shiba states .

In this section we will study the electronic properties of "0B"-"4mer" composite supramolecular lattice shown in Fig. 4.17 (a) where "0B" sub-supramolecular lattice (marked by blue dashed circle) is embed inside "4mer" supramolecular lattices.

We start with the "0B" molecules inside the "0B" sub-supramolecular lattice. The linecut of variation of symmetrized dI/dV (expression (4.1)) is shown in Fig. 4.23 (b), it tells us the spectra signature along the blue arrow in (a) which crosses "4mer", "0B" sub-supramolecular lattices and Pb surface. The horizontal colored dashed lines correspond to locations of points with same color in (a). i.e. from 0 nm to 2.8 nm the spectra are measured on "4mer" molecules, between 2.8 nm and 9 nm on "0B" molecules inside the sub-lattice and after 9 nm on bare Pb surface.

For spectra measured on "4mer" molecules (red and green dashed lines), SF excitations are observed. For spectra of "0B" molecules inside the lattice (between blue and orange lines), a pair of Shiba states of energy around ± 0.95 meV (± 2.3 mV in SIS dI/dV spectra) emerge and out-gap SF features disappear. The spatial distribution of these Shiba states in (e-f) has a similar pattern to the situation of "0B" molecules inside "1B" rows (Fig. 4.22 (e-f)). For bare Pb surface, only phonon mode feature exists.

Now we focus on the molecules near interface which exhibit strange bubble shape in dI/dV map Fig. 4.23 (f) which was never observed before. From topography image Fig. 4.24 (a), the molecules on either side of the interface lie very close each other, it seems that their macrocycle are interacting through pyrrole-pyrrole bond.

The variation of symmetrized dI/dV (expression (4.1)) along blue arrow by 1 and 2 are respectively shown in Fig. 4.24 (b) & (d) and (c) & (e) respectively. These linecuts cross both "4mer" and "0B" molecules at either side of the interface. Horizontal colored dashed lines in (b) & (d) and (c) & (e) correspond to specific locations marked by points with same colors in (a). Red and orange points respectively indicate two ends of "4mer" and "0B" molecules while green indicates the interface.

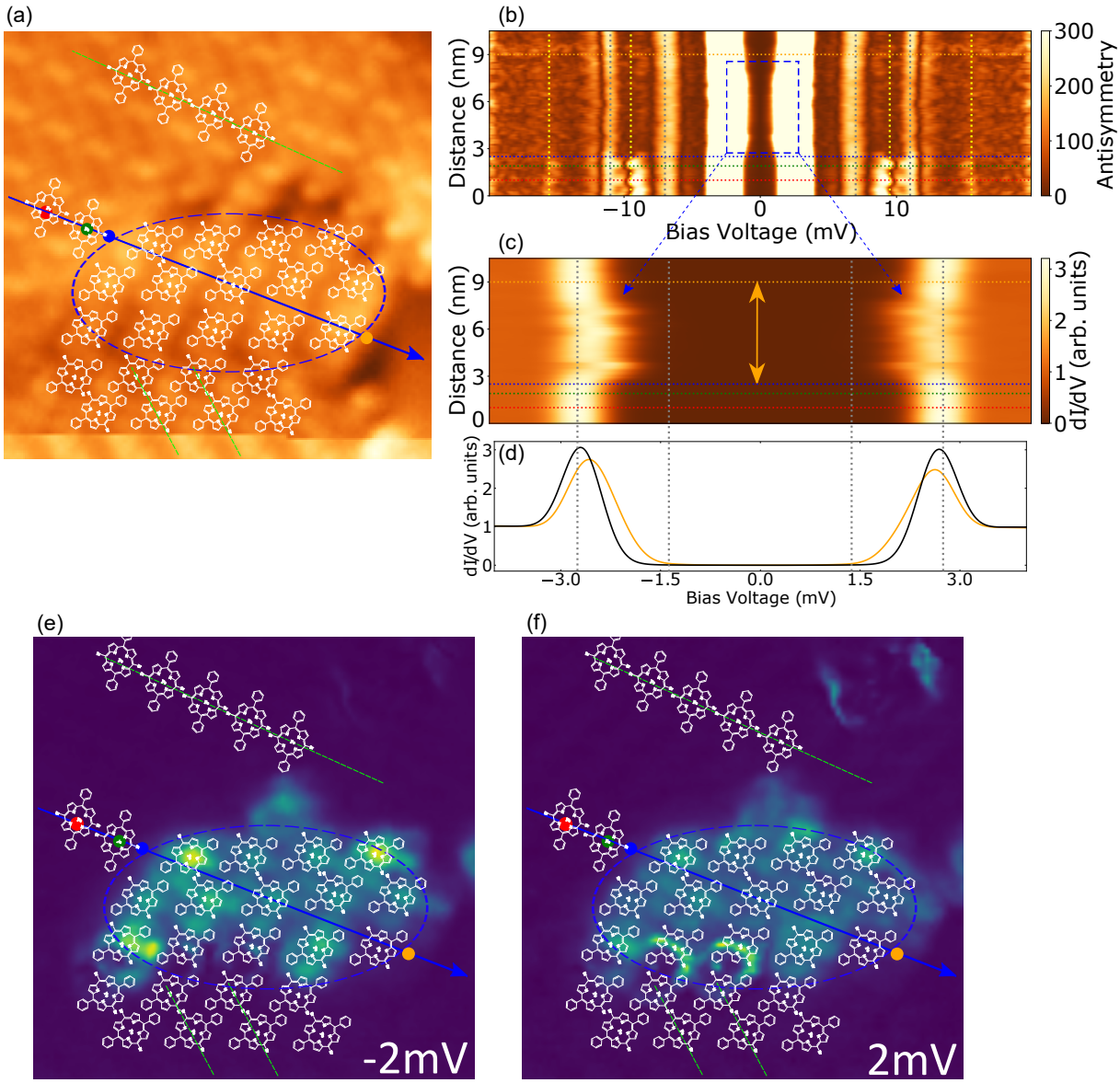

Figure 4.23: Spectroscopic data of $\mathrm{Fe-DBrDPP}$ **molecules inside "0B" sub-supramolecular lattice embed in "4mer" supramolecular lattices.** (a) Topographic image ($10\mathrm{x}10\mathrm{nm}^2$, setpoint: 100 mV, 100 pA, -250 pm) showing "0B" "4mer" composite supramolecular lattice where "0B" sub-supramolecular lattice marked by blue dashed circle is embed inside "4mer" supramolecular lattice which is described by green dashed lines of molecules. (b) Stacking plot of point value of expression (4.1) along the blue arrow in (a)(Setpoint: 100 mV, 100 pA, -250 pm, Lock-in parameters: $V_m = 0.2$ mV, $f = 750$ Hz). Horizontal red, green, blue and orange dashed lines mark the positions of points of same colors in (a) where red and green are the centers of two "4mer" $\mathrm{Fe-DBrDPP}$ molecules, blue and orange are two points at perimeter of "0B" sub-supramolecular lattice. Vertical gray dashed lines mark the bias voltage of ± 7 mV and ± 11 mV that are energies of phonon modes, vertical yellow dashed lines mark the bias voltage of ± 9.5 mV and ± 15.5 mV that corresponds to the SF energies. (c) Stacking plot of point SIS dI/dV spectra along blue arrow in (a) showing the in-gap features which was overexposed in blue dashed square region in (b). Vertical gray dashed lines mark the bias voltage of ± 1.35 mV and ± 2.7 mV. (d) SIS dI/dV spectra in which orange curve represent the spectra averaged between blue and orange points on blue arrow which is marked by orange two-way arrow in (b). Black curve measured on Pb(110) surface. (e)(f) SIS dI/dV maps of bias ± 2.0 mV showing the distribution of in-gap feature of "0B" sub-supramolecular lattice. All spectra are smoothed and normalized.

In Fig. 4.24 (b) & (d) and (c) & (e), three typical regions exhibiting different spectral features are observed: 1). Between red and green dashed lines, only SF excitation at around ± 9 mV and ± 15 mV is observed, it corresponds the spectral signature of "4mer" molecule. 2). Between green and blue dashed lines, the SF feature changes its energy to around ± 5 mV and shifts towards gap edge, in the meantime in-gap peaks emerge and coexist with out-gap SF feature. 3). Between blue and orange dashed lines, in-gap peaks cross Fermi level and out-gap SF feature disappears.

Following the trajectory along the arrow direction (from red to orange points), it appears that out-gap SF feature crosses gap and becomes in-gap states, we call this observation as **gap-crossing phenomena**.

The evolution of such gap-crossing feature can also be visualized in symmetrized dI/dV (expression (4.1)) maps [8] at different bias voltages shown in Fig. 4.24 (f)-(j). In (f) at 8 mV, SF excitation pattern of "4mer" supramolecular lattice is observed in (f) (same as Fig. 4.18 (e)). In (g) at 5 mV, out-gap feature localizes at the interface between "4mer" and "0B" molecules, this feature should correspond to SF excitation but with a reduced SF energy (magnetic anisotropy).

In the study of $\mathrm{Fe-DPyDBrPP/Au(111)}$ system, we know that the SF energy of a single magnetic molecule is the same no matter which molecular orbital we are tunneling through [32]. If this statement still holds, the SF feature of 5 mV localized at the interface (in Fig. 4.24 (g)) should not be generated by the "4mer" molecule which already exhibits a SF feature of energy 9 mV. The only explanation will be that this 5 mV SF feature originates from "0B" molecule which lies on top of interface. The most probable reason that it behaves like a "4mer" molecules is the inter-molecular coupling across the interface.

From Fig. 4.24 (f)-(j), as bias decreases, the SF density probability at interface spreads out towards "0B" molecule and exhibits a bubble shape. This spreading process as bias decreases can also be visualized as opening of bubble shown in 3D plot (see supplementary Fig. 4.38). The continuous evolution from the interface to the "0B" macrocycle further proves that both in-gap Shiba states and out-gap SF excitation should be generated by "0B" molecule and have the same molecular orbital origin.

For standard "0B" molecules, it is clear that they have stronger coupling with substrate than standard "4mer" molecules, as the "0B" molecules show in-gap feature while "4mer" molecules show out-gap feature. However a continuous evolution of gap-crossing feature for a single "0B" molecule is not expected, the most probable reason for such strange phenomena is the tip effect. Which means when performing STS experiment, "0B" molecules feel different tip interaction strength depending on the tunneling locations. The tip interaction changes the interaction between "0B" molecule and substrate, resulting a magnetic anisotropy dominated out-gap SF behavior or coupling dominated in-gap state behavior.

The direct effect of tip interaction is to tune the coupling between molecule with substrate (increase of decrease) by changing the structure of molecule. It has been shown that in molecular system to significantly vary the energies of out-gap SF feature or in-gap Shiba feature [31, 93,

[8] $|\ (d^2I/dV^2|_{V>0} - d^2I/dV^2|_{V<0})\ |$ is invariant by changing the sign of bias $V \to -V$

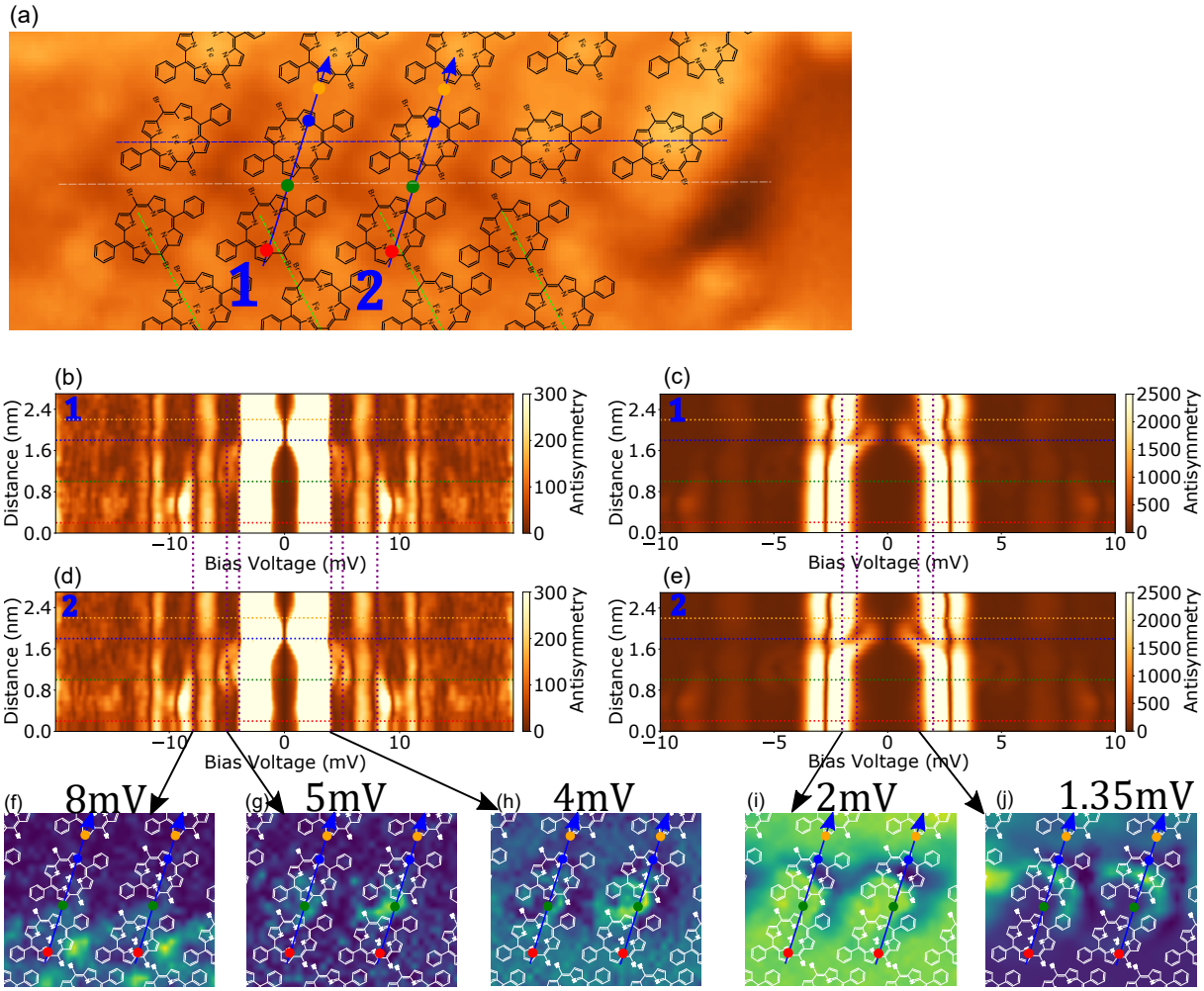

Figure 4.24: Spectroscopic data of $\mathrm{Fe-DBrDPP}$ **molecules on interface between "0B" sub-supramolecular lattice and "4mer" supramolecular lattices.** (a) Topographic image ($10\mathrm{x}3.5\mathrm{nm}^2$, setpoint: 100 mV, 100 pA, -250 pm) showing $\mathrm{Fe-DBrDPP}$ molecules on either sides of interface (marked by white dashed line) between "0B" sub-supramolecular lattice (marked by blue dashed line) and "4mer" supramolecular lattices (marked by green dashed lines). (b)(d) Stacking plot of point value of expression (4.1) along the blue arrow labeled by 1 and 2 in (a)(Setpoint: 100 mV, 100 pA, -250 pm, Lock-in parameters: $V_m = 0.2$ mV, $f = 750$ Hz). Horizontal red, green, blue and orange dashed lines mark the positions of points of same colors on corresponding arrow in (a). Vertical purple dashed lines mark the bias voltage of ± 8 mV, ± 5 mV and ± 4 mV. (c)(e) Same as (b)(d) but with smaller contrast and energy scale in which in-gap feature can be well distinguished. Vertical purple dashed lines mark the bias voltage of ± 2 mV and ± 1.35 mV. (f)-(j) $\mid (d^2I/dV^2|_{V>0} - d^2I/dV^2|_{V<0}) \mid$ maps of bias 8.0 mV, 5.0 mV, 4.0 mV, 2.0 mV and 1.35 mV showing the distribution of out-gap (f-h) and in-gap (i-j) feature.

103, 110] in a range like what we observed here (larger than 4 mV) requires a large tip-molecule distance variation. In our case, the tip effect on energy variation of SF feature inside "4mer" supramolecular lattice Fig. 4.18 (b) or of Shiba states inside "0B" sub-supramolecular lattice Fig. 4.23 (b-c) are reasonable for a constant setpoint STS experiment, while for the gap-crossing signature of "0B" molecule it is too large than expected. Hence there must be other parameter from structure change that results gap-crossing phenomena. We believe this parameter is the inter-molecular interaction across the interface (geometry effect) that results molecular orbital reorganization which involves charge fluctuation and makes "0B" molecules extremely sensitive to external perturbation, especially the presence of the tip.

To end this section we discuss about the bubble shape of this gap-crossing feature in conductance maps. According to interpretation of tip-molecule interaction, the distribution of in-gap states at specific energy should also reflect the location where "0B" molecule feels the tip interaction strength corresponding to this energy, e.g. in (j) the in-gap feature exhibits a ring shape distribution, it also reflects the location where tip interaction tunes the molecule-substrate coupling to generate Shiba states with energy of 0 meV. We also find that molecules exhibiting bubble shape can usually be found near the interface (not only "0B-4mer" interface) but not all molecules near interface show this behavior (see supplementary figure Fig. 4.39). We are still investigating different $\mathrm{Fe-DPyDBrPP}$ molecules exhibiting such strange behavior in conductance maps to better understand the relation between molecules' geometry with the bubble shape.

Tip effect on "0B" supramolecular lattice

In this section we will focus on the evolution of tip-induced in-gap states in "0B" molecules near the interface between supramolecular lattices of different orderings. The target molecules are in the "0B" supramolecular assemblies shown in Fig. 4.25 which consists of three parallel "0B" rows indicated by blue arrow 1, 2 and 3. As already mentioned before the molecules at the extremities of the molecular rows (marked by blue dashed circle) might be in a meso-stable geometry and could be sensitive to tip interaction.

Fig. 4.26 (b)-(d) shows the variation of deconvoluted DOS along trajectory 1 shown in (a) at tip-sample distances of -75 pm, -150 pm and -300 pm respectively (corresponding SIS data shown in supplementary figure Fig. 4.40). Along the opposite direction of trajectory 1 four successive "0B" molecules are labeled from 1a to 1d. Their center macrocycles are marked by semi-transparent blue rectangles which are guides to the eyes.

In Fig. 4.26 (b) the tip-molecule interaction is weakest. 1a, 1c and 1d molecules exhibit two pairs of Shiba states (The zero energy state in 1a macrocycle is the signature of delocalized state generated by the presence of 2a molecule (see Fig. 4.27)). The Shiba state that is closer to the gap edge locates strictly on the macrocycle correspond to CS2. The Shiba state closer to Fermi level shows a continuous decrease of energy from 1a to 1d (i.e. ${}_{-75pm}E_1^{1a} > {}_{-75pm}E_1^{1c} > {}_{-75pm}E_1^{1d}$ with ${}_{\Delta z}E_n^M$ represents the average energy of channel n Shiba state of molecule M at relative tip distance Δz), indicating a monotonous increasing or decreasing of coupling strength with

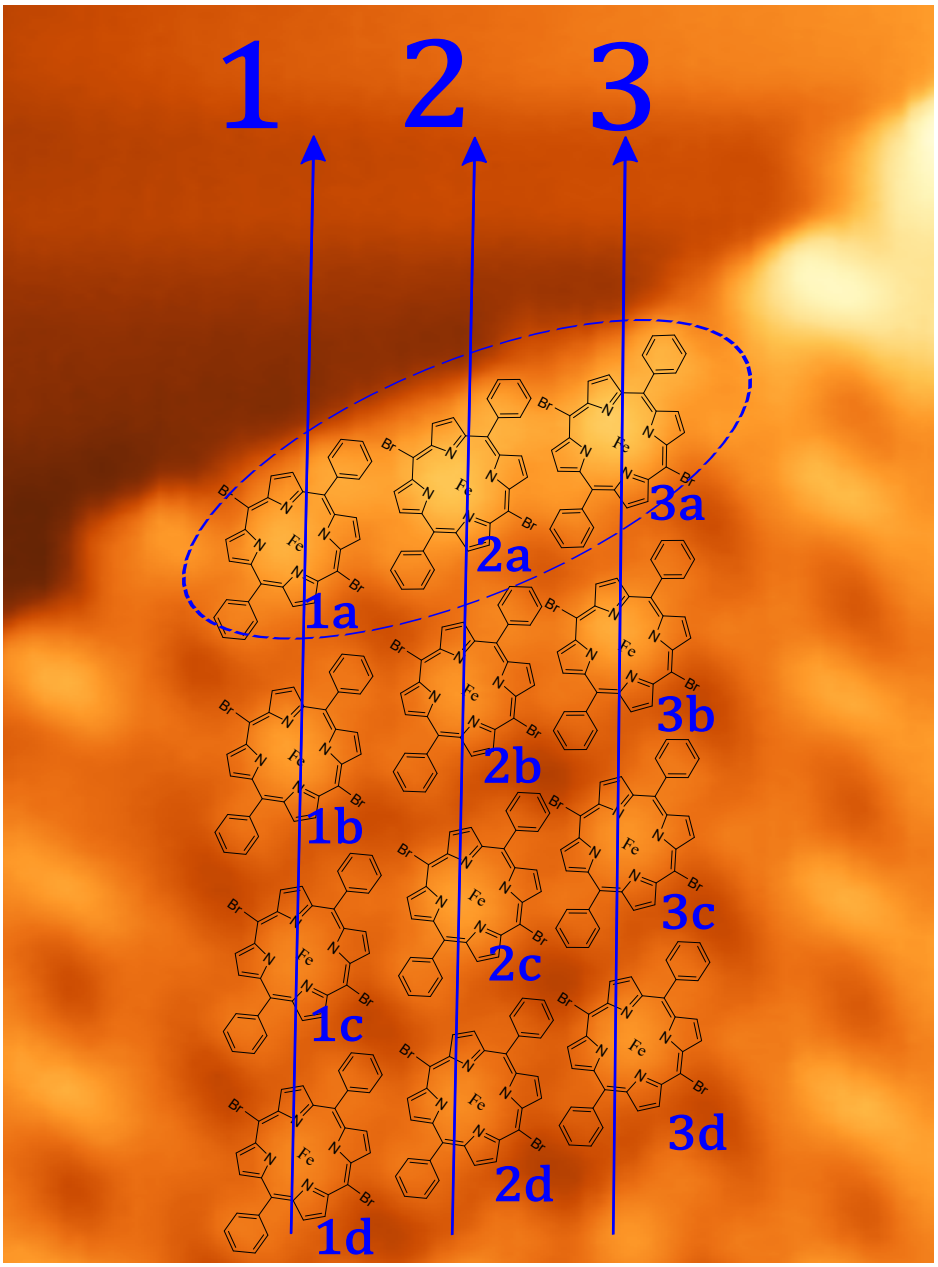

Figure 4.25: Topographic image of well-ordered $Fe-DBrDPP$ **"0B" supramolecular lattice consisting of three parallel rows of "0B" molecules.** Topography image ($6.5x8.7nm^2$, setpoint: 150 mV, 100 pA, -75 pm) showing well-ordered $Fe-DBrDPP$ "0B" supramolecular lattice consisting of three parallel rows of "0B" labeled by 1, 2 and 3. Blue dashed circle marked three "0B" molecules at the extremities of the rows. The "0B" supramolecular lattice is embed inside "4mer" supramolecular lattice where "0B" molecular rows 1 and 3 are near two different interfaces.

substrate due to molecule's geometry. Such spatial energy variation of Shiba state is similar to what we have seen for CS1 of A-type domains (Fig. 4.12). Hence we attribute the low-energy Shiba state to CS1. 1b molecule behaves like a standard "0B" molecule where CS1 show delocalized behavior of its electron-like component and CS2 localizes on macrocycle.

We also notice that CS2 here remain almost unchanged while CS1 varies obviously, this is in consistent with what we have observed for "1B" supramolecular lattice in section (4.6.3). This observation indicates that molecular orbital 1 which generates CS1 is easier to be perturbed by environment (geometry effect and tip effect) with respect to molecular orbital 2 that gives rise to CS2.

Comparing with 1b molecule, in the case of 1a, 1c and 1d molecules, CS2 peaks shift to lower energy, becoming distinguishable in (b), while CS1 do not exhibit obvious delocalized character and become sensitive to perturbation. This unusual behavior is due to geometry effect that makes 1a, 1c and 1d molecules behave differently from standard molecules, nevertheless, we still use the notion CS1 and CS2 to characterize two Shiba states generated by these "0B" molecules.

Now we study the effect of tip interaction on these molecules by comparing Fig. 4.26 (b)(c)(d) in which tip-molecule distance Δz is variable.

When tip moves closer to the molecule (from (b) to (d)), its effect is to decrease CS1's energy. For 1a, 1c, 1d molecules, CS1 peaks shift closer to Fermi level ($_{-75pm}E_1^M > _{-150pm}E_1^M$ for M = 1a,1c,1d) and eventually cross Fermi level, indicating that channel 1 undergoes quantum phase transition[9]. This effect is the same as the one induced geometry effect along opposite direction of trajectory 1. Interestingly, when CS1 peaks cross Fermi level, CS2 peaks feature suddenly disappear in the spectra. Also 1b molecule appears not responding to tip interaction at all for both CS1 and CS2.

Fig. 4.28 and Fig. 4.29 respectively show the variation DOS along trajectories 2 and 3 of Fig. 4.25. No spatial variation of CS1 energy is observed, probably indicating that geometry effect is weak for molecules in rows 2 and 3.

According to the behavior of in-gap states, the molecules studied in "0B" supramolecular lattice can be broadly divided into three types.

1. Type1 "0B" molecules. 1b, 2b, 2c, 3a and 3b molecules correspond to this type. CS2 stay close to the gap edge and CS1 exhibits electron-like component delocalization. This type also corresponds to the standard "0B" molecules introduced in sections (4.6.3), (4.6.3). More importantly Type1 "0B" molecules are immune against tip effect.

2. Type2 "0B" molecules. 1a, 1c, 1d, 2d, 3c and 3d molecules correspond to this type. CS2 locates at around ± 0.9 mV and CS1 is sensitive to tip effect. Excepts 2d molecule which CS1 and CS1 remain degenerate.

3. Exotic "0B" molecules. 2a molecule corresponds to this type in which we observe only

[9] In this scenario average energy description $_{\Delta z}E_n^M$ is no long proper.

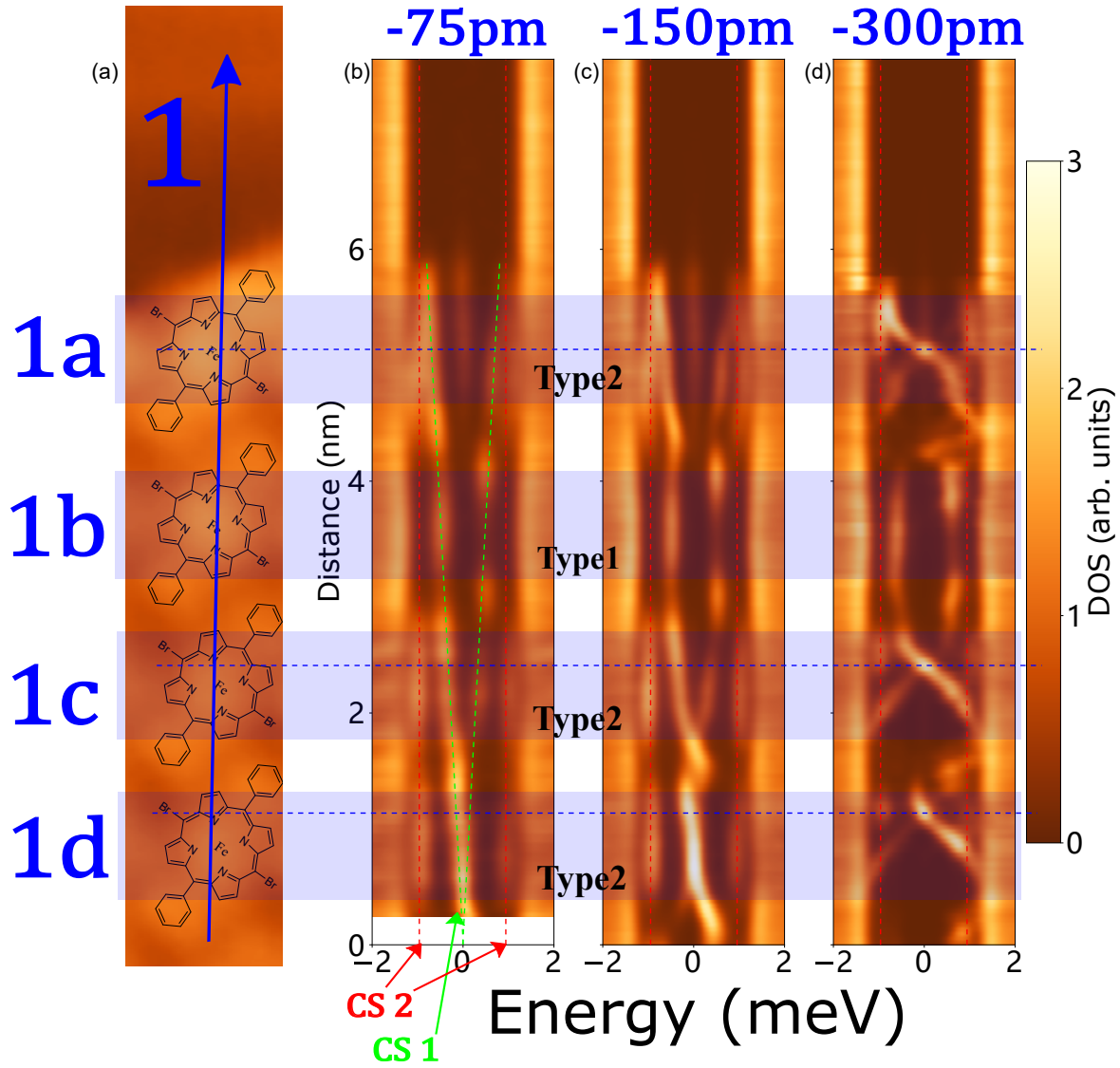

Figure 4.26: Tip distance dependence of in-gap states of line 1 "0B" $Fe-DBrDPP$ **molecules.** (a) Topography image showing "0B" molecular row 1 on which four successive "0B" molecules are labeled by 1a, 1b, 1c and 1d in opposite direction along the arrow. (b)-(d) Stacking plot of point DOS along the blue arrow 1 in (a)(Setpoint: 150 mV, 100 pA, $-75/-150/-300$ pm). Vertical red dashed lines mark the energies of ± 0.9 meV which correspond to CS2's energy, sloping green dashed lines roughly mark CS1's peaks, horizontal blue lines indicate the location when CS1 crosses Fermi level for 1a, 1c and 1d molecules. Semi-transparent blue rectangles mark the region of macrocycles of "0B" molecules.

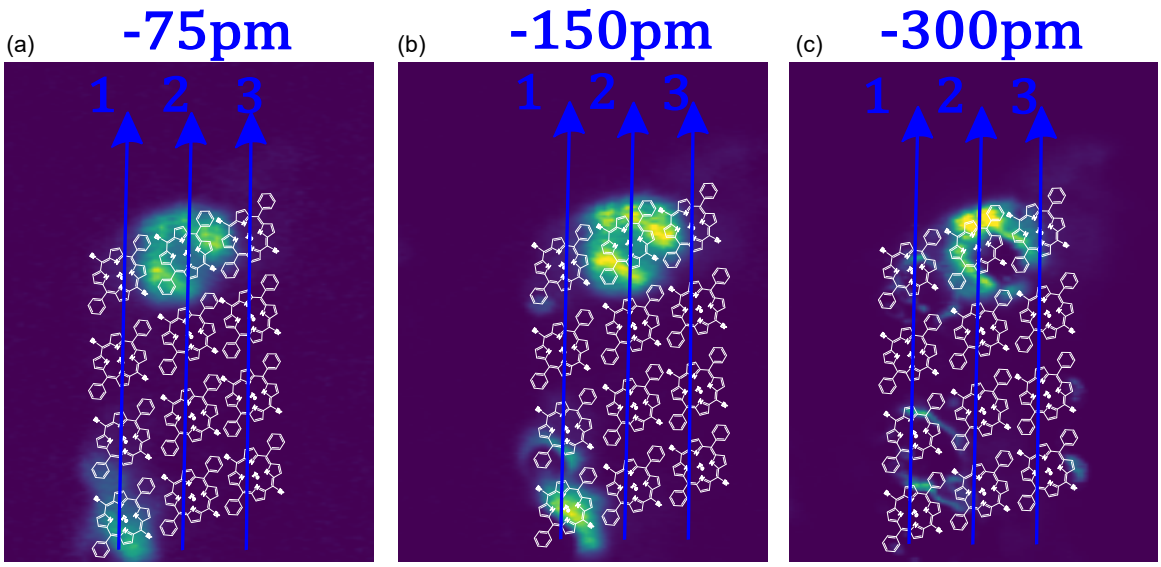

Figure 4.27: Zero energy DOS map of "0B" supramolecular lattice (a)-(c) Zero energy DOS maps of "0B" supramolecular lattice shown in Fig. 4.25 measured at different tip-sample distances. Setpoint: 150 mV, 100 pA, $-75/-150/-300$ pm.

one peak at zero energy, it exhibits a strong delocalized character (Fig. 4.27) and appears not affected upon tip interaction.

4.6.4 Analysis

Finally in this section, we will analyze the contents presented in previous two sections to figure out the orbital origin, ground state properties of $\mathrm{Fe-DBrDPP}$ molecules in different orderings, and understand how tip and local geometry affects molecules' electronic properties.

Orbital origin of Shiba states

To explain all kinds of behavior of in-gap states of $\mathrm{Fe-DBrDPP}$ molecule on Pb(110) surface, we must first track the original molecular orbitals that give rise to in-gap states. We know that "4mer" $\mathrm{Fe-DBrDPP}$ molecule on Pb(110) surface exhibits S = 1 state, and it shows SF excitation which is very similar to $\mathrm{Fe-DPyDBrPP}$ molecule on Au(111) surface. Thus we first assume that FOA (originated from Fe d_{z^2} orbital) and FOB (hybridized molecular orbital of macrocycle π orbital with Fe $d_\pi(d_{xz}, d_{yz})$ orbitals) are responsible for the spin excitation channels for all $\mathrm{Fe-DBrDPP}$ molecules in different regimes.

We have observed a continuous evolution of out-gap SF feature and in-gap Shiba feature in "0B" molecules near interface which indicate that these features should originate from the same molecular orbital. By comparing Fig. 4.24 (b-e), Fig. 4.37 (b-e) and 1a, 1c,1d (Type2 "0B" molecules) in Fig. 4.26 (d), we consider that FOB is responsible for the continuous gap-crossing phenomena. Which means FOB should be the origin of CS1. But it should be noted that

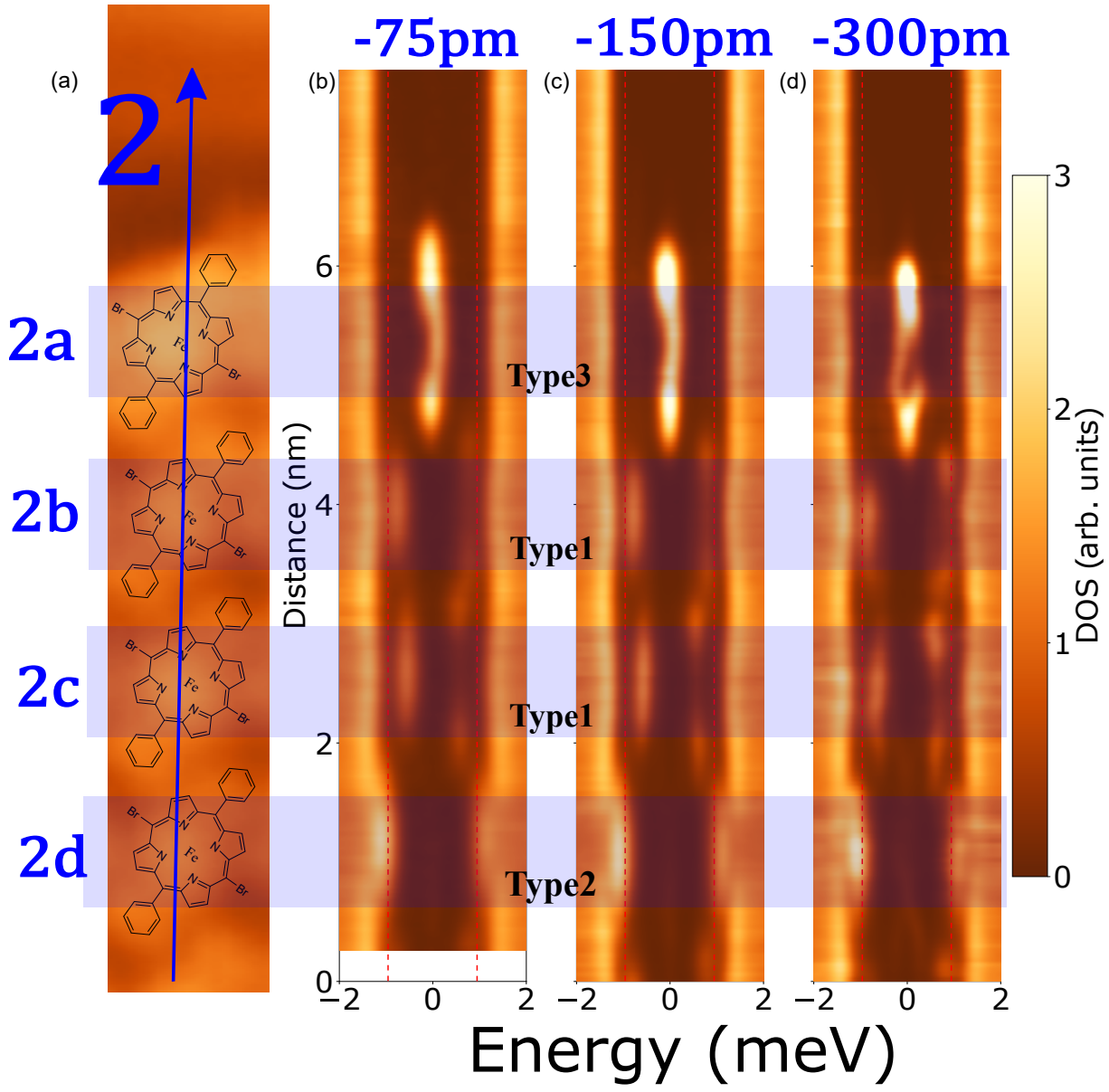

Figure 4.28: Tip distance dependence of in-gap states of line 2 "0B" $Fe-DBrDPP$ **molecules.** (a) Topography image showing "0B" molecular row 2 on which four successive "0B" molecules are labeled by 2a, 2b, 2c and 2d in opposite direction along the arrow. (b)-(d) Stacking plot of point DOS along the blue arrow 2 in (a)(Setpoint: 150 mV, 100 pA, $-75/-150/-300$ pm). Vertical red dashed lines mark the energies of ± 0.9 meV. Semi-transparent blue rectangles mark the region of macrocycles of "0B" molecules.

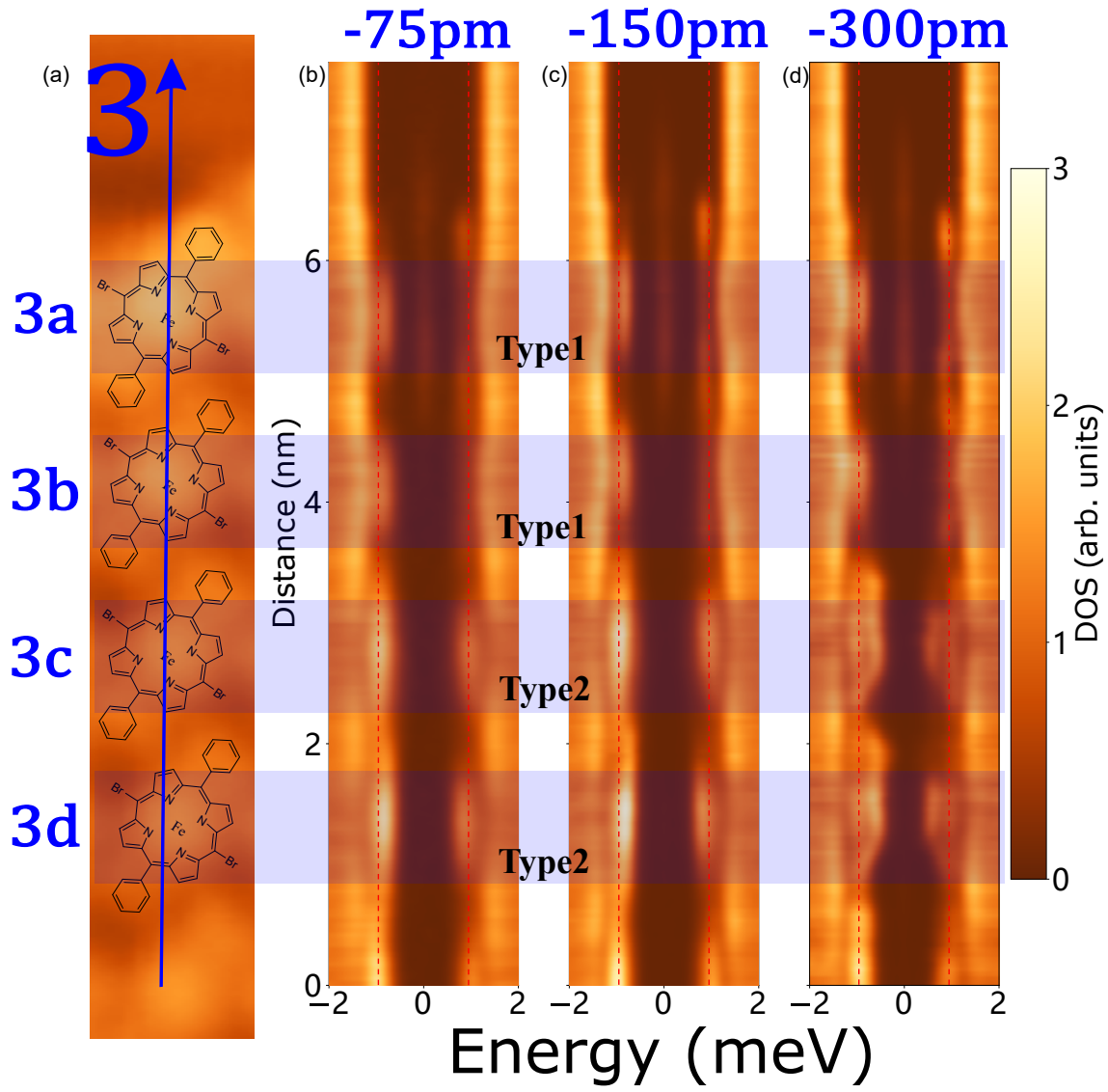

Figure 4.29: Tip distance dependence of in-gap states of row 3 "0B" $\mathrm{Fe-DBrDPP}$ **molecules.** (a) Topography image showing "0B" molecular row 3 on which four successive "0B" molecules are labeled by 3a, 3b, 3c and 3d in opposite direction along the arrow. (b)-(d) Stacking plot of point DOS along the blue arrow 3 in (a)(Setpoint: 150 mV, 100 pA, $-75/-150/-300$ pm). Vertical red dashed lines mark the energies of ± 0.9 meV. Semi-transparent blue rectangles mark the region of macrocycles of "0B" molecules.

during gap-crossing phenomena, molecular orbital reorganization occurs and the compositions of FOB are modified under charge fluctuation.

Then FOA should be the origin of CS2 that always locate on the macrocycle of $\mathrm{Fe-DBrDPP}$ molecule. Unlike $\mathrm{Fe-DPyDBrPP}$/Au(111) system where the FOA is mainly contributed from d_{z^2} orbital, here for $\mathrm{Fe-DBrDPP}$/Pb(110) system FOA distributes over macrocycle, indicating a more important contribution from macrocycle π orbital.

From now on we adapt the same notion of FOA and FOB to describe the frontier molecular orbitals that give rise to CS2 and CS1 Shiba states of "0B" molecules.

Ground state and excited state characterization

Now we will determine the ground state and excited state properties of $\mathrm{Fe-DBrDPP}$ molecule with the help of gap-crossing phenomena reproduced in Fig. 4.30. Before we begin, let's first review the relative spectral weight behavior of standard "0B", "1B" molecules (Type1 "0B" and "1B"). For spectra measured on the macrocycle of standard molecules, hole-like component of Shiba state always exhibits stronger spectral weight than the electron-like component ("1B": Fig. 4.19, "0B": Fig. 4.22), this implies that the standard molecules are in same regime, which can be either weak coupling regime that favors free-spin state or strong coupling regime that favors Kondo-screened state.

Fig. 4.30 reproduces the results of tip interaction driven gap-crossing feature shown in Fig. 4.24 and in-gap state evolution feature shown in Fig. 4.26 on "0B" molecules near the interface. Upon tip interaction, "0B" molecules can be in three different regimes: SF, S1 and S2 regimes with SF corresponds to spin-flip regime in which the molecule exhibit out-gap SF features, S1 corresponds the coexistence of single in-gap state and out-gap feature, S2 is the regime where two in-gap states are observed. These regimes are labeled in Fig. 4.30 (c)(e).

For molecules in SF regime, the coupling with substrate J is weakest and the ground state can be written as $(Q = 0, S_z = 0)$ where Q denotes the number of bound quasiparticles to the impurity and S_z the projection of the total spin ($S_z = 0$ indicates a positive uniaxial anisotropy) and the excited state will be $(0, \pm 1)$ (see Fig. 1.2 (b)) whose energy with respect to ground state is determined only by magnetic anisotropy D and E.

In S1 regime, out-gap SF feature and one in-gap Shiba feature coexist, indicating a moderate coupling strength J that is comparable with anisotropy D and CS1 should be in weak coupling regime. The ground state is then the same as SF regime which is $(0, 0)$, a free-spin ground state. The out-gap and in-gap excitation feature should correspond to the excited states of $(0, \pm 1)$ and $(1, \pm 1/2)$ respectively. Such coexistence of SF and Shiba phenomena has also been reported in [103] but for a S = 3/2 MnPc molecule.

For S2 regime, both CS1 and CS2 exhibit standard relative spectral weight behavior, which is reversed with respect to that of weak coupling CS1 (electron-like component stronger than hole-like one). This implies that CS1 in S2 regime has entered strong coupling regime and a quasiparticle is bounded to channel 1. Hence the ground state of S2 regime will be determined by CS2. From the relative spectral weight point of view, CS2 exhibits standard relative spectral

weight behavior i.e. also in strong coupling regime. Then the higher energy of CS2 with respect to CS1 in strong coupling regime refers to a stronger coupling strength $J_2 > J_1$ (see Fig. 1.13), this is in agreement with the assumption of FOA (d_{z^2} related) origin which should have stronger coupling with substrate due to d_{z^2} orbital nature. Hence the ground state of S2 regime should be $(2, 0)$ and excited state will be $(1, \pm 1/2)$

It is astonishing that from S1 to S2 regimes two quasiparticles bound to impurity simultaneously. To understand this behavior we study the crossover from S1 to S2 regimes illustrated in Fig. 4.30. Blue point indicates the transition point where CS1 peaks merge at Fermi level. Between black and blue dashed lines molecule is in S1 regime with ground state $(0, 0)$ and out-gap SF excitation coexists with CS1. Tracking from black to blue lines, CS1 peaks move closer to each other, indicating an increase of J_1. When J_1 is large enough and two peaks merge with each other at Fermi level, a quasiparticle is bounded to channel 1, resulting a reduction of total spin by 1/2, i.e. $\Delta Q = +1$, S = 1 reduced to S = 1/2. For a S = 1 impurity, the reduction of spin by 1/2 strongly renormalises magnetic anisotropy D which determines the energy of SF excitation (see section (1.2.5), equation (1.9)). This sudden reduction of spin explains the disappearance of SF feature at transition point. In the meantime, channel 2 becomes freed from magnetic anisotropy and couple with substrate by bounding another quasiparticle, giving rise to CS2 and reduce the total spin to 0, i.e. $\Delta Q = +2$, S = 1/2 further reduced to S = 0[10].

Yet, for S1 regime it is still very puzzling as we observe only CS1 inside the gap, while channel 2 that has stronger coupling strength with substrate appears to be "pushed" outside the gap and become SF feature. So far we cannot interpret the behavior of S1 regime, but we believe there must be a more complex competition (relation) between the parameters of J_1, J_2, Δ, D_{eff} (effective magnetic anisotropy after renormalisation due to coupling, charge fluctuation) that is beyond the theoretical framework introduced in section (1.3.4).

Geometry effect and tip effect

Once the orbital characterization and ground state are determined we can discuss about the geometry effect and tip effect. By reviewing Fig. 4.26 (b) we can quickly determine the tip effect: For $\Delta z > -300$ pm (setpoint: 150 mV, 100 pA), when tip-molecule distance decreases, coupling strength J_1 decreases as well, indicating that tip applies an attractive force on molecule and decreases overlapping of FOB with surface Pb atom.

To understand the geometry effect, we can compare Type1 and Type2 "0B" molecules produced by geometry effect.

For a Type1 "0B" molecule (e.g. 1b in Fig. 4.26), CS2 always lies very close to the gap edge, indicating a rather strong coupling strength J_2 while CS1 can adopt different energies depending on adsorption sites (e.g. 2b, 2c in Fig. 4.28). The most impressive point is that, no matter what energy CS1 adopts, so long as CS2 stays close to gap edge, CS1 remains immune against tip interaction (e.g. 1b, 2b, 2c and 3a, 3b).

[10]However in the work of Hatter et. al. for a S = 1 system a different scenario is observed when CS1 binds a quasiparticle.

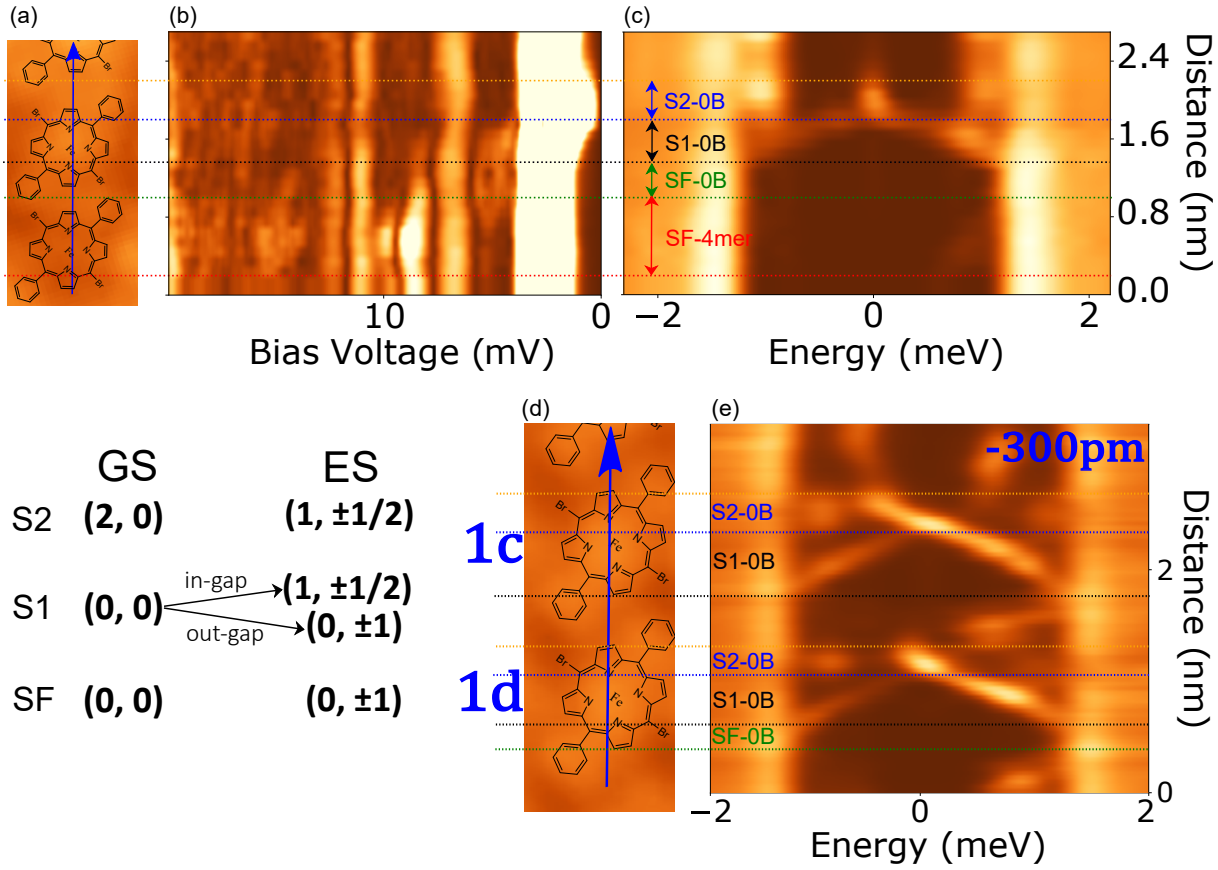

Figure 4.30: Illustration of gap-crossing feature of "0B" Fe − DBrDPP **molecule near interface.** (a) Topography image showing linecut across "4mer" and "0B" on the either sides of interface. Cropped from Fig. 4.24 (a). (b) Stacking plot of point value of expression (4.1) along linecut in (a). Cropped from Fig. 4.24 (b). (c) Stacking plot of point DOS along linecut in (a). Cropped from Fig. 4.37 (c). (d) Topography image showing linecut across 1c, 1d molecules in Fig. 4.26. (e) Stacking plot of point DOS along linecut in (d). Cropped from Fig. 4.26 (d). Table to the left bottom shows the ground state (GS) and excited state (ES) for spin-flip (SF) and Shiba (S1, S2) excitation in different regimes that are also labeled in (c)(e).

If CS2 shifts away from gap edge (at around ± 0.9 meV), molecules will become Type2 "0B" molecule and CS1 become sensitive to tip interaction (e.g. 1a, 1c, 1d, 3c, 3d). For example in Fig. 4.29 (c) 3b (Type1) and 3c (Type2) molecules both exhibit a pair of peaks inside the gap at ± 0.9 meV but 3c has stronger spectral weight than 3b, this means that CS1 and CS2 peaks merge with each other in 3c molecule (i.e. $J_1 = J_2$), resulting an enhanced spectral weight. While under strong tip interaction in Fig. 4.29 (d), the degeneracy of CS1 and CS2 in 3b molecule is lifted, CS1 peaks shift towards lower energy while CS2 remains unchanged. In fact the behavior of Type2 "0B" 3c molecule is exactly the same as blue point marked "0B" molecule in Fig. 4.22.

Hence we can conclude that inter-molecular interaction is the main contributor to geometry effect. It occurs essentially near the interface between lattices of different orderings. It direct consequence should be to induce molecular orbital reorganization which results two types of "0B" molecules. Both of them exhibit identical topography character but FOB of Type2 "0B" molecules are much more sensitive to external perturbation.

Another consequence of the geometry effect is to induce charge fluctuation that greatly shifts molecular orbital for strong coupling "1B" molecules introduced in section (4.6.3).

Classification of $\mathrm{Fe-DBrDPP}$ molecules

In general, we can make a classification of $\mathrm{Fe-DBrDPP}$ molecules on Pb(110) surface with post-annealing temperature of 400 K in Fig. 4.31.

From top to bottom, the first line shows three basic orderings of "4mer", "0B" and "1B" depending on their coupling strength with substrate and topography character.

The second line shows that "0B" and "1B" $\mathrm{Fe-DBrDPP}$ molecules can be further classified into two sub-types as a result of geometry effect. For "0B" molecule, the direct consequence of geometry effect is to induce reorganization of frontier molecular orbitals, resulting Type1 and Type2 "0B" molecules. For "1B" molecule, the direct consequence is to induce charge fluctuation that quenches the molecular orbital resulting a depression center in topography and zero in-gap feature in spectroscopy for Type2 "1B" molecules.

The third and fourth line show the regimes of different types of $\mathrm{Fe-DBrDPP}$ molecules. In SF regime, molecules exhibit out-gap inelastic spin-flip excitation feature, indicating a magnetic anisotropy dominated free-spin ground state $(0, 0)$ and the excited states are $(0, \pm 1)$. In S1 regime, in-gap Shiba state and out-gap SF feature coexists, the ground state should be $(0, 0)$ and possible excited states are $(0, \pm 1)$ and $(1, \pm 1/2)$. In S2 regime, there are always two Shiba states, the ground state and excited state are $(2, 0)$ and $(1, \pm 1/2)$, respectively.

For $\mathrm{Fe-DBrDPP}$ molecules inside the supramolecular lattice, most of them are in SF (for "4mer") or S2 (for "0B", "1B") regimes which respectively stand for weak and strong coupling case. S1 is an intermediate regime which can only be observed with large tip effect, it usually occurs in Type2 "0B" molecules that locate near the interface and are sensitive to tip effect. Tip effect can also drive a switching between SF, S1 and S2 regimes. Only Type2 "1B" molecules do not exhibit low-energy excitation, indicating a quench of magnetism due to charge fluctuation.

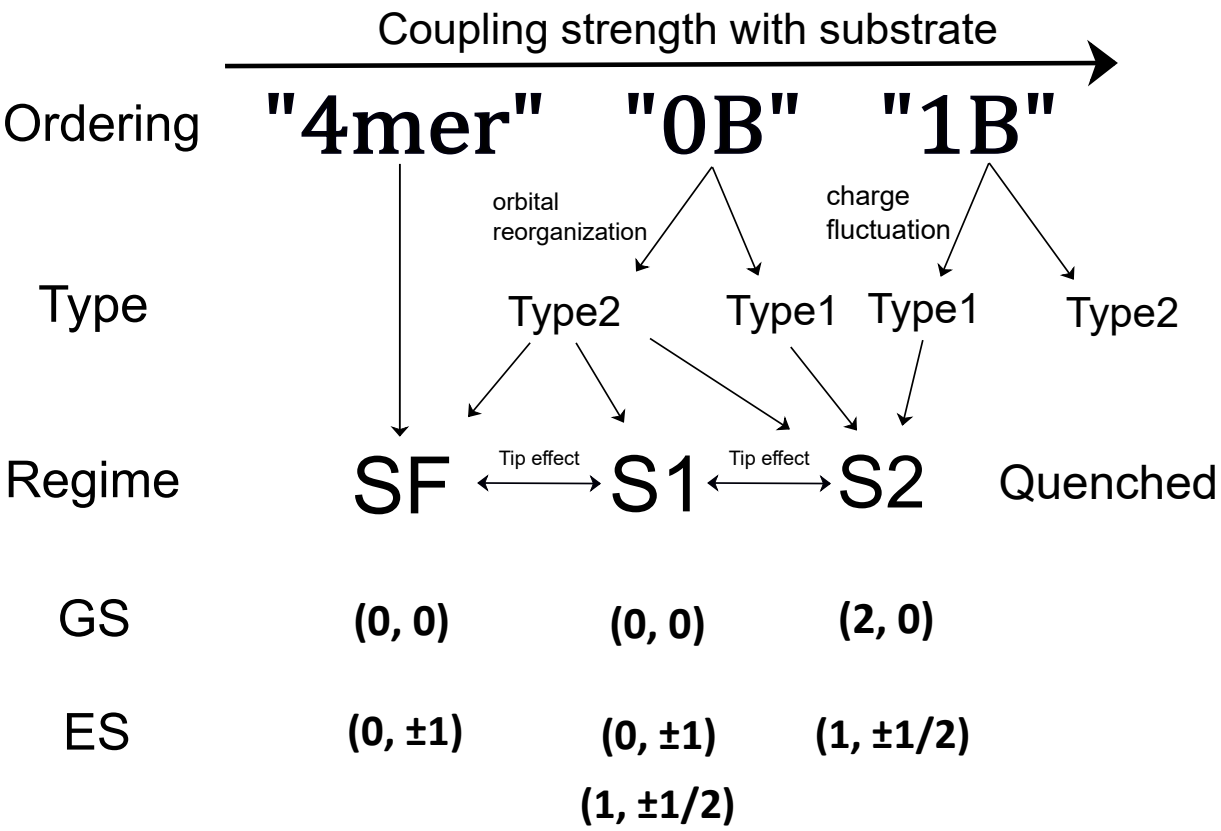

Figure 4.31: Classification of $\mathrm{Fe-DBrDPP}$ **molecules on Pb(110) surface with post-annealing temperature of 400 K.** First line: Three basic orderings are successively presented according to the molecule-substrate interaction strength indicated by top horizontal black arrow. Second line: Depending on molecule geometry, "0B", "1B" ordering can be further classified into two types. Third line: Regimes that describe the low-energy excitation behavior of molecules. GS and ES refers to ground state and excited state of different regimes. "Quenched" means Type2 "1B" molecule exhibits no low-energy excitation feature due to charge fluctuation which quenched the molecular orbital.

4.6.5 Conclusion

To summarize, we have presented our results on $\mathrm{Fe-DBrDPP}$ molecules on superconducting Pb(110) surface with post-annealing temperature of 400 K. We observe a more fruitful molecular orderings compared with annealing temperature of 360 K case, but unfortunately none of them is molecular network based on covalent bonding. Nevertheless in this section we have determined the electronic properties including ground state and molecular orbital origin of S = 1 molecules, and revealed the relation between electronic properties and molecular geometry. The effect of geometry has many consequences, e.g. it can make $\mathrm{Fe-DBrDPP}$ molecule sensitive to tip so that molecules can switch between different regimes upon tip interaction. There are 3 regimes based on the low-energy excitation behavior: SF, S1 and S2 where each of them possesses different ground states or excited states. We have also found an additional regime in which geometry effect induces quenched molecular orbital.

4.7 Supplementary section: $\mathrm{Fe-DBrDPP}$ on Pb(110)

4.7.1 Low-temperature phase

Molecule sketch adjustment

For those supramolecular lattices where we can not easily distinguish the molecular ordering from topography, we will use spectroscopy to determine the molecular ordering.

Fig. 4.32 shows one example of how we determine the molecular ordering, it usually follows the steps of:

1. Compare the topography and spectroscopy images (dI/dV or DOS maps) of target supramolecular lattice and find out a spectroscopy image that shows a clear Shiba states feature which has the periodicity of the supramolecular lattice, for example in Fig. 4.32 (a) we can see the Shiba DOS pattern at -0.52 meV shows an obvious periodicity.

2. Use a 2D linear grid to fit the Shiba pattern as shown in Fig. 4.32 (b). We can then put the molecule inside the 2D grid, here we match the center of the molecule to the intersections of grid, such choice is not always exact because Shiba feature does not always localize at magnetic center, but in any case the ordering of molecules should follow the periodicity of grid.

3. Verify the ordering in Fig. 4.32 (b) for topography image (Fig. 4.32 (c)) and other conductance maps (Fig. 4.32 (d)). If it does not match we return to the second step, readjust the ordering of molecules (relative position to the intersections and rotation of molecule) and redo third step again until we obtain an ordering that can describe topography and spectroscopy.

Such treatment is not very a rigorous approach because we do not taken into account many factors including supramolecular lattice mismatch effect, inter-molecule interaction, molecule deformation, etc. but it should yield a reasonable molecular ordering. Yet to know the real molecular ordering, it should not only match topography and spectroscopy behavior but also energetically favorable i.e. a systematic chemical study is needed.

B-type self-assembled supramolecular lattice of $\mathrm{Fe-DBrDPP}$ molecules

The electronic properties of one of the antiphase B-type domains is presented in Fig. 4.33.

Compared with A-type domains where most of molecules exhibit CS1 which energy is around 0.66 meV and CS2 close to the gap, for B-type domains, CS1 shows energy around 0.9 meV and CS2 around 1.17 meV. These two states are close to each other and locate near gap, making them to be indistinguishable in stacking plot figures shown in (f)-(i). But we observe two exotic molecules marked by cyan arrows, one of which is the first molecule in arrow 2 and the other is the second molecule in arrow four, in these two molecules, CS1 shifts towards Fermi

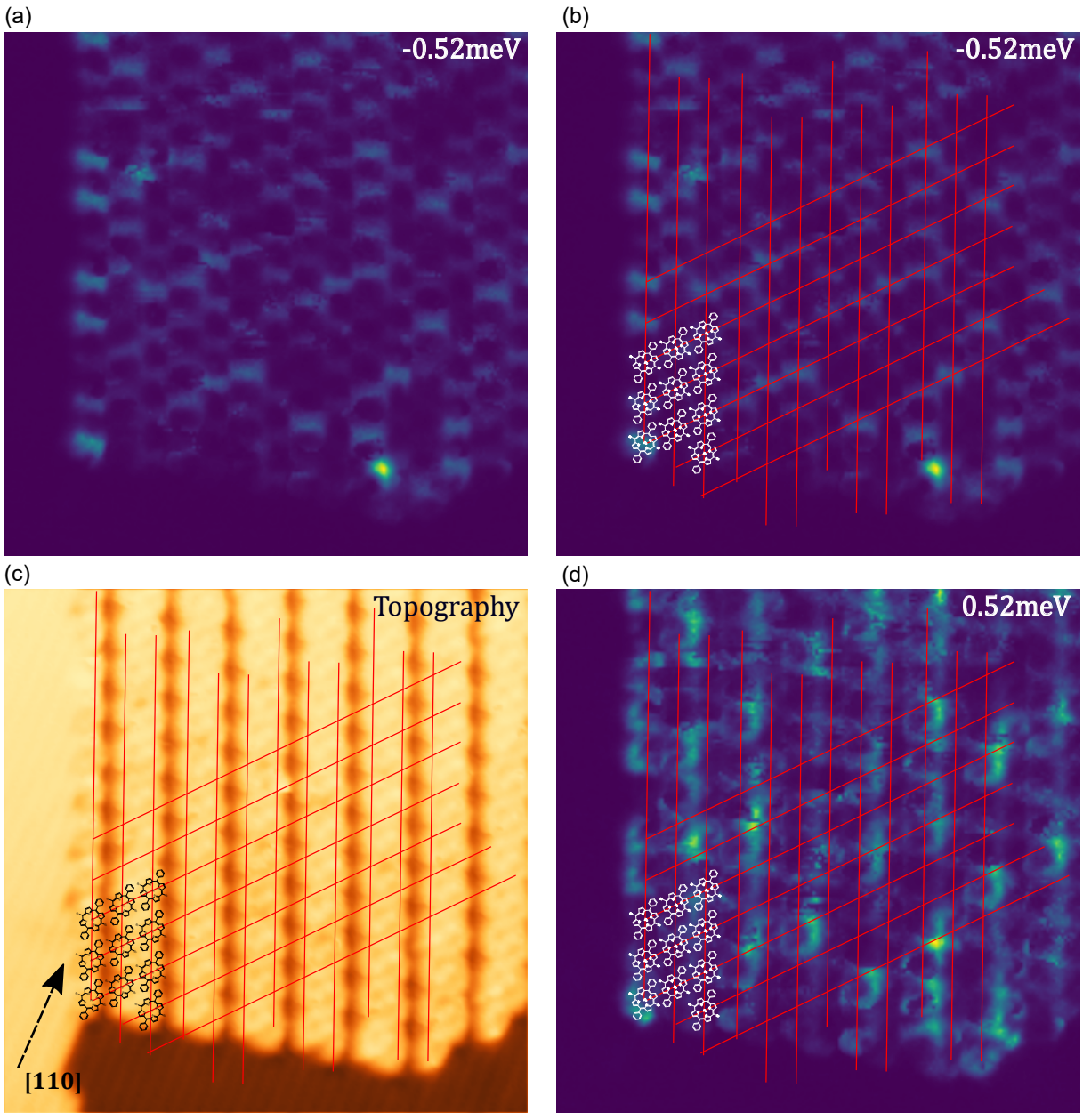

Figure 4.32: Procedure to determine molecular ordering. (a) Find out a spectroscopic image (dI/dV or DOS map) that shows distinguishable periodic feature. (b) Use 2D grid to match the periodic feature in (a). The molecules should follow the periodicity of the grid. (c)(d) Comparing topography image, other spectroscopy images with the 2D grid and determine the relative position and orientation of molecules.

level and becomes separated from CS2, making it possible to distinguish both Shiba states in (g) (red dashed line) and (i) (green dashed line).

The spatial distribution of CS1 and CS1 of B-type domains is shown DOS maps shown (b)-(e). For CS1 the hole-like and electron-like components distribution can be visualized respectively in DOS maps (b) and (c) of energies -0.8 meV and 0.8 meV. The hole-like component shows a round shape locating on macrocycle of molecules while the electron-like component delocalizes from the molecule and distributes around. Between rows 2,3 the electron-component shows a similar pattern to A-type case, indicating that α Br$\cdots\pi$ halogen bonds and pyrrole-pyrrole bonds are responsible for delocalization behavior.

Generally speaking, in B-type domains, we have found similar spatial distribution to the A-type assemblies and the difference appears to be that energies of CS1 and CS2 are lower. This indicates that A-type or B-type domains of $\mathrm{Fe-DBrDPP}$ molecule do not significantly influence the molecules electronic properties.

4.7.2 High-temperature phase

Spectroscopic characterization of "4mer" molecules

Fig. 4.34 shows the topographic and spectroscopic data of a $\mathrm{Fe-DBrDPP}$ "4mer" supramolecular lattice which consists of both "4mer-A" and "4mer-B" molecules. From the topography image shown in (a) we can see that along single "4mer" molecular row "4mer" molecule can be "A" type or "B" type. "4mer-B" molecules adopt saddling conformation and exhibits distinguishable molecule center as shown in Fig. 4.16 (b). While "4mer-A" molecule is impossible to be distinguished as topographic weight transferred to the phenyl rings that connect to other "4mer-A" molecules in adjacent molecular rows. This could imply that phenyl rings of "4mer-B" molecule lie in a planar way in which the phenyl rings are parallel to the surface, resulting a weak topographic weight on phenyl rings. The phenyl rings of "4mer-A" molecules may lie vertically to the surface, resulting an enhanced topographic weight on phenyl rings that make center indistinguishable. Nevertheless the different ordering "4mer-A" and "4mer-B" may adopt, neither of them can induce in-gap states ((b) and (c)), indicating that "4mer" phase is a stable ordering of $\mathrm{Fe-DBrDPP}$ on Pb(110) surface, but decoupled from it. When the local distortion exists in "4mer" supramolecular lattice, it is possible to recover in-gap feature as shown by red curves in (b) which is taken at the red cross position in (a).

Exotic "4mer" molecules

Fig. 4.35 shows the SIS dI/dV data of exotic "4mer" molecules inside the supramolecular lattice. In topography image (a) three exotic molecules marked by red, green and blue points do not exhibit unusual topographic characters, indicating there is no obvious conformation distortion for them. But in stacking plot of symmetrized dI/dV data along the green arrow, the SF feature that locates at ± 9.5 mV and ± 15.5 mV for standard "4mer" molecules do not hold for blue and green ones (blue and green points marked molecule, here for simplicity). The blue one

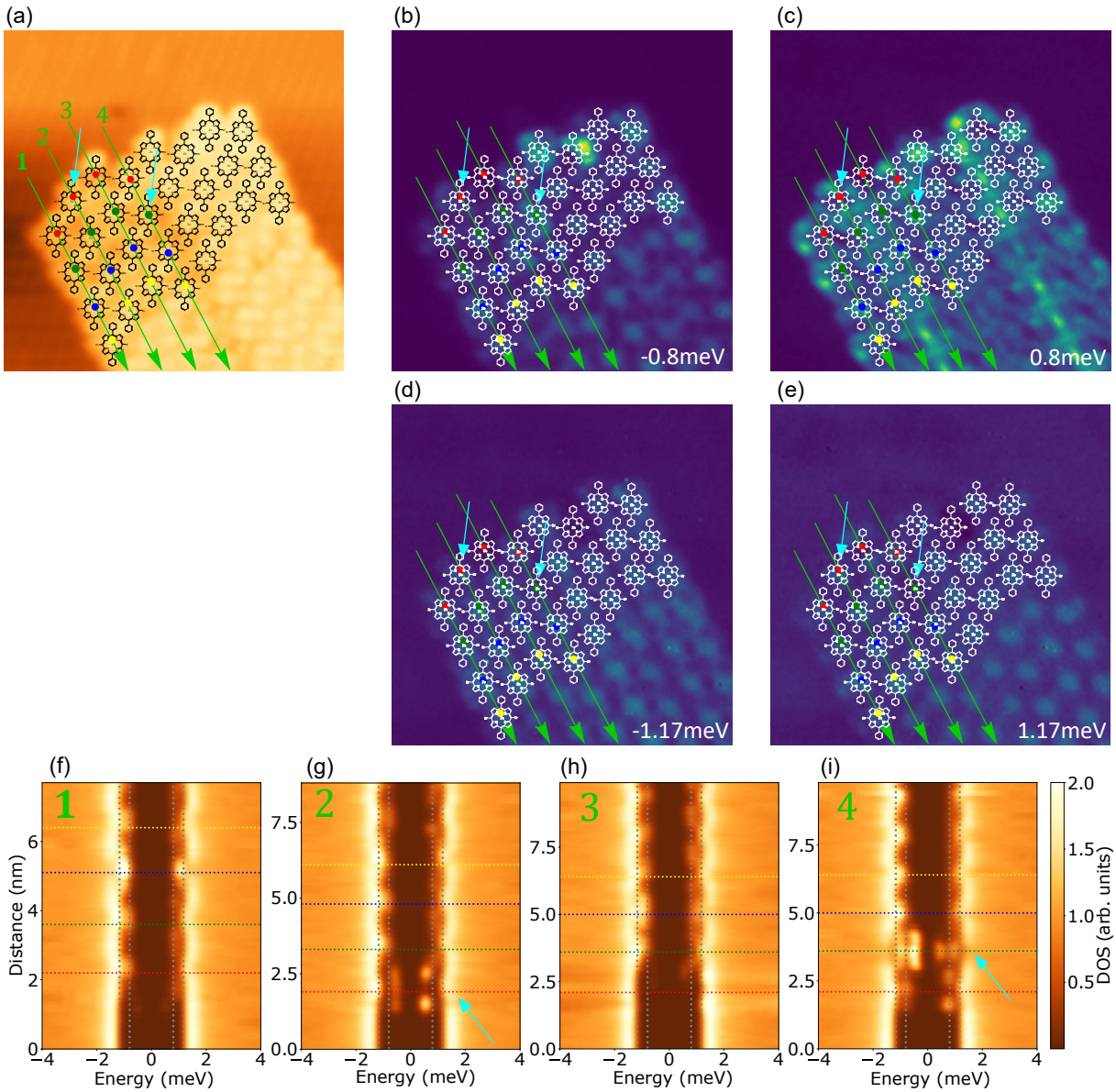

Figure 4.33: Spectroscopy data of B-type domains $\mathrm{Fe-DBrDPP}$ **supramolecular lattice on Pb(110) surface.** (a) Same topography image as Fig. 4.11 (a), green arrows labeled from 1 to 4 refer to four successive molecular rows. (b)-(e) DOS maps at energies of -0.8 meV, 0.8 meV, -1.17 meV and 1.17 meV respectively. (f)-(i) Stacking plot of point DOS along green arrow labeled from 1 to 4 in (a). Vertical gray dashed lines mark the energies of ± 0.8 meV and ± 1.17 meV. Horizontal colored dashed lines mark the positions of points of same colors on corresponding arrow in (a)-(e). Cyan arrows mark two exotic molecules on rows 2 and 4 respectively.

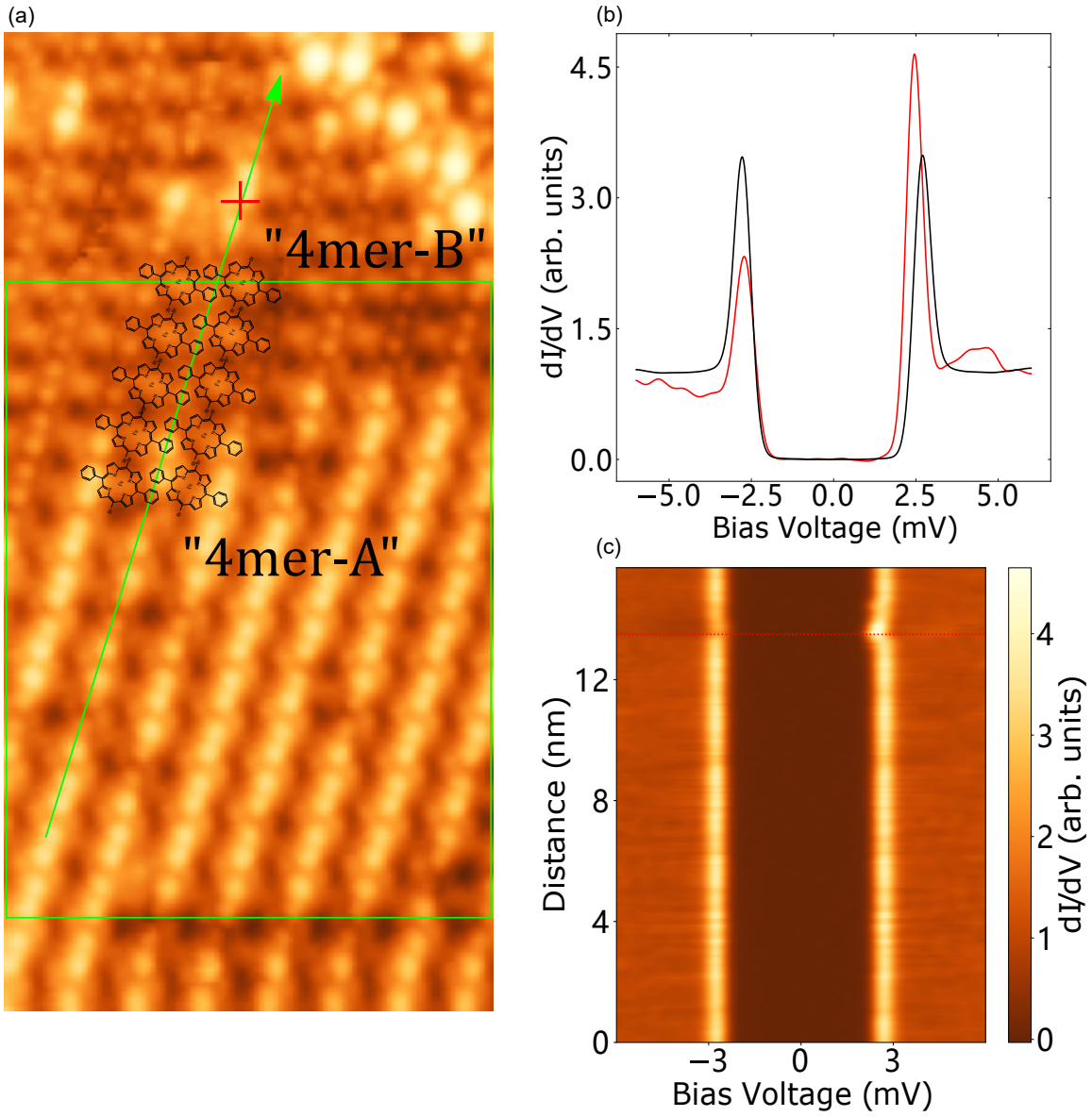

Figure 4.34: "4mer" supramolecular lattice consisting of "4mer-A" and "4mer-B" $\mathrm{Fe-DBrDPP}$ **molecules.** (a) Topography image ($10\mathrm{x}20\mathrm{nm}^2$, setpoint: 8 mV, 50 pA) of $\mathrm{Fe-DBrDPP}$ "4mer" supramolecular lattice that consists of both "4mer-A" and "4mer-B" molecules. $\mathrm{Fe-DBrDPP}$ molecule sketch is placed to match topographic feature. (b) Black curve: averaged SIS dI/dV spectra over green square covered region in (a) in which both "4mer-A" and "4mer-B" molecules are included. Red: SIS dI/dV spectra measured on red cross marked position in (a). (c) Stacking plot of point SIS dI/dV spectra along the green arrow parallel to molecular row in (a) that crosses phenyl rings of "4mer-A" and "4mer-B" molecules.

shows a spectroscopic feature where two pairs of SF peaks shift to 6 mV which is close to the phonon mode step at 7 mV, while for the green one, two SF peaks at positive energy seem to shift closer to each other and the higher energy peak overlap with the phonon mode step at 11 mV. These feature could imply that for blue molecule, both uniaxial magnetic anisotropy D and transverse anisotropy E are strongly reduced, resulting SF features locate close to the gap, and for green molecule, only E is reduced, resulting two SF peaks at positive energy shift closer. For red molecule, the SF feature is just like standard "4mer" molecules but it also exhibits in-gap feature that can energetically continuously vary, the energy variation behavior seems very well to a tip effect. All these effects can be explained as the result of hydrogen atoms adsorbed on "4mer" $\mathrm{Fe-DBrDPP}$ molecules: An adsorbed hydrogen atom might not significantly alter topography character and can modify the magnetic properties of substrate molecule/atom [44, 161, 164, 255], or explained as supramolecular lattice distortion that induces charge fluctuation like what we have stated in the main text.

"1B" mismatch

The mismatch of "1B" molecules inside supramolecular lattice with respect to Pb(110) surface atoms' arrangement is shown in Fig. 4.36. Here the yellow grid represents the arrangement of Pb atoms of (110) surface where the intersections correspond to the center of Pb atoms. Red $\mathrm{Fe-DBrDPP}$ sketch marked molecules are Type1 "1B" molecules that exhibit in-gap feature, white ones are Type2 that show no in-gap feature. Unfortunately we can not find any obvious evidence that proves the relation between mismatch and being Type1 or Type2 "1B" molecule.

"0B-4mer" interface - DOS

The origin SIS dI/dV spectra and deconvoluted DOS that correspond to stacking plot in Fig. 4.24 (c)(e) are shown in Fig. 4.37 where "0B" molecule exhibits only one pair of in-gap peaks. Although it is not obvious, we can still observe that the Shiba states resolved on "0B" macrocycle exhibit a stronger electron-like component spectral weight than hole-like component, this reversed relative spectral weight feature is also observed in Type2 "0B" molecule studied in section (4.6.3) Fig. 4.26, Fig. 4.28 and Fig. 4.29

"0B-4mer" interface - Bubble

The gap-crossing feature can be visualized as opening/closing of bubble shape in 3D plots Fig. 4.38 where the blue dashed lines roughly mark the opening of bubble feature as bias decreases.

"0B-4mer" interface - Two other lines

Fig. 4.39 shows the linecut 1' and 2' across two other "4mer-0B" molecules. For 1' we do not observed delocalized SF feature generated by "0B" molecule which energy is just outside the gap but instead, in the stacking plot along the row (b), the SF feature suddenly disappears outside the

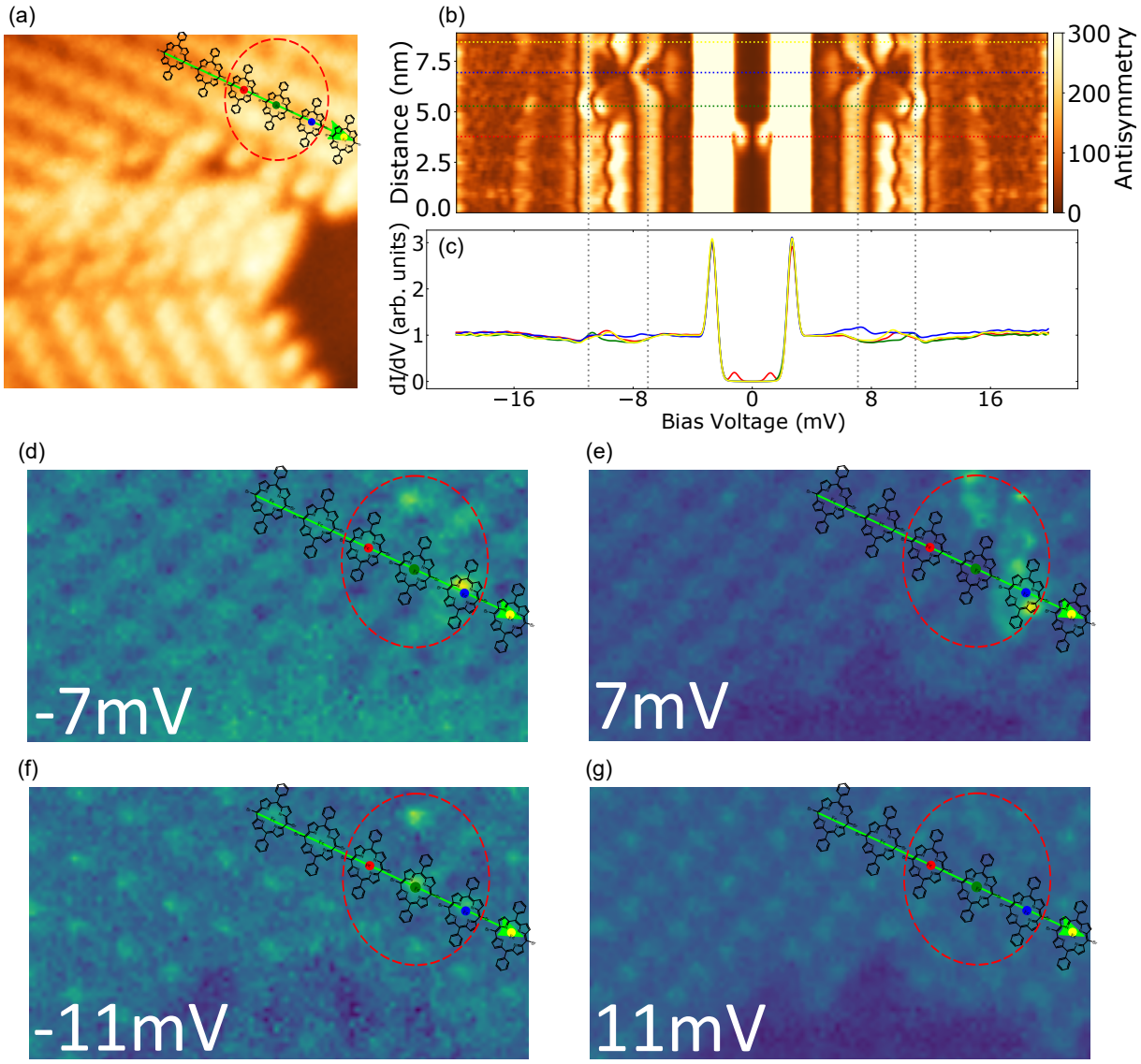

Figure 4.35: Spectroscopic data of exotic "4mer" $\mathrm{Fe-DBrDPP}$ **molecules.** (a) Topographic image ($10\mathrm{x}10\mathrm{nm}^2$, setpoint: 200 mV, 100 pA, -20 pm) showing exotic "4mer" $\mathrm{Fe-DBrDPP}$ molecules marked by red dashed circle. (b) Stacking plot of point value of expression (4.1) along the green arrow in (a)(Setpoint: 100 mV, 100 pA, -250 pm, Lock-in parameters: $V_m = 0.2$ mV, $f = 750$ Hz). Horizontal red, green, blue dashed lines mark the positions of points of same colors in (a) which are the center of three successive exotic $\mathrm{Fe-DBrDPP}$ molecules along the arrow, yellow line indicates a standard "4mer" molecule. Vertical gray dashed lines mark the bias voltage of ± 7 mV and ± 11 mV that are energies of phonon modes. (c) SIS dI/dV spectra measured at crosses position with same colors in (a). All spectra are smoothed and normalized. (d)-(g) SIS conductance map at bias voltage of -7 mV, 7 mV, -11 mV and 11 mV of exotic "4mer" molecules.

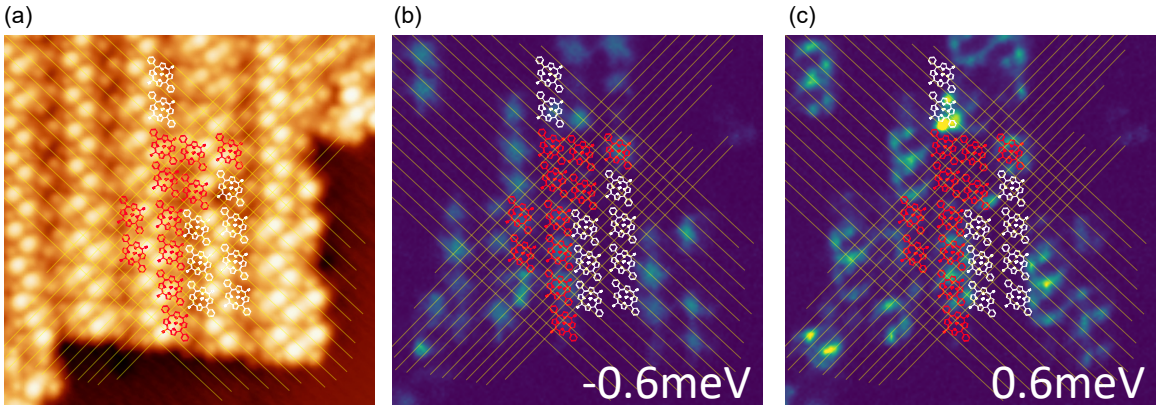

Figure 4.36: "1B" supramolecular lattice mismatch with respect to Pb atoms of Pb(110) surface. (a) Topography image ($14.7\text{x}14.7\text{nm}^2$, setpoint: 8 mV, 50 pA) of $\text{Fe}-\text{DBrDPP}$ "1B" supramolecular lattice. Type1 and Type2 "1B" $\text{Fe}-\text{DBrDPP}$ molecules inside the supramolecular lattice are fitted by red and white $\text{Fe}-\text{DBrDPP}$ sketch. Yellow grid represents the arrangement of Pb atoms of (110) surface where the intersections correspond to the center of Pb atoms. (b)(c) DOS of same region of (a) at energies of $+0.6$ meV and -0.6 meV.

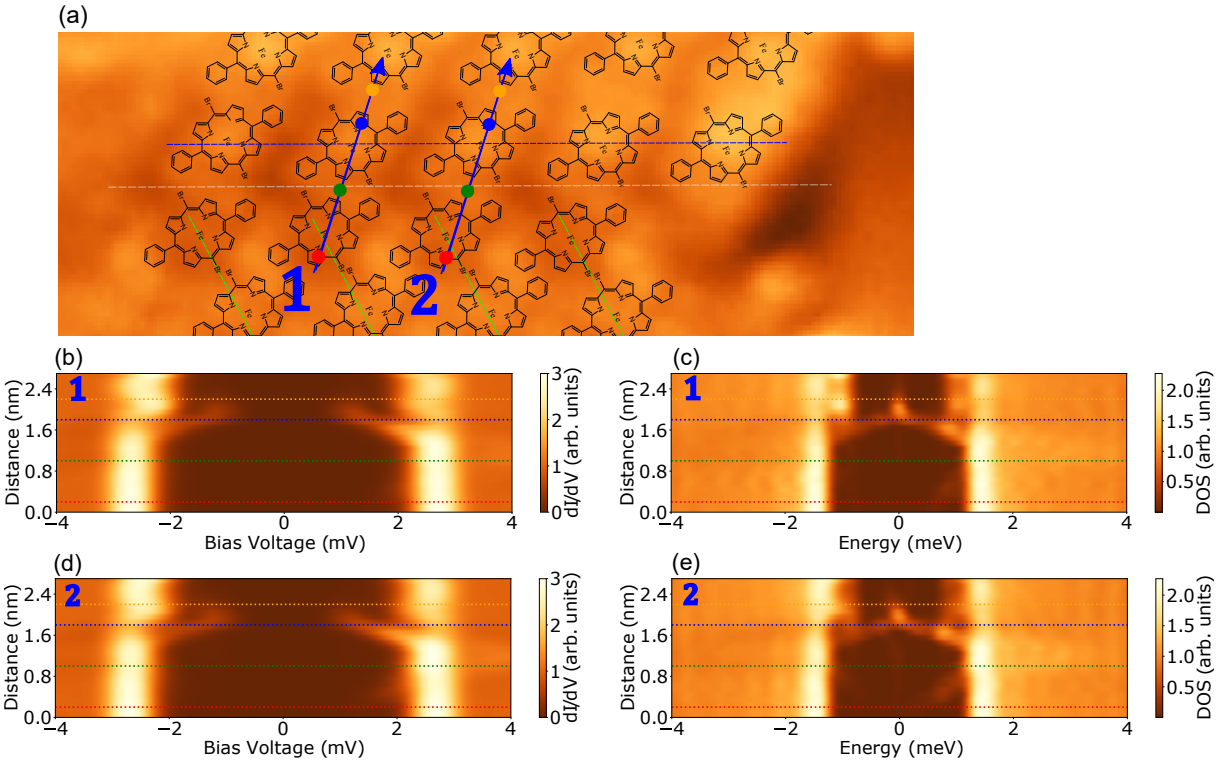

Figure 4.37: SIS dI/dV spectra and DOS along linecuts of "0B" $\text{Fe}-\text{DBrDPP}$ **molecules on interface between "0B" sub-supramolecular lattice and "4mer" supramolecular lattices.** (a) Topographic image ($10\text{x}3.5\text{nm}^2$, setpoint: 100 mV, 100 pA, -250 pm) showing $\text{Fe}-\text{DBrDPP}$ molecules on either sides of interface (marked by white dashed line) between "0B" sub-supramolecular lattice (marked by blue dashed line) and "4mer" supramolecular lattices (marked by green dashed lines). (b)(d) Stacking plot of point SIS dI/dV spectra along the blue arrow labeled by 1 and 2 in (a)(Setpoint: 100 mV, 100 pA, -250 pm, Lock-in parameters: $V_m = 0.2$ mV, $f = 750$ Hz). Horizontal red, green, blue and orange dashed lines mark the positions of points of same colors on corresponding arrow in (a). (c)(e) Stacking plot of point deconvoluted DOS along the blue arrow 1 and 2.

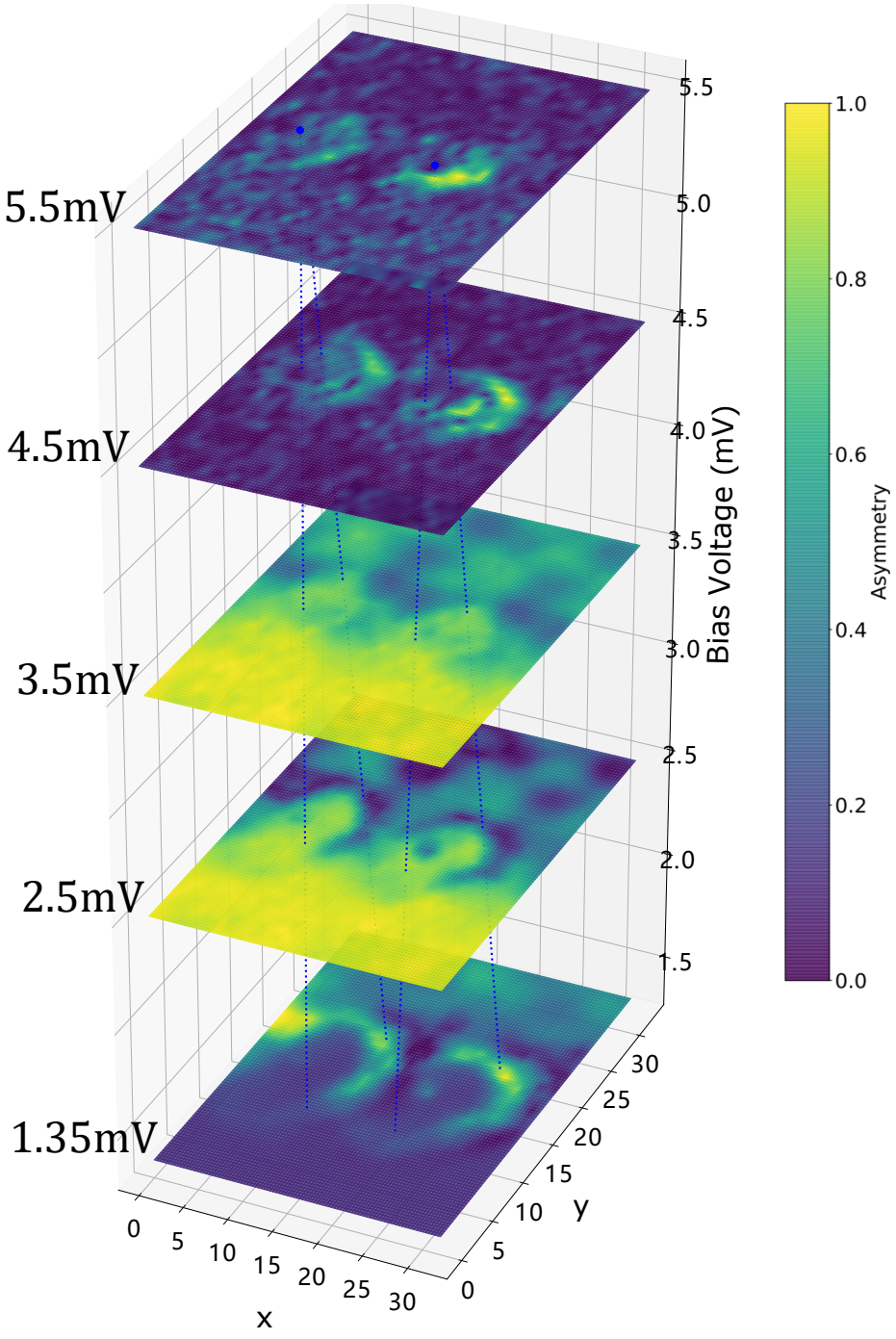

Figure 4.38: SF feature to in-gap feature as opening of bubble. 3D plot of of expression (4.1) maps ($3.5\text{x}2.9\text{nm}^2$) showing evolution of out-gap SF feature to in-gap Shiba feature near "0B-4mer" interface shown in Fig. 4.24 (g-j). From top to bottom, maps of bias 5.5 mV, 4.5 mV, 3.5 mV, 2.5 mV and 1.35 mV. Blue dashed lines roughly indicate the opening of bubble feature as bias decreases.

"4mer" molecule and in-gap feature appears for "0B" molecule (c). Although the in-gap state energy still significantly varies in real space which is probably due to tip interaction, the absence of gap-crossing feature seems to be more "normal". For linecut 2' (d)(e), the in-gap feature does not significantly vary upon tip interaction anymore, indicating that the "0B" molecules in linecut 1 and 2 in Fig. 4.24 are in a less stable geometry which makes them easier to be perturbed by the tip.

Tip effect on "0B" supramolecular lattice - SIS

Stacking plot of original SIS dI/dV spectra corresponding to Fig. 4.26, Fig. 4.28 and Fig. 4.29 are shown in Fig. 4.40, Fig. 4.41 and Fig. 4.42 respectively. The error feature in Fig. 4.40 (d) is due to the average process over points exhibiting spike noise.

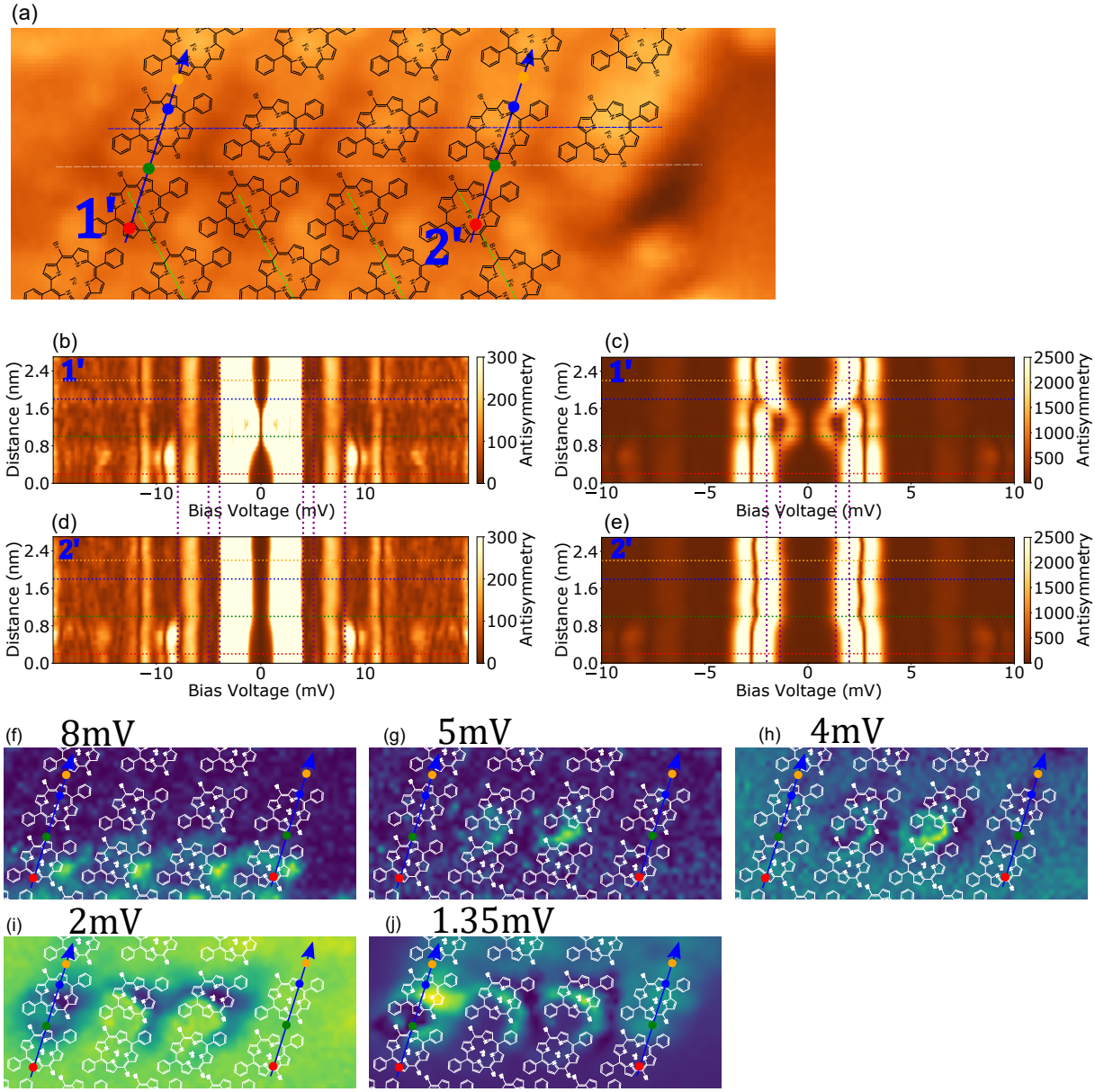

Figure 4.39: Spectroscopic data of $\mathrm{Fe-DBrDPP}$ **molecules on interface between "0B" sub-supramolecular lattice and "4mer" supramolecular lattices.** (a) Topographic image ($10\mathrm{x}3.5\mathrm{nm}^2$, setpoint: 100 mV, 100 pA, -250 pm) showing $\mathrm{Fe-DBrDPP}$ molecules on either sides of interface (marked by white dashed line) between "0B" sub-supramolecular lattice (marked by blue dashed line) and "4mer" supramolecular lattices (marked by green dashed lines). (b)(d) Stacking plot of point value of expression (4.1) along the blue arrow labeled by 1' and 2' in (a) (Setpoint: 100 mV, 100 pA, -250 pm, Lock-in parameters: $V_m = 0.2$ mV, $f = 750$ Hz). Horizontal red, green, blue and orange dashed lines mark the positions of points of same colors on corresponding arrow in (a). Vertical purple dashed lines mark the bias voltage of ± 8 mV, ± 5 mV and ± 4 mV. (c)(e) Same as (b)(d) but with smaller contrast and energy scale in which in-gap feature can be well distinguished. Vertical purple dashed lines mark the bias voltage of ± 2 mV and ± 1.35 mV. (f)-(j) $|\ (d^2I/dV^2|_{V>0} - d^2I/dV^2|_{V<0})\ |$ maps of bias 8.0 mV, 5.0 mV, 4.0 mV, 2.0 mV and 1.35 mV showing the distribution of out-gap (f-h) and in-gap (i-j) feature.

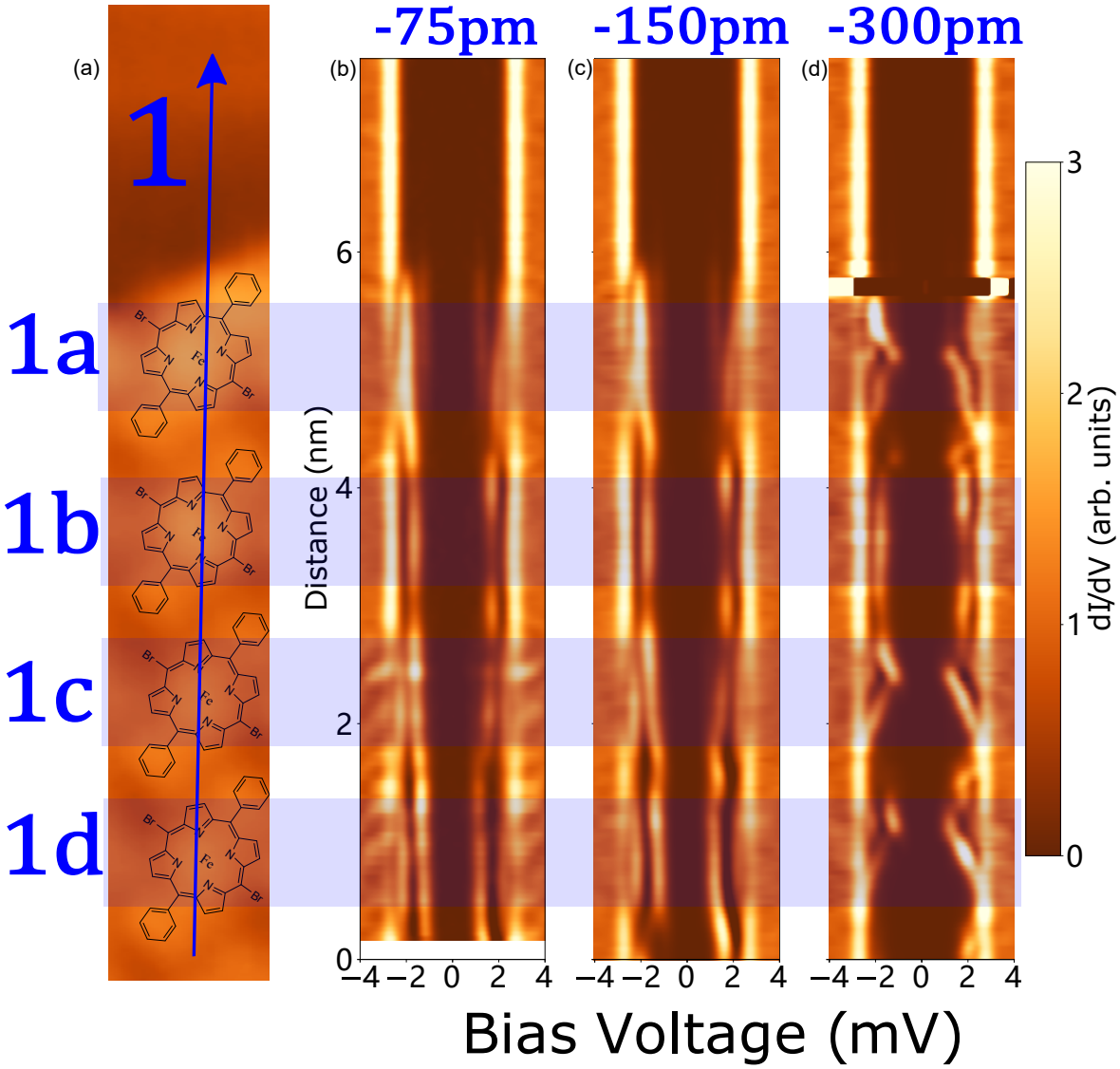

Figure 4.40: Tip distance dependence of in-gap states of line 1 "0B" $\mathrm{Fe-DBrDPP}$ **molecules.** (a) Topography image showing "0B" molecular row 1 on which four successive "0B" molecules are labeled by 1a, 1b, 1c and 1d in opposite direction along the arrow. (b)-(d) Stacking plot of point SIS dI/dV spectra along the blue arrow 1 in (a)(Setpoint: 150 mV, 100 pA, $-75/-150/-300$ pm). Semi-transparent blue rectangles mark the region of macrocycles of "0B" molecules.

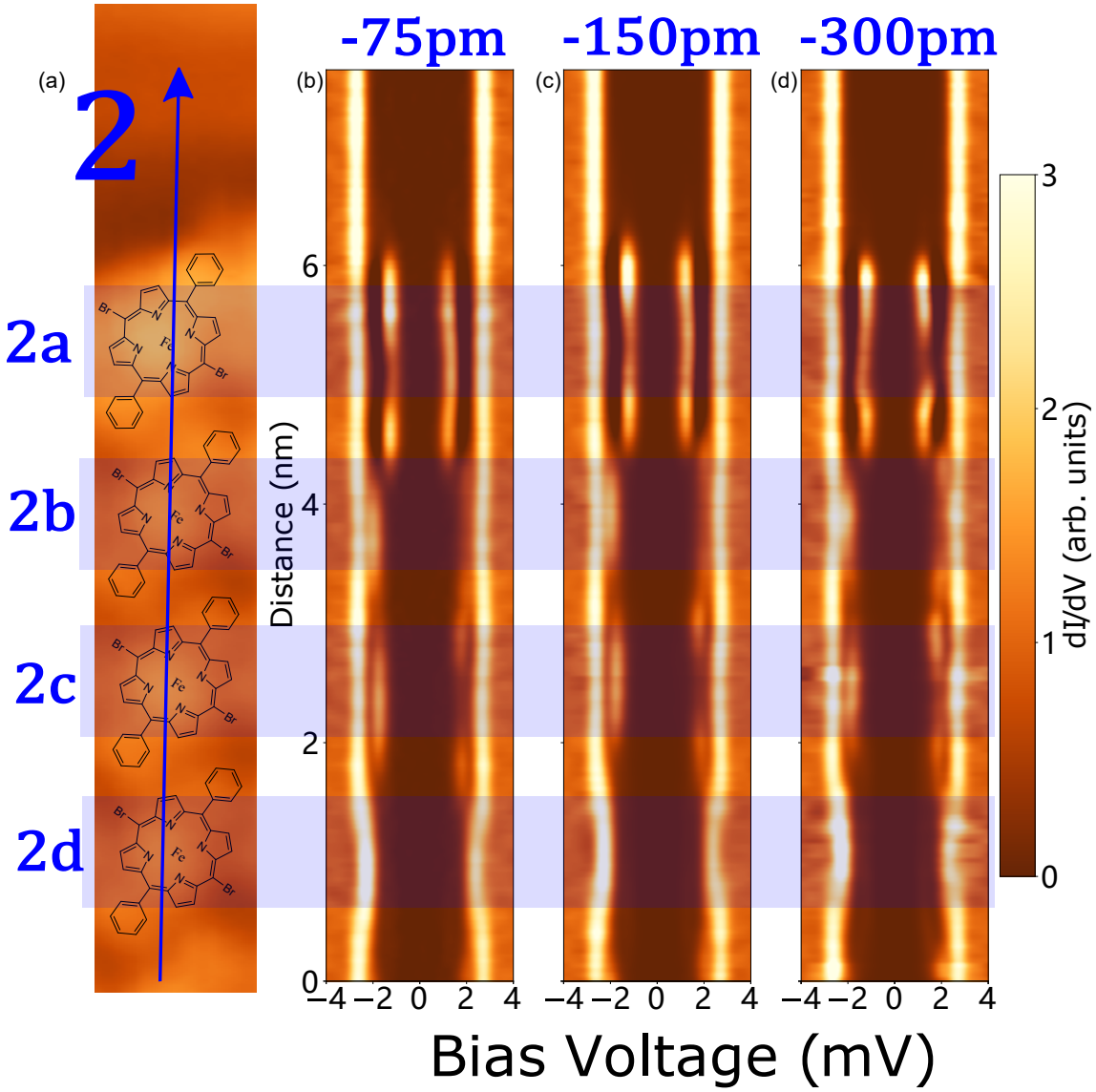

Figure 4.41: Tip distance dependence of in-gap states of line 2 "0B" $\mathrm{Fe-DBrDPP}$ **molecules.** (a) Topography image showing "0B" molecular row 2 on which four successive "0B" molecules are labeled by 2a, 2b, 2c and 2d in opposite direction along the arrow. (b)-(d) Stacking plot of point SIS dI/dV spectra along the blue arrow 2 in (a)(Setpoint: 150 mV, 100 pA, $-75/-150/-300$ pm). Semi-transparent blue rectangles mark the region of macrocycles of "0B" molecules.

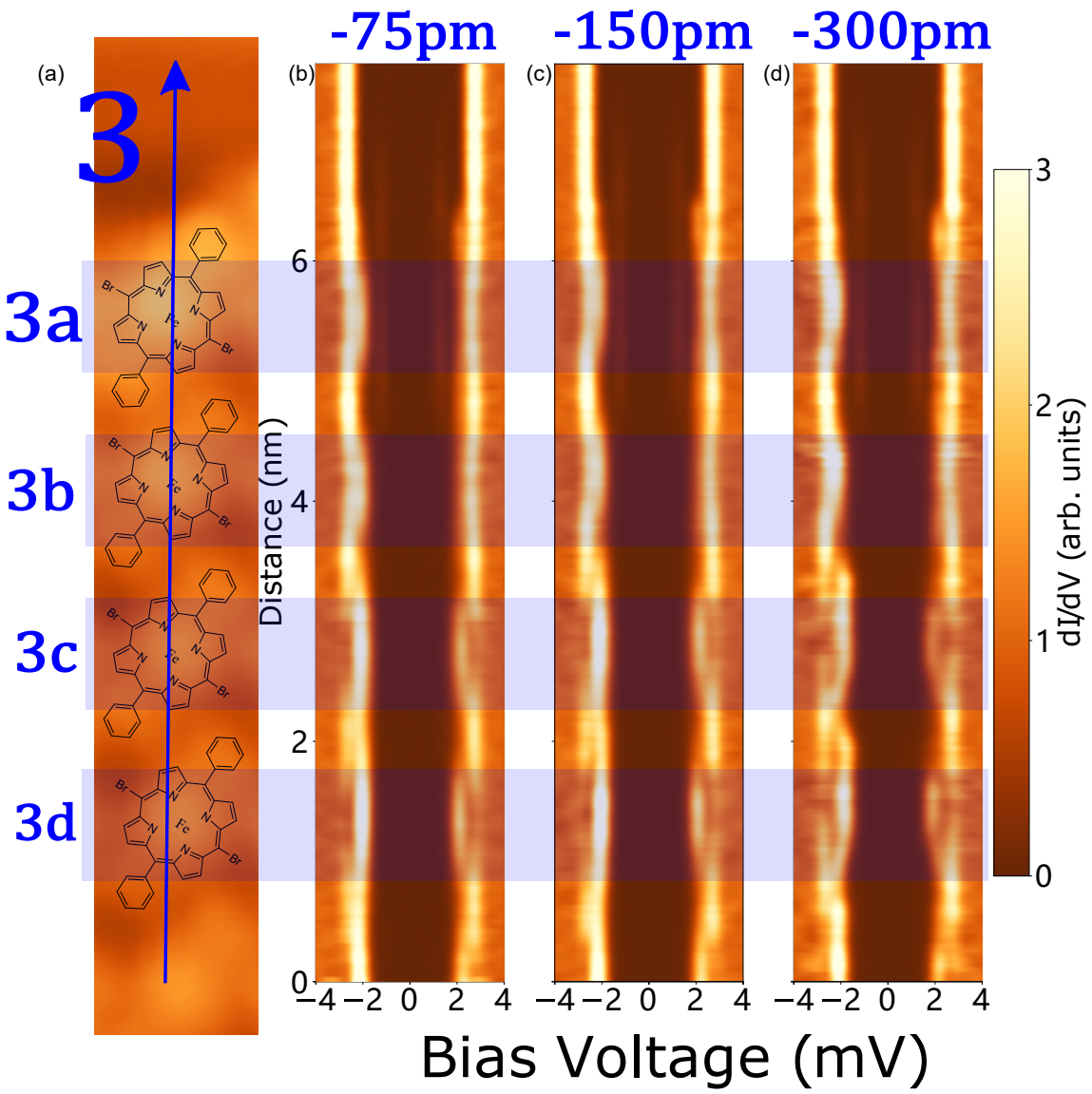

Figure 4.42: Tip distance dependence of in-gap states of line 3 "0B" $\mathrm{Fe-DBrDPP}$ **molecules.** (a) Topography image showing "0B" molecular row 3 on which four successive "0B" molecules are labeled by 3a, 3b, 3c and 3d in opposite direction along the arrow. (b)-(d) Stacking plot of point SIS dI/dV spectra along the blue arrow 3 in (a)(Setpoint: 150 mV, 100 pA, $-75/-150/-300$ pm). Semi-transparent blue rectangles mark the region of macrocycles of "0B" molecules.

Conclusion

In this thesis we have presented and discussed the results about correlated system where different magnetic molecules are deposited on normal and superconducting metal surfaces. We have focused our studies on the following two cases:

1. $\mathrm{Fe-DPyDBrPP}$ molecules on Au(111) surface.
2. $\mathrm{Fe-DBrDPP}$ molecules on superconducting Pb(110) surface.

In the first case we have reported the spin state switching between S = 1 and mixed-valence states where the former one exhibits inelastic spin-flip excitation step signature in low-energy spectrum while the latter one exhibits Abrikosov-Suhl or Kondo resonance at Fermi level. It has been observed that the spin state configuration is controlled by the adsorption site of molecules on Au(111) surface which induces charge fluctuation. We have also revealed in experiments and DFT calculations that the direct consequence of charge fluctuation is to tune the energies of two molecular frontier orbitals which are respectively closest to the Fermi level in positive and negative energies. These two frontier orbitals are responsible for the low-energy spin excitation that occurs near Fermi level. Under the condition of relative small charge fluctuation two frontier orbitals are far from Fermi level the molecule has a well defined S = 1 spin state, while under relative strong charge fluctuation these two orbitals can cross Fermi level, resulting mixed-valence state configuration. By implementing tip manipulation, we have also succeeded in applying a mediate charge fluctuation so that molecule can enter intermediate states. In this case, two frontier orbitals can merge at Fermi level and become degenerate, the molecule will then exhibit a Fano-like lineshape in low-energy excitation spectra as predicted by David Jacob [17].

For the second case we have studied the S = 1 magnetic molecule on superconductor surface. We have demonstrated the intimate relation between electronic properties and geometry of molecule which is determined by molecule's conformation, lattice mismatch and inter-molecular interaction. We have found that depending on topographic character and coupling strength with substrate, $\mathrm{Fe-DBrDPP}$ molecules on Pb(110) surface can be roughly categorized into three ordering "4mer", "0B" and "1B". "4mer" molecules exhibit only out-gap inelastic spin-flip excitation signature in low-energy spectra while "0B" and "1B" molecules exhibit two in-gap Shiba states. Both Shiba states are in Kondo-screened regime and originate from different molecular orbitals, one exhibit strong electron-component delocalization pattern in spectroscopic maps

while the other strictly localizes on macrocycle of the molecule for both hole- and electron components. Furthermore we have also discovered that the local geometry of molecule also plays an important role in molecule's electronic properties. For "1B" molecule, local geometry (lattice mismatch) can induce charge fluctuation resulting Type2 "1B" molecule which molecular orbital localizes at center become quenched and low-energy excitation can no more be observed. While for "0B" molecule, local geometry (inter-molecular interaction) can make "0B" molecule extremely sensitive to local environment, thanks to which we are able to observe the evolution of out-gap SF feature to in-gap Shiba feature under tip interaction. Impressively the evolution process resolved in spectroscopic maps behave as continuous opening/closing of bubble shape and we also observed an intermediate regime where both in-gap and out-gap feature coexists, such exotic behavior has also been reported in a S = 3/2 molecular system [103].

The results we have presented in this thesis should help us better understand the relation between porphyrin-based spin-1 molecule's geometry(adsorption site, conformation, lattice mismatch and inter-molecular interaction) and its electronic properties on different metal surfaces. The emerging geometry-induced charge effect observed in both systems could possibly be utilized for spin state control which is essential for developing molecular spintronic devices. Further work of studying porphyrin-based molecule consisting of different ligands and center transition metals on different metal surfaces can be implemented. For example the deposited covalently bonded $\mathrm{Fe-DPyDBrPP}$ molecular chain on a more chemically active silver surface can possible become a Kondo chain and develop inter-molecular spin-spin interaction. Additionally STM tip assisted artificial on-surface covalent bond formation is also worth trying where we can apply voltage pulse to molecules to dissociate bromine atoms and artificially form covalent bond dimer. For example in "4mer" $\mathrm{Fe-DBrDPP}$ lattices two bromine atoms of neighbor molecules are very close which could be dissociated simultaneously by voltage pulse and form covalent bond.

Bibliography

[1] M. A. Ruderman, C. Kittel
Indirect Exchange Coupling of Nuclear Magnetic Moments by Conduction Electrons
Physical Review 96 (1954), 99–102.

[2] Tadao Kasuya
A Theory of Metallic Ferro- and Antiferromagnetism on Zener's Model
Progress of Theoretical Physics 16 (1956), 45–57.

[3] Kei Yosida
Magnetic Properties of Cu-Mn Alloys
Physical Review 106 (1957), 893–898.

[4] W.J. de Haas, J. de Boer, G.J. van dën Berg
The electrical resistance of gold, copper and lead at low temperatures
Physica 1 (1934), 1115–1124.

[5] Jun Kondo
Resistance Minimum in Dilute Magnetic Alloys
Progress of Theoretical Physics 32 (1964), 37–49.

[6] Markus Ternes, Andreas J Heinrich, Wolf-Dieter Schneider
Spectroscopic manifestations of the Kondo effect on single adatoms
Journal of Physics: Condensed Matter 21 (2008), 053001.

[7] A. A. Abrikosov
Electron scattering on magnetic impurities in metals and anomalous resistivity effects
Physics Physique Fizika 2 (1965), 5–20.

[8] H. Suhl
Dispersion Theory of the Kondo Effect
Physical Review 138 (1965), A515–A523.

[9] Yosuke Nagaoka
Self-Consistent Treatment of Kondo's Effect in Dilute Alloys
Physical Review 138 (1965), A1112–A1120.

[10] D. L. Cox, A. Zawadowski
Exotic Kondo effects in metals: Magnetic ions in a crystalline electric field and tunnelling centres
Advances in Physics 47 (1998), 599–942.

[11] O. Yu. Kolesnychenko et al.
Real-space imaging of an orbital Kondo resonance on the Cr(001) surface
Nature 415 (2002), 507–509.

[12] A. J. Keller et al.
Emergent SU(4) Kondo physics in a spin–charge-entangled double quantum dot
Nature Physics 10 (2014), 145–150.

[13] A. W. Holleitner et al.
Pseudospin Kondo correlations versus hybridized molecular states in double quantum dots
Physical Review B 70 (2004), 075204.

[14] Pablo Jarillo-Herrero et al.
Orbital Kondo effect in carbon nanotubes
Nature 434 (2005), 484–488.

[15] Emi Minamitani et al.
Symmetry-Driven Novel Kondo Effect in a Molecule
Physical Review Letters 109 (2012), 086602.

[16] P. W. Anderson
Localized Magnetic States in Metals
Physical Review 124 (1961), 41–53.

[17] David Jacob
Renormalization of single-ion magnetic anisotropy in the absence of the Kondo effect
Physical Review B 97 (2018), 075428.

[18] David Jacob, Joaquin Fernández-Rossier
Competition between quantum spin tunneling and Kondo effect
The European Physical Journal B 89 (2016), 210.

[19] J. R. Schrieffer, P. A. Wolff
Relation between the Anderson and Kondo Hamiltonians
Physical Review 149 (1966), 491–492.

[20] Peter Fulde
Electron correlations in molecules and solids
Vol. 100. Springer Science & Business Media, 1995.

[21] Deung-Jang Choi, Nicolás Lorente
Magnetic Impurities on Surfaces: Kondo and Inelastic Scattering
Handbook of Materials Modeling: Applications: Current and Emerging Materials. Ed. by Wanda Andreoni, Sidney Yip. Cham: Springer International Publishing, 2018, pp. 1–32. ISBN: 978-3-319-50257-1.

[22] Ph Nozières, Blandin A.
Kondo effect in real metals
J. Phys. France 41 (1980), 193–211.

[23] R. Žitko, R. Peters, Th. Pruschke
Properties of anisotropic magnetic impurities on surfaces
Physical Review B 78 (2008), 224404.

[24] J. Gan, P. Coleman, N. Andrei
Coexistence of Fermi liquid and magnetism in the underscreened Kondo problem
Physical Review Letters 68 (1992), 3476–3479.

[25] A. Mugarza et al.
Electronic and magnetic properties of molecule-metal interfaces: Transition-metal phthalocyanines adsorbed on Ag(100)
Physical Review B 85 (2012), 155437.

[26] Hendrik Antoon Kramers
Théorie générale de la rotation paramagnétique dans les cristaux
Proc. Acad. Amst 33 (1930).

[27] A. J. Heinrich et al.
Single-Atom Spin-Flip Spectroscopy
Science 306 (2004), 466–469.

[28] John Lambe, RC Jaklevic
Molecular vibration spectra by inelastic electron tunneling
Physical Review 165 (1968), 821.

[29] J. J. Parks et al.
Mechanical Control of Spin States in Spin-1 Molecules and the Underscreened Kondo Effect
Science 328 (2010), 1370–1373.

[30] Noriyuki Tsukahara et al.
Adsorption-Induced Switching of Magnetic Anisotropy in a Single Iron(II) Phthalocyanine Molecule on an Oxidized Cu(110) Surface
Physical Review Letters 102 (2009), 167203.

[31] R. Hiraoka et al.
Single-molecule quantum dot as a Kondo simulator
Nature Communications 8 (2017), 16012.

[32] Carmen Rubio-Verdú et al.
Orbital-selective spin excitation of a magnetic porphyrin
Communications Physics 1 (2018), 15.

[33] Ruoning Li et al.
Tuning the spin-related transport properties of FePc on Au(111) through single-molecule chemistry
Chem. Commun. 54 (2018), 9135–9138.

[34] Jenny C. Oberg et al.
Control of single-spin magnetic anisotropy by exchange coupling
Nature Nanotechnology 9 (2014), 64–68.

[35] F. Delgado, C.F. Hirjibehedin, J. Fernández-Rossier
Consequences of Kondo exchange on quantum spins
Surface Science 630 (2014), 337–342.

[36] Avraham Schiller, Lorenzo De Leo
Phase diagram of the anisotropic multichannel Kondo Hamiltonian revisited
Physical Review B 77 (2008), 075114.

[37] Alexander F. Otte et al.
The role of magnetic anisotropy in the Kondo effect
Nature Physics 4 (2008), 847–850.

[38] Aidi Zhao et al.
Controlling the Kondo Effect of an Adsorbed Magnetic Ion Through Its Chemical Bonding
Science 309 (2005), 1542–1544.

[39] Xi Chen et al.
Probing Superexchange Interaction in Molecular Magnets by Spin-Flip Spectroscopy and Microscopy
Physical Review Letters 101 (2008), 197208.

[40] Aitor Mugarza et al.
Spin coupling and relaxation inside molecule-metal contacts
Nature Communications 2 (2011), 490.

[41] J. Granet et al.
Adsorption-Induced Kondo Effect in Metal-Free Phthalocyanine on Ag(111)
J. Phys. Chem. C 124 (2020), 10441–10452.

[42] Brigitte Surer et al.
Multiorbital Kondo physics of Co in Cu hosts
Physical Review B 85 (2012), 085114.

[43] Andriy H. Nevidomskyy, P. Coleman
Kondo Resonance Narrowing in d- and f-Electron Systems
Physical Review Letters 103 (2009), 147205.

[44] A. A. Khajetoorians et al.
Tuning emergent magnetism in a Hund's impurity
Nature Nanotechnology 10 (2015), 958–964.

[45] S. Gardonio et al.
Excitation Spectra of Transition-Metal Atoms on the Ag (100) Surface Controlled by Hund's Exchange
Physical Review Letters 110 (2013), 186404.

[46] Annamária Kiss, Yoshio Kuramoto, Shintaro Hoshino
Numerical study of Kondo impurity models with strong potential scattering: Reverse Kondo effect and antiresonance
Physical Review B 84 (2011), 174402.

[47] Markus Ternes
Spin excitations and correlations in scanning tunneling spectroscopy
New Journal of Physics 17 (2015), 063016.

[48] Piers Coleman
Introduction to many-body physics
Cambridge University Press, 2015.

[49] N. Néel et al.
Two-Site Kondo Effect in Atomic Chains
Physical Review Letters 107 (2011), 106804.

[50] JH Van Vleck
Note on the interactions between the spins of magnetic ions or nuclei in metals
Reviews of Modern Physics 34 (1962), 681.

[51] C. Jayaprakash, H. R. Krishna-murthy, J. W. Wilkins
Two-Impurity Kondo Problem
Physical Review Letters 47 (1981), 737–740.

[52] P. Wahl et al.
Exchange Interaction between Single Magnetic Adatoms
Physical Review Letters 98 (2007), 056601.

[53] Jakob Bork et al.
A tunable two-impurity Kondo system in an atomic point contact
Nature Physics 7 (2011), 901–906.

[54] Henning Prüser et al.
Interplay between the Kondo effect and the Ruderman-Kittel-Kasuya-Yosida interaction
Nature Communications 5 (2014), 5417.

[55] A Spinelli et al.
Exploring the phase diagram of the two-impurity Kondo problem
Nature communications 6 (2015), 1–6.

[56] N David Mermin, Herbert Wagner
Absence of ferromagnetism or antiferromagnetism in one-or two-dimensional isotropic Heisenberg models
Physical Review Letters 17 (1966), 1133.

[57] Noriyuki Tsukahara et al.
Evolution of Kondo Resonance from a Single Impurity Molecule to the Two-Dimensional Lattice
Physical Review Letters 106 (2011), 187201.

[58] Marianna Maltseva, M Dzero, P Coleman
Electron cotunneling into a Kondo lattice
Physical review letters 103 (2009), 206402.

[59] Jan Girovsky et al.
Long-range ferrimagnetic order in a two-dimensional supramolecular Kondo lattice
Nature Communications 8 (2017), 15388.

[60] Rouzhaji Tuerhong et al.
Two-Dimensional Organometallic Kondo Lattice with Long-Range Antiferromagnetic Order
J. Phys. Chem. C 122 (2018), 20046–20054.

[61] Ying Jiang et al.
Real-space imaging of Kondo screening in a two-dimensional O2 lattice
Science 333 (2011), 324–328.

[62] Jie Hou et al.
Enhanced magnetic spin-spin interactions observed between porphyrazine derivatives on Au(111)
Communications Chemistry 3 (2020), 36.

[63] Nicolas Néel et al.
Controlling the Kondo effect in CoCu n clusters atom by atom
Physical Review Letters 101 (2008), 266803.

[64] Giulia E. Pacchioni et al.
Two-Orbital Kondo Screening in a Self-Assembled Metal-Organic Complex
ACS Nano 11 (2017), 2675–2681.

[65] Violeta Iancu, Aparna Deshpande, Saw-Wai Hla
Manipulation of the Kondo Effect via Two-Dimensional Molecular Assembly
Physical Review Letters 97 (2006), 266603.

[66] Andrew DiLullo et al.
Molecular Kondo Chain
Nano Lett. 12 (2012), 3174–3179.

[67] Jing Liu et al.
Collective Spin Manipulation in Antiferroelastic Spin-Crossover Metallo-Supramolecular Chains
ACS Nano 14 (2020), 11283–11293.

[68] Benjamin Mallada et al.
On-surface synthesis of one-dimensional coordination polymers with tailored magnetic anisotropy
ACS Applied Materials & Interfaces 13 (2021), 32393–32401.

[69] Heike KAMERLINGH ONNES
The superconductivity of mercury
Comm. Phys. Lab. Univ. Leiden 122 (1911), 122–124.

[70] Walther Meissner, Robert Ochsenfeld
Ein neuer effekt bei eintritt der supraleitfähigkeit
Naturwissenschaften 21 (1933), 787–788.

[71] Herbert Fröhlich
Theory of the superconducting state. I. The ground state at the absolute zero of temperature
Physical Review 79 (1950), 845.

[72] Emanuel Maxwell
Isotope effect in the superconductivity of mercury
Physical Review 78 (1950), 477.

[73] CA Reynolds et al.
Superconductivity of isotopes of mercury
Physical Review 78 (1950), 487.

[74] J. Bardeen, L. N. Cooper, J. R. Schrieffer
Theory of Superconductivity
Phys. Rev. 108 (1957), 1175–1204.

[75] James F Annett et al.
Superconductivity, superfluids and condensates
Vol. 5. Oxford University Press, 2004.

[76] Vitaly L Ginzburg, Lev D Landau
On the theory of superconductivity
In: On superconductivity and superfluidity. Springer, 2009, pp. 113–137.

[77] Pierre-Gilles De Gennes, Philip A Pincus
Superconductivity of metals and alloys
CRC Press, 2018.

[78] Yoichiro Nambu
Quasi-particles and gauge invariance in the theory of superconductivity
Physical Review 117 (1960), 648.

[79] L Yu
Bound State in Superconuctors with Paramagnetic Impurities
Wu Li Hsueh Pao (China) Supersedes Chung-Kuo Wu Li Hsueh For English translation see Chin. J. P
21 (1965).

[80] Hiroyuki Shiba
Classical Spins in Superconductors
Progress of Theoretical Physics 40 (1968), 435–451.

[81] AI Rusinov
Theory of gapless superconductivity in alloys containing paramagnetic impurities
Sov. Phys. JETP 29 (1969), 1101–1106.

[82] Haonan Huang et al.
Quantum phase transitions and the role of impurity-substrate hybridization in Yu-Shiba-Rusinov states
Communications Physics 3 (2020), 199.

[83] Koji Satori et al.
Numerical Renormalization Group Study of Magnetic Impurities in Superconductors
Journal of the Physical Society of Japan 61 (1992), 3239–3254.

[84] Osamu Sakai et al.
Numerical Renormalization Group Study of Magnetic Impurities in Superconductors. II. Dynamical Excitation Spectra and Spatial Variation of the Order Parameter
Journal of the Physical Society of Japan 62 (1993), 3181–3197.

[85] Johannes Bauer, Jose I. Pascual, Katharina J. Franke
Microscopic resolution of the interplay of Kondo screening and superconducting pairing: Mn-phthalocyanine molecules adsorbed on superconducting Pb(111)
Physical Review B 87 (2013), 075125.

[86] Jian Li et al.
Majorana spin in magnetic atomic chain systems
Physical Review B 97 (2018), 125119.

[87] Rok Žitko, Oliver Bodensiek, Thomas Pruschke
Effects of magnetic anisotropy on the subgap excitations induced by quantum impurities in a superconducting host
Physical Review B 83 (2011), 054512.

[88] A. V. Balatsky, I. Vekhter, Jian-Xin Zhu
Impurity-induced states in conventional and unconventional superconductors
Rev. Mod. Phys. 78 (2006), 373–433.

[89] K. J. Franke, G. Schulze, J. I. Pascual
Competition of Superconducting Phenomena and Kondo Screening at the Nanoscale
Science 332 (2011), 940.

[90] Nino Hatter et al.
Magnetic anisotropy in Shiba bound states across a quantum phase transition
Nature Communications 6 (2015), 8988.

[91] Anand Kamlapure et al.
Correlation of Yu–Shiba–Rusinov States and Kondo Resonances in Artificial Spin Arrays on an s-Wave Superconductor
Nano Letters 21 (2021). PMID: 34351781, 6748–6755.

[92] Benjamin W. Heinrich, Jose I. Pascual, Katharina J. Franke
Single magnetic adsorbates on s-wave superconductors
Progress in Surface Science 93 (2018), 1–19.

[93] Laëtitia Farinacci et al.
Tuning the Coupling of an Individual Magnetic Impurity to a Superconductor: Quantum Phase Transition and Transport
Physical Review Letters 121 (2018), 196803.

[94] Toshio Soda, Tamifusa Matsuura, Yosuke Nagaoka
s-d Exchange Interaction in a Superconductor
Progress of Theoretical Physics 38 (1967), 551–567.

[95] J. Zittartz, E. Müller-Hartmann
Theory of magnetic impurities in superconductors. I
Zeitschrift für Physik A Hadrons and nuclei 232 (1970), 11–31.

[96] Tamifusa Matsuura
The Effects of Impurities on Superconductors with Kondo Effect
Progress of Theoretical Physics 57 (1977), 1823–1835.

[97] Carmen Rubio-Verdú et al.
Coupled Yu-Shiba-Rusinov States Induced by a Many-Body Molecular Spin on a Superconductor
Physical Review Letters 126 (2021), 017001.

[98] Laëtitia Farinacci et al.
Interfering Tunneling Paths through Magnetic Molecules on Superconductors: Asymmetries of Kondo and Yu-Shiba-Rusinov Resonances
Physical Review Letters 125 (2020), 256805.

[99] Ali Yazdani et al.
Probing the local effects of magnetic impurities on superconductivity
Science 275 (1997), 1767–1770.

[100] Michael Ruby et al.
Orbital Picture of Yu-Shiba-Rusinov Multiplets
Phys. Rev. Lett. 117 (2016), 186801.

[101] Gerbold C. Ménard et al.
Coherent long-range magnetic bound states in a superconductor
Nature Physics 11 (2015), 1013–1016.

[102] Howon Kim et al.
Long-range focusing of magnetic bound states in superconducting lanthanum
Nature Communications 11 (2020), 4573.

[103] Shawulienu Kezilebieke et al.
Observation of Coexistence of Yu-Shiba-Rusinov States and Spin-Flip Excitations
Nano Lett. 19 (2019), 4614–4619.

[104] Deung-Jang Choi et al.
Mapping the orbital structure of impurity bound states in a superconductor
Nature communications 8 (2017), 1–6.

[105] Lucas Schneider et al.
Topological Shiba bands in artificial spin chains on superconductors
Nature Physics 17 (2021), 943–948.

[106] Philip Beck et al.
Spin-orbit coupling induced splitting of Yu-Shiba-Rusinov states in antiferromagnetic dimers
Nature communications 12 (2021), 1–9.

[107] Markus Etzkorn et al.
Mapping of Yu-Shiba-Rusinov states from an extended scatterer
arXiv preprint arXiv:1807.00646 (2018).

[108] Felix von Oppen, Katharina J. Franke
Yu-Shiba-Rusinov states in real metals
Physical Review B 103 (2021), 205424.

[109] B. W. Heinrich et al.
Protection of excited spin states by a superconducting energy gap
Nature Physics 9 (2013), 765–768.

[110] Benjamin W Heinrich et al.
Tuning the magnetic anisotropy of single molecules
Nano Letters 15 (2015), 4024–4028.

[111] Lucas Schneider et al.
Magnetism and in-gap states of 3d transition metal atoms on superconducting Re
npj Quantum Materials 4 (2019), 42.

[112] A A Abrikosov, L P Gor'kov
CONTRIBUTION TO THE THEORY OF SUPERCONDUCTING ALLOYS WITH PARAMAGNETIC IMPURITIES
Zhur. Eksptl'. i Teoret. Fiz. ().

[113] A Yu Kitaev
Unpaired Majorana fermions in quantum wires
Physics-Uspekhi 44 (2001), 131–136.

[114] Jian Li et al.
Two-dimensional chiral topological superconductivity in Shiba lattices
Nature Communications 7 (2016), 1–7.

[115] V. Gurarie, L. Radzihovsky
Zero modes of two-dimensional chiral p-wave superconductors
Phys. Rev. B 75 (2007), 212509.

[116] Lucas Schneider et al.
Precursors of Majorana modes and their length-dependent energy oscillations probed at both ends of atomic Shiba chains
Nature Nanotechnology 17 (2022), 384–389.

[117] Shawulienu Kezilebieke et al.
Coupled Yu–Shiba–Rusinov states in molecular dimers on NbSe2
Nano letters 18 (2018), 2311–2315.

[118] Michael Ruby et al.
Wave-Function Hybridization in Yu-Shiba-Rusinov Dimers
Phys. Rev. Lett. 120 (2018), 156803.

[119] Hao Ding et al.
Tuning interactions between spins in a superconductor
Proceedings of the National Academy of Sciences 118 (2021), e2024837118.

[120] Gufei Zhang et al.
Yu-Shiba-Rusinov bands in ferromagnetic superconducting diamond
Science Advances 6 (2020), eaaz2536.

[121] Harald Schmid et al.
Quantum Yu-Shiba-Rusinov dimers
Physical Review B 105 (2022), 235406.

[122] N. Y. Yao et al.
Phase diagram and excitations of a Shiba molecule
Phys. Rev. B 90 (2014), 241108.

[123] S. Nadj-Perge et al.
Proposal for realizing Majorana fermions in chains of magnetic atoms on a superconductor
Phys. Rev. B 88 (2013), 020407.

[124] Stevan Nadj-Perge et al.
Observation of Majorana fermions in ferromagnetic atomic chains on a superconductor
Science 346 (2014), 602–607.

[125] Michael Ruby et al.
Exploring a proximity-coupled Co chain on Pb (110) as a possible Majorana platform
Nano letters 17 (2017), 4473–4477.

[126] Michael Kleinert (Ruby)
Magnetic Impurities on a Superconductor: from Single Atoms to Coupled Chains
PhD thesis. 2017.

[127] Gerbold C Ménard et al.
Yu-Shiba-Rusinov bound states versus topological edge states in Pb/Si (111)
The European Physical Journal Special Topics 227 (2019), 2303–2313.

[128] Alexandra Palacio-Morales et al.
Atomic-scale interface engineering of Majorana edge modes in a 2D magnet-superconductor hybrid system
Science Advances 5 (2019), eaav6600.

[129] Shawulienu Kezilebieke et al.
Topological superconductivity in a van der Waals heterostructure
Nature 588 (2020), 424–428.

[130] Julia J. Goedecke et al.
Correlation of Magnetism and Disordered Shiba Bands in Fe Monolayer Islands on Nb(110)
2022.

[131] Thomas P Vaid
A Porphyrin with a C C Unit at Its Center
Journal of the American Chemical Society 133 (2011), 15838–15841.

[132] K. Schouteden et al.
Probing Magnetism in 2D Molecular Networks after in Situ Metalation by Transition Metal Atoms
J. Phys. Chem. Lett. 6 (2015), 1048–1052.

[133] Sujoy Karan et al.
Spin control induced by molecular charging in a transport junction
Nano letters 18 (2018), 88–93.

[134] Yi Wang, Xinrui Miao, Wenli Deng
Halogen Bonds Fabricate 2D Molecular Self-Assembled Nanostructures by Scanning Tunneling Microscopy
Crystals 10 (2020), 1057.

[135] Ram KR Jetti et al.
Polar host–guest assembly mediated by halogen π interaction: Inclusion complexes of 2, 4, 6-tris (4-halophenoxy)-1, 3, 5-triazine (halo= chloro, bromo) with trihalobenzene (halo= bromo, iodo)
Chemical Communications (2001), 919–920.

[136] Jinxing Li et al.
Geometry symmetry of conjugated cores along C–Br bond effect on the 2d self-assembly by intermolecular H··· Br and Br··· Br Bonds
The Journal of Physical Chemistry C 122 (2018), 15338–15343.

[137] Jan Homberg et al.
Inducing and controlling molecular magnetism through supramolecular manipulation
ACS nano 14 (2020), 17387–17395.

[138] Catherine Doyle
An investigation of the structural and electronic properties of covalently bonded molecular networks on metal surfaces formed through debromination reactions.
Ireland: Dublin City University, 2013.

[139] F. Ullmann, Jean Bielecki
Ueber Synthesen in der Biphenylreihe
Berichte der deutschen chemischen Gesellschaft 34 (1901), 2174–2185.

[140] Leonhard Grill et al.
Nano-architectures by covalent assembly of molecular building blocks
Nature nanotechnology 2 (2007), 687–691.

[141] Xiong Zhou et al.
On-surface synthesis approach to preparing one-dimensional organometallic and poly-p-phenylene chains
Materials Chemistry Frontiers 1 (2017), 119–127.

[142] Y. Y. Zhang, S. X. Du, H.-J. Gao
Binding configuration, electronic structure, and magnetic properties of metal phthalocyanines on a Au(111) surface studied with ab initio calculations
Physical Review B 84 (2011), 125446.

[143] Lei Tao, Yu-yang Zhang, Shixuan Du
Structures and electronic properties of functional molecules on metal substrates: From single molecule to self-assemblies
Wiley Interdisciplinary Reviews: Computational Molecular Science 12 (2022), e1591.

[144] Qiang Sun et al.
Magnetic Interplay between π-Electrons of Open-Shell Porphyrins and d-Electrons of Their Central Transition Metal Ions
Advanced science (2022), 2105906.

[145] Syed Mohammad Fakruddin Shahed et al.
Observation of Yu–Shiba–Rusinov States and Inelastic Tunneling Spectroscopy for Intramolecule Magnetic Exchange Interaction Energy of Terbium Phthalocyanine (TbPc) Species Adsorbed on Superconductor NbSe2
ACS Nano 16 (2022). PMID: 35467334, 7651–7661.

[146] Iulia Emilia Brumboiu et al.
Influence of electron correlation on the electronic structure and magnetism of transition-metal phthalocyanines
Journal of Chemical Theory and Computation 12 (2016), 1772–1785.

[147] Emi Minamitani et al.
Spatially extended underscreened Kondo state from collective molecular spin
Physical Review B 92 (2015), 075144.

[148] Weihua Wang et al.
Intramolecularly resolved Kondo resonance of high-spin $\mathrm{Fe(II)}$-porphyrin adsorbed on $\mathrm{Au(111)}$
Physical Review B 91 (2015), 045440.

[149] Liwei Liu et al.
Revealing the Atomic Site-Dependent g Factor within a Single Magnetic Molecule via the Extended Kondo Effect
Physical Review Letters 114 (2015), 126601.

[150] Jörg Meyer et al.
Influence of organic ligands on the line shape of the Kondo resonance
Physical Review B 93 (2016), 155118.

[151] Hui Chen et al.
Evidence for Ultralow-Energy Vibrations in Large Organic Molecules
Nano Lett. 17 (2017), 4929–4933.

[152] U. G. E. Perera et al.
Spatially Extended Kondo State in Magnetic Molecules Induced by Interfacial Charge Transfer
Physical Review Letters 105 (2010), 106601.

[153] Saurabh Pradhan, Jonas Fransson
Yu-Shiba-Rusinov states of a single magnetic molecule in an s-wave superconductor
Physical Review B 102 (2020), 085136.

[154] A. Mugarza et al.
Orbital Specific Chirality and Homochiral Self-Assembly of Achiral Molecules Induced by Charge Transfer and Spontaneous Symmetry Breaking
Physical Review Letters 105 (2010), 115702.

[155] Manuela Garnica et al.
Probing the Site-Dependent Kondo Response of Nanostructured Graphene with Organic Molecules
Nano Lett. 14 (2014), 4560–4567.

[156] Sujoy Karan et al.
Spin Manipulation by Creation of Single-Molecule Radical Cations
Physical Review Letters 116 (2016), 027201.

[157] Aidi Zhao et al.
Kondo effect in single cobalt phthalocyanine molecules adsorbed on Au(111) monoatomic steps
J. Chem. Phys. 128 (2008), 234705.

[158] Qiushi Zhang et al.
Switching Molecular Kondo Effect via Supramolecular Interaction
ACS Nano 9 (2015), 12521–12528.

[159] Cornelius Krull et al.
Site- and orbital-dependent charge donation and spin manipulation in electron-doped metal phthalocyanines
Nature Materials 12 (2013), 337–343.

[160] Xiangyang Li et al.
Molecular molds for regularizing Kondo states at atom/metal interfaces
Nature Communications 11 (2020), 2566.

[161] Liwei Liu et al.
Reversible Single Spin Control of Individual Magnetic Molecule by Hydrogen Atom Adsorption
Scientific Reports 3 (2013), 1210.

[162]
Reversible Change of the Spin State in a Manganese Phthalocyanine by Coordination of CO Molecule
Physical Review Letters 109 (2012), 147202.

[163] Min Hui Chang et al.
Tuning and sensing spin interactions in Co-porphyrin/Au with NH_3 and NO_2 binding
Physical Review B 100 (2019), 245406.

[164] Yu Wang et al.
Spin switch in iron phthalocyanine on Au(111) surface by hydrogen adsorption
J. Chem. Phys. 147 (2017), 134701.

[165] Howon Kim et al.
Switching and sensing spin states of Co–porphyrin in bimolecular reactions on Au (111) using scanning tunneling microscopy
ACS nano 7 (2013), 9312–9317.

[166] Maider Ormaza et al.
Controlled spin switching in a metallocene molecular junction
Nature communications 8 (2017), 1–8.

[167] Cosme Ayani et al.
Switchable molecular functionalization of an STM tip: from a Yu-Shiba-Rusinov tip to a Kondo tip
arXiv preprint arXiv:2206.02533 109 (2022), 147202.

[168] Yuqing Xing et al.
Reversible switching of Kondo resonance in a single-molecule junction
Nano Research 15 (2022), 1466–1471.

[169] Luigi Malavolti et al.
Tunable Spin-Superconductor Coupling of Spin 1/2 Vanadyl Phthalocyanine Molecules
Nano Lett. 18 (2018), 7955–7961.

[170] Chen Chen et al.
Local electronic structure of a single-layer porphyrin-containing covalent organic framework
ACS nano 12 (2018), 385–391.

[171] Johannes V. Barth
Molecular Architectonic on Metal Surfaces
Annual Review of Physical Chemistry 58 (2007). PMID: 17430091, 375–407.

[172] Shawulienu Kezilebieke et al.
Hierarchy of Chemical Bonding in the Synthesis of Fe-Phthalocyanine on Metal Surfaces: A Local Spectroscopy Approach
J. Phys. Chem. Lett. 5 (2014), 3175–3182.

[173] T. R. Umbach et al.
Ferromagnetic Coupling of Mononuclear Fe Centers in a Self-Assembled Metal-Organic Network on Au(111)
Phys. Rev. Lett. 109 (2012), 267207.

[174] Yuxu Wang et al.
Structural reconstruction and spontaneous formation of Fe polynuclears: a self-assembly of Fe–porphyrin coordination chains on Au (111) revealed by scanning tunneling microscopy
Physical Chemistry Chemical Physics 18 (2016), 14273–14278.

[175] K. Seufert et al.
Porphine Homocoupling on Au(111)
The Journal of Physical Chemistry C 123 (2019), 16690–16698.

[176] G. Binnig et al.
Tunneling through a controllable vacuum gap
Applied Physics Letters 40 (1982), 178–180.

[177] Gerd Binnig et al.
Surface studies by scanning tunneling microscopy
Physical Review Letters 49 (1982), 57.

[178] Gerd Binnig, Heinrich Rohrer
Scanning tunneling microscopy
Surface science 126 (1983), 236–244.

[179] G. C. B. Ménard
2D superconductors perturbed by local magnetism : from Yu-Shiba-Rusinov bound states to Majorana quasiparticles
Paris: Sorbonne University, 2016, p. 147202.

[180] R. Wiesendanger
SBound State in Superconuctors with Paramagnetic Impuriy
Ed. by Cambridge University Press. Vol. 109. Cambridge, 1994, p. 147202. ISBN: 9780511524356.

[181] J. Bardeen
Tunnelling from a Many-Particle Point of View
Physical Review Letters 6 (1961), 57–59.

[182] J. Tersoff, D. R. Hamann
Theory and Application for the Scanning Tunneling Microscope
Physical Review Letters 50 (1983), 1998–2001.

[183] J. Tersoff, D. R. Hamann
Theory of the scanning tunneling microscope
Physical Review B 31 (1985), 805–813.

[184] A. Selloni et al.
Voltage-dependent scanning-tunneling microscopy of a crystal surface: Graphite
Physical Review B 31 (1985), 2602–2605.

[185] A. Selloni et al.
Erratum: Voltage-dependent scanning-tunneling microscopy of a crystal surface: Graphite
Physical Review B 34 (1986), 7406–7406.

[186] C. Julian Chen
Theory of scanning tunneling spectroscopy
Journal of Vacuum Science & Technology A 6 (1988), 319–322.

[187] C Julian Chen, Walter F Smith
Introduction to scanning tunneling microscopy
American Journal of Physics 62 (1994), 573–574.

[188] C. Julian Chen
Tunneling matrix elements in three-dimensional space: The derivative rule and the sum rule
Physical Review B 42 (1990), 8841–8857.

[189] Roland Wiesendanger
Spin mapping at the nanoscale and atomic scale
Rev. Mod. Phys. 81 (2009), 1495–1550.

[190] B. Verlhac et al.
Atomic-scale spin sensing with a single molecule at the apex of a scanning tunneling microscope
Science 366 (2019), 623.

[191] Xue Zhang et al.
Electron spin resonance of single iron phthalocyanine molecules and role of their non-localized spins in magnetic interactions
Nature Chemistry 14 (2022), 59–65.

[192] Øystein Fischer et al.
Scanning tunneling spectroscopy of high-temperature superconductors
Reviews of Modern Physics 79 (2007), 353.

[193] Francesco Giazotto et al.
Opportunities for mesoscopics in thermometry and refrigeration: Physics and applications
Rev. Mod. Phys. 78 (2006), 217–274.

[194] Markus Ternes et al.
Subgap structure in asymmetric superconducting tunnel junctions
Physical Review B 74 (2006), 132501.

[195] V. Madhavan et al.
Tunneling into a Single Magnetic Atom: Spectroscopic Evidence of the Kondo Resonance
Science 280 (1998), 567–569.

[196] Ugo Fano
Effects of configuration interaction on intensities and phase shifts
Physical Review 124 (1961), 1866.

[197] HO Frota, LN Oliveira
Photoemission spectroscopy for the spin-degenerate Anderson model
Physical Review B 33 (1986), 7871.

[198] HO Frota
Shape of the Kondo resonance
Physical Review B 45 (1992), 1096.

[199] Henning Prüser et al.
Long-range Kondo signature of a single magnetic impurity
Nature Physics 7 (2011), 203–206.

[200] Henning Prüser et al.
Mapping itinerant electrons around Kondo impurities
Physical Review Letters 108 (2012), 166604.

[201] K. Nagaoka et al.
Temperature Dependence of a Single Kondo Impurity
Phys. Rev. Lett. 88 (2002), 077205.

[202] Yong-hui Zhang et al.
Temperature and magnetic field dependence of a Kondo system in the weak coupling regime
Nature communications 4 (2013), 1–6.

[203] Sebastian Frank, David Jacob
Orbital signatures of Fano-Kondo line shapes in STM adatom spectroscopy
Physical Review B 92 (2015), 235127.

[204] Donald M Eigler, Erhard K Schweizer
Positioning single atoms with a scanning tunnelling microscope
Nature 344 (1990), 524–526.

[205] DM Eigler et al.
Imaging Xe with a low-temperature scanning tunneling microscope
Physical Review Letters 66 (1991), 1189.

[206] Gregory Czap et al.
Probing and imaging spin interactions with a magnetic single-molecule sensor
Science 364 (2019), 670–673.

[207] Wilson Ho
Single-molecule chemistry
The Journal of chemical physics 117 (2002), 11033–11061.

[208] Ignacio Horcas et al.
WSXM: A software for scanning probe microscopy and a tool for nanotechnology
Review of scientific instruments 78 (2007), 013705.

[209]
ESI Group
2012.

[210] Pauli Virtanen et al.
SciPy 1.0: fundamental algorithms for scientific computing in Python
Nature methods 17 (2020), 261–272.

[211] William H Press, Saul A Teukolsky
Savitzky-Golay smoothing filters
Computers in Physics 4 (1990), 669–672.

[212] JD Pillet et al.
Andreev bound states in supercurrent-carrying carbon nanotubes revealed
Nature Physics 6 (2010), 965–969.

[213] R. C. Dynes, V. Narayanamurti, J. P. Garno
Direct Measurement of Quasiparticle-Lifetime Broadening in a Strong-Coupled Superconductor
Phys. Rev. Lett. 41 (1978), 1509–1512.

[214] Ronald D Parks
Superconductivity: In Two Volumes: Volume 1
Vol. 1. Routledge, 2018, p. 147202.

[215] Andrei Nikolaevich Tikhonov et al.
Numerical methods for the solution of ill-posed problems
Vol. 328. Springer Science & Business Media, 1995, p. 147202.

[216]
Productionizing and scaling python ML workloads simply | Ray
2012.

[217]
NumPy/SciPy-compatible Array Library for GPU-accelerated Computing with Python
2012.

[218] HE Farnsworth et al.
Ion Bombardment-Cleaning of Germanium and Titanium as Determined by Low-Energy Electron Diffraction
Journal of Applied Physics 26 (1955), 252–253.

[219] Kuppusamy Senthil Kumar, Mario Ruben
Emerging trends in spin crossover (SCO) based functional materials and devices
Coordination Chemistry Reviews 346 (2017), 176–205.

[220] Gábor Molnár et al.
Spin crossover nanomaterials: from fundamental concepts to devices
Advanced Materials 30 (2018), 1703862.

[221] Jens Kügel et al.
Jahn-Teller Splitting in Single Adsorbed Molecules Revealed by Isospin-Flip Excitations
Physical Review Letters 121 (2018), 226402.

[222] J. V. Barth et al.
Scanning tunneling microscopy observations on the reconstructed Au(111) surface: Atomic structure, long-range superstructure, rotational domains, and surface defects
Phys. Rev. B 42 (1990), 9307–9318.

[223] S. LaShell, B. A. McDougall, E. Jensen
Spin Splitting of an Au(111) Surface State Band Observed with Angle Resolved Photoelectron Spectroscopy
Phys. Rev. Lett. 77 (1996), 3419–3422.

[224] W. Chen et al.
Scanning Tunneling Microscopy Observation of an Electronic Superlattice at the Surface of Clean Gold
Phys. Rev. Lett. 80 (1998), 1469–1472.

[225] J.A. Meyer et al.
Preferential island nucleation at the elbows of the Au(111) herringbone reconstruction through place exchange
Surface Science 365 (1996), L647–L651.

[226] Sylvain Clair et al.
Monitoring Two-Dimensional Coordination Reactions: Directed Assembly of CoTerephthalate Nanosystems on Au(111)
J. Phys. Chem. B 110 (2006), 5627–5632.

[227] K. Schouteden, P. Lievens, C. Van Haesendonck
Fourier-transform scanning tunneling microscopy investigation of the energy versus wave vector dispersion of electrons at the Au(111) surface
Phys. Rev. B 79 (2009), 195409.

[228] Willi Auwärter et al.
Porphyrins at interfaces
Nature chemistry 7 (2015), 105–120.

[229] Howon Kim et al.
Mapping the electronic structures of a metalloporphyrin molecule on Au(111) by scanning tunneling microscopy and spectroscopy
Physical Review B 80 (2009), 245402.

[230] Yingzheng Gao et al.
Manipulation of the magnetic state of a porphyrin-based molecule on gold: From Kondo to quantum nanomagnet via the charge fluctuation regime
arXiv preprint arXiv:2301.01101 109 (2023), 147202.

[231] Xiangzhi Meng et al.
Controlling the Spin States of FeTBrPP on Au (111)
ACS Nano 109 (2022), 147202.

[232] Yu Wang, Xiao Zheng, Jinlong Yang
Environment-modulated Kondo phenomena in FePc/Au(111) adsorption systems
Physical Review B 93 (2016), 125114.

[233] L. Gao et al.
Site-Specific Kondo Effect at Ambient Temperatures in Iron-Based Molecules
Physical Review Letters 99 (2007), 106402.

[234] Xiaoli Wang et al.
Precise Control of Local Spin States in an Adsorbed Magnetic Molecule with an STM Tip: Theoretical Insights from First-Principles-Based Simulation
J. Phys. Chem. Lett. 9 (2018), 2418–2425.

[235] Ying-Shuang Fu et al.
Identifying Charge States of Molecules with Spin-Flip Spectroscopy
Physical Review Letters 103 (2009), 257202.

[236] P. Giannozzi et al.
Quantum ESPRESSO: A modular and open-source software project for quantum simulations of materials
J. Phys.: Condens. Matter 21 (2009), 395502.

[237] P. Giannozzi et al.
Advanced capabilities for materials modelling with Quantum ESPRESSO
J. Phys.: Condens. Matter 29 (2017), 465901.

[238] Peter E Blöchl
Projector augmented-wave method
Physical review B 50 (1994), 17953.

[239] John P. Perdew, Kieron Burke, Matthias Ernzerhof
Generalized Gradient Approximation Made Simple
Phys. Rev. Lett. 77 (1996), 3865–3868.

[240] David Jacob
Simulation of inelastic spin flip excitations and Kondo effect in STM spectroscopy of magnetic molecules on metal substrates
Journal of Physics: Condensed Matter 30 (2018), 354003.

[241] J. FernÁndez, A. A. Aligia, A. M. Lobos
Valence fluctuations in a lattice of magnetic molecules: Application to iron(II) phtalocyanine molecules on Au(111)
EPL (Europhysics Letters) 109 (2015), 37011.

[242] R Žitko et al.
Iron phthalocyanine on Au (111) is a "non-Landau" Fermi liquid
Nature communications 12 (2021), 1–9.

[243] Sergey Trishin et al.
Moiré Tuning of Spin Excitations: Individual Fe Atoms on $\mathrm{MoS_2/Au(111)}$
Physical Review Letters 127 (2021), 236801.

[244] EI Rashba
Symmetry of energy bands in crystals of wurtzite type. 1. Symmetry of bands disregarding spin-orbit interaction
Soviet Physics-Solid State 1 (1959), 368–380.

[245] Michael Ruby et al.
Experimental Demonstration of a Two-Band Superconducting State for Lead Using Scanning Tunneling Spectroscopy
Phys. Rev. Lett. 114 (2015), 157001.

[246] J. R. Schrieffer, D. J. Scalapino, J. W. Wilkins
Effective Tunneling Density of States in Superconductors
Phys. Rev. Lett. 10 (1963), 336–339.

[247] D. J. Scalapino, J. R. Schrieffer, J. W. Wilkins
Strong-Coupling Superconductivity. I
Phys. Rev. 148 (1966), 263–279.

[248] GM Eliashberg
Interactions between electrons and lattice vibrations in a superconductor
Sov. Phys. JETP 11 (1960), 696–702.

[249] D Rainer, JA Sauls
Strong-coupling theory of superconductivity
In: Superconductivity: From Basic Physics to the Latest Developments. Vol. 109. World Scientific, 1995, pp. 45–78.

[250] Léon Van Hove
The Occurrence of Singularities in the Elastic Frequency Distribution of a Crystal
Phys. Rev. 89 (1953), 1189–1193.

[251] Andrea Floris et al.
Two-band superconductivity in Pb from ab initio calculations
Phys. Rev. B 75 (2007), 147202.

[252] David Peyrot, Fabien Silly
On-surface synthesis of two-dimensional covalent organic structures versus halogen-bonded self-assembly: Competing formation of organic nanoarchitectures
ACS nano 10 (2016), 5490–5498.

[253] Xing Lu et al.
Scanning tunneling microscopy of metal phthalocyanines: d7 and d9 cases
Journal of the American Chemical Society 118 (1996), 7197–7202.

[254] Mehdi Bouatou et al.
Direct Observation of the Reduction of a Molecule on Nitrogen Pairs in Doped Graphene
Nano Letters 20 (2020). PMID: 32830982, 6908–6913.

[255] B. Cirera et al.
Lanthanide-porphyrin species as Kondo irreversible switches through tip-induced coordination chemistry
Nanoscale 13 (2021), 8600–8606.

RÉSUMÉ

La réalisation de nouveaux états quantiques tels que les états topologiques a suscité une grande attention dans les études actuelles sur la matière condensée. Une façon prometteuse d'induire des propriétés topologiques est de construire des assemblages d'impuretés magnétiques à la surface des supraconducteurs conventionnels, ce qui a déjà été largement mis en œuvre et a donné des résultats fructueux. Dans cette thèse, nous avons utilisé la microscopie et la spectroscopie à effet tunnel pour étudier les assemblages de molécules magnétiques auto-organisés sur des surfaces normales et supraconductrices. Grâce aux propriétés uniques des molécules organiques à base de porphyrine, nous avons réussi à contrôler l'état magnétique d'une molécule S = 1 sur la surface Au(111) par effet de fluctuation de charge, ce qui ouvre une nouvelle perspective sur le comportement de valence mixte d'un aimant quantique. Nous avons également révélé la présence de différents régimes pour une molécule S = 1 sur une surface supraconductrice de Pb(110), où la molécule peut présenter des états Yu-Shiba-Rusinov dans le gap, une excitation de retournement de spin inélastique dehors le gap ou la coexistence de ces deux. Nos résultats montrent comment les molécules magnétiques à base de porphyrine modifient leurs propriétés magnétiques sur différentes surfaces, ce qui aidera la communauté à mieux comprendre ce sujet.

MOTS CLÉS

Supraconductivité, états Yu-Shiba-Rusinov, spectroscopie à effet tunnel, microscopie à effet tunnel, effet Kondo, excitation inélastique par retournement de spin, Au(111), Pb(110), impureté magnétique, molécule magnétique, réseaux moléculaires auto-assemblés, fluctuation de charge, anisotropie magnétique, système corrélé.

ABSTRACT

Realisation of novel quantum states such as topological states has drawn great attention in present condensed matter studies. One promising way to induce topological properties is to build magnetic impurity assemblies on the surface of conventional superconductors, which has already been widely implemented and produced fruitful results. In this thesis we have used scanning tunneling microscopy and spectroscopy to study self-organized magnetic molecule assemblies on normal and superconductor surfaces. Because of the unique properties of porphyrin-based organic molecules, we succeed in controlling magnetic state of a S = 1 molecule on Au(111) surface by charge fluctuation effect, which opens a new sight into mixed-valence behavior of a quantum magnet. And we have also revealed the presence of different regimes for a S = 1 molecule on superconducting Pb(110) surface where the molecule can exhibit in-gap Yu-Shiba-Rusinov states, out-gap inelastic spin-flip excitation or the coexistence of them. Our results show how porphyrin-based magnetic molecules change their magnetic properties on different surfaces, which will help the community to have a better understanding on this topic.

KEYWORDS

Superconductivity, Yu-Shiba-Rusinov bound states, scanning tunneling spectroscopy, scanning tunneling microscopy, Kondo effect, inelastic spin-flip excitation, Au(111), Pb(110), magnetic impurity, magnetic molecule, self-assembled molecular lattices, charge fluctuation, magnetic anisotropy, correlated system.